# A Computational Study of a Lifting Wing in Close Proximity to a Moving Ground Plane

Evan M. Smuts



A dissertation submitted to the
Department of Mechanical Engineering,
University of Cape Town,
in partial fulfilment of the requirements for the degree of
Master of Science in Engineering

February 2009

# DECLARATION

I know the meaning of plagiarism and declare that all the work in the document, save for that which is properly acknowledged, is my own.

Signature ……

Name: Smuts, E. M.

# ABSTRACT

Commercial software packages Fluent® and Gambit® were used to develop a 3D Computational Fluid Dynamics (CFD) model to determine the aerodynamic characteristics of a DHMTU lifting wing flying in ground effect. In particular, the performance of the wing in the presence of waves was of interest. But first a reliable computational model had to be developed to simulate waves flowing past the wing. Therefore the objective of this study was to develop such a model.

Initially, the model was tested in the presence of a flat ground plane, before modifying the model to include the presence of waves in the ground plane. A flat ground plane was used so that the model could be validated against previously obtained experimental data. The lift, drag, and pitching moment coefficients were determined at a Reynolds Number of 2.21 x $10^5$ for four relative ground clearances ($h_0$) of 0.06, 0.12, 0.50 and 1.3 and seven angles of attack, between 1 and 13 degrees, in two degree increments. It was found that the lift coefficient determined by the CFD model compared well to the experimental values for the mid-range angles of attack. The drag coefficient values were very inaccurate for most cases, sometimes with more than a 50% error. The pitching moment coefficient values were similar to the experimental ones.

The inclusion of waves into the ground plane was achieved by using a sliding mesh. The wavy ground plane was modelled as a solid boundary, and then made to slide past the stationary wing. For the purposes of this project, the waves were made to move at the same velocity as the free stream velocity. The wing was set at 7° and 11° angles of attack and then tested against four different wavelengths, as well as at four different wave heights. Using the reliability of the flat ground plane model as a reference, it was found that the wavy ground plane model provided reliable force and moment coefficients. From the results, it was concluded that the wing was largely affected by the change in wave heights (for a constant wavelength), but less affected by a changing wavelength (for a constant wave height).

# ACKNOWLEDGEMENTS

I would like to extend my gratitude to the following people for their valuable help and support during the course of the project:

Prof. Sayers: for being my supervisor and offering guidance during the course of the project.

Steven Rhodes: for his help at understanding the nature of his experimental work.

Dr. Meyer: for his helpful talks on the inner-workings of CFD.

Jean-Paul Pelteret, Case Bakker, and Harish Appa: for their help and guidance with the software packages Fluent® and Gambit® and as well as the Ubuntu operating system.

# TABLE OF CONTENTS

Abstract i
Acknowledgements ii
Table of Contents iii
List of Figures viii
List of Tables x
Glossary xi
List of Symbols xiii

1. Introduction 1
2. Aerodynamic Theory and Ground Effect 6
    2.1 Trailing Vortices and Induced Drag 6
        2.1.1 Spanwise Flow Variation over a Finite Span Aerofoil 6
        2.1.2 Lift and Downwash 7
        2.1.3 Induced Drag 8
    2.2 The Effect of a Ground Plane 9
        2.2.1 Restricted Development of Wingtip Vortices 9
        2.2.2 Increased Static Pressure on the Underside of the Wing 10
    2.3 Height Classification of Ground Effect 10
    2.4 Waves in the Ground Plane 13
        2.4.1 Wave Profile 13
        2.4.2 Wave period and Frequency 14
        2.4.3 Wave Speed 15
    2.5 The Effect of Waves on the Airflow near the Ground 15
        2.5.1 Shear-Flow Model of Wave Formation 15
        2.5.2 The “Sheltering Effect” of Waves 17
        2.5.3 A Final Note on the Airflow over Waves 17
    2.6 Dynamic Response of a Wing near a Wavy Ground Plane 17
        2.6.1 Factors Affecting the Wing near a Wavy Ground Plane 18
        2.6.2 Fluctuations in the Force Coefficients 19

2.6.3 Phase Angle Offset 20
2.6.4 Course Angle 21
3. Computational Modelling With CFD 22
3.1 Description of the CFD Software 22
3.1.1 The Pre-Processor 22
3.1.2 The Solver 22
3.1.3 The Post-Processor 23
3.2 Mesh Generation 23
3.2.1 Tetrahedral Cells vs. Hexahedral Cells 23
3.2.2 Structured vs. Unstructured Meshes 24
3.2.3 Conventional Aerofoil Mesh Models 25
3.3 Turbulence Modelling 26
3.3.1 The k-ε Model 27
3.3.2 The k-ω Model 28
3.3.3 The Spalart-Allmaras Model 28
3.4 Treatment of Boundary Layers 29
3.4.1 Wall Functions vs. Near Wall Model 29
3.4.2 Mesh Requirements for Turbulence Models and $y+$ Values 29
4. Development of a 3D Model for a Flat Ground Plane 31
4.1 Problem Identification 31
4.1.1 Angle of Attack ($\alpha$) 31
4.1.2 Relative Ground Clearance ($h_0$) 32
4.1.3 Hardware and Software Specifications 32
4.2 Geometric Model 33
4.2.1 Experimental Model 33
4.2.2 DHMTU Aerofoil Profile 34
4.3 Mesh Generation with GAMBIT® 35
4.3.1 Computational Domain Shape 35
4.3.2 Boundary Layer Mesh 35
4.3.3 Merging the Structured and Unstructured Grids 36
4.3.4 Mesh Distribution along the Length of the Wing 38
4.3.5 Chordwise Cell Distribution 39

4.3.6 Turbulent Viscosity Problems 40
4.4 Boundary Conditions 41
4.4.1 Inlet – Velocity Inlet 42
4.4.2 Outlet – Outflow 43
4.4.3 Ground Plane – Wall 43
4.4.4 Wing – Wall 45
4.4.5 Side and Top Faces – Velocity Inlet 45
4.4.6 Symmetry Boundary Condition 45
4.5 Computational Domain Size 45
4.6 Solver Settings 46
4.7 Turbulence Modelling 48
4.8 Boundary Layer Mesh 49
4.9 Residuals and Force Monitors 50
4.10 Initialisation and Iteration 50
5. Development of a 3D Model for a Wavy Ground Plane 51
5.1 Waves in the Ground Plane 51
5.1.1 Wavelengths and Wave Heights 51
5.1.2 Wave Speed 52
5.1.3 Phase Angle ($\varphi$) 52
5.2 Methods of Wave Modelling 53
5.2.1 Multi-Phase Model 53
5.2.2 Sliding Mesh Model 54
5.3 Implementation of the Sliding Mesh Model 55
5.3.1 Sliding Region 55
5.3.2 Length of the Sliding Region 56
5.3.3 Meshing the New Sliding Region 58
5.4 Boundary Conditions for the Sliding Mesh 60
5.4.1 Interface between Sliding and Stationary Regions 60
5.4.2 Wavy Ground Plane – Wall 61
5.4.3 Stationary and Sliding Outlet Boundaries – Outflow 61
5.4.4 Other Boundary Conditions 61
5.5 Time Dependant Solver Settings 62

5.5.1 Time Step Size 62
5.5.2 Number of Iterations per Time Step 63
5.5.3 Varying the Time Step Size 64
5.5.4 Maximum Calculation Time 64
5.6 Initialisation and Iteration of the Wavy Ground Plane Model 65
6. Results for the Flat Ground Plane 67
6.1 Lift Coefficient 67
6.2 Drag Coefficient 68
6.3 Pitching Moment Coefficient 69
6.4 Observations from CFD Post-Processing 70
6.4.1 Increased Static Pressure on Lower Surface of Wing 70
6.4.2 Increased Trailing Edge Pressure and Early Flow Separation 71
6.4.3 Increased Upwash Due to the Presence of the Ground Plane 73
6.4.4 Restricted Vortex Development 73
7. Results for the Wavy Ground Plane 76
7.1 Lift Coefficient 77
7.2 Drag Coefficient 80
7.3 Pitching Moment Coefficient 81
7.4 Phase Angle 82
7.5 Non-Dimensional Number Plots against Strouhal Number 83
7.5.1 Lift Coefficient vs. Strouhal Number 84
7.5.2 Phase Angle vs. Strouhal Number 85
7.6 Observations from CFD Post-Processing 86
7.6.1 Increased Static Pressure on Lower Surface of Wing 86
7.6.2 Vortex Development over the Waves 88
8. Conclusions 90
8.1 Reasonable Performance of the Flat Ground Plane Model 90
8.2 Successful Modelling of Waves with Sliding Mesh Model 91
8.3 Turbulent Viscosity Problems and Mesh Quality 92
8.4 Performance of the Wing in the Presence of Waves 92
9. Recommendations 93
9.1 Resolve Poor $C_D$ Performance 93

9.2 Investigate the Performance of a Finer Mesh 93
9.3 Investigate Wing Performance at Smaller $h_0$ with a Wavy Ground Plane 93
10. References 94

# LIST OF APPENDICES

A –Results for Flat Ground Plane A-1
B –Results for Wavy Ground Plane B-1
C – Summary of Mesh Settings C-1
D – Wave profile Data D-1

# LIST OF FIGURES

Figure 1: The Russian Ekranoplan developed during the Cold War 1
Figure 2: Cruising power requirements of different forms of transport 2
Figure 3: A small four passenger craft built for recreational purposes 3
Figure 4: Flow over a finite span aerofoil resulting in trailing vortices 7
Figure 5: Effect of downwash on the wing 8
Figure 6: Streamlines illustrating the flow field in and out of ground effect 9
Figure 7: Pressure distribution on a wing while in and out of ground effect 10
Figure 8: Flow field at very large clearances 11
Figure 9: Flow field at large clearances 12
Figure 10: Flow field at medium clearances 12
Figure 11: Flow field at small clearances 12
Figure 12: Flow field at very small clearances 13
Figure 13: Wave diagram with labels 14
Figure 14: Airflow in close proximity to wave surface 16
Figure 15: Vortices formed due to the reversal of flow in close proximity to wave surface 17
Figure 16: Variables affecting ground effect flow for the wavy ground plane 18
Figure 17: Amplitude of wave-induced unsteady $C_L$ vs. Strouhal number 19
Figure 18: Phase angle of wave-induced unsteady lift force vs. Strouhal number 21
Figure 19: Hex (a, b) and Tet (c, d) mesh cells 24
Figure 20: Unstructured (left) and structured mesh patterns 24
Figure 21: Different meshes for an aerofoil in the free stream 26
Figure 22: Variables affecting the flat ground plane model 32
Figure 23: Picture showing Rhodes' experimental setup in the wind tunnel 33
Figure 24: Profile shape of the DHMTU 10-40-2-10-2-60-21-5 aerofoil 34
Figure 25: Boundary layer mesh around wing and domain mesh 36
Figure 26: Pave mesh joining the boundary layer mesh and domain mesh 37
Figure 27: Unstructured mesh on the wingtip 37
Figure 28: Concentration of cells at the wingtip in an H-type grid 38

Figure 29: Cell distribution along the span of the wing 39
Figure 30: Cell distribution around the wing 40
Figure 31: Boundary conditions for the flat ground plane 41
Figure 32: Velocity inlet specification window in Fluent® 43
Figure 33: Moving wall specification window in Fluent® 44
Figure 34: Dimensions of the computational domain 46
Figure 35: Phase shift between the force coefficients and the wave profile 53
Figure 36: Original mesh domain with new sliding mesh region below 56
Figure 37: Comparison of different length sliding regions (2D) 57
Figure 38: Start and end position of the sliding mesh (with dimensions) 58
Figure 39: $C_L$ comparison between different sliding region mesh densities 59
Figure 40: Side view of sliding region mesh 59
Figure 41: Boundary conditions for the sliding mesh 62
Figure 42: $C_L$ variation with changing time step size (2D) 63
Figure 43: Time dependant solver settings 66
Figure 44: $C_L$ vs. $\alpha$ for both experimental and CFD results 68
Figure 45: $C_D$ vs. $\alpha$ for both experimental and CFD results 69
Figure 46: $C_{M1/4MAC}$ vs. $\alpha$ for both experimental and CFD results 70
Figure 47: Static pressure plots on the lower surface of the wing for each $h_0$ 71
Figure 48: Pressure (top) and velocity plots of wing at $h_0$ of 0.06 and 1.30 72
Figure 49: Velocity vectors for $h_0$ 1.30 (left) and 0.06 showing upwash at leading edge 73
Figure 50: Front view showing vortex position and size change due to changing $h_0$ 74
Figure 51: Top view illustrating the development of the wingtip vortex with changing $h_0$ 75
Figure 52: $C_L$ for wing at 7° for each wavelength and wave height combination 77
Figure 53: $C_L$ vs. wavelength for $\alpha$ = 7° (lines of constant wave height) 78
Figure 54: $C_L$ vs. wave height for $\alpha$ = 7° (lines of constant wavelength) 79
Figure 55: $C_L$ vs. flow time for different wavelengths ($\alpha$ = 7°) 80
Figure 56: $C_D$ for wing at 7° for each wavelength and wave height combination 81
*Figure 57:* $C_{M1/4MAC}$ for wing at 7° for each wavelength and wave height combination 82

*Figure 58:* $C_L$ phase angle vs. relative wavelength ($\alpha = 7°$) (lines of constant wave height) 83
Figure 59: $F/F_0$ ratio vs. Strouhal Number ($\alpha = 7°$) 85
*Figure 60:* $C_L$ phase angle vs. relative wavelength ($\alpha = 7°$) (lines of constant wave height) 86
Figure 61: Pressure plots of underside of wing at 7° for a wavelength of 4*c* and a wave height of 4*h* 87
Figure 62: Flow pathlines over a wavy ground plane ($\alpha = 7°$) 89

## LIST OF TABLES

Table 1: Frequency of occurrence of different wave heights 14
Table 2: Hardware and software specifications 32
Table 3: Accuracy of wind tunnel balance measurements 34
Table 4: CFD solver specifications 47
Table 5: Discretisation schemes 47
Table 6: Under-relaxation factors 47
Table 7: Turbulence model comparison for the 2D NACA 2612 aerofoil model 48
Table 8: Spalart-Allmaras turbulence model constants 49
Table 9: Comparison of new spanwise mesh with old mesh 55

# GLOSSARY

| | |
|---|---|
| Boundary Conditions | the settings at the perimeter of the computational domain defining how the fluid should interact with the boundaries. |
| Boundary Layer | the viscous affected region of flow close to the body's surface. |
| Cell | an individual area/volume in which the governing flow equations are cells. Many cells form the mesh. |
| Computational Domain | the region in which the flow will be calculated. This region is meshed with cells. |
| Convergence | the point at which the solution is no longer changing with successive iterations. |
| Drag | force on the body acting in the direction of the flow. It is a combination of friction and pressure drag acting on the body. |
| Friction Drag | the drag on the body caused by the viscous effect of the fluid on the body. |
| Ground Effect | the altered flow pattern around a wing created when flying in close proximity to a solid ground plane. |
| Laminar Flow | orderly flow, with fluid pathlines flowing parallel to each other. |
| Leading Edge/Face | the face or edge of a body that is the furthest upstream in the flow. |
| Lift | force acting on a body. It is perpendicular to the direction of fluid flow. |
| MAC | Mean Aerodynamic Chord – the mean chord line of the wing. |
| Mesh | the structure remaining after dividing the computational domain into finite volumes/areas in which the solution variables can be calculated. |
| Pressure Drag | the drag on a body caused by the pressure differential between the front and back of the body. |
| Reynolds Number | a parameter representing the ratio between the inertial and viscous forces of the fluid particles. |
| Separation | it is the process whereby the boundary layer begins to stagnate and physically leave the body's surface. |

| | |
|---|---|
| Steady State | flow effects are considered constant, with all time dependant effects averaged out, also known as non-transient. |
| Transient | modelling the flow as it changes with time, thus capturing time dependant effects, also known as time dependent. |
| Turbulent Flow | flow characterised by continuous disorderly fluctuations. |
| Wake | the region of flow behind a body once the boundary layer has separated. It is characterised by turbulence and low pressure. |
| WIG | Wing-In-Ground Effect –vehicles that operate in ground effect can be collectively known as WIG vehicles. |

# LIST OF SYMBOLS

**GREEK**

| | |
|---|---|
| $\alpha$ | angle of attack, usually in degrees (°) |
| $\beta$ | course angle (°) |
| $\varepsilon$ | turbulent kinetic energy dissipation rate ($m^2/s^3$) |
| $\lambda$ | wavelength (m) |
| $\mu$ | dynamic viscosity (kg/m.s) |
| $\mu_t$ | turbulent viscosity (kg/m.s) |
| $\omega$ | specific turbulent kinetic energy dissipation rate ($s^{-1}$) |
| $\varphi$ | phase (offset) angle (°) |
| $\rho$ | density ($kg/m^3$) |
| $\tau$ | shear stress (Pa) |

**ROMAN**

| | |
|---|---|
| $A$ | reference area of wing (= $bc$) ($m^2$) |
| $a_W$ | wave amplitude (m) |
| $b$ | wing span (m) |
| $c$ | wing chord (m) |
| $C_D$ | drag coefficient |
| $C_L$ | lift coefficient |
| $C_M$ | pitching moment coefficient |
| $C_{M1/4MAC}$ | pitching moment coefficient corrected to be at ¼ MAC |
| $D$ | drag force (N) |
| $f$ | wave frequency (Hz) |
| $h$ | height of wing trailing edge above ground plane (m) |
| $h_0$ | relative ground clearance (= $h/c$) |
| $k$ | turbulent kinetic energy ($m^2/s^2$) |
| $k$ | Strouhal number |
| $l$ | characteristic length (chord in case of aerofoil) (m) |
| $L$ | lift force (N) |
| $L/D$ | lift/drag ratio |
| $L_W$ | relative wavelength ($\lambda/c$) |

| | |
|---|---|
| $M$ | pitching moment (N.m) |
| $Re$ | Reynolds number |
| $T$ | wave period (s) |
| $v$ | fluid velocity (m/s) |
| $y_p$ | distance from wall to mid-point of first cell adjacent to the wall (m) |

# 1. INTRODUCTION

Ground effect is a phenomenon that is known to all aircraft pilots. It is the tendency of their aircraft to "float" in the air as they approach the ground during landing. Conversely, it is also the effect that some pilots exploit to aid take-off. Wings operating in ground effect display different aerodynamic characteristics to those that operate at high altitude, far away from a ground plane. Flying close to a ground plane dramatically increases the lift and reduces the drag experienced by the wing, resulting in the floating sensation experienced by pilots. Any vehicle that takes advantage of this ground effect is known as a Wing-In-Ground Effect (WIG) vehicle.

The high lift-drag (*L/D*) ratio of wings operating in ground effect has made WIG technology very appealing to many groups, particularly military organisations. In fact, ground effect technology was being studied as early as the 1920's, and in 1935 a craft was designed and constructed by Finnish engineer Kaario which was able to take advantage of the ground effect [1]. While there were a number of developments in WIG technology during the 1900's, the bulk of its development was conducted during the Cold War era. Russian Rostislav Alekseev and German Alexander Lippisch, who worked independently on the technology, made significant contributions to the field. The Russian Ekranoplans (ekran - screen, plan – plane) were flying behemoths (see Figure 1), over 100m long and weighing up to 550 tonnes. They could travel at speeds over 400 km/h, just a few meters above the ground [2].



Figure 1: The Russian Ekranoplan developed during the Cold War [2]

The western world only took the technology seriously after US spy satellites discovered a WIG aircraft developed by the Russians near the Caspian Sea. This large craft was initially mistaken for an incomplete aircraft, and was dubbed the Caspian Sea Monster. The importance of WIG technology to the military was clear. It allowed for the creation of an aircraft with a large load carrying capacity that was able to travel much faster than any naval fleet.

Large WIG craft can have high lift/drag ratios of 15 to 30, and can cruise at speeds between 100 and 400 km/h. In the commercial sector, this makes them ideally suited to fill the transport gap between low-cost/low-speed shipping and high-cost/high-speed aircraft. This is illustrated in the diagram of Figure 2, which shows the cruising power requirements per unit weight, the P/W ratio, of many modern forms of transport. When compared to other forms of high-speed transport, the efficiency of WIG aircraft is clear.

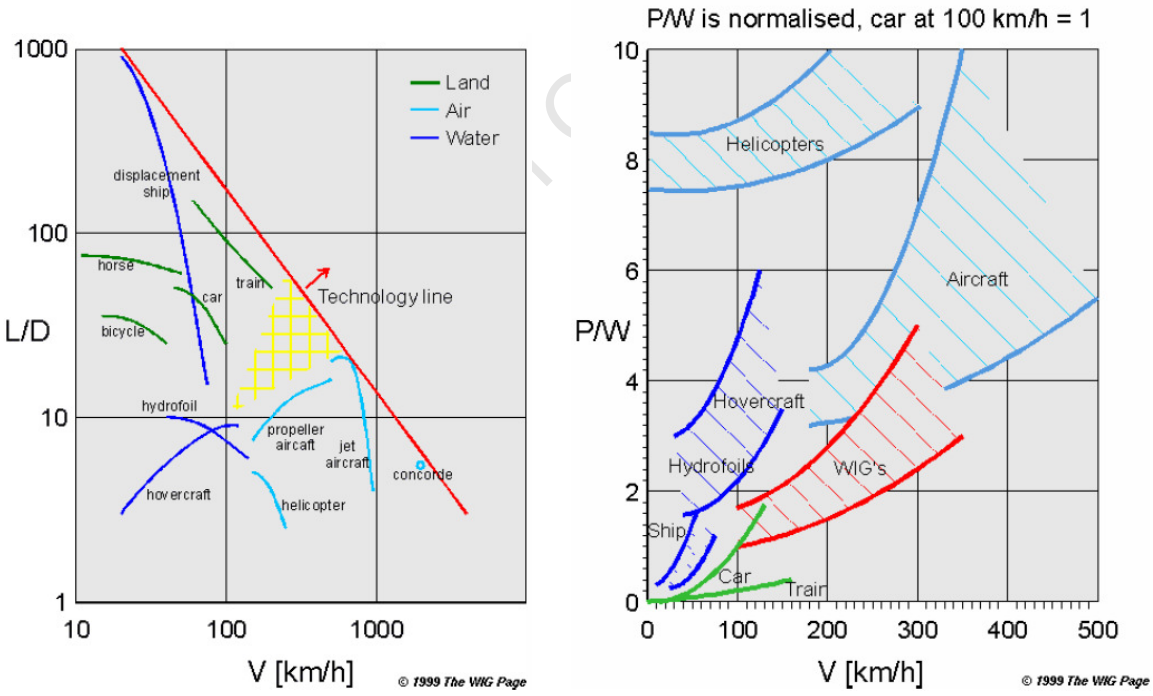


Figure 2: Cruising power requirements of different forms of transport [3]

A modern example of a WIG craft is Boeing's concept aircraft, the Pelican. Boeing claims the craft is capable of transporting 750 tons over 10,000 nautical miles (18,530 km) when cruising in ground effect, but can carry the same load only 6,500 nautical miles

(12,045 km) when out of ground effect [2]. This further illustrates the significance of utilising ground effect to improve transport efficiency.

Even with the benefits of WIG technology, WIG craft have failed to gain popularity in the commercial sector on any significant level. Due to the nature of large WIG craft, they tend to be very expensive to design and build, and so are not financially viable. Even some militaries have decided against WIG craft, mostly due to the high initial cost of design and production. With smaller craft, the efficiency benefits obtainable with larger WIG craft are not as pronounced, meaning that they are not always worth the extra cost of development. However, there are a few small enterprises using WIG craft as ferries, an example of which is shown in Figure 3.


Figure 3: A small four passenger craft built for recreational purposes [2]

One reason for the lack of interest in WIG craft is its requirement for an effectively flat ground plane, due to the low altitudes the vehicles travel at. Consequently, WIG technology is seen as unpractical for travelling over land. Variations in the gradient would decrease the speed that the craft can reach as it has to negotiate these obstacles. Therefore WIG craft are primarily developed for use over large bodies of open water, such as oceans, which act as the ground plane. Large bodies of water present some challenges of their own, namely the fact that the surface is not always entirely flat. Waves are commonplace on large bodies of water and consequently these WIG craft need complex control systems to maintain stability over the irregular water surface.

Most of the development of ground effect craft and their specialised airfoils have been carried out by various militaries or private companies. Consequently there is little quantitative data available on the performance of wings in ground effect, particularly for wings that are used to produce lift when in the presence of the ground, which is the type of ground effect that this report is concerned with. Two sources that have documented their experimental work on DHMTU wings are Rhodes [4] and Moore et al [5].

Based on the fact that WIG craft would spend most of their flying time over open water, a logical start for this project would be to look at the behaviour of the wing in the presence of waves in the ground plane. This is something which cannot be done easily in a wind tunnel experiment. Therefore the ground plane in the computational model was modified to mimic the form of waves travelling below the wing. Simulations with these wave shapes were performed in Fluent®. As there was no experimental data with which to compare these results, the strength of these results was judged according to the accuracy of the simulations used for the flat ground plane.

This report makes use of Computational Fluid Dynamics (CFD) to investigate the behaviour of a particular DHMTU wing when flying in ground effect. As CFD proves its usefulness, more and more work is being conducted on ground effect wings using CFD. However, most of the current work on wings in ground effect concentrates on using some sort of endplate on the wingtip to further enhance the benefits of flying in ground effect. Therefore, to the knowledge of the author, there is no current computational work on plain, lifting airfoils in ground effect.

In this study, the lift, drag, and pitching moment of the wing are measured. The pitching moment is an important factor when considering the stability of a WIG craft. As CFD is not yet an exact science, especially in complex flow regimes, it is important to verify any results with experimental data. Good experimental data will help validate the CFD results and aid in developing a suitable mesh/model setup that provides accurate results. To this end, the experimental data of Rhodes [4] will be used. Rhodes conducted a study of a single wing operating at different heights above a flat moving ground plane. The angle of attack of the wing was also altered. His studies may have been limited – only one wing

was tested – but his results would provide valuable data with which to establish a workable and accurate model for further CFD work on WIG's. The CFD software package that was used during this study was Fluent® from Ansys.

Therefore the objective of this study was to develop a 3D computational model to simulate the presence of waves flowing in the ground plane in close proximity to the wing. In order to do this, a model for a flat ground plane was first constructed and tested. Once a reliable model was obtained for a flat ground plane, it could be modified to include the effects of waves in the ground plane.

This report therefore documents the development of a 3D computational model of a wing flying in close proximity to a wavy ground plane. But first, the important flow features that characterise ground effect are introduced in Section 2, as well as some aspects of wavy ground planes. Section 3 introduces some basic concepts of computational modelling. Then the development of the model for the flat ground plane is discussed in Section 4. From the study of the flat ground plane, the model was extended to include waves in the ground plane. The development of this model is presented in Section 5. Following this, the results for the respective models are discussed in Sections 6 and 7. Finally the results are analysed and conclusions are drawn. Some recommendations were also made based on the conclusions.

# 2. AERODYNAMIC THEORY AND GROUND EFFECT

Ground effect is the name given to the aerodynamic characteristics that are inherent of vehicles travelling in close proximity to a ground plane. It is characterised by two separate interactions of the flow [6]. The first interaction is between the ground and the trailing vortices in the wake, while the second interaction, which usually only occurs at much lower levels of flight, is the influence that the ground has on the flow underneath the wing. This includes the interaction of the boundary layer on the underside of the wing, and the boundary layer on the ground.

## 2.1 TRAILING VORTICES AND INDUCED DRAG

Drag on an infinite-span, 2D aerofoil comprises of friction drag (friction on the wing surface) and form drag (the wake formed behind the aerofoil). But all "practical" wings are of finite span. The free end of a finite span wing introduces other effects into the flow regime surrounding the wing.

### 2.1.1 Spanwise Flow Variation over a Finite Span Aerofoil

A wing produces lift through a pressure difference between its upper and lower surface, with the pressures on the upper surface being generally lower than those on the lower surface. However, for a finite span, there can be no pressure discontinuity at the wing tips. Consequently, the pressure value at the tip must lie between the values of the upper and lower surface pressures at the root of the wing. Thus a spanwise pressure gradient is formed on both surfaces. On the upper surface the pressure increases from root to tip, while on the lower surface, the pressure decreases from root to tip.

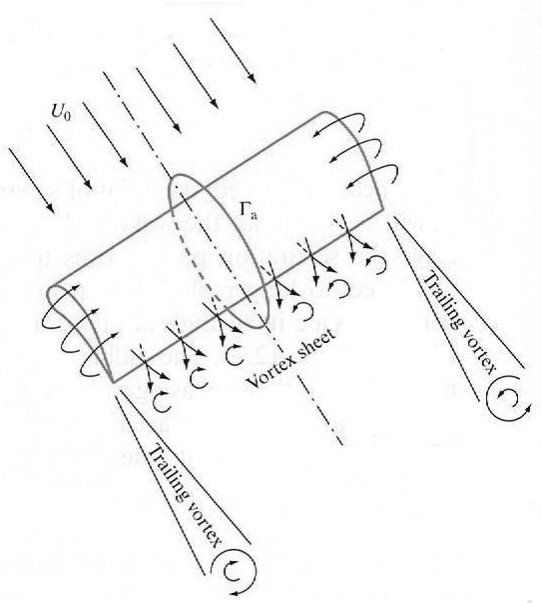


Figure 4: Flow over a finite span aerofoil resulting in trailing vortices [7]

Thus the air flowing over the upper surface will acquire an inward velocity component, while the air flowing over the lower surface will have an outward velocity component. Therefore, at any spanwise position, the flow leaving the wing will be moving in two different directions. Consequently vortices will be continuously formed and then shed along the trailing edge. But these vortices are unstable, and quickly merge to form two large vortices leaving the wing at a point near the wing tips [8]. These are the wing-tip, or trailing, vortices.

### 2.1.2 Lift and Downwash

The main consequence of these vortices is that the air leaving the wing acquires a downward velocity component. This phenomenon is known as induced downwash, or simply downwash.

The effect of downwash is to reduce the effective angle of attack of the wing by the downwash angle, $\varepsilon$ (see Figure 5). The lift of the wing is determined by this effective angle of attack ($\alpha_{eff}$), thus the wing is not able to produce as much lift as would be expected from its geometric angle of attack ($\alpha$). Since $\varepsilon$ increases with increasing lift, the lift of a 3D wing increases less rapidly with increasing $\alpha$ than for a 2D wing which has no trailing vortices [9].

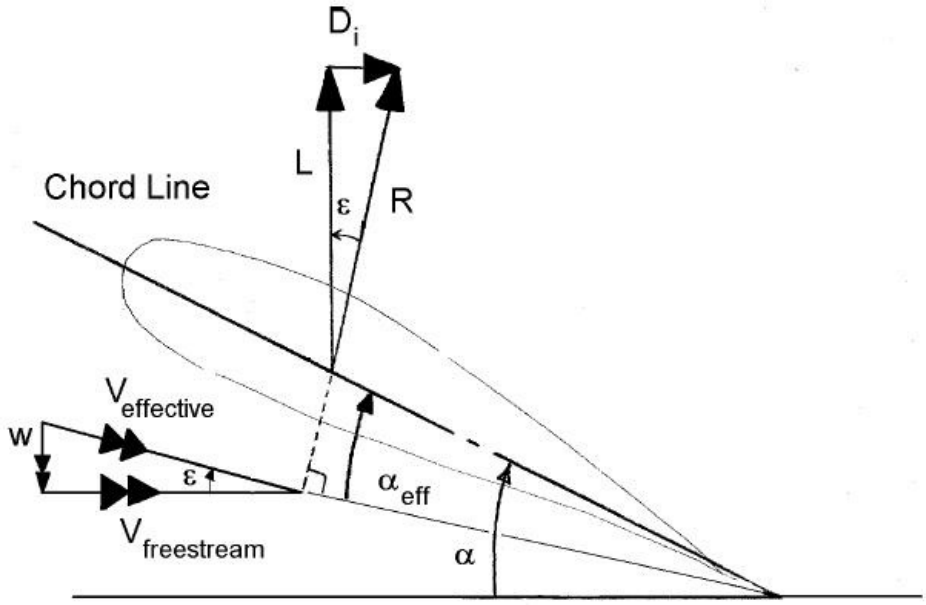


Figure 5: Effect of downwash on the wing [10]

A secondary effect of downwash is to alter the flow downstream of the wing. Other lifting surfaces, such as a tailplane, that are located downstream of the main wing will be influenced by the vortices leaving the main wing. Therefore tailplanes have to account for the large downward induced velocity components behind the main wing. This is an important consideration in terms of the stability of the aircraft [8].

### 2.1.3 Induced Drag

As a result of the downwash altering the effective flow velocity, the lift force vector that is generated by the wing is angled rearwards. When the resulting forces are resolved, it is found that an extra drag component has been created. This drag component is known as induced drag, since it is formed as a result of the induced flow generated by the trailing vortices [8]. Given that induced drag is formed a result of the wing generating lift, it can also be called drag due to lift. The force component of induced drag, labelled $D_i$, is illustrated in Figure 5. It should be noted that induced drag is only a characteristic of finite length airfoils and not infinite length airfoils as it is a result of the trailing vortices formed at the tips of a finite length aerofoil. In fact, the further apart the wing-tip vortices are, the less effective they will be in generating downwash and its resultant drag. This explains the improved performance of high aspect ratio wings with respect to induced drag [9].

While induced drag can never be totally eliminated, it can be reduced, especially when flying in ground effect. Other types of drag, such as skin friction drag, are dependant on factors that are not directly changed when flying in close proximity to the ground. Therefore they are not significantly affected when flying in ground effect.

## 2.2 THE EFFECT OF A GROUND PLANE

Ground effect is the phenomenon caused by the presence of a solid boundary in close proximity to, and usually below, a wing that is generating lift. The boundary alters the flow of the air around the wing, resulting in an increase in the lift of the wing and a reduction in the induced drag of the wing. The effect becomes more pronounced the closer the wing is to the boundary.

### 2.2.1 Restricted Development of Wingtip Vortices

The change in the flow field around the wing has the effect of reducing the downwash angle, and thus increasing the effective angle of incidence of the wing. Accordingly, the resultant lift force is angled further forwards. This results in an increase of the resultant lift component and a reduction of the induced drag component, thus increasing the *L/D* ratio. An increase in the *L/D* ratio provides a gain in efficiency. The drag reduction provides the benefit of a reduced thrust, and therefore reduced fuel consumption requirement for cruising flight [10]. Figure 6 illustrates the change in the flow streamline pattern.



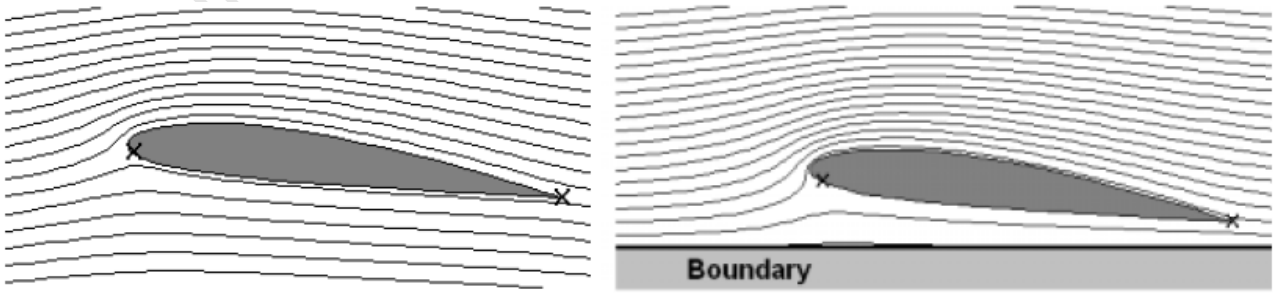


Figure 6: Streamlines illustrating the flow field in and out of ground effect [10]

### 2.2.2 Increased Static Pressure on the Underside of the Wing

The solid boundary does not allow the flow under the wing to expand as it would in free air, thus raising the pressure under the wing [10]. Since the total pressure remains constant throughout the flow field, the sum of the static and dynamic pressures must also remain constant. As the flow is forced into the region between the wing and the ground, the decrease in dynamic pressure is transformed into a rise in static pressure. The resulting pressure distribution causes a net increase in the lift. This rise in the static pressure is often referred to as 'ram pressure' [1].

A further result of the changing pressure field around the wing is its effect on the pitching moment of the wing. Wings generally have a nose down pitching moment in cruising flight. Ground effect causes this moment to increase [10]. The ram pressure on the underside of the wing produces a near uniform pressure distribution along the lower surface of the wing, while the distribution along the upper surface is not significantly altered [10] (see Figure 7). Therefore greater stabilising systems are required for ground effect craft, thereby increasing weight and drag.

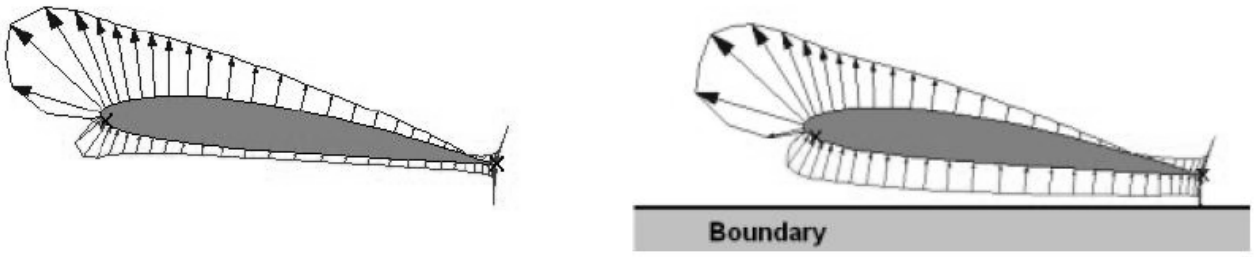


Figure 7: Pressure distribution on a wing while in and out of ground effect [10]

## 2.3 HEIGHT CLASSIFICATION OF GROUND EFFECT

The flow field around the wing is not only affected by the presence of the ground plane, but more importantly how close the wing is to the ground. For instance, as the wing approaches the ground, the development of trailing vortices is restricted. However, these effects usually only become apparent at ground clearances of less than the length of the Mean Aerodynamic Chord (MAC). For this reason, ground clearances are usually non-dimensionalised with respect to the MAC of the primary lifting surface of the aircraft.

This relative ground clearance is denoted by $h_0 = h/c$, where h is the ground clearance and c represents the MAC of the wing.

The ground clearance between a wing and the ground has several classifications, each with their own flow fields [6]. There is generally a measurable change in the forces at values of $h_0 \approx 1$, but the effect tends to be most advantageous for ground clearances below 25% of the chord.

**Very Large Clearance ($h_0 < b$, $h_0 > c$)**

The presence of the ground plane begins to restrict the development of the trailing vortices in the wake, and starts to push the vortices outward (Figure 8).

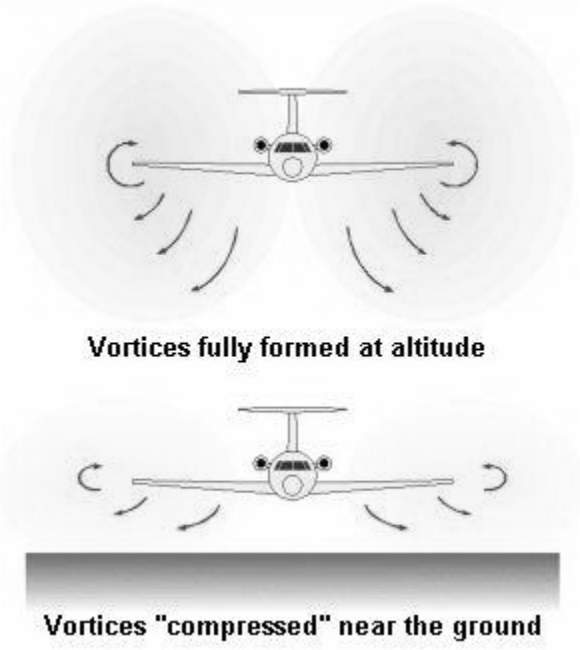


Figure 8: Flow field at very large clearances [2]

**Large Clearance ($h_0 \approx c$)**

The presence of the ground starts to influence the velocity distribution under the wing, as well as the development of the boundary layer on the wing surface. The wing is sufficiently far enough away from the ground so that no significant boundary layer develops on the ground due to the presence of the wing (Figure 9).

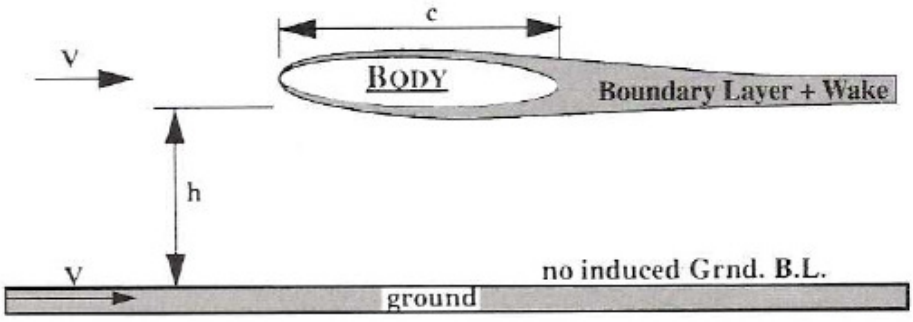


Figure 9: Flow field at large clearances [6]

**Medium Clearance ($h_0 \approx ½\, c$)**

The wing is now very much affected by the presence of the ground plane, and is close enough to induce a boundary layer to develop on the ground. There is still a region of potential flow between the two boundary layers (Figure 10).

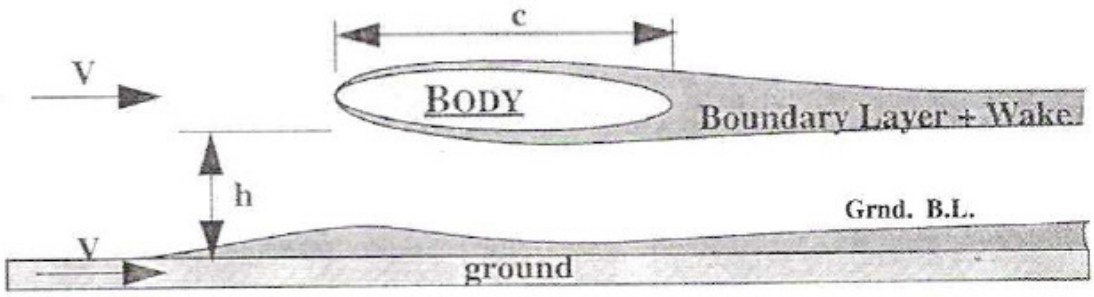


Figure 10: Flow field at medium clearances [6]

**Small Clearance ($h_0 \approx ¼\, c$)**

The boundary layers of the wing and of the ground start to interact, but there is little mixing in the streamwise direction of the wing (Figure 11).

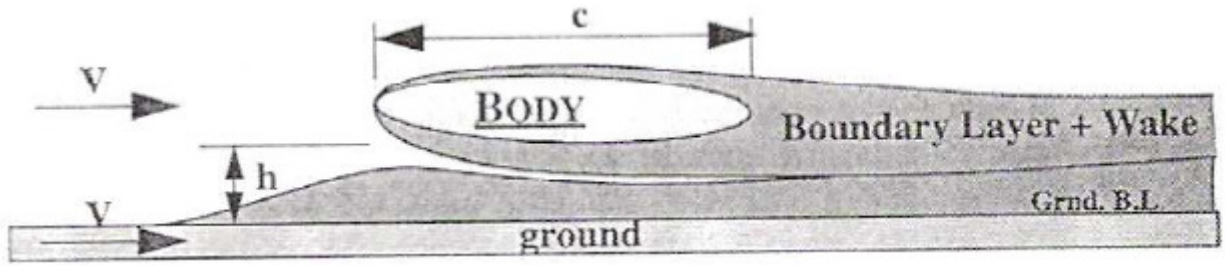


Figure 11: Flow field at small clearances [6]

**Very Small Clearance ($h_0 < 0.1c$)**

At such low clearances the air can stagnate below the wing. Viscous forces tend to control the fluid motion as the flow essentially becomes creeping flow (Figure 12).

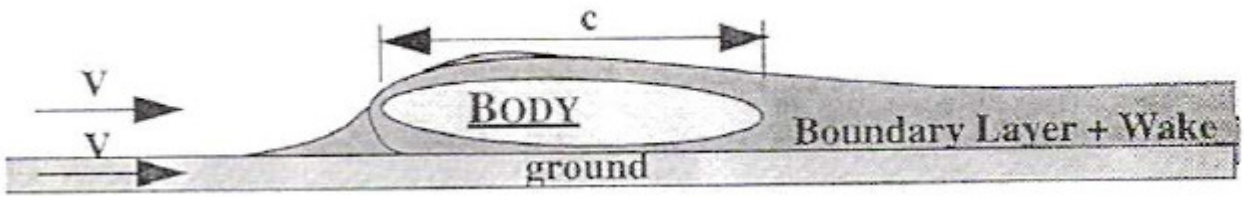


Figure 12: Flow field at very small clearances [6]

## 2.4 WAVES IN THE GROUND PLANE

Due to the low altitudes that WIG craft fly at, the most obvious flight path for these craft is over the open water of seas, oceans and possibly even large lakes. This is due to the relative flatness of the ground plane when compared to the hills and mountains often found on overland routes. Unfortunately, open water is rarely perfectly flat and waves tend to form quite easily on large bodies of water. These waves produce an uneven ground surface which in turn produces unsteady airflow patterns over them. Therefore it is important to understand how the presence of waves in the ground plane affects the airflow over wings operating in ground effect, particularly when considering the stability of the aircraft.

Most waves found in open waters are generated by wind blowing over the waters' surface, so the following discussion of wave characteristics will be limited to these "wind waves". Even once a wave has become fully developed, the airflow over the waters' surface continues to affect its shape.

### 2.4.1 Wave Profile

One of the most common wave profiles is that of the sinusoidal wave, where the wave profile follows that of a sine or cosine wave. However, these ideal wave profiles are rarely found at sea. Waves generated by wind are irregular in shape, and successive waves can differ markedly in height and shape [11]. The profiles of low swell and

tsunamis can sometimes resemble a sinusoidal wave close enough for the approximation to be used. The diagram below illustrates a simple wave pattern (a roughly drawn sine wave) with a few labels of the important features of a wave profile.

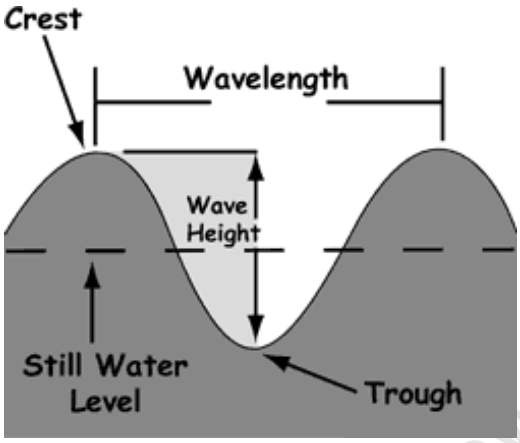


Figure 13: Wave diagram with labels [12]

Wave heights are always much smaller than their respective wavelengths. When waves become too high they can become unstable and fall apart [11]. One theory, proposed by Stokes, sets the upper limit of the H/$\lambda$ ratio at 1/7 [11]. Bigelow and Edmondson [11] compiled a frequency table that estimates the frequency of different wave heights that occur in the ocean. Their table, taken from Kinsman [11], is reproduced below. An important observation is that 45% of waves are less than 4 feet (1.22 m) high.

Table 1: Frequency of occurrence of different wave heights [11]

| Wave Height (ft.) | 0-3 | 3-4 | 4-7 | 7-12 | 12-20 | Over 20 |
|---|---|---|---|---|---|---|
| Frequency of Occurrence (%) | 20 | 25 | 20 | 15 | 10 | 10 |

## 2.4.2 Wave Period and Frequency

An important property of a wave, related to the speed that a wave travels at, is the wave period, *T*. The period is the time taken for 1 wavelength ($\lambda$) to pass through a fixed point. The smaller the time, the faster the wave is travelling.

As the water is worked on by the wind, the period of the waves gradually increases in length, with a resulting decrease in the frequency. Fully developed waves generally have a period of 1 – 30 seconds [12], resulting in a frequency of 1 to 0.5 Hz.

### 2.4.3 Wave Speed

The transverse speed of a wave is denoted by $c$. It is defined as the wavelength travelled divided by the period of the wavelength.

$$c = \lambda/T \tag{1}$$

Determining a wave's speed in reality can be misleading. In open water, individual waves cannot sustain a constant velocity indefinitely, and individual waves can also be affected by interference from other waves. Consequently, it becomes difficult to observe and measure the fixed speed of a changing wave over any distance [11].

Moreover, determining the speed of a group of waves poses its own problems. A group of waves radiating from a source do not all travel at the same speed. Waves of longer length run at faster speeds, and over time will move to the front of the group. Therefore waves at the front of a group will have longer wavelengths than those at the rear, meaning that wave group patterns are not steady along there length. As such, wave speeds should only be used as a guideline when comparing different waves.

## 2.5 THE EFFECT OF WAVES ON THE AIRFLOW NEAR THE GROUND

The interaction between the air and a solid ground plane changes the behaviour of the air in that region due to boundary layers and other effects. When the surface becomes undulating, such as the surface of an ocean, the flow pattern changes even more.

### 2.5.1 Shear-Flow Model of Wave Formation

The shear flow model is one of the central theories used to explain the formation of waves by the air flowing over the water. It is presented here to illustrate some of the

expected airflow patterns over waves in the ground plane. Like most models it uses idealised assumptions to explain the occurrence of different processes. It assumes that the air/water interface is of constant, steady profile, and isn't changed by the presence of the wind. The airflow is assumed to be inviscid, incompressible and that the streamlines will remain “quasi-parallel” as they follow the waviness of the water's surface [11].

While the air away from the surface has a mean flow velocity, the air in contact with the wave surface slows down due to frictional effects between the two mediums. In fact, the streamlines near the surface actually reverse their flow direction to run against the direction of both the waves and the mean airflow. This is illustrated in Figure 14. There is a critical distance from the surface where the flow has zero velocity, i.e. where the mean airspeed ($U$) equals the wave speed ($c$). The reversal of flow can potentially create eddies in the flow as illustrated by Phillips [13] in Figure 15.

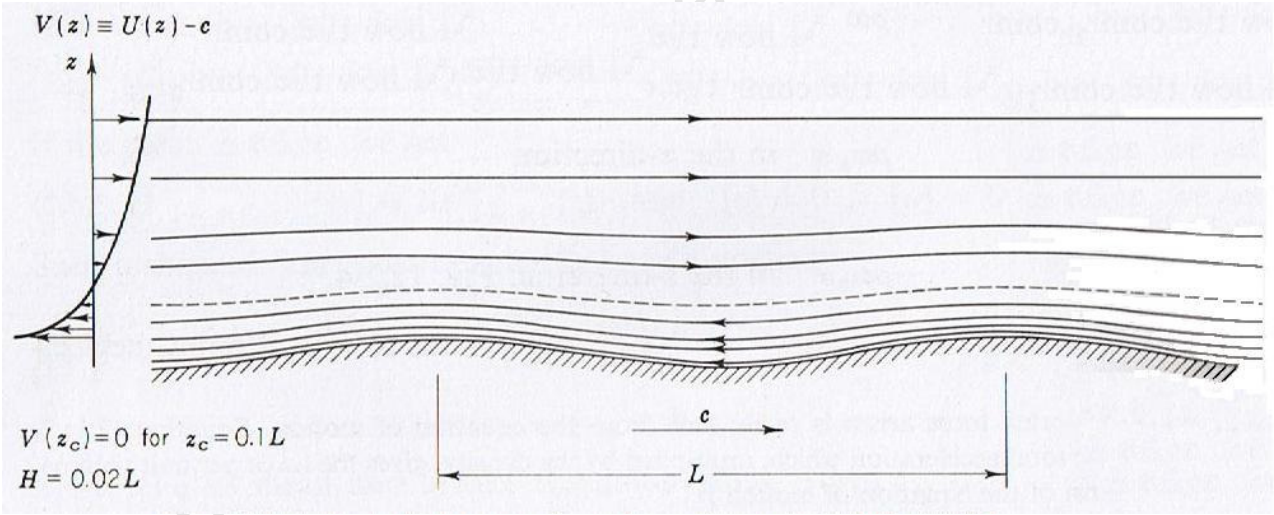


Figure 14: Airflow in close proximity to wave surface [11]

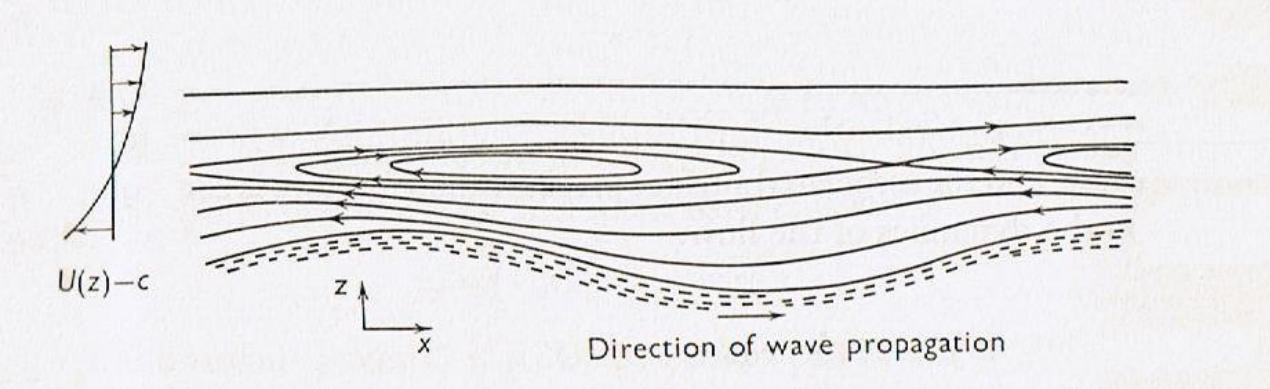


Figure 15: Vortices formed due to flow reversal in close proximity to wave surface [13]

### 2.5.2 The "Sheltering Effect" of Waves

One of the earliest theories on the formation of waves due to wind action was proposed by Jeffreys [12], and suggested that waves formed due to the waves sheltering the air on the downwind side. This produced a pressure difference across the moving wave which increased the size of the wave. It was later found that the resultant pressure difference was not sufficient to produce the observed results. While the theory was discredited [12], it does highlight another interaction between the wind and waves. The waves create pockets of high and low pressure on their windward and leeward sides respectively.

### 2.5.3 A Final Note on Airflow over Waves

The turbulent nature of the airflow over the varying surface of the ocean will lead to unsteady flow patterns over the waves. This turbulent flow will further affect both the airflow and the shape of the waves. Therefore the wave and airflow patterns experienced in reality will be irregular and essentially random. Consequently, to simplify the problem, it was decided to assume that the waves and airflow will at least enter the domain in a steady, uniform manner.

## 2.6 DYNAMIC RESPONSE OF A WING NEAR A WAVY GROUND PLANE

The lift, drag and moment characteristics of a WIG aerofoil are very dependant on the distance between the wing and the ground plane. When the ground plane is flat, the

ground clearance can be maintained constant. Therefore the wing's behaviour remains steady. However, when the clearance between the wing and the ground changes with time, due to wave motion for example, the behaviour of the wing will also change with time.

### 2.6.1 Factors Affecting the Wing near a Wavy Ground Plane

In addition to the variables considered for ground effect over a flat ground plane, there are a number of other variables to take into account when looking at ground effect over a wavy ground plane. These variables are illustrated in the figure below.

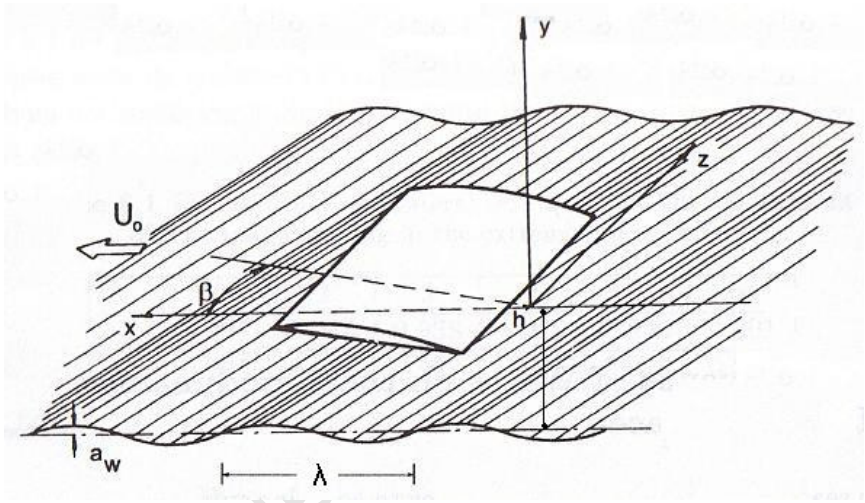


Figure 16: Variables affecting ground effect flow for the wavy ground plane [14]

The ground clearance height ($h$) is now no longer defined as being relative to the ground plane as such, but is now relative to the mean height of the wave. To non-dimensionalise the relationship between the wave amplitude and the ground clearance, the term $\overline{a}_W$ is defined as the ratio of the wave amplitude ($a_w$) to the ground clearance ($h$).

Due to the harmonic nature of the wavy ground plane, and its subsequent relationship with the aerofoil, Rozhdestvensky [14] defines a Strouhal Number based on the ratio of the wavelength to the chord ($L_w$). Rozhdestvensky's definition is defined in Equation 2. This number is essentially the wavenumber that has been non-dimensionalised by multiplying it by the chord of the wing. The wavenumber is analogous to the spatial representation of the wave frequency.

$$k = 2\pi / L_w \qquad (2)$$

### 2.6.2 Fluctuations in the Force Coefficients

From the mathematical theory of Rozhdestvensky, it was shown that fluctuations exist in the wave-induced lift coefficients due to the fluctuating gap between the wing and the wave surface. It was found that the lift co-efficient could be broken up into two components, the non-fluctuating "cruise co-efficient" (co-efficient of the wing in the presence of a flat ground plane) and the time-dependant (unsteady) component due to the presence of the waves. The fluctuating component was found to be of the order of $\overline{\alpha}\,\overline{a}_W$, where $\overline{\alpha}$ is the relative angle of attack ($\alpha/h$), with $\alpha$ in radians [14].

The following figure, created by Rozhdestvensky [14], illustrates how the amplitude of the wave-induced unsteady lift co-efficient differs for different aspect ratios when plotted in relation to the Strouhal Number (for a rectangular wing). The ratio $F/F_0$ is the ratio of unsteady force to the steady force (flat ground plane). It can be seen that for each aspect ratio there is a corresponding Strouhal Number where the amplitude of the unsteady lift is at a minimum. The curve labelled "2D" is for an infinitely long aerofoil.

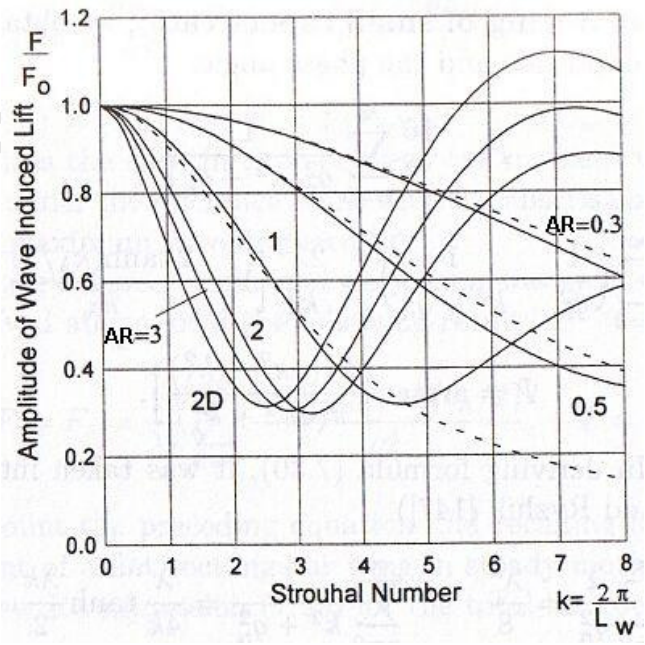


Figure 17: Amplitude of wave-induced unsteady $C_L$ vs. Strouhal Number [14]

This graph indicates that for wings of smaller aspect ratio, the minimum amplitude shifts towards waves of shorter wavelength. For an aspect ratio of 3, the Strouhal Number for the minimum amplitude is roughly 2.85.

### 2.6.3 Phase Angle Offset

As should be expected in real systems where inertia effects exist, the timing of the force coefficient fluctuations does not entirely coincide with the timing of the wave height fluctuations. This difference can be measured in terms of the phase angle, or phase difference, $\varphi$. The time difference, expressed as an angle in degrees, characterises this time shift between the moment the wave crest passes under the trailing edge of the wing, and the moment the wave-induced lift reaches its maximum. The larger the time difference, the larger the phase angle. The phase angle is given in radians by Equation 3.

$$\varphi = 2.\pi.f.\Delta t$$

where: $$f = \frac{c}{\lambda}$$

therefore: $$\varphi = 2.\pi.\frac{c}{\lambda}.\Delta t \qquad (3)$$

Figure 18 shows how the phase angle (in radians) varies with Strouhal Number for wings of different aspect ratio. From this graph it can be seen that, for an aspect ratio of 3, the phase angle becomes negative after a Strouhal Number of 2.75 (wavelength of 2.28 chord lengths).This means that the phase angle changes from a positive (lagging) to a negative (leading) angle at a wavelength of 2.28 chord lengths. A negative, or leading, phase angle means that the force oscillation precedes that of the wave oscillation.

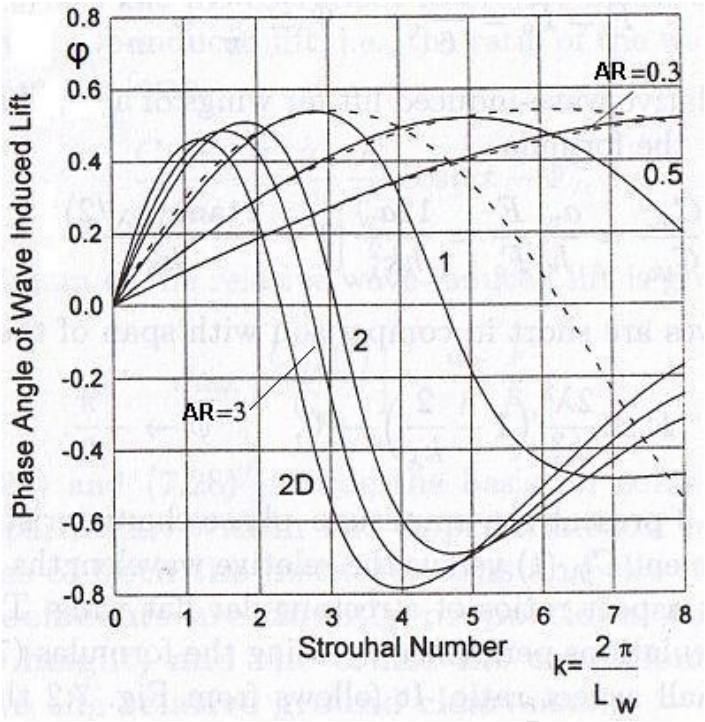


Figure 18: Phase angle of wave-induced unsteady lift force vs. Strouhal Number [14]

### 2.6.4 Course Angle

This study is only concerned with the situation where the wing is flying along the same axis as the translational direction of the waves, i.e. the angle between the wing motion and wave motion is zero. However, when flying at an angle to the oncoming waves, other effects are introduced that change the wing's behaviour. The unsteady component of the lift co-efficient reduces, as well as rolling moments are introduced. These effects have been ignored in this study.

# 3. COMPUTATIONAL MODELLING WITH CFD

Fluent® uses the Finite Volume Method to calculate the flow through the fluid domain. This requires the domain to be divided up into a number of small, "finite" volumes, so that the governing flow equation can be solved. Therefore a mesh of the finite volumes needed to be constructed around the model geometry. Gambit® was the program used to generate the mesh. This section of the report outlines the basic theory of CFD and the different options that were suitable for use with airfoils.

## 3.1 DESCRIPTION OF THE CFD SOFTWARE

No matter which software packages are used to solve a CFD problem, there are three basic stages that must be followed in the creation of a CFD model, namely the Pre-Processor, the Solver, and the Post-Processor. These three stages are sometimes handled by different software packages that culminate in a single solution. They are briefly outlined below.

### 3.1.1 The Pre-Processor

Most numerical modelling methods make use of the technique of reducing the computational domain into a number of smaller finite volumes. This was achieved through the use of the software package Gambit®.

Before the problem can be solved, it has to be properly defined, with all the flow parameters and known values specified as boundary conditions. To define the flow problem on the grid, the software package called Fluent® was used.

### 3.1.2 The Solver

The solver program is designed to solve the governing flow equations over the computational domain. Most packages use the more popular method known as the Finite Volume Method (FVM). This method requires the solver to first integrate the governing equations of fluid flow over the control volume, discretise the equations to create an approximate numerical solution, and then solve the equations by an iterative method [15].

The Navier-Stokes equations are used as the governing equations for the Finite Volume Method. These equations are manipulated to include approximations for turbulent flow. This is done because modelling these flows directly would be too computationally expensive.

### 3.1.3 The Post-Processor

The solver can only solve the governing flow equations, and so needs a postprocessor to take the results from the solver and display them in a form that is easily understood by the user. Post-processors are powerful tools for producing visual images of the results such as flow streamlines or pressure distributions around the model. Therefore the user can analyse the results in terms of vector or surface plots of the parameters of interest. In many cases the solver and post-processor are combined into one program. This is the case for Fluent®.

## 3.2 MESH GENERATION

Most CFD codes make use of the Finite Volume Method to calculate the flow solution. In this method, the governing equations of the flow are discretised over small control volumes, or cells. Therefore the entire flow region, or computational domain, must be filled with these cells. The collection of cells is known as a mesh. Over the years a number of different mesh shapes and patterns have been created, each with their own merits. These will be discussed now in relation to modelling the flow over an airfoil.

### 3.2.1 Tetrahedral Cells vs. Hexahedral Cells

The two most commonly used cells are Tetrahedral (tet) and Hexahedral (hex) cells. These cells are illustrated in Figure 19, where two different node configurations for each element are shown. It is at these nodes that the scalar variables (e.g. pressure) are calculated. By increasing the number of nodes in a cell, a higher accuracy can be obtained for the same number of cells. However, adding more nodes to a cell would require more memory for the same number of cells.

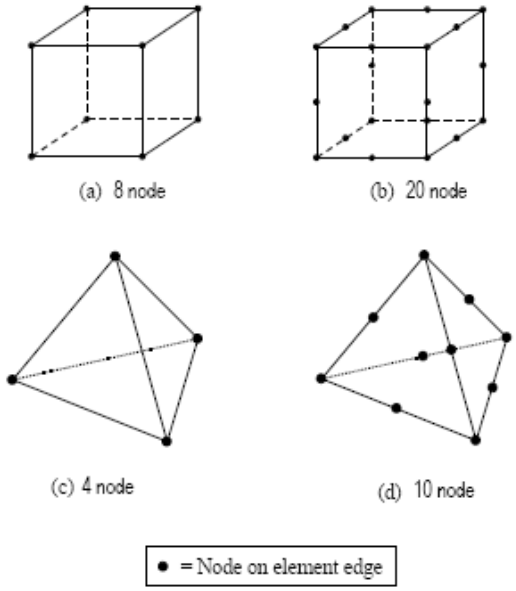


Figure 19: Hex (a, b) and Tet (c, d) mesh cells [16]

### 3.2.2 Structured vs. Unstructured Meshes

Since the domain is broken up into individual cells, the arrangement of cells can either be neatly ordered (structured) or become essentially random (unstructured). These patterns are illustrated in Figure 20. Unstructured meshes are often generated automatically by special meshing algorithms within the mesh program. They can adapt themselves to fit basically any geometry. Alternatively, structured meshes are usually created manually and so are often only found around more regular geometries where the mesh can be more easily aligned with the geometry. Mesh structure and cell quality greatly affect the results produced by the model and so should be suitably defined to resolve the flow problem.



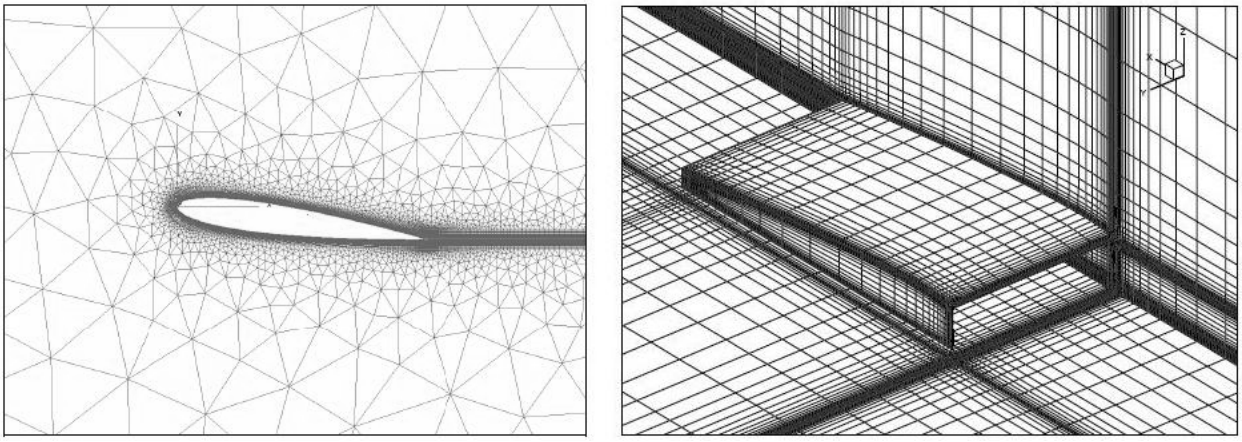

Figure 20: Unstructured (left) and structured mesh patterns [17, 18]

There are two factors that ultimately determine the difference between the accuracies obtained by different meshes, namely grid density and alignment with the flow. In areas where the flow is changing rapidly, or where there are flow features of interest, it is better to have a denser grid so that the relevant flow features can be more accurately resolved. An important implication of this is that the changes in the flow variables would not be too large across each cell. Errors can be introduced if cells are too large because the approximations do not always hold over large distances between cell nodes.

Aligning the cells with the flow direction is important in determining the accuracy of a mesh. Slight numerical errors are introduced if there is a misalignment between the flow trajectory and the cell face. This small error can become substantial if a large number of cells are affected. This is why structured grids are preferred over unstructured grids, as the cells can be aligned with the flow, when the flow direction is known. Often the mesh around the geometry, where the important flow features usually are, is more structured, while the mesh far away from the geometry is simply made unstructured as the flow in this region is often deemed to be less important. As a result of this, many grids are constructed as a hybrid of structured and unstructured patterns.



### 3.2.3 Conventional Aerofoil Mesh Models

Of the literature that is available for flow over airfoils, most is concerned with 2D airfoils in the free stream flow, i.e. away from any other geometry. This allows greater flexibility with the mesh design. 2D meshes also allow more cells to be used because the required computer memory is lower. Furthermore, an aerofoil in the free stream has no other geometry around itself that restricts the mesh distribution. As a result, a number of different styles of aerofoil mesh have been developed over the years. The three more common styles of structured meshes are shown in Figure 21. The figure on the left illustrates an “O-type” mesh where the cells radiate outwards from the airfoil’s surface [19]. The figure on the right shows a mesh known as an “H-type” mesh [18]. This is because the cells are aligned vertically and horizontally with the main axes (orthogonal mesh), forming an H type pattern. Lastly, the “C-type” mesh (bottom) is a combination of the two with a partial O-type mesh curving around the leading edge of the airfoil, and an orthogonal mesh stretching downwind from the trailing edge [20].

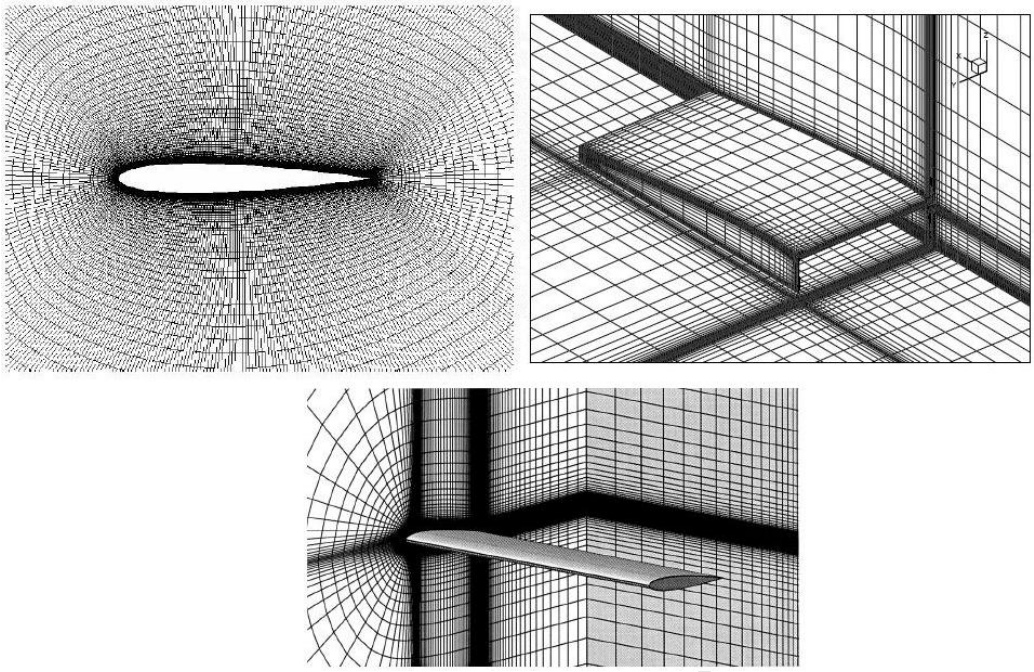

Figure 21: Different meshes for an aerofoil in the free stream [18, 19, and 20]

Considering that the initial geometry being used in this study is bounded by a flat ground plane, the H-type mesh would be the most appropriate as the general cell structure would neatly line up with the ground plane boundary.

## 3.3 TURBULENCE MODELLING

Turbulent flow is characterised by small to large scale fluctuations in the flow pattern. Since these fluctuations can be of small scale and high frequency, it can become very impractical (computationally expensive) to model all of these fluctuations directly. For many practical engineering applications, it can even be unnecessary to model the small scale fluctuations exactly. Therefore a suitable approximation is required. The flow equations that govern the flow can be time-averaged to remove the small scale fluctuations, thus simplifying the calculation and reducing calculation time. The resulting equations are known as Reynolds-Averaged Navier-Stokes (RANS) equations. The RANS equations for mass and momentum are given by Equations 4 and 5 respectively in Cartesian tensor form.

$$\frac{\partial \rho}{\partial t} + \frac{\partial}{\partial x_i}(\rho u_i) = 0 \tag{4}$$

$$\frac{\partial}{\partial t}(\rho u_i) + \frac{\partial}{\partial x_j}(\rho u_i u_j) = -\frac{\partial p}{\partial x_i} + \frac{\partial}{\partial x_i}\left[\mu\left(\frac{\partial u_i}{\partial x_j} + \frac{\partial u_j}{\partial x_i} - \frac{2}{3}\delta_{ij}\frac{\partial u_i}{\partial x_i}\right)\right] + \frac{\partial}{\partial x_j}\left(-\rho\overline{u}_i'\overline{u}_j'\right) \tag{5}$$

Unfortunately, in performing the time-averaging operations, new variables are introduced resulting in six additional unknown quantities [15]. These new quantities, the so-called Reynolds-stresses, need to be solved in order to close the resulting system of equations. The more common method of solving for these Reynolds-stresses involves the use of Boussinesq's eddy-viscosity approximation. This approximation (given by Equation 6) relates the Reynolds-stresses to the mean rates of deformation, i.e. the mean velocity gradients. Boussinesq's approximation is used as a basis for the k-ε, the k-ω and Spalart-Allmaras models.

$$-\rho\overline{u}_i'\overline{u}_j' = \mu_t\left(\frac{\partial u}{\partial x_j} + \frac{\partial u_j}{\partial x_i}\right) - \frac{2}{3}\left(\rho k + \mu_t\frac{\partial u_i}{\partial x_i}\right)\delta_{ij} \tag{6}$$

Fluent® offered a number of turbulence models, each with there own strengths and weaknesses. However, as a RANS type approach was going to be used, the three most suitable turbulence models were the k-ε, the k-ω and Spalart-Allmaras models.

### 3.3.1 The k-ε Model

The k-ε model is a two-equation model, which requires two equations to be solved to close the system of governing equations. It is commonly regarded as the standard, most widely used turbulence model as it has been shown to be robust, economical and reasonably accurate for a very wide range of flows [15]. As the model has been improved over the years, a number of variations have been introduced. Fluent® offered three versions of the k-ε model, the standard, the RNG, and the realizable model. The RNG and realizable models are attempts to increase the accuracy of the model under more demanding flow conditions.

**RNG (Renormalisation Group Theory) k-ε Model**

The most notable improvement made by the RNG model was its enhanced ability to handle swirling flows. The model can also account for low-Reynolds-number effects, provided that the near-wall region has been properly resolved.

**Realizable k-ε Model**

The term "realizable" indicates that the model satisfies certain mathematical constraints on the Reynolds stresses, which are consistent with the physics of turbulent flows. This gives the model improved performance in flows with rotation, boundary layers under strong adverse pressure gradients, separation and recirculation. One limitation with this model is its tendency to generate non-physical turbulent viscosities, particularly in cases which involve rotating fluid regions [21].

### 3.3.2 The k-ω Model

The standard k-ω model used by Fluent® is based on the standard Wilcox k-ω model [22]. It is also a two-equation model. The k-ω model can be used to model wall-bounded and free-shear flows. A modification on the standard model, the Shear-Stress Transport or SST model, was also available in Fluent®.

The SST model was developed by Menter [23] to blend the near-wall region performance of the k-ω model with the free-stream behaviour of the k-ε model in the far field. To this end a blending function is used to smooth the transition between the two models. This refinement of the model allows the SST k-ω model to be more accurate and reliable for flows which include adverse pressure gradients, such as would be encountered around airfoils [21].

### 3.3.3 The Spalart-Allmaras (SA) Model

The Spalart-Allmaras model is a relatively simple one-equation model. It was designed specifically for aerospace applications which involve wall-bounded flows and as a result was particularly well suited for aerofoil applications [21, 22]. It has also been shown to give good results for boundary layers that are subject to adverse pressure gradients. The original SA model was effectively a low-Reynolds number model which required the

viscous affected region of the boundary layer to be properly resolved. In other words, a fine mesh is required to correctly model the boundary layer. However, in Fluent®, the SA model has been modified to make use of wall functions when the mesh resolution is not fine enough.

## 3.4 TREATMENT OF BOUNDARY LAYERS

As boundary layer behaviour and turbulence are very much linked, turbulence models also seek to model the boundary layer as well. There are two distinct approaches to this, namely the wall-function and the near-wall region methods.

### 3.4.1 Wall Functions vs. Near Wall Model

Wall functions, as used by the k-ε and k-ω models, use a semi-empirical formula to bridge the viscosity affected region between the wall and the fully turbulent region. This means that the viscosity affected region (viscous sub-layer and buffer layer) is not directly resolved. Therefore the turbulence models do not have to be modified to take into account the presence of the walls.

The near-wall model on the other hand, forces the turbulence model to resolve the viscosity affected region. With this method, the turbulence models are modified so that they can resolve the viscosity affected region all the way to the wall. This method requires a finer grid to allow the model to correctly resolve the viscous region right up to the wall.

Wall functions can save on computational expense as the required mesh can be much coarser. However, they are more suited to higher Reynolds number flows as it less important to resolve the viscosity affected region correctly. Low Reynolds number flows are more dependent on the correct behaviour of the boundary layer.

### 3.4.2 Mesh Requirements for Turbulence Models and *y*+ Values

Depending on which boundary layer approximation is used, different mesh densities are required in close proximity to the wall. In order to determine when the mesh is fine enough to correctly resolve the boundary layer, a non-dimensional value called *y*+ is

used. This value relates certain flow properties to the mesh geometry. Therefore the $y+$ value is very much solution dependant and is not a fixed geometrical quantity. The definition of the $y+$ value is given in Equation 7, where $\mu_t$ is the turbulent viscosity and $y_p$ is the distance from wall to mid-point of first cell adjacent to the wall. The $y+$ value is calculated at the centre of the first cell adjacent to the wall. It has to be maintained within a certain range so that the turbulence model can correctly model the boundary layer.

$$y^+ = \frac{\rho u_t y_P}{\mu} \tag{7}$$

As the SA model resolves the boundary layer right up to the wall, it requires a fine mesh. The mesh has to be fine enough to maintain a $y+$ value between 1 and 5, preferably closer to 1. As the k-ε and k-ω models use the wall function approach, their mesh cells in contact with the wall can be much larger. Therefore they only have to maintain a y+ value between 30 and 300.

# 4. DEVELOPMENT OF A 3D MODEL FOR A FLAT GROUND PLANE

This section of the report outlines the design of the computer model used to calculate the forces on the wing in the presence of a flat ground plane. The different settings that were selected for the model are also discussed.

## 4.1 PROBLEM IDENTIFICATION

This section introduces the different variable and geometric aspects that had to be considered during the investigation of the flat ground plane models. The physical definitions of these variables are illustrated in Figure 22.

### 4.1.1 Angle of Attack ($\alpha$)

To reduce the vast amount of data produced by Rhodes [4], it was decided to limit the angle of attack to those which would probably be more common in everyday flight. Furthermore, it has been found over the years that the complex flow around highly angled airfoils can be difficult to model properly due to difficulties in modelling the separation point and increased turbulence. This has been one of the limitations with turbulence modelling for airfoils. As will be shown later, Fluent® had trouble with resolving the flow even at an angle of attack of 13 degrees.

In order to further limit the range of test variables, the negative angles of attack investigated by Rhodes have been ignored. This was satisfactory as these wings would never be used at negative angles of attack. This fact is emphasized by the discovery of Rhodes in his experiments that this DHMTU wing generates significantly less lift at negative angles of attack, and even negative lift at the more extreme negative angles.

### 4.1.2 Relative Ground Clearance ($h_0$)

The effects of ground effect become enhanced when flying at very low levels, i.e. in extreme ground effect (EGE). Therefore the two lowest relative ground clearances were tested, namely 0.06 and 0.12. Apart from EGE, it is also important to know how the wing behaves as it moves away from the ground, and possibly even out of ground effect. Therefore two additional relative ground clearances of 0.50 and 1.30 were also tested.

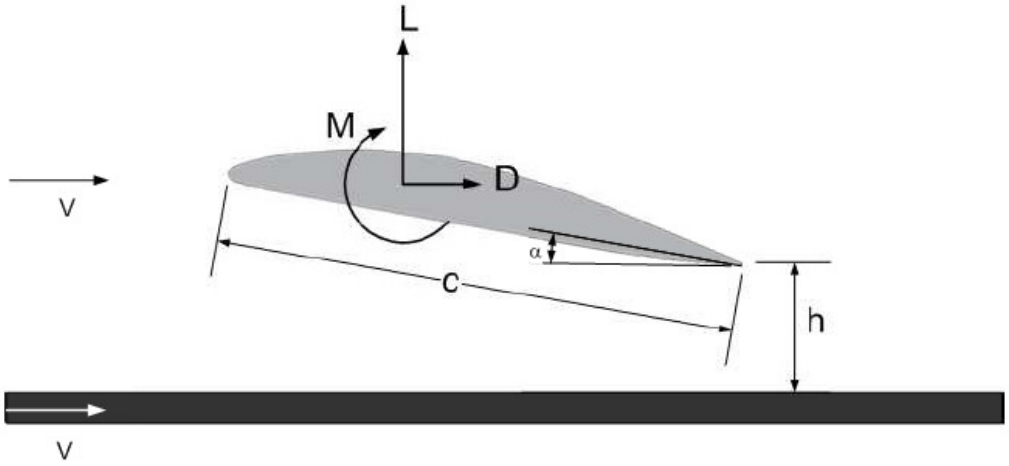


Figure 22: Variables affecting the flat ground plane model [4]

### 4.1.3 Hardware and Software Specifications

The table below outlines some of the important specifications of the computer hardware that was used during this study. Computer hardware can often place restrictions on the size of the problem to be solved, because more complex problems require more memory and also take longer to solve. Software version numbers are also given for completeness.

Table 2: Hardware and software specifications

| **Hardware** | |
|---|---|
| CPU | Intel® Core 2 Duo (Dual Core) 2 GHz |
| Memory (RAM) | 2 Gb |
| Video | On-board graphics |
| | |
| **Software** | |
| Operating System | Ubuntu 8.04 (Linux based OS) |
| Fluent® | v. 6.3.26 |
| Gambit® | v. 2.4.6 |

## 4.2 GEOMETRIC MODEL

In order to match the experimental results of Rhodes [4], the computational model had to mimic the experimental model used by him.

### 4.2.1 Experimental Model

Figure 23 illustrates the experimental setup, which was simply an aerofoil suspended above the ground plane by three struts. The struts were necessary for the experimental model so that the forces and pitching moment could be measured. Modelling of the struts would be unnecessary and since the experimental data was corrected for the interference of the struts, the results should be comparable. Therefore the resulting computational model would only need to model the DHMTU wing and the flat ground plane.

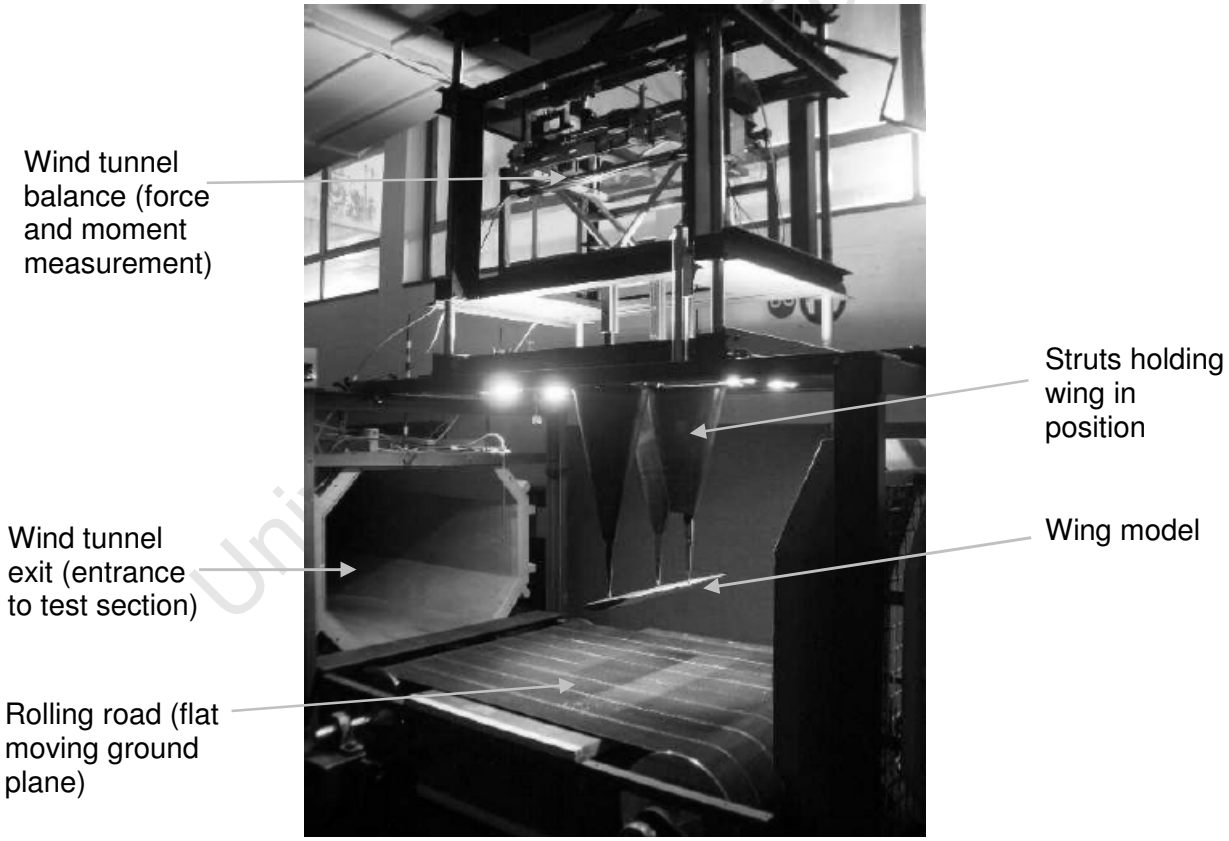


Figure 23: Picture showing Rhodes' experimental setup in the wind tunnel [4]

Force and moment data was measured experimentally using the wind tunnel balance situated above the wing model. The load range and transducer accuracy are given in

Table 3. Rhodes also corrected his experimental readings to account for flow interference effects caused by the wing support struts, flow section blockage due to the experimental model and boundary effects due to the presence of the wind tunnel walls. His corrected values were used for comparison with the computational model.

Table 3: Accuracy of wind tunnel balance measurements

| Component | Load Range | Accuracy |
|---|---|---|
| Lift | 0-90 N | 0.222 N |
| Drag | 0-36 N | 0.089 N |
| Pitching Moment | 0-1.7 N.m | 0.017 N.m |

### 4.2.2 DHMTU Aerofoil Profile

DHMTU aerofoil profiles were developed by the Department of Hydromechanics of the Marine Technical University in St. Petersburg. These airfoils were developed specifically for use in ground effect applications and are characterised by a flat section on their lower surface [3].

Rhodes used a DHMTU aerofoil of aspect ratio 3. The profile of his aerofoil was designated 10-40-2-10-2-60-21-5. The span of the wing was limited to 465mm, which resulted in a chord length of 155mm for the selected aspect ratio. This aerofoil was relatively slender, with a maximum thickness of only 10% of the chord at a distance of 40% chord from the leading edge. An interesting feature of this DHMTU aerofoil was that it had a flat section on the lower surface from 10% to 60% of the chord length. The profile of this DHMTU aerofoil is illustrated in Figure 24. To ensure the accuracy of the computer model, Rhodes' CAD model of the DHMTU wing was used for this project.



Figure 24: Profile shape of the DHMTU 10-40-2-10-2-60-21-5 aerofoil [4]

## 4.3 MESH GENERATION WITH GAMBIT®

A fully structured grid with hexagonal elements is the preferred grid design for any 3D mesh. This important factor was kept in mind during the development of a mesh for this problem.

### 4.3.1 Computational Domain Shape

In order to have a mesh that was as structured as possible, it was decided to create a hexagonal (3D rectangle) shaped domain. This allowed the block shaped hexagonal elements to fit exactly into the domain without any distortions. This had the added bonus that the majority of the cells would be neatly aligned with the flow, which would reduce the error generated by numerical diffusion [21]. The resulting domain would then also have a flat surface in the correct position for the flat ground plane that would need to be modelled.

### 4.3.2 Boundary Layer Mesh

As this project was concerned with the accurate modelling of the forces generated by the wing, it was important to resolve the important flow features around the wing. In particular, the boundary layer of the air at the surface of the wing needed to be resolved with sufficient accuracy. The boundary layer is crucial in determining the behaviour of the flow over the wing, and the resultant forces generated by the wing.

Therefore it was important to have a well structured grid in contact with the wing, where the cells could align themselves to the contours of the wing. For the sake of accurate boundary layer modelling, it was also important to control the $y+$ values in contact with the wall, as well as the vertical cell distribution away from the wall. This would allow the boundary layer to develop as freely and as accurately as possible. As will be discussed further in Section 4.7, the Spalart-Almaras turbulence model was used and therefore the $y+$ values had to be maintained between 1 and 5 in order for the turbulence model to correctly model the boundary layer. The details of the boundary layer construction can be found in Appendix C.

### 4.3.3 Merging the Structured and Unstructured Grids

When meshing the curved sides of an aerofoil, it becomes more difficult to match the regular cells on the boundary with cells at different orientations along the wing's surface. It becomes particularly difficult at higher angles of attack. Moreover, due to the presence of the flat ground plane, the traditional structured aerofoil meshes were not suitable for use in this application. Therefore a suitable compromise needed to be obtained.

**Boundary Layer Tool**

It was decided that the mesh of primary importance, was that around the wing's surface. Therefore the boundary layer tool in Gambit® was used to mesh the region around the upper and lower surfaces of the wing. This created a layer of cells that wrapped around the contour of the aerofoil (shown in Figure 25).

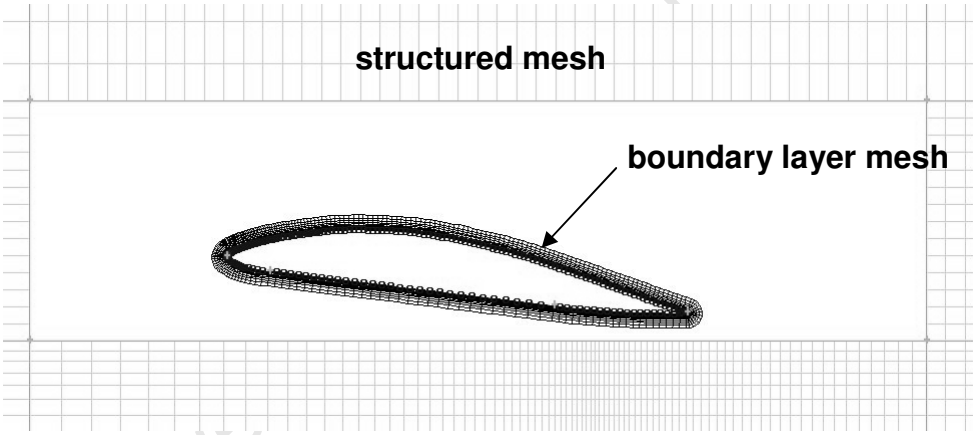


Figure 25: Boundary layer mesh around wing and domain mesh

**Unstructured Region**

To blend the mesh around the wing with the structured, orthogonal mesh of the rest of the domain it was decided to use a region of unstructured mesh. Gambit's® "pave" mesh scheme was used to create this unstructured region. This region is illustrated in Figure 26.

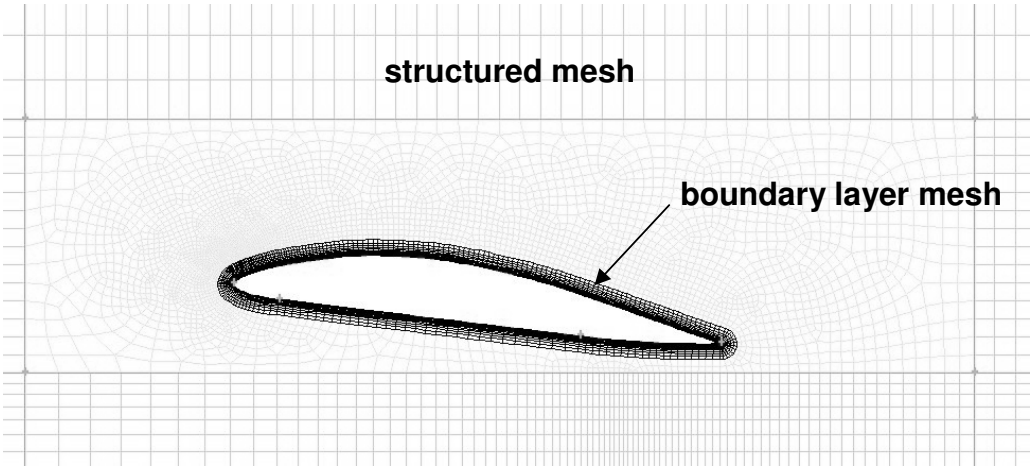


Figure 26: Pave mesh joining the boundary layer mesh and domain mesh

Unstructured regions are not ideal, especially around regions of importance, as they can lead to numerical diffusion in the solution [21]. However, since there would be a structured boundary layer around the wing, this unstructured region would be far enough away from the really important flow. An additional benefit of this unstructured region was that it allowed the fine mesh around the wing to be coarsened in order to match the coarser mesh of the rest of the domain.



**Meshing the Wingtip**

Meshing the tip of the wing was also made difficult by the curved aerofoil shape of the wing. Therefore an unstructured mesh was used at the tip of the wing.

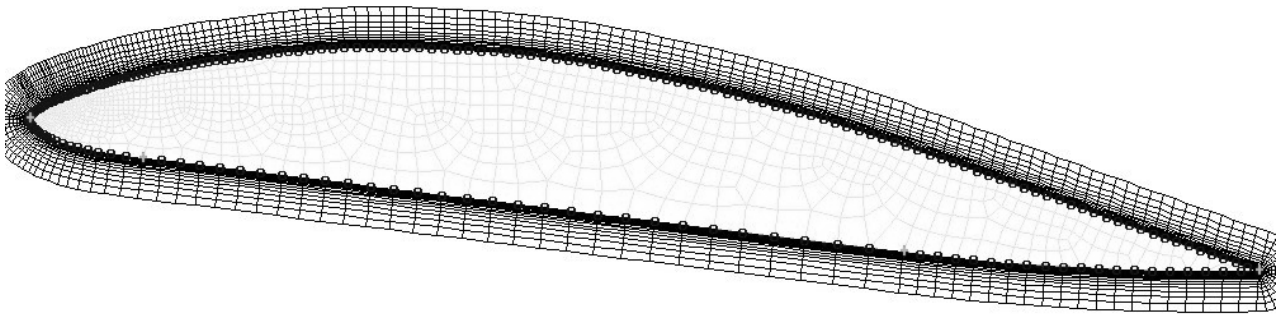

Figure 27: Unstructured mesh on the wingtip

Once the basic surfaces had been meshed, this mesh had to be extended to fill the entire volume of the computational domain.

**Meshing the Volume – Cooper Mesh**

Once a 2D mesh had been created on the symmetry plane of the model, this mesh could be extruded outwards to create a 3D mesh. It was felt that this method would ensure a good mesh around the wing, and give the best transition at the wingtip. Extrusion of the 2D mesh into a 3D mesh was done using Gambit's® "Cooper" meshing scheme

## 4.3.4 Mesh Distribution along the Length of the Wing

It is important to refine the cells in a region where there would be a large change in the flow from cell to cell. While the flow is not very strong towards the centre of the wingspan, the flow at the wingtip can be particularly intense as the flow from the wing's upper and lower surfaces swirl around to form the trailing vortices. Therefore the cells can be coarse towards the middle of the wing, but should be smaller (finer) at the wingtip. This is illustrated by the H-type grid shown in Figure 28. The dark lines in the figure indicate regions of high cell concentration. It is also obvious that the cell size growth rate in this particular grid is quite large, with large cells appearing quite soon after the wing. Many H-type grids use this style of cell distribution.

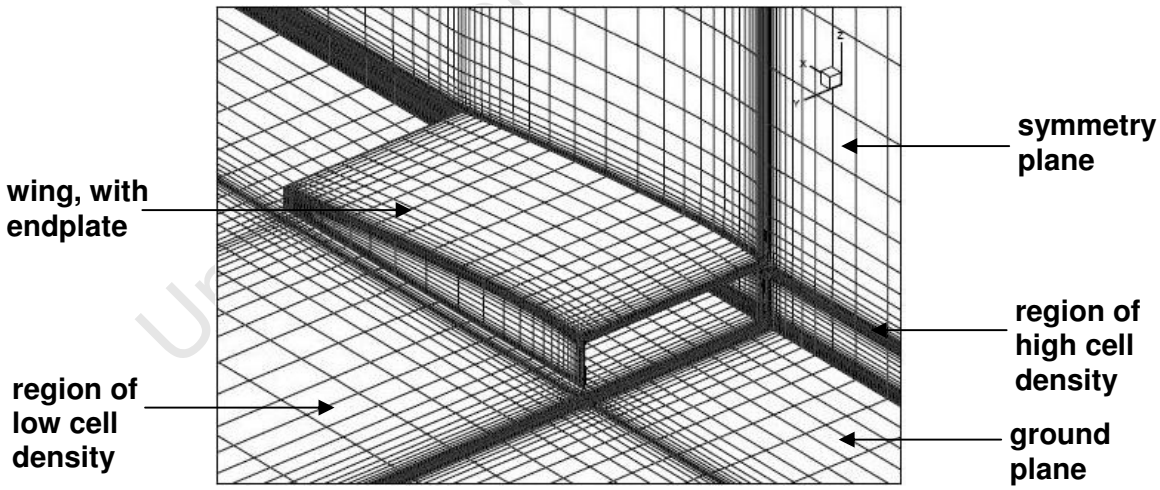


Figure 28: Concentration of cells at the wingtip in an H-type grid [18]

Consequently it was decided to use this type of cell distribution along the wing, especially at the wingtip. The cell distribution used in the final model is given in Figure 29. Unfortunately the amount of cells that could be used in this direction was limited due to the computer hardware that was available at the time. Therefore, to determine the best

distribution of cells along the wing, the sensitivity of the force and moment coefficients to the distribution of cells along the wing had to be tested. The test results for the wing at 7° angle of attack at $h_0$ = 0.06 and 0.50 are presented and discussed in more detail in Appendix C (Section C.2).

Increasing the number of cells on the wing to 40 cells does not make a significant difference to the results. Furthermore, increasing the number of cells does not make much difference either. Therefore it can be concluded that the results are independent of the spanwise mesh densities that were tested. The final mesh distribution that was chosen (Figure 29) would be less computationally expensive than the other meshes.

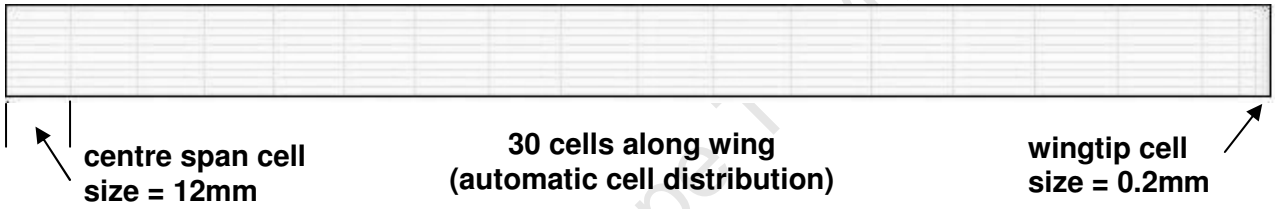


Figure 29: Cell distribution along the span of the wing

### 4.3.5 Chordwise Cell Distribution

To determine the most suitable cell distribution around the aerofoil, four different configurations were created. The differences made by the number of cells and their distribution along the wing's upper surface were investigated. The four configurations were tested at an $\alpha$ of 1°, 7°, 13° and at two different $h_0$ positions (0.06 an 0.50). Three different cell counts of 90, 150 and 220 cells were tested, at four different cell distributions (150 cells were tested for two different distributions). Results of the investigation are discussed in more detail in Appendix C (Section C.1).

While the results for the different meshes are all very similar, they do indicate an important point. The number of cells in the mesh does not affect the values as much as the distribution of the cells. In other words, the more cells that are distributed near the leading edge, the better the flow is resolved. This assumes however, that the wing is not near the stall angle. When the flow starts separating near the trailing edge at higher angles of attack, more cells would be needed near the trailing edge as well.

From the results, the 150 cell mesh with the leading edge ratio of 1.035 was chosen. This gave the model better accuracy than the 90 cell model, without the excessive number of cells of the 220 cell model. The ratio of 1.035 would distribute more cells around the leading edge of the wing, which would more accurately predict the flow behaviour here. The final mesh distribution around the wing is given in Figure 30.

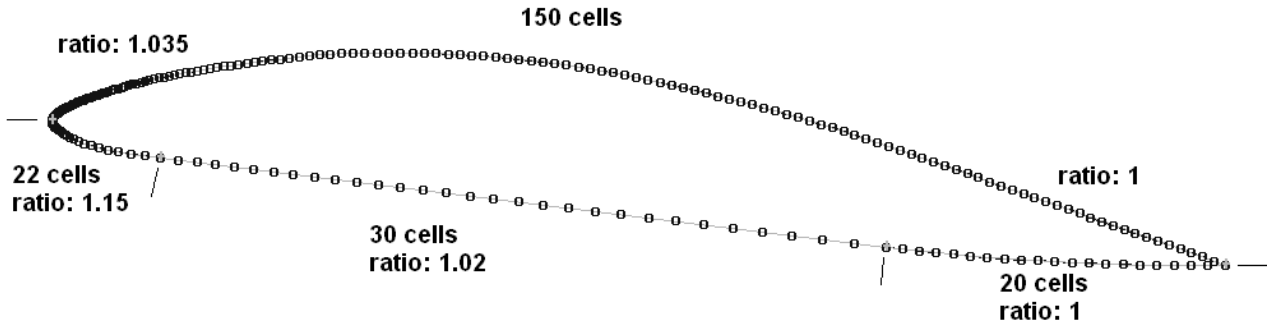


Figure 30: Cell distribution around the wing



### 4.3.6 Turbulent Viscosity Problems

Due to the nature of the flow around the wingtip, large changes in the flow variables can be expected. Thus it is important that there are a large enough number of cells around the wingtip to allow the solver to properly resolve the changes in the flow. If the cell size grows from fine to coarse too quickly, then the solver can encounter problems when trying to resolve the large changes in the flow variables. In Fluent®, this was usually identified by a very high turbulent viscosity ratio that occurred in the wingtip region.

This ratio is defined as the ratio of turbulent viscosity at a point to the viscosity of the non-turbulent air at that point. If this ratio becomes too high, it is usually an indication of physically-incorrect behaviour within the flow. It can be likened to a region of very viscous liquid (e.g. molasses) flowing through a low viscosity fluid like air. The upper limit of this ratio was set at $1x10^6$ for the duration of this study. This was one order of magnitude higher than the default setting, and it was felt that all values below this limit were acceptable.

High turbulent viscosity was encountered a number of times during the mesh development, and was particularly noticeable in the region around and behind the wingtip. Adjusting the spanwise distribution of cells did allow the viscosity ratio to be reduced to acceptable levels. While increasing the number of cells helped due to a smaller size change, having large cells with a slow change in cell size also prevented high turbulent viscosity ratios from occurring in the flow. This meant that the cells in contact with the wingtip wall would not be small enough to correctly model the boundary layer.

## 4.4 BOUNDARY CONDITIONS

Once the mesh had been created, the next step in setting up the model was to define the boundary conditions. These would help define the problem by mimicking the real life experimental scenario that was being modelled. Figure 31 illustrates the different boundary conditions and where they were applied in the domain. Following that, each of the boundary conditions is then discussed.

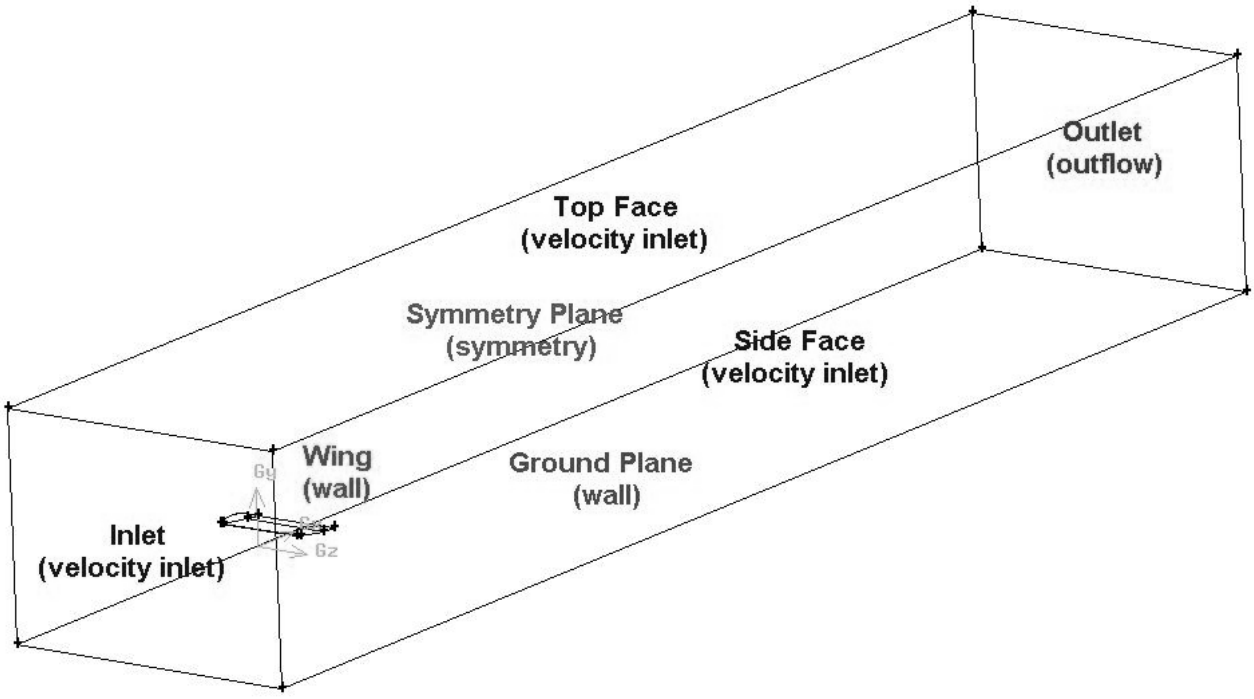


Figure 31: Boundary conditions for the flat ground plane

### 4.4.1 Inlet – Velocity Inlet

The inlet face of the computational domain represents the beginning of the wind tunnel test section and so the "velocity inlet" boundary condition was used. Here the flow velocity is specified across the face.

Rhodes [4] used a boundary layer splitter plate to remove the boundary layer created by the wall of the tunnel. Therefore it was assumed that the flow entering the domain was uniform along the vertical axis. As the flow was also uniform along the width of the tunnel, the velocity boundary condition was specified as being a constant 20.827 m/s in the flow direction.

The turbulence properties of the flow also needed to be specified at the inlet as these properties would affect the entire flow field downstream of the inlet. As the turbulence intensity of the wind tunnel flow was known to be 0.4%, it was decided to use the specification method of "intensity and length scale". The exact length scale was not known however, and was therefore approximated to be of the order of 0.002 m. The velocity inlet specification window, with the relevant values, is shown in Figure 32.

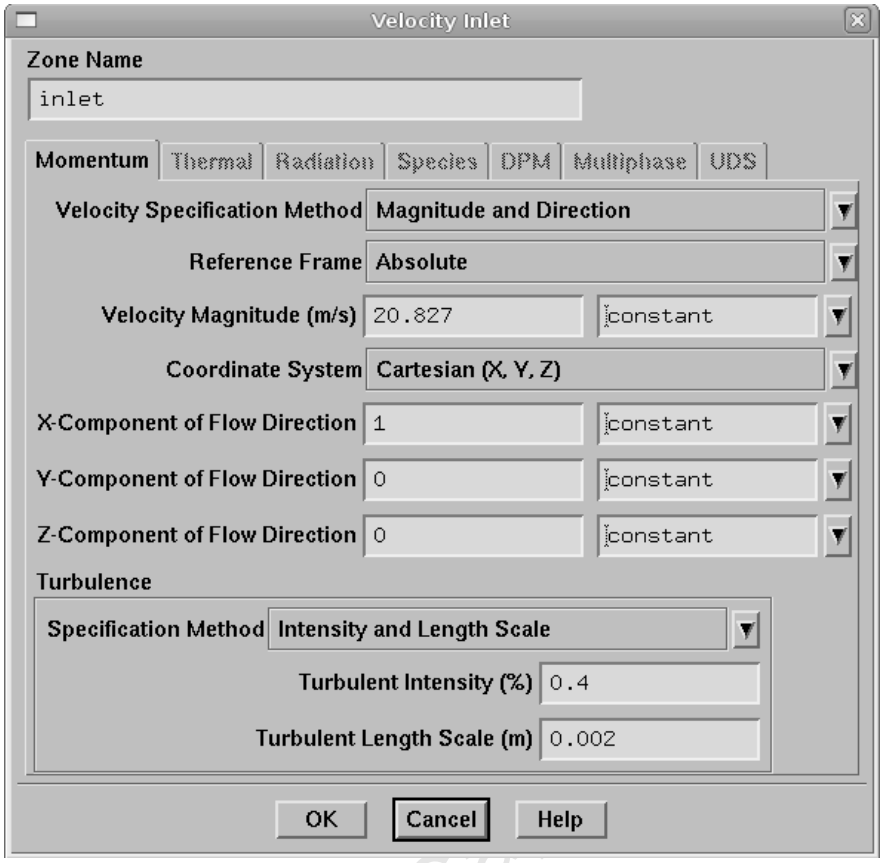


Figure 32: Velocity inlet specification window in Fluent®

### 4.4.2 Outlet – Outflow

The outlet boundary had to correspond to the velocity inlet condition specified at the inlet. Therefore an "outflow" boundary condition was specified. This boundary can be specified where the details of the flow velocity and pressure at the flow exits are not known prior to the solution of the problem [21]. If more than one outflow condition has been specified, the proportion of the mass flow leaving that respective face must be specified. As all of the flow was expected to leave this face, a flow weighting of 1 was specified.

### 4.4.3 Ground Plane – Wall

The ground plane in the model presented itself as a solid boundary, and so was modelled as a "wall" boundary. In the experiments conducted by Rhodes [4], the ground plane moved at the same speed as the air. To replicate this, the wall was given a translational velocity of 20.827 m/s relative to the stationary mesh zone, in the direction of the flow.

A “no-slip” condition was also specified for the wall. This meant that the air in direct contact with the wall would have zero velocity relative to the wall. This condition simulates the behaviour of a flow in contact with a wall and usually results in the formation of a boundary layer. However, as the air is moving at the same speed as the wall (at least up to the wing) no boundary layer will form along the ground plane.

As can be seen near the bottom of Figure 33, the roughness of the wall can also be specified. For this study, it has been assumed that the ground plane is a smooth surface with zero roughness. This is not strictly true however, as the ground plane used in the wind tunnel did in fact have some roughness. Unfortunately the nature of the roughness of the experimental ground plane could not be exactly identified. Therefore, for simplicity, the ground plane for the CFD model was assumed to be smooth.


Figure 33: Moving wall specification window in Fluent®

### 4.4.4 Wing – Wall

As a solid body within the fluid, the outer surface of the wing was also modelled with a "wall" boundary condition. Like the model in the wind tunnel, the wing was held stationary with respect to the moving fluid, and so the wall was modelled as stationary without any relative velocities. Again a no-slip condition was specified for the wall.

### 4.4.5 Side and Top Faces – Velocity Inlet

As the wind tunnel used for the experimental testing had an open test section, it was felt that the domain should also remain "open". In other words, no wall boundaries other than the ground were specified, as is common in many CFD simulations of airfoils.

It was decided to model the remaining two faces of the domain with "velocity inlet" boundary conditions. For this condition to be valid, it was assumed that these boundaries were far enough away from the disturbed flow around the wing to be sufficiently close to free stream conditions. The free stream flow values for velocity and turbulence (intensity and length scale) were specified at these boundaries, which were the same values as for the inlet face (see Section 4.4.1).

In the case of the side and top faces, the velocity did not actually enter into the domain, but rather ended up flowing tangentially along the surface in the same direction as the general flow. The velocity was specified in component form in order to ensure that it followed the same direction as the flow from the inlet boundary.



### 4.4.6 Symmetry Boundary Condition

Flow around a wing is widely considered to be symmetrical about the centreline under most conditions. Therefore only half of the wing had to be modelled. This reduced the number of cells in the mesh to half of what would be required for a full wing.

## 4.5 COMPUTATIONAL DOMAIN SIZE

The ideal computational domain is one that is small enough to limit the number of cells required to mesh it, but that is large enough not to impede the development of the important flow features.

The resulting dimensions of the domain are shown in Figure 34, the rectangle on the left being the front view with the side view on the right. From the results of the simulations (Section 6.4), it was clear that the spanwise dimension (5.2 chord lengths) of the domain would have to be much larger than the vertical dimension (3.9 chord lengths) due to the outward movement of the trailing vortices. The downstream portion of the domain was made much longer than the other dimensions (19.3 chord lengths) to allow the trailing vortices to develop properly.

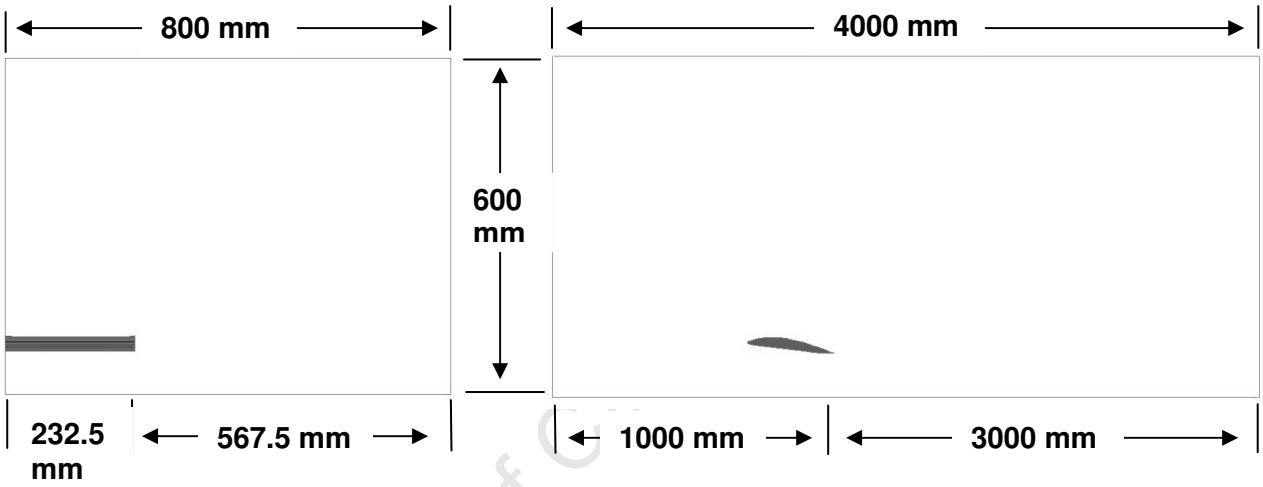


Figure 34: Dimensions of the computational domain

## 4.6 SOLVER SETTINGS

This section is only intended to summarise the different solver settings that were used during the report. The important solver settings are given in Tables 4 to 6. The choice of the different schemes is also briefly mentioned.

Since the problem that was being modelled was that of a low-speed incompressible fluid, a pressure-based, implicit solver was used. The pressure based solver was a segregated solver, which meant that the governing equations were solved sequentially. A coupled solver could be used, i.e. where the equations are solved at the same time. However this requires roughly 50% more memory than the segregated solver. One benefit of the coupled solver is that is can reach a converged solution much quicker than the segregated solver due to the manner in which the calculations are handled. The Green-Gauss node based option is known to be more accurate than the default cell-based option [21].

Table 4: CFD solver specifications

| | |
|---|---|
| Solver Type | Pressure-based, segregated solver |
| Solver Accuracy | Double Precision |
| Formulation | Implicit |
| Time Dependence | Steady State |
| Cell Gradient Option | Green Gauss Node Based |
| Space | 3D |

The default pressure-velocity coupling option of SIMPLE was chosen. The other schemes did not offer any benefits to the solution procedure and in many cases took longer to converge. The coupled solver was also tested. This solver offered much quicker convergence times due to the manner in which the pressure and momentum equations are solved. Unfortunately the coupled solver requires about 50% more memory than the segregated solver, which would then limit the number of cells available for the mesh. For the same mesh, the coupled solver had to be used with the single-precision solver, and as a result did not provide any improvement on accuracy.

Table 5: Discretisation schemes

| | |
|---|---|
| Pressure-Velocity Coupling | SIMPLE |
| Pressure Discretisation | Standard |
| Momentum Discretisation | Second Order Upwind |
| Modified Turbulent Viscosity | First Order Upwind |

The default under-relaxation factors were used as there was no reason to change them. The solution converged easily for most geometries and therefore there was no need to change them.

Table 6: Under-relaxation factors

| | |
|---|---|
| Pressure | 0.3 |
| Density | 1 |
| Body Force | 1 |
| Momentum | 0.7 |
| Modified Turbulent Viscosity | 0.8 |
| Turbulent Viscosity | 1 |

## 4.7 TURBULENCE MODELLING

The three most suitable turbulence models that were offered by Fluent® were the k-ε, k-ω, and Spalart-Allmaras (SA) models. From the literature survey, there was no clear preference as to which model was more appropriate for this type of situation. A number of different models have been used for airfoils and also for slightly different geometries. Some researchers had even used algebraic turbulence models instead of the more common one or two-equation models. Therefore it was decided to test the more promising models with a well known source of experimental data. A 2D model of the NACA 2612 aerofoil was generated using a "C-type" mesh.

This model was used to test the k-ε realizable and RNG, k-ω SST, and SA models. It was found that all three models agreed well at low $\alpha$, all being very accurate. However as α was increased, both the k-ε and the k-ω model did not perform as well, with all of them giving turbulent viscosity ratio warnings and ultimately erroneous values. The values generated by this test are shown in Table 7, with the exception of the RNG tests as they were very similar to the k-ε realizable values. The spaces that are left blank indicate where errors occurred during the solution. None of the models performed well above 12° due to turbulent viscosity problems.



Table 7: Turbulence model comparison for the 2D NACA 2612 aerofoil model

| **α** | **Experimental** | | **SA** | | **k-ε realizable** | | **k-ω SST** | |
|---|---|---|---|---|---|---|---|---|
| ° | **$C_D$** | **$C_L$** | **$C_D$** | **$C_L$** | **$C_D$** | **$C_L$** | **$C_D$** | **$C_L$** |
| 0 | 0.0085 | 0.23 | 0.0061 | 0.27 | 0.0061 | 0.28 | 0.0061 | 0.26 |
| 4 | 0.010 | 0.64 | 0.010 | 0.66 | 0.0108 | 0.64 | 0.0109 | 0.65 |
| 8 | 0.0145 | 1.00 | 0.0153 | 1.04 | 0.015 | 1.10 | 0.0150 | 1.04 |
| 12 | 0.0220 | 1.36 | 0.0264 | 1.37 | | | | |

When these turbulence models were tested in a 3D model, they again gave very similar results. However the k-ε and k-ω models were more prone to turbulent viscosity problems, particularly the k-ε realizable model, which was to be expected. The k-ε RNG model seemed the most stable of the three.

The Spalart-Allmaras model provided results that were more accurate and stable than for the other models. It was also less computationally expensive than the other models as it

was a one-equation model instead of a two-equation model. Therefore it was decided to implement the SA model for this study. Furthermore, the model was modified to include Strain/Vorticity based production. This was done with the thought that the model would be better equipped to predict the turbulence generated by the swirling flows near the wingtip.

The transport equation that needs to be solved as part of the SA model is given by Equation 8. The transported variable $\tilde{\nu}$ is identical to the turbulent kinematic viscosity, except for in the near wall (viscous affected) region. In this equation $G_\nu$ is the production of turbulent viscosity, $Y_\nu$ is the destruction of turbulent viscosity that occurs in the near wall region due to wall blocking and viscous damping, $\sigma_\nu$ and $C_{b2}$ are constants, $\nu$ is the molecular kinematic viscosity and $S_\nu$ is a user-defined source term. The model constants used for the Spalart-Allmaras model are given in Table 8.

$$\frac{\partial}{\partial t}(\rho\tilde{\nu}) + \frac{\partial}{\partial x_i}(\rho\tilde{\nu}u_i) = G_\nu + \frac{1}{\sigma_{\tilde{\nu}}}\left[\frac{\partial}{\partial x_j}\left\{(\mu+\rho\tilde{\nu})\frac{\partial\tilde{\nu}}{\partial x_j}\right\} + C_{b2}\rho\left(\frac{\partial\tilde{\nu}}{\partial x_j}\right)^2\right] - Y_\nu + S_{\tilde{\nu}} \qquad (8)$$

Table 8: Spalart-Allmaras turbulence model constants

| | |
|---|---|
| $C_{b1}$ | 0.1355 |
| $C_{b2}$ | 0.662 |
| $C_{v1}$ | 7.1 |
| $C_{w2}$ | 0.3 |
| $C_{w3}$ | 2 |
| $C_{prod}$ | 2 |
| Prandtl No. | 0.667 |

An important implication of choosing this model was that the *y*+ values in the boundary layer had to be controlled properly. The SA model requires that the *y*+ values be between 1 and 5 towards the centre of the first cell in the boundary layer.

## 4.8 BOUNDARY LAYER MESH

The SA model had the lowest *y*+ value requirement of the different turbulence models that were tested. Consequently, it would require the finest mesh to correctly resolve the

boundary layer. The $y+$ values had to be maintained at the centre of the first cell in contact with the wall, i.e. at half the height of the first cell ($y_p$). Therefore, to achieve the correct $y+$ value, the height of the first cell was determined to be 0.2mm.

As a result of the chosen boundary layer mesh, the $y+$ values were maintained within their recommended limit. In general, on the upper surface of the airfoil, the $y+$ in the leading edge region was maintained at about 4, while in the trailing edge region the value was roughly 1. Along the flat section on the underside of the wing the value was maintained at about 2. The value along the wingtip was kept at 4 due to the spanwise mesh spacing that was used.

## 4.9 RESIDUALS AND FORCE MONITORS

In order to determine when the flow has finally converged to its final flow pattern, the solver must monitor certain values to know when to stop the calculation. Residuals are calculated as the solution iterates. When the values of the residuals fall below a user-defined value, the solution is deemed stable and converged.

During this study, residuals of continuity (mass conservation), x, y, and z-velocity, and turbulent viscosity were monitored. It was decided that when these residuals fell below a value of $1x10^{-4}$ the force and moment coefficient values had sufficiently converged. This was one order of magnitude lower than the default value. Fluent® did not explicitly monitor the force and moment coefficients for convergence, but these values could also be monitored as the solution was iterating.

## 4.10 INITIALISATION AND ITERATION

Before the solution can begin, the pressure and velocity values have to be initialised so that Fluent® has a starting point for the values for the first iteration. The solution was initialised using Fluent's® automatic initialisation scheme. It initialised the values in the domain to those specified at the inlet boundary. Once the flow field had been initialised, the solution was iterated until convergence of the residuals occurred.

# 5. DEVELOPMENT OF A 3D MODEL FOR A WAVY GROUND PLANE

Based on the relative success of the CFD model for the flat ground plane, that model was extended to incorporate a wavy ground plane. The design of this model is presented below.

## 5.1 WAVES IN THE GROUND PLANE

This section of the report looks at what factors had to be considered before modelling the waves in the ground plane.

### 5.1.1 Wavelengths and Wave Heights

The lengths of the waves were chosen to be multiples of the wing chord length. The heights of the respective waves were chosen as fractions of the wavelength. Since the maximum height of a wave is limited to $1/7^{th}$ of the wavelength, this set the upper limit for the wave heights. For the longer wavelengths, smaller wave heights were also used in order to compare waves of different wavelengths while keeping the wave height the same.

For this study, four wavelengths of one to four times the chord length were chosen. The resulting relative wavelength ($L_W$) values would then be 1, 2, 3 and 4. This was to give a broad range of wavelengths and to test whether the results would match the mathematical theory of Rozhdestvensky [14] (see Section 2.6). For a wing of aspect ratio 3, he stated that the amplitudes of the lift coefficients would reach their minimum at a Strouhal Number of 2.85, which translates into a wavelength of 2.20 chord lengths.

The maximum resulting wave height from the 4$c$ wavelength would result in a wave height to chord ratio of 4/7. For most realistic wing sizes, this is much higher than would normally be expected in the open oceans as indicated by Table 1. Therefore this should represent the "worst-case-scenario" that would be experienced in flight. In fact, even the

third level wave heights would be greater than the more commonly experienced wave heights.

The different wave heights correspond to the maximum heights for the different wavelengths. The number 2*h*, for example, shall denote the maximum height of the wave for the 2*c* wavelength. The 4*c* wavelength may have a wave height of 2*h*, but the 1*c* wavelength is limited to a wave height of 1*h* and thus cannot have a wave height of 2*h*.

### 5.1.2 Wave Speed

As for the flat ground plane, the speed of the ground plane was chosen to be equal to that of the air. Therefore the ground plane moved along at 20.827 m/s relative to the wing. However, in reality, waves in the open ocean will have there own velocity which would mean that there would be a difference between the wind and wave speed. This factor was assumed to be negligible for this study.

### 5.1.3 Phase Angle ($\varphi$)

As the gap between the wing and the wave changes, so do the forces and moments generated by the wing. Since these variations in the ground plane are periodic, the variations in the forces will also be periodic. However, there is a slight delay between the movements of the waves and the forces generated by the wing, since it takes time for the flow field around the wing to adjust to the varying height geometry. This lag creates a time delay between the response of the force coefficients and the oscillation of the physical wave. This time delay, or phase shift, is described by the phase angle. This lag is most apparent when looking at the peaks and troughs of the coefficients and how they relate to the physical peaks and troughs of the waves in the ground plane. The phase shift is clearly illustrated in the following graph where the lift coefficient is plotted against the wave profile. The lift coefficient reaches its peak before the physical wave has peaked and is therefore said to have a leading phase angle. The wave profile is drawn relative to the trailing edge of the wing, i.e. the height of the wave at a particular moment in time is the height below the trailing edge of the wing.

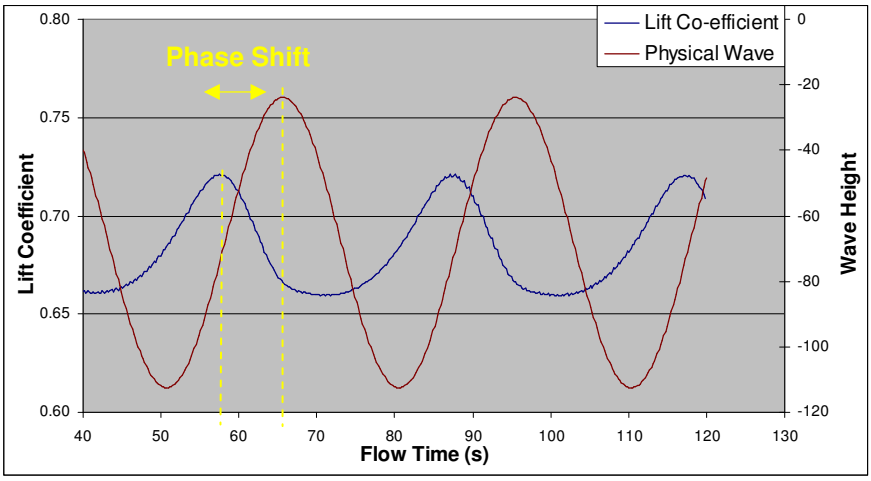


Figure 35: Phase shift between the force coefficients and the wave profile

## 5.2 METHODS OF WAVE MODELLING

There were two very different methods of introducing waves into the domain. The more obvious method would be to create a multi-phase model by introducing actual waves of water flowing through the lower portion of the domain. This would be analogous to having a wave tank at the bottom of the domain. The other option would be to create a wavy solid boundary that could move past the wing like a set of waves. This latter method could be accomplished through the use of a sliding mesh. According to Rozhdestvensky [14], the deformation of the water's surface due to the presence of the WIG craft can be considered negligible, because the density ratio between air and water is so low that the waters' surface behaves as if it were solid. Therefore the waves could be modelled as a solid surface in the sliding mesh model.



### 5.2.1 Multi-Phase Model

A Multi-Phase model can handle two distinctly different fluids that interact with each other in the model. Fluent® offered a number of different multi-phase models, each with their own strengths of flow regimes. The more suitable model for modelling waves in contact with air was the Volume of Fluid (VOF) model.

The VOF model is a surface-tracking technique that is used on a fixed Eulerian mesh [21]. It was designed to model two or more immiscible fluids, where the position of the interface between the fluids was of interest. In the VOF model, a single set of momentum equations was shared by all of the fluids, and the volume fraction of fluid in each cell was tracked throughout the domain.

The VOF model would have allowed for a domain of fixed size and shape. An extra region of mesh could be added to the bottom of the domain to contain the volume of water that would flow through the domain. The height of the body of water could be controlled as it entered the domain to create the shape of waves travelling through the domain.

The downside to using the VOF model is that it would result in a huge increase in computational complexity from the simple flat ground plane model. Not only would a fine mesh be required for VOF, but for each new fluid, a variable would have to be solved for in each of the cells [20]. An increase in complexity usually requires an increase in computational power and solution time. Another problem is that when the viscosity ratio between the fluids is greater than $1x10^3$ the solution can struggle to converge. Fluent® has schemes to get around this issue, but could not totally eradicate the problem.



### 5.2.2 Sliding Mesh Model

The sliding mesh model would also require an extra region of cells below the domain. Unlike the VOF model however, the waves would be modelled as a solid boundary and air would be the only fluid in the entire domain, resulting in a much simpler problem. In Fluent®, the sliding mesh model allows for different regions of the mesh to be given either rotational or translational motion. This is ideal for the problem, as the solid boundary would have to be dragged past the wing at the correct translational velocity to mimic the movement of the waves.

Due to its simplicity and its minimal extra computational expense, the sliding mesh method was chosen to model the wavy ground plane.

## 5.3 IMPLEMENTATION OF THE SLIDING MESH MODEL

The sliding mesh model would provide a similar wave motion to the VOF model, while being simpler to work with and computationally less expensive. This section outlines the implementation of the sliding mesh model to incorporate waves into the ground plane.

### 5.3.1 Sliding Region

After the results for the flat ground plane model were analysed, it was found that the mesh used for the flat ground plane model was acceptable. Therefore it was decided that the old model would be used, with a new region added below which would form the sliding region. The mesh for the $h_0$ = 0.06 ground clearance would be used for the stationary region as this allowed the entire waveform of the highest waves to fit into the new sliding region, while maintaining the correct clearances.

However, after subsequent testing, it was found that the spanwise distribution of cells was causing turbulent viscosity ratio problems. This was probably due to the large changes in cell size from cell to cell. This meant that the grid could not properly resolve any extreme flow effects and so would generate high viscosity in the turbulent region, which is not realistic. So, with the added affect of the waves, this mesh would not work as well as for the flat ground plane model. Therefore it was decided to use a much coarser cell distribution in order to alleviate this problem. This new cell distribution was tested on the flat ground plane model and found to produce similar results to the original model. A brief comparison between the original and new mesh distribution at different $h_0$ and $\alpha$ is given in Table 9. It can be seen that these new results were very similar to the original model. Therefore it was decided that this new cell distribution was acceptable since the resultant force coefficients did not change significantly with the new cell distribution.

Table 9: Comparison of new spanwise mesh with old mesh

| $h_0$ | $\alpha$ (°) | Original Mesh | | New Mesh | |
|---|---|---|---|---|---|
| | | $C_L$ | $C_D$ | $C_L$ | $C_D$ |
| 0.06 | 1 | 0.214 | 0.008 | 0.219 | 0.007 |
| 0.06 | 7 | 0.958 | 0.035 | 0.961 | 0.033 |
| 0.50 | 1 | 0.253 | 0.016 | 0.253 | 0.011 |
| 0.50 | 7 | 0.671 | 0.039 | 0.670 | 0.039 |

This new configuration is shown in Figure 36. The new region is very low as it only has to be large enough to enclose the largest wave size. The sliding region is not aligned with the original domain and stretches out far ahead of it because Fluent® only allows the region to move from its original position. Therefore the sliding region had to be created in its start position.

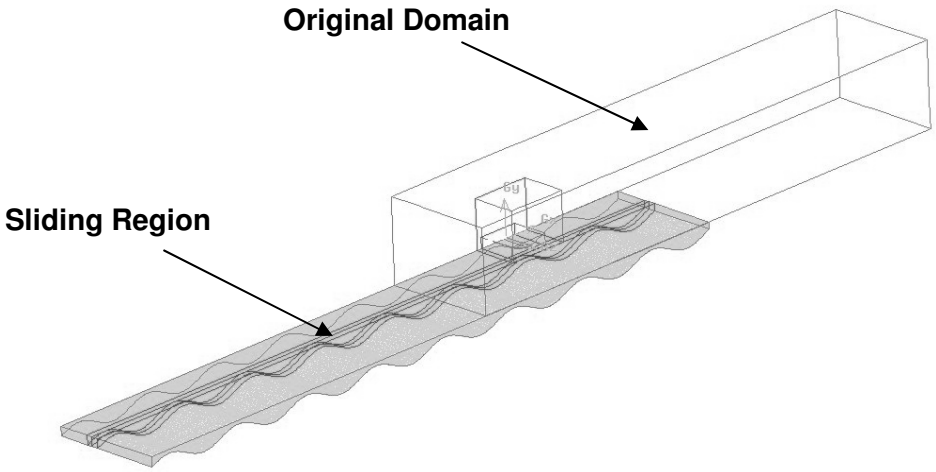


Figure 36: Original mesh domain with new sliding mesh region below

The sliding mesh region will translate along the bottom surface of the stationary domain. As the waves had to move at the same speed as the air, the whole domain was made to translate at 20.827 m/s. The upper surface of the sliding domain and the lower surface of the stationary domain were required to intersect in order to allow proper mating between the two regions. By setting the correct boundary conditions, Fluent® would detect where the two domains would or wouldn't overlap. This is discussed further in Section 5.4.1.

### 5.3.2 Length of the Sliding Region

The sliding region had to move past the wing for a sufficient length of time to capture the fluctuations of the force and moment coefficients. Ideally, it would also overlap with the entire length of the original domain to avoid unnatural step changes in the geometry. However, it could only be of a finite length unlike the "infinite" length of moving water waves in the VOF model. A longer slider length also had the implication of a greater number of cells in the mesh.

To determine the ideal length of the sliding region, a 2D model was constructed to compare the changes. The 2D model simulated the flow along the symmetry plane of the model. The results of the 2D comparison are shown in Figure 37. The dashed line indicates the height of the wave profile under the trailing edge of the wing at that moment in time. In theory a longer slider would have a longer travel time and allow the flow more time to settle into a periodic pattern as well as allowing the sliding region to overlap the entire domain for a longer period of time. From the graph, it is evident that a longer travel time is better, since the peak and troughs settle to the same values for consecutive oscillations. Furthermore, it seems that a longer slider does offer better results, even for the same short travel time.

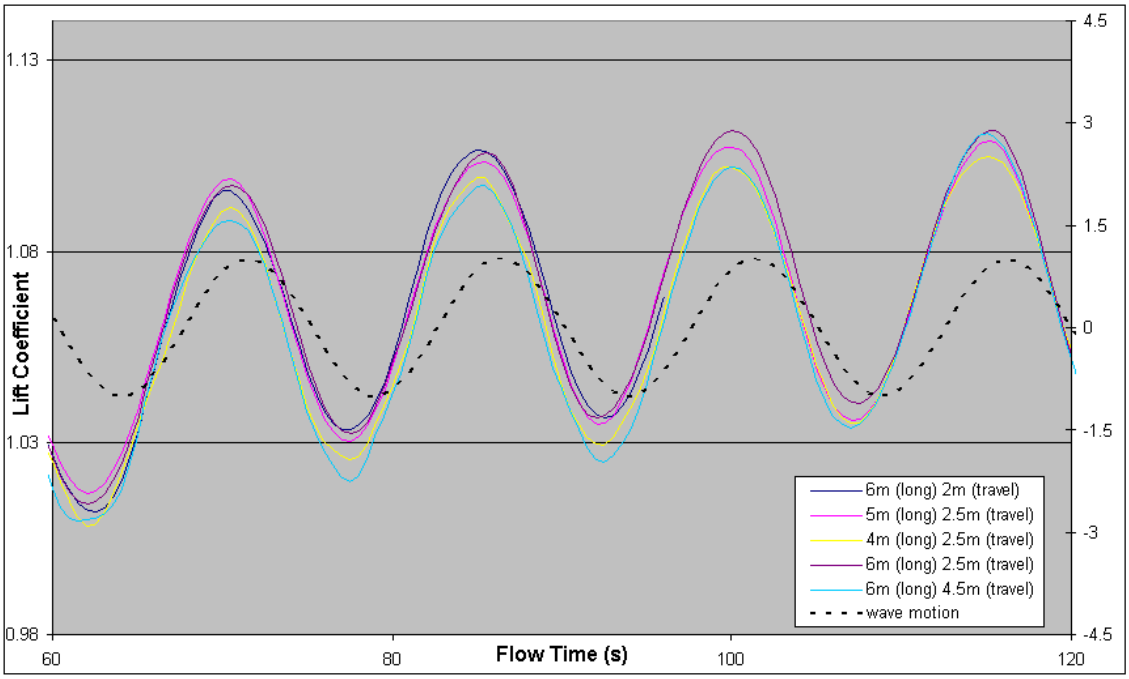


Figure 37: Comparison of different length sliding regions (2D)

However, a longer region would have a higher cell count, and longer travel times would mean that the solution would have to compute for much longer. Therefore a compromise was made. Figure 38 illustrates the movement of the sliding region showing the start (top) and end (bottom) positions. Final dimensions of the region are also given in the figure. The sliding region was set to be 5m long, stretching out 4m from the trailing edge of the wing while in the start position. The region would move 2.5m during the 120s solution time.

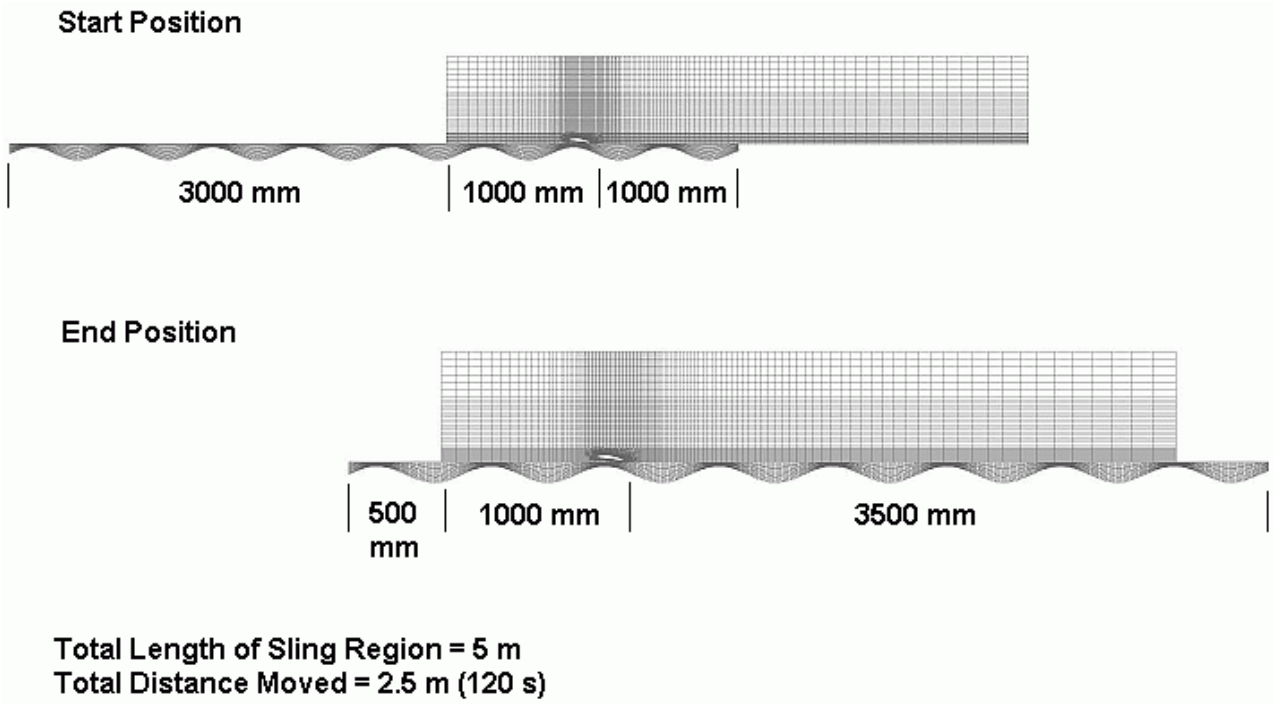


Figure 38: Start and end position of the sliding mesh (with dimensions)

### 5.3.3 Meshing the New Sliding Region

In order to determine the best cell distribution in the region, the 2D model was again used for quick comparisons between different mesh densities. Initially, an arbitrary mesh distribution of 500 cells in the streamwise direction and 16 cells vertically was chosen. It was thought that cells 10 units long would be sufficient to model the flow in the sliding region. A denser mesh could have been used as only the region below the wing was of real importance, but as a large portion of the sliding region would move under the wing, it would have resulted in a very large cell count.

Finally it was decided that a cell distribution of 400 (streamwise) by 14 (vertical) cells would be adequate, as it produced similar results to the 500 x 16 mesh. The graph in Figure 39 illustrates the $C_L$ values for three different meshes that were compared against each other. A higher mesh density was not tested as the cell count would have been too high for the RAM specification of the computer. Figure 40 illustrates the mesh distribution that was used.

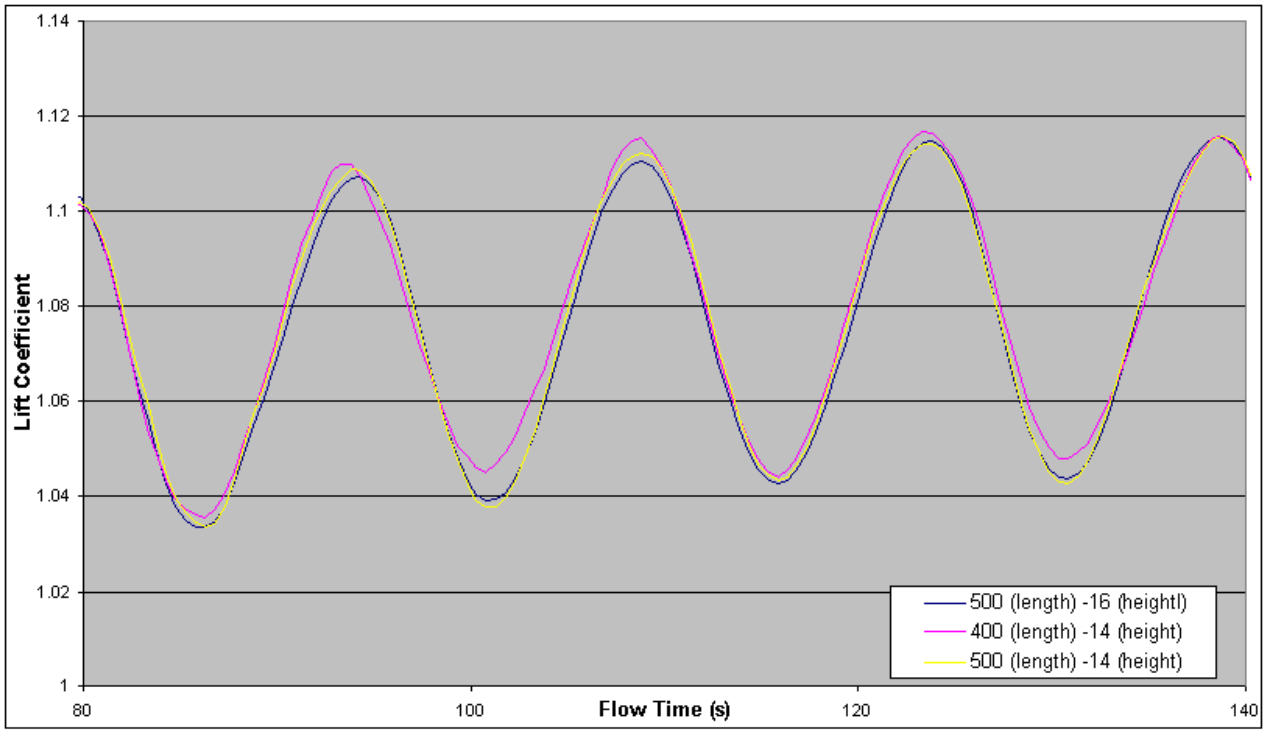


Figure 39: $C_L$ comparison between different sliding region mesh densities

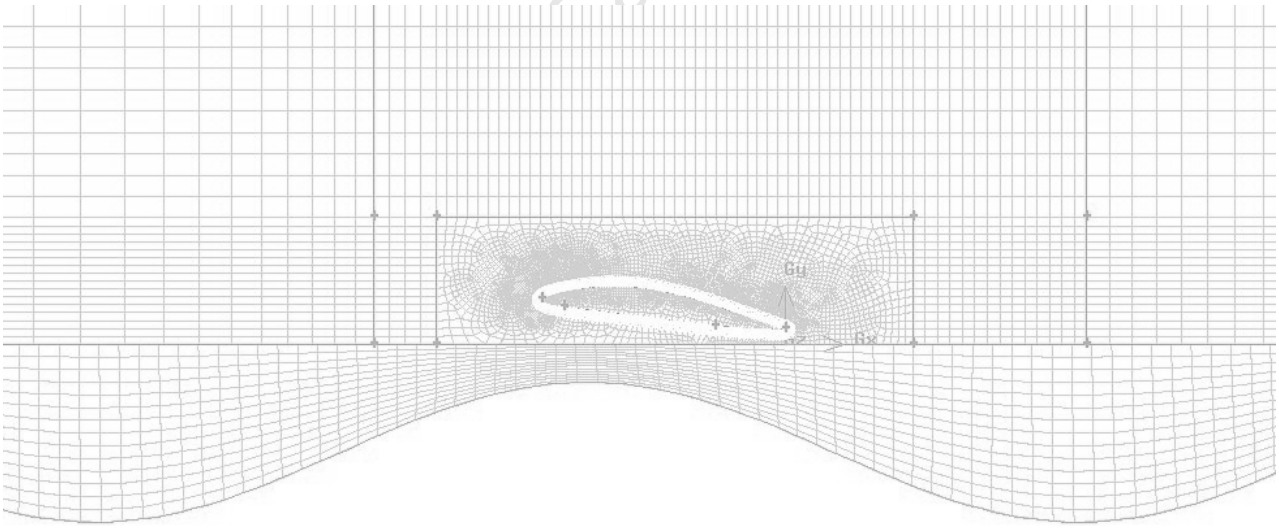

Figure 40: Side view of sliding region mesh

The spanwise distribution of cells was chosen to be identical to that of the stationary domain. This was done in order to minimise the error introduced by interpolating values between the stationary and moving nodes. This meant that the values would only have to be interpolated in the streamwise direction.

Furthermore, it was decided that the boundary layer of the wavy ground plane would not be explicitly modelled. This was in order to reduce the complexity of the grid and reduce the number of cells. Only the area under the wing would be of prime importance, and this region would only be affected by the boundary when the wave crests were high enough to get close to the trailing edge of the wing. Moreover, as the air and wavy ground plane were moving at the same translational velocity, there would be no need to model the boundary layer upwind of the wing.

## 5.4 BOUNDARY CONDITIONS FOR THE SLIDING MESH

Many of the boundary conditions for the new volume have been carried over from the flat ground plane model, while a new boundary condition is needed to control the interface between the two regions.

### 5.4.1 Interface between Sliding and Stationary Regions

The specification of an interface boundary condition would indicate to Fluent® that the particular boundary would be an interface between two movable regions. As a result, Fluent® would track the interface and detect which cells at the boundary overlap between the two regions. Air would be allowed to flow between the two regions where they overlapped. Moreover, for the regions that did not overlap, Fluent® would have to specify a new type of boundary to indicate the behaviour of the flow at those faces.

To complete the boundary specification, it was decided to make the non-overlapping regions a wall boundary. This meant that no air could flow in or out of the domain through these surfaces. These wall boundaries were also given a translational motion to prevent the air in contact with them developing a boundary layer. This was particularly important in the upwind region of the domain, thereby ensuring that the air reaching the wing had not been altered unnaturally.

### 5.4.2 Wavy Ground Plane – Wall

The wavy surface of the new volume became the new ground plane and was modelled as a solid wall boundary. The no-slip condition was again imposed on the surface, and zero roughness was specified. The wall motion was specified to be an absolute velocity of 20.827 m/s. As the whole region was moving at this speed, the resultant effect would be that the air would be travelling at the same speed as the wall.

### 5.4.3 Stationary and Sliding Outlet Boundaries – Outflow

An outflow boundary was again specified for the outlet of the sliding region. The only boundary value that must be specified for the outflow boundary is the proportion of the mass flow that is flowing out of the boundary. Therefore the two outflow boundaries had to share the total mass outflow of the system. As the flow was assumed to be incompressible, the ratio of mass flowing out of the domain through the outlet boundaries would only be a function of area and velocity. As the velocity field was not known ahead of time, it was assumed that the split of the mass flow would be proportional to the area of the outlets. Therefore the stationary outlet had a flow weighting of 0.89 and the sliding region outlet had a flow weighting of 0.11, thereby accounting for the total stationary and sliding inlet mass flow.

### 5.4.4 Other Boundary Conditions

The rest of the boundary conditions were essentially the same as for the flat ground plane model. Both the inlet and side boundary conditions have again been specified as velocity inlet type boundary conditions. The symmetry plane has also been used again. Figure 41 shows the different boundaries used.

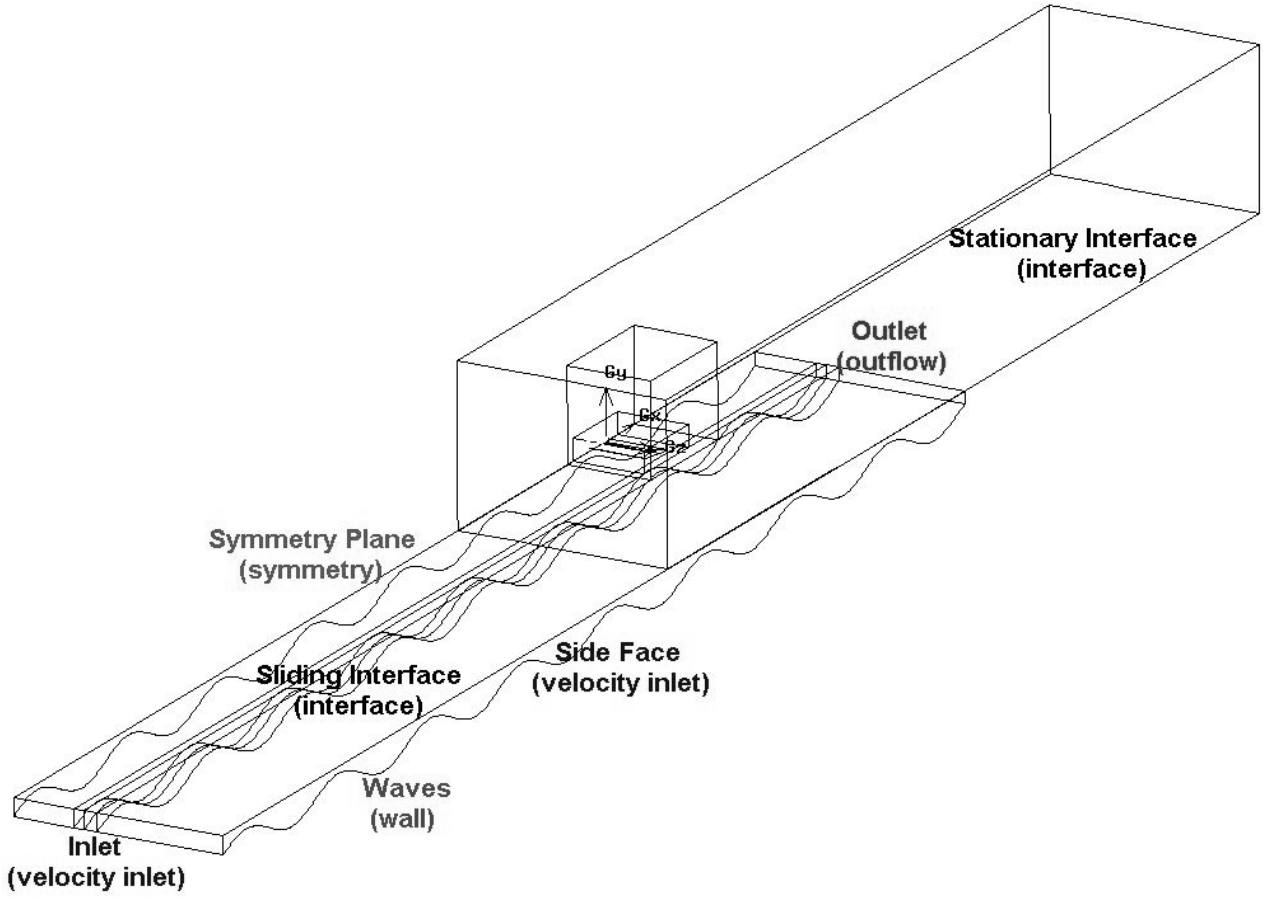


Figure 41: Boundary conditions for the sliding mesh

## 5.5 TIME DEPENDANT SOLVER SETTINGS

Due to the unsteady nature of the changing wave geometry, the solution had to be conducted as a time dependant calculation. This meant specifying how the solver would advance with time so as to generate an accurate result within the shortest amount of time.

### 5.5.1 Time Step Size

The correct time step size is very important. Small time steps result in better solutions because the different flow effects are allowed to develop over small time intervals. Time steps that are too small would result in a solution time that is excessively long. Therefore a balance between solution accuracy and calculation time is required.

To identify the best time step to use, the 2D mesh was employed again. The results of the investigation can be seen in Figure 42. Initially an arbitrary time step of 0.2s was chosen. When compared against a time step size of 0.1s, the results did not change significantly, which meant that not much more accuracy could have been gained by halving the time step (effectively doubling the solution time). Therefore it was decided to use the 0.2s time step size.

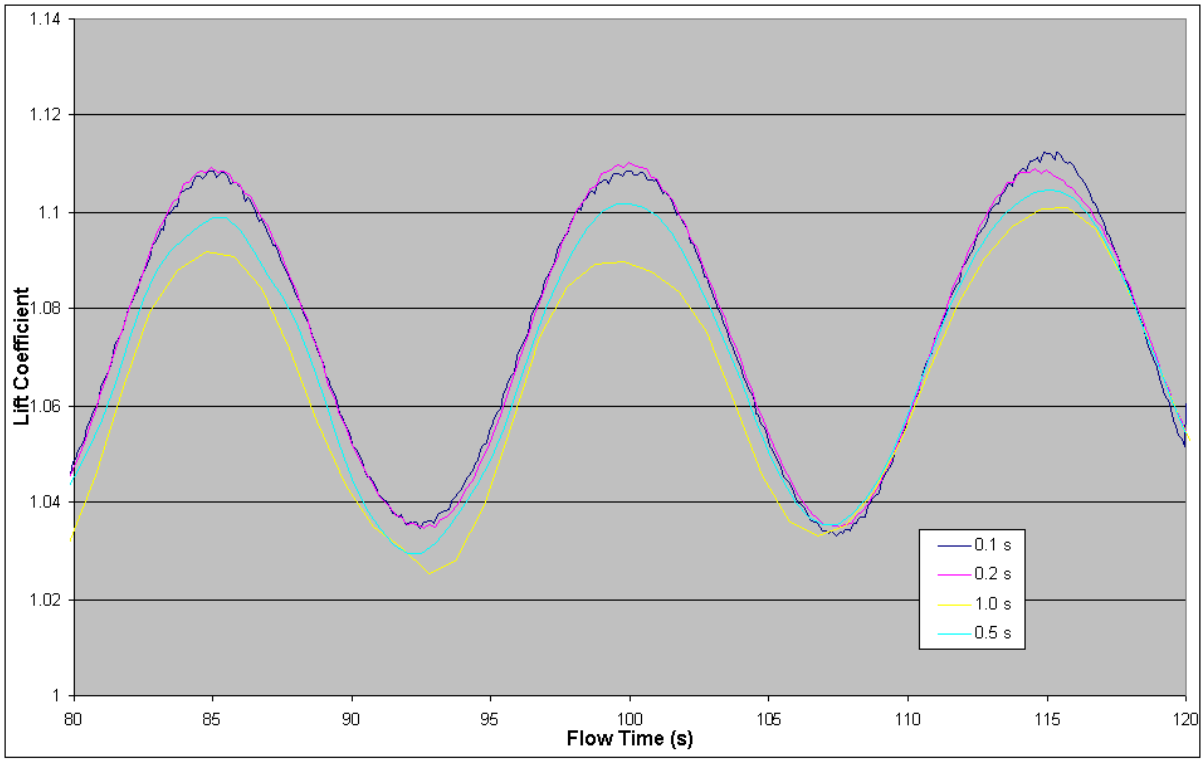


Figure 42: $C_L$ variation with changing time step size (2D)

## 5.5.2 Number of Iterations per Time Step

Another constraint in the solution time is the number of iterations per time step for the solution to converge. Ideally the solution should converge within about 10 iterations. However, because of the time step size that was used, it took roughly 40 iterations per time step to converge. Sometimes, especially during the early time steps the solution would take even longer to converge. Therefore an upper limit of 70 iterations per time step was set so as not to delay the solution unnecessarily.

### 5.5.3 Varying the Time Step Size

In an attempt to solve this problem, without always using a small time step, it was decided to make use of Fluent's® adaptive time step size option. With this option Fluent® would alter the time step size within the constraints set by the author. This meant that Fluent® would use the largest specified time step until there was a problem with convergence. So if the solution had not converged by the 70$^{th}$ iteration, then the time step was reduced automatically by Fluent® while remaining within the specified constraints. This usually resulted in the solution converging much quicker during the next time step.

Small time steps usually allow the solution to converge quicker for each time step. Unfortunately though, the 3D simulations did not converge significantly quicker, and it therefore still took longer to solve the overall problem. This was another reason for using the 0.2s time step.

### 5.5.4 Maximum Calculation Time

The maximum, or total, solution time defined when the calculation would stop calculating, and so had to be considered very carefully. It had to allow enough time for the solution to stabilise, and then be able to capture a number of the force and moment coefficient oscillations. The more oscillations it captured, the higher the certainty would be as to whether the oscillations had stabilised to produce the same values every time. In particular, the longer wavelengths, with their longer periods, would define the minimum amount of time needed to run the calculation.

After running the 2D simulations for 140 seconds, and sometimes for 160 seconds, it was found that these time limits were much larger than necessary. Therefore it was decided to limit the calculation to 120 seconds. This would allow the 4$c$ wavelengths sufficient time to settle down. Consequently, each solution would take a very long time to solve, as the maximum time step size was set to 0.2 seconds.

It is also important to note that this time limit would determine how far the sliding region would move along the domain. By the end of 120 seconds, the sliding region would have moved about 2.5m.

## 5.6 INITIALISATION AND ITERATION OF THE WAVY GROUND PLANE MODEL

The flow in CFD models take time to reach the final solution. Therefore if the calculation was just allowed to run, the flow would still be settling down while the geometry kept changing. This may have led to inaccuracies in the results as the force and moment coefficients may not have been affected only by the changing geometry, but also by the unsettled flow.

In order to synchronise the solution of the flow with the position of the waves, it was decided that the first time instant ($t = 0$) had to be as accurate as possible Therefore the flow at this time instant had to be solved until convergence before the solution could be carried out. However, the number of iterations per time step was limited to 70. Therefore, in order to speed up convergence for the first time instant, the solution from the 7°, $h_0 = 0.06$ flat ground plane model was used to initialise the flow. The solution of that model was interpolated onto the new mesh of the wavy ground plane model. Therefore the "initial guess" of the flow was fairly close to the final solution of the time step. This would minimise the time needed to converge the solution for the first time step.

After initialising the first time step, the solution was then solved according to the parameters discussed in this section of the report. A summary of the time dependant solver settings is shown in Figure 43, which shows the options that Fluent® allows for the time based solver.

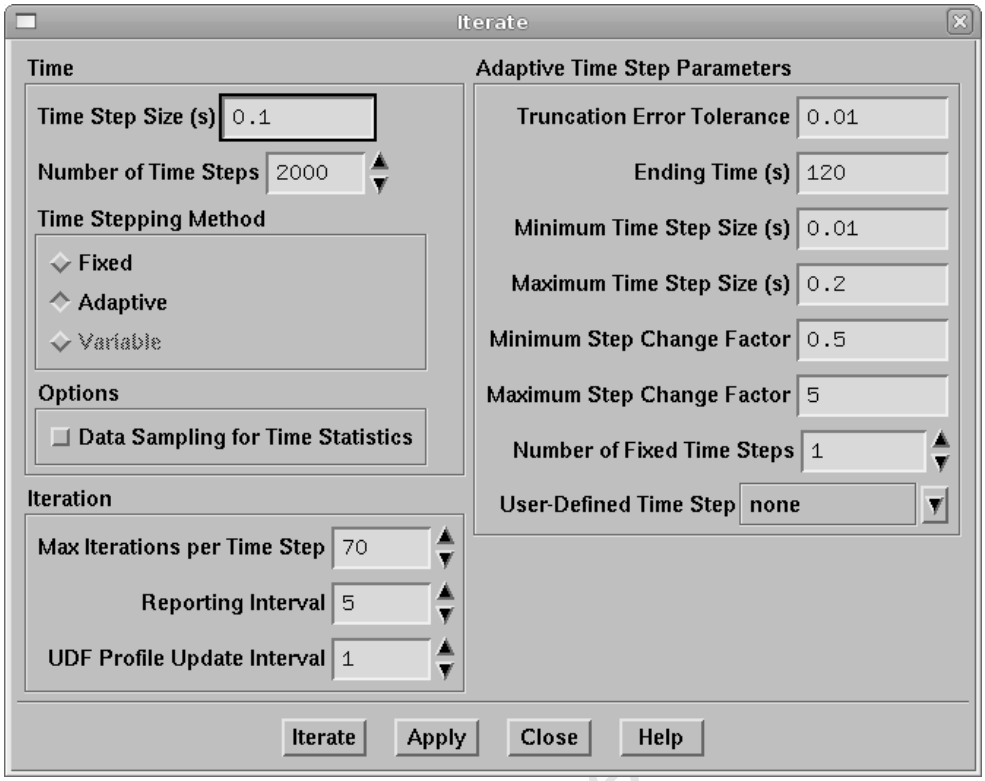


Figure 43: Time dependant solver settings

# 6. RESULTS FOR THE FLAT GROUND PLANE

The results from the simulations are discussed in this section. The results from the flat ground plane CFD model will be compared to those of Rhodes [4]. They will be analysed in such a way so as to determine the effectiveness of CFD to properly re-create the experimental results, and its suitability for use in further work on ground effect airfoils. As the results in this section are intended to mirror Rhodes' work, they will not be analysed to determine the wing's performance characteristics. The full set of data regarding the flat ground plane model can be found in Appendix A. Experimental data for $\alpha$ of -1° and 15° has been included in all graphs comparing experimental results to CFD in order to further indicate the trends of the experimental data.

## 6.1 LIFT COEFFICIENT

Figure 44 shows the $C_L$ characteristics of the wing for all of the angles of attack that were tested. Both the experimental (solid) and CFD (dashed) values have been plotted to illustrate the difference between the two sets of data.

It was found that most of the lift values were within 10% of Rhodes' experimental values. However, for angles of attack of 1° and 3°, many of the values showed a difference of more than 20%. For $h_0$ values of 0.06 and 0.12, the values at the low angles of attack of 3° and 5° were generally more accurate. However, as the wing angle increased, the error became greater. Interestingly, the converse is true for the two higher ground clearances, as the errors reduced to within 5% for some cases. A trend that seems to apply for all ground clearances is that the errors range from underestimating the lift at low angles, to overestimating them at the higher angles.

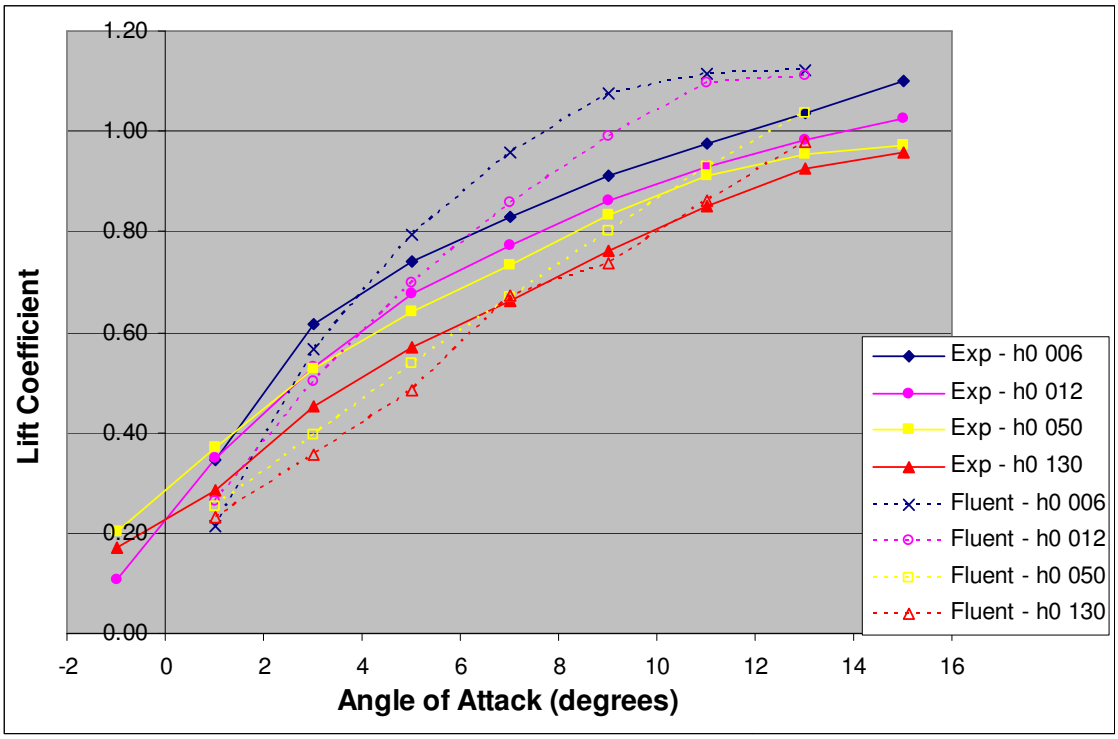


Figure 44: $C_L$ vs. $\alpha$ for both experimental and CFD results

## 6.2 DRAG COEFFICIENT

Fluent® was incapable of determining the drag on the airfoil to any reasonable degree of accuracy. In many cases (1° to 7°) the error was more than 50%, while the error only marginally improved as the angle of attack was increased. A graph of $C_D$ versus $\alpha$ is shown in Figure 45 to illustrate the differences between the experimental and CFD drag values.

From the graph, it is clear that Fluent® could only match the expected drag values when the angle of the wing was high enough to provide sufficient frontal area for Fluent® to resolve the pressure drag component of the total drag. The viscous component of drag, which dominates at low angles of attack, obviously could not be properly calculated by Fluent®. As a result of this, all graphs relating other coefficients and values to drag (e.g. lift to drag ratios) will be substantially different from the corresponding experimental values.

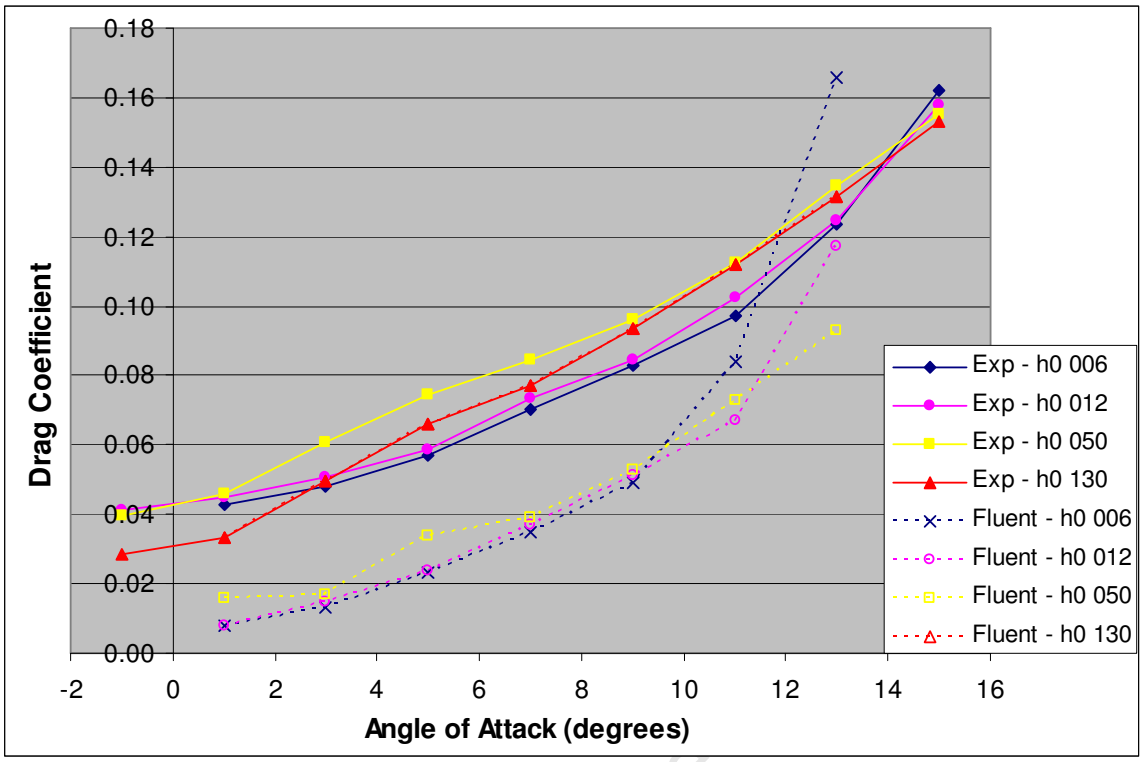


Figure 45: $C_D$ vs. $\alpha$ for both experimental and CFD results

## 6.3 PITCHING MOMENT COEFFICIENT

The results of the moment coefficient will be discussed relative to the ¼ MAC position, i.e. in terms of the $C_{M1/4MAC}$. Figure 46 shows these values plotted against $\alpha$. Wing pitching moments are a result of the lift and drag forces generated by the wing (and their respective positions). This is clearly shown in Figure 46. Initially, where both the lift and drag values at low $\alpha$ are smaller than the experimental values, the magnitude of the $C_M$ is much lower than the experimental values. As the lift and drag values rise above the experimental values, the $C_M$ values move closer to the experimental values. Therefore Fluent® is picking up the correct behaviour of the pitching moments. If the drag values were correct, then the $C_M$ values would match closely.

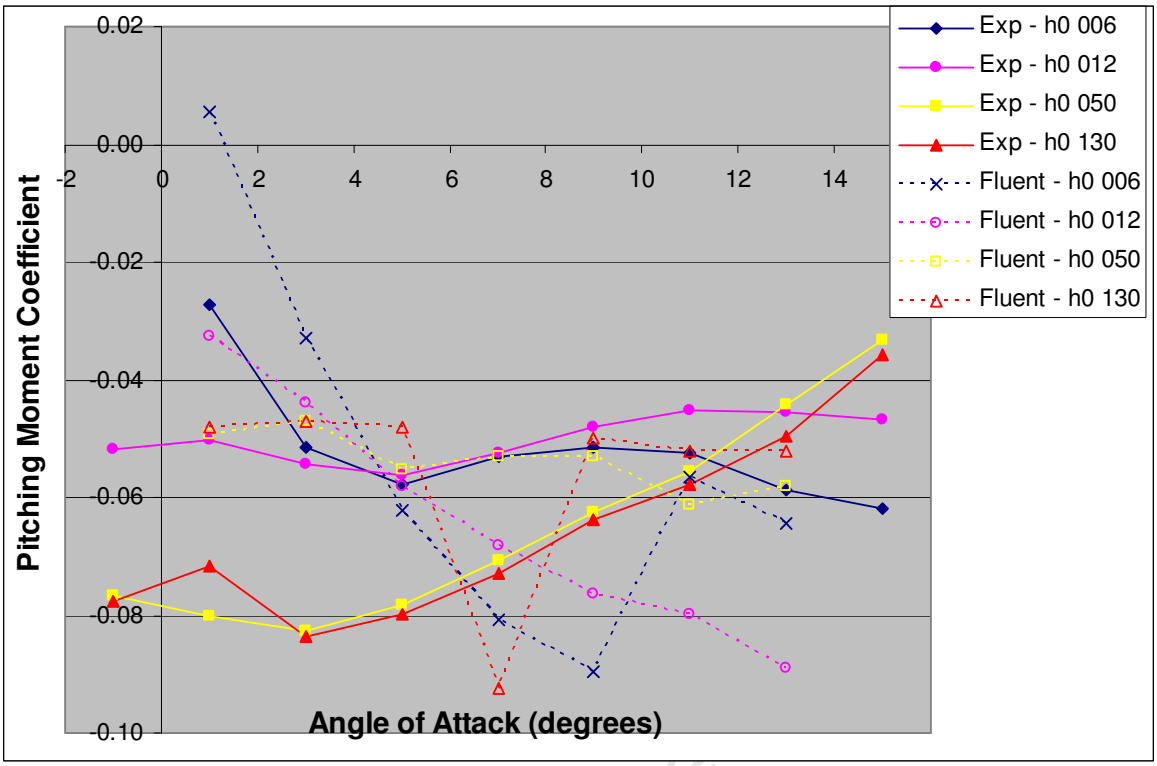


Figure 46: $C_{M1/4MAC}$ vs. $\alpha$ for both experimental and CFD results

## 6.4 OBSERVATIONS FROM CFD POST-PROCESSING

One of the key advantages of CFD analysis is the ease with which the flow field can be visualised. This allows the engineer to gain a great insight into the behaviour the flow and to identify any flow features of significance.

### 6.4.1 Increased Static Pressure on Lower Surface of Wing

One of the reasons that WIG wings generate more lift than conventional wings is that as the wing moves closer to the ground the air becomes trapped under the wing. The resulting increase in pressure aids the wing in generating more lift (see Section 2.2.2). This characteristic is illustrated in Figure 47, where the static pressure distribution around the wing and symmetry plane is given for each of the tested ground clearances. Each frame is taken from below and in front of the wing, looking towards the symmetry plane. The skewed line at the bottom of each frame represents the line where the symmetry plane meets the ground plane. The wing is at 7°. The plots show gauge pressure which is measured in Pascals.

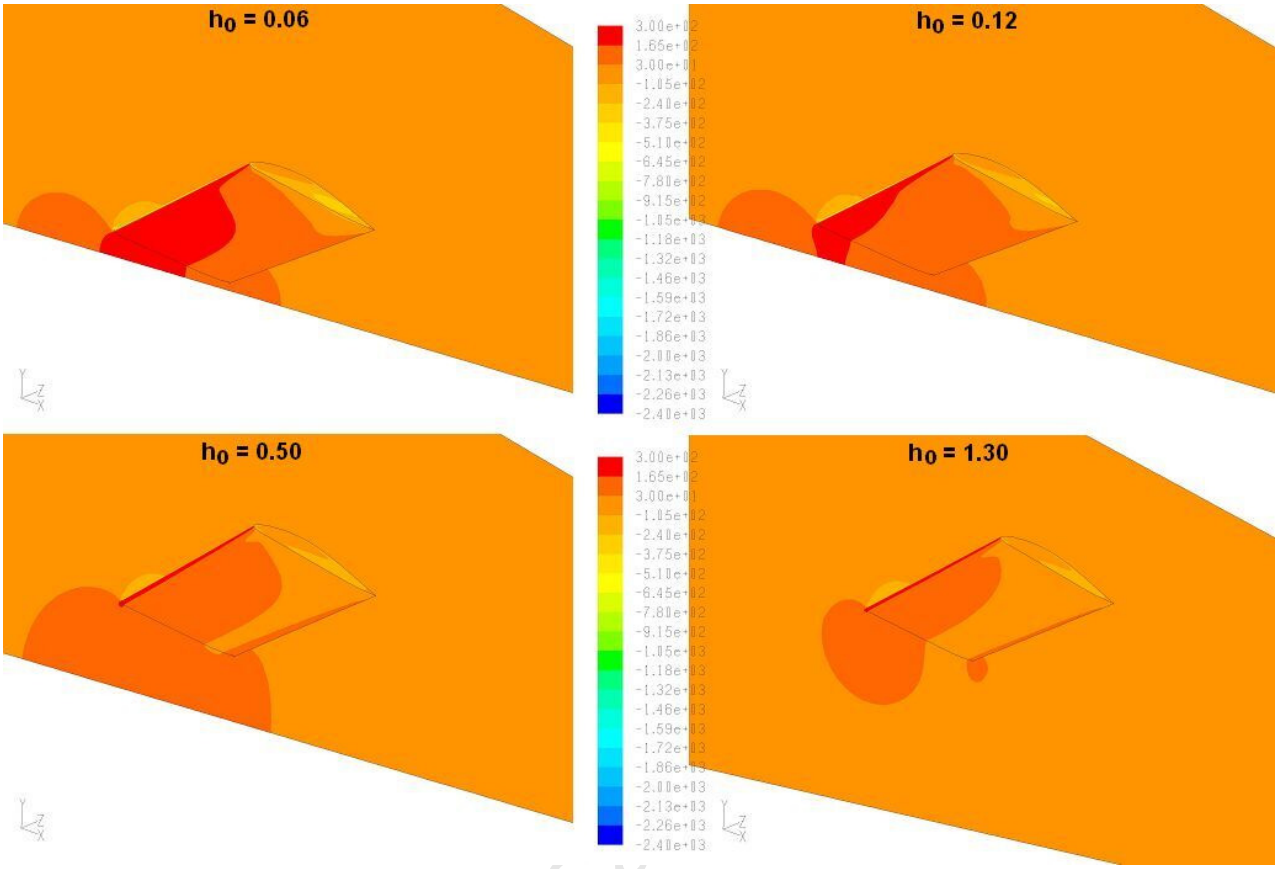


Figure 47: Static pressure plots on the lower surface of the wing for each $h_0$

The pressure plots in Figure 47 show how the pressure on the underside of the wing increases as it approaches the ground. This is most notable in the vicinity of the leading edge, and toward the centreline of the wing. The lower pressure at the wingtip is consistent with wings of finite span where the underside pressure reduces toward the tip. It is this higher pressure under the wing that gives these wings their superior performance at low ground clearances, particularly at clearances below $0.1c$. It is also this higher pressure that increases the nose down pitching moment of WIG wings.

### 6.4.2 Increased Trailing Edge Pressure and Early Flow Separation

While the increased pressure on the underside of the wing is considered advantageous, the pressure plots indicate that the high pressure region spills over onto the upper surface of the trailing edge of wing. This generates an adverse pressure gradient along the trailing edge region of the wing. The resulting pressure gradient is of particular importance when considering the performance of the boundary layer and its effect on flow separation.

Usually an adverse pressure gradient is not ideal as it causes the boundary layer to separate much earlier than a negative or neutral gradient. Earlier separation leads to much reduced lift generated by the wing and hence a lower stall angle.

The velocity plots of Figure 48 shows signs of early flow separation from the upper surface of the wing, which is probably caused by the region of increased pressure along the trailing edge. While the flow does separate earlier at lower ground clearances, the increased lift from the pressure on the underside of the wing prevents the wing from stalling.

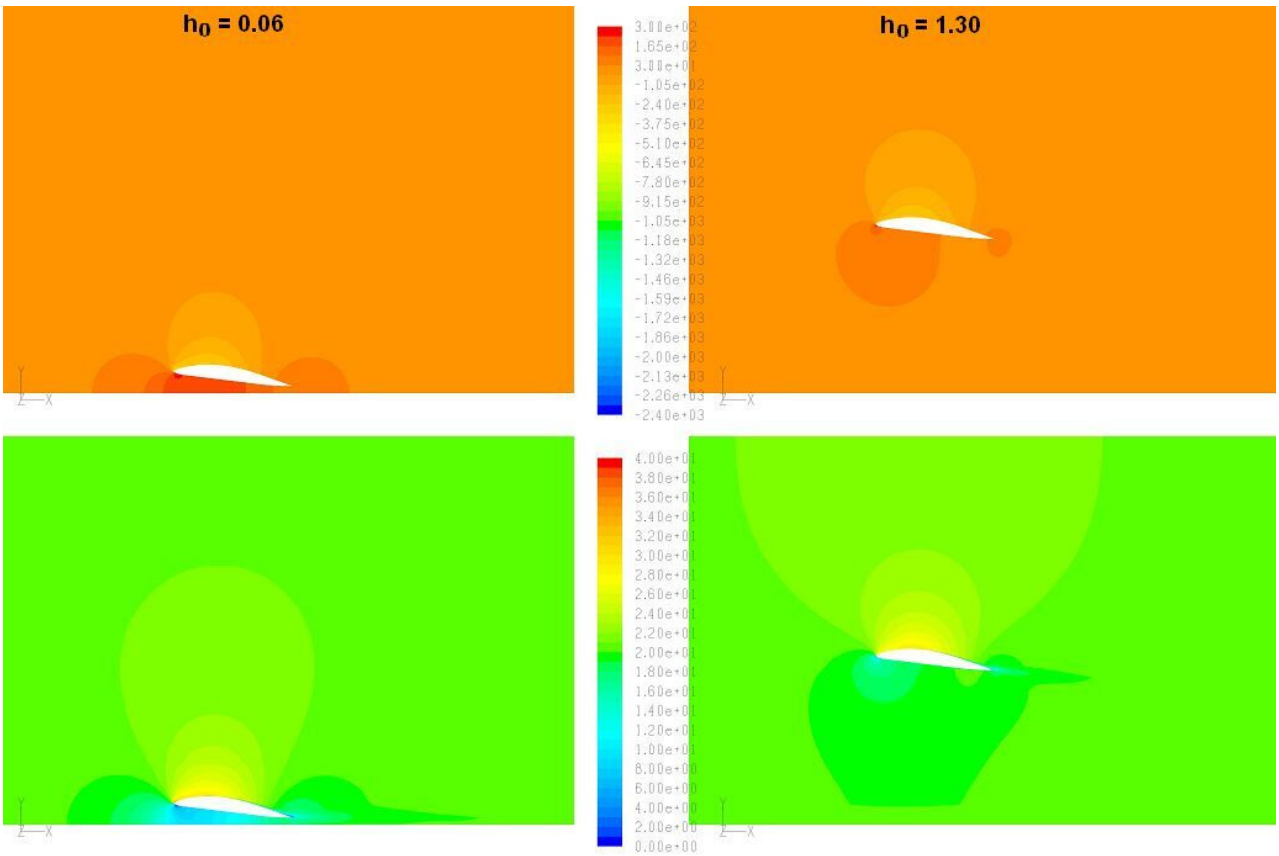


Figure 48: Pressure (top) and velocity plots of wing at $h_0$ of 0.06 and 1.30

### 6.4.3 Increased Upwash Due to the Presence of the Ground Plane

Another flow effect that changes due to the presence of the ground is the upwash at the leading edge of the wing. Velocity vectors in Figure 49 illustrate the direction of the flow around the leading edge of the wing. The figure on the left shows the flow at an $h_0$ of

1.30, while the figure on the right shows the flow at an $h_0$ of 0.06. The figure clearly shows how the upwash angle increases as the ground is approached. The increased upward angle of the flow is probably due to the increased pressure on the underside of the wing causing the air to find alternate routes around the wing. The higher pressure under the wing also slows the flow in this area, as is indicated by the smaller vector lengths. The increased upwash angle may also influence the tendency of the air to separate from the wing at low ground clearances, as the air has a more severe direction change around the leading edge than for higher ground clearances.

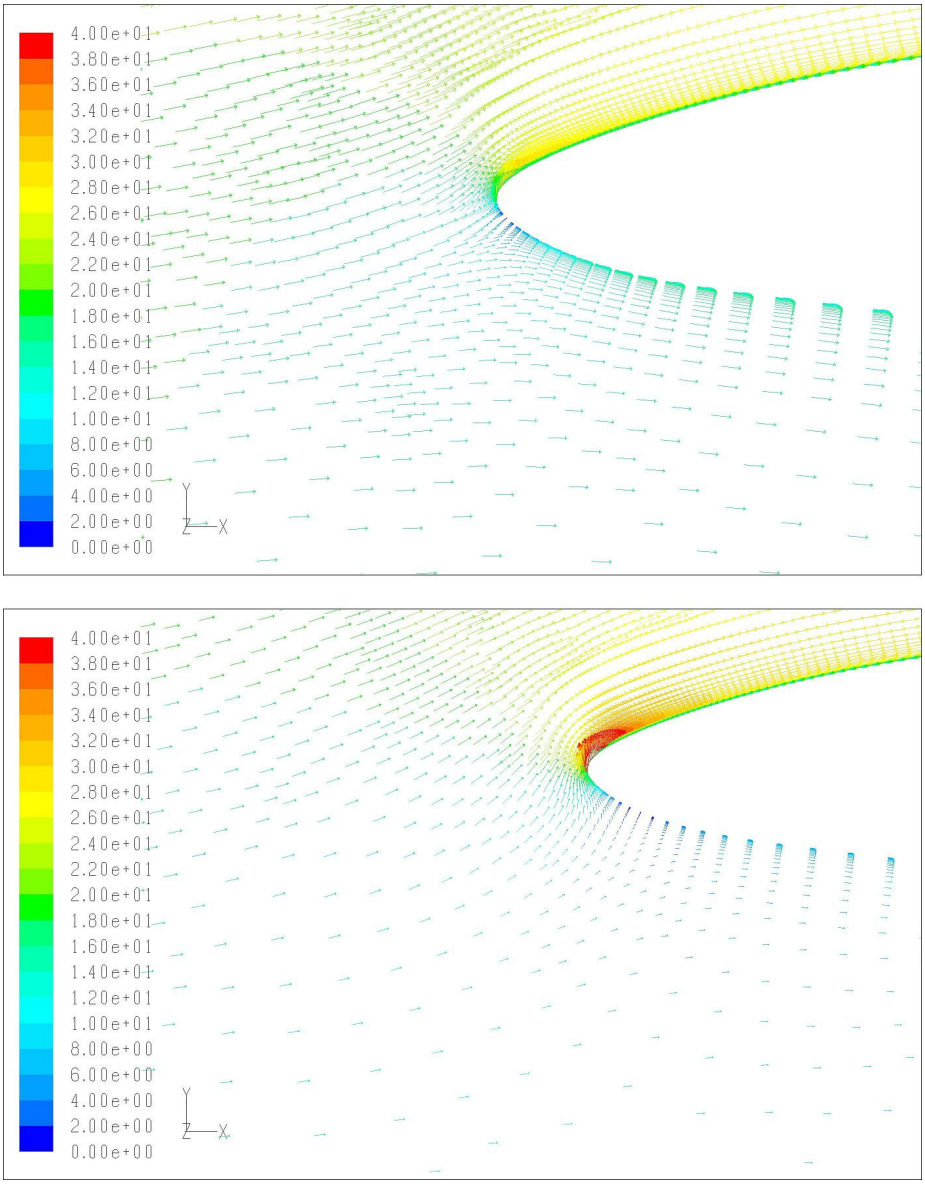


Figure 49: Velocity vectors for $h_0$ 1.30 (left) and 0.06 showing upwash at leading edge

### 6.4.4 Restricted Vortex Development

Flow pathlines around the wing, make it possible to visualise the flow pattern around the wing. Flying in close proximity to the ground limits the development of the wingtip vortices and so reduces their impact on the wing efficiency (see Section 2.2.2). In Figure 50, the flow pathlines illustrate the size and position of the resulting wingtip vortex for a wing at 11° angle of attack. The figure shows an elevated front view of the wing at both $h_0$ at 0.06 and 1.30 (left and right respectively).

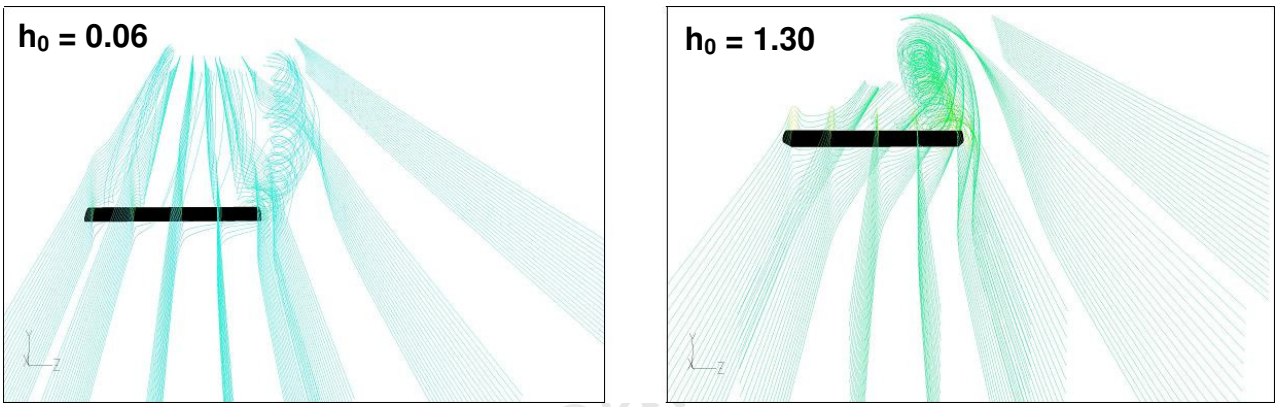


Figure 50: Front view showing vortex position and size change due to changing $h_0$

For an $h_0$ of 1.30, the vortex travels straight downwind from the wingtip. However, when the wing is close to the ground, the vortex tends to be pushed outwards away from the wingtip. This is illustrated by the top view of the pathlines in Figure 51 where the outward motion of the vortex centre can be seen. High aspect ratio wings are less affected by wingtip vortices, since the vortices are far apart from each other and their interaction is limited [9]. Ground effect produces the same effect for low aspect ratio airfoils as the wing-tip vortices are pushed away from each other and so cannot interact as strongly.

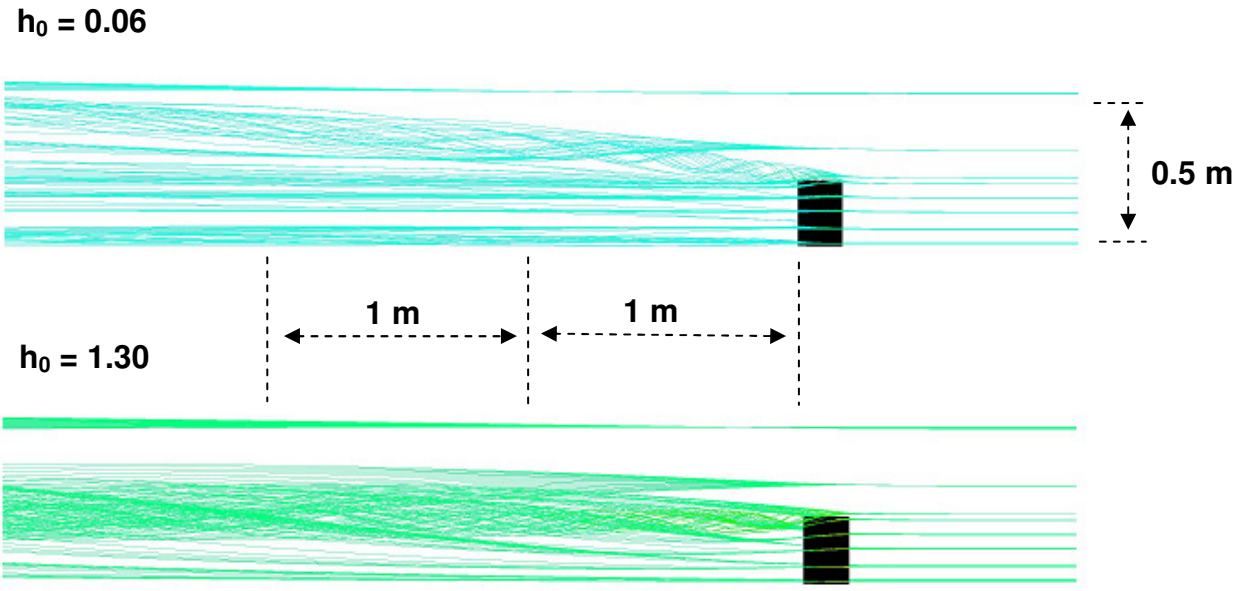


Figure 51: Top view illustrating the development of the wingtip vortex with changing $h_0$

What is also evident from these pictures is that the cross-sectional width of the vortex is also affected by the presence of the ground plane. It is not uncommon for the wingtip vortices to grow very large, the further they travel downstream. However, the ground plane restricts the size of the vortex. For an $h_0$ of 1.30 the vortex is concentrated behind the wingtip, but the air around it is still affected and caused to swirl. For the case of $h_0$ = 0.06, the vortex does not have sufficient room to develop and thus does not become as wide, or as high, as it would at higher ground clearances.

# 7. RESULTS FOR THE WAVY GROUND PLANE

The results from the simulations for the wing in close proximity to the wavy ground plane are discussed in this section. To the author's knowledge, there is no experimental data with which to compare the following CFD results. So any comments made on the validity of these results are made in relation to the CFD simulations studied by the author for the flat ground plane. The results for the wavy ground plane models can be found in Appendix B.

Simulations were only conducted for angles of attack of 7° and 11°. This would give an idea of the performance of the wing over a range of angles of attack. An angle of attack of 1° or 3° was not attempted as it was felt that the results for the flat ground plane were not accurate enough to provide any meaningful results. The simulations were conducted for varying wavelengths and wave heights while a constant clearance between the wing and the wave centreline (mean height) was maintained ($h_0$ = 0.50). This was done to determine the effect of the changing gap between the wing and the wave (by changing the height of the wave) and the speed at which the gap changed (done by changing the wavelength).

Due to the periodic nature of the wing forces, each of the coefficients will be considered in terms of the maximum, minimum, and mean values that resulted from the wavy ground plane. The maximum and minimum values (solid lines) have been plotted, along with the mean values (dashed) to illustrate the distribution and trends of the data. All of the graphs and figures provided in this section display the results for $\alpha$ = 7°, but the trends discussed here also apply for $\alpha$ = 11°.

## 7.1 LIFT COEFFICIENT

Figure 52 shows the $C_L$ characteristics of the wing for all of the wave length/height combinations that were tested. The plotted values start from the smallest wavelength and lowest wave height combination on the left, and increase in wave height for each wavelength towards the right. The data from Figure 52 is re-arranged in Figure 53 and Figure 54 to illustrate the effect of changing the wavelength and the wave height respectively.

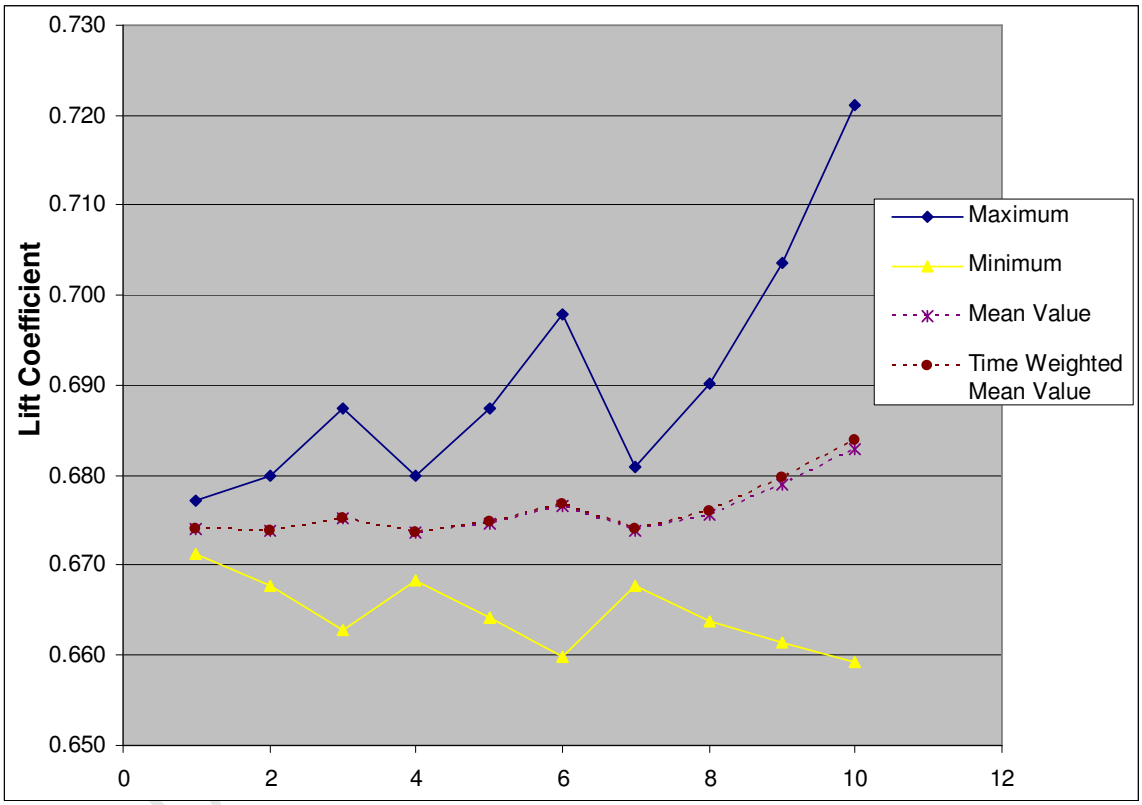


Figure 52: $C_L$ for wing at 7° for each wavelength and wave height combination

All of the maximum $C_L$ values obtained for the wavy ground plane are higher than the $C_L$ value for the flat ground plane ($C_L$ = 0.671 for $\alpha$ = 7° and $h_0$ = 0.50). For a wavelength equal to the chord ($L_W$ = 1), the $C_L$ increased by only 1%, but at $L_W$ = 4, and at the highest wave height, the $C_L$ value was 7.5% higher. The minimum $C_L$ should also be considered, as this would be the limiting case for the performance of any vehicle using the wing to produce lift. Figure 52 shows that while the $C_L$ minimum is lower than that for the flat ground plane, the average $C_L$ value is higher. The average $C_L$ value increases as the

wavelength and wave height are increased. This is because the maximum $C_L$ values grow in magnitude much quicker than the minimum values (7.5% versus 2% for the $L_W = 4$ and largest wave height). Therefore this wing, on average, generates more lift in the presence of waves than for the flat ground plane. This trend was expected by Rozhdestvensky in his paper [1]. For $\alpha = 11°$, the peak $C_L$ value at $L_W = 4$ is only 6.5% higher. Furthermore, for $\alpha = 11°$, the minimum $C_L$ is actually slightly higher than for the flat ground plane ($C_L = 0.930$) at the lower wavelengths, but the values quickly fall below 0.930. This small discrepancy would be due to small differences in the numerical solution.

When plotting the $C_L$ against the wavelength (for constant wave heights), the data shows that the $C_L$ does increase slightly with increasing wavelength (Figure 53). The increase in $C_L$ seems to be greater for higher wave heights, where the larger changes in wave geometry lead to larger changes in the wing's response. Furthermore, as the wavelength reduces, so the $C_L$ value tends to the value for the flat ground plane.

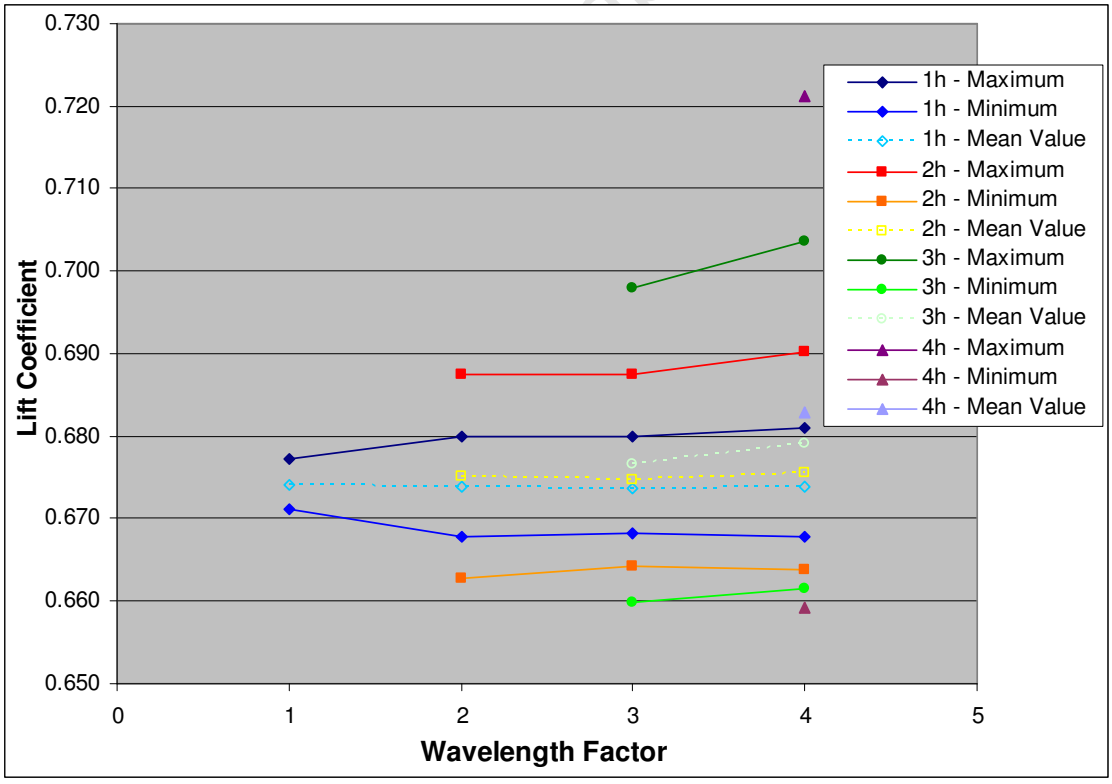


Figure 53: $C_L$ vs. wavelength for $\alpha = 7°$ (lines of constant wave height)

Figure 54 shows that as the wave height reduces from highest to lowest, the $C_L$ tends towards the value for the flat ground plane ($C_L$ = 0.671). This trend is also illustrated by the mean value curve. This trend is correct, because as the wave height reduces to zero, so the wave resembles a flat ground plane. Furthermore, the wing is found to be more sensitive to changes in wave height (for constant wavelength) than changes in wavelength (for a constant wave height).

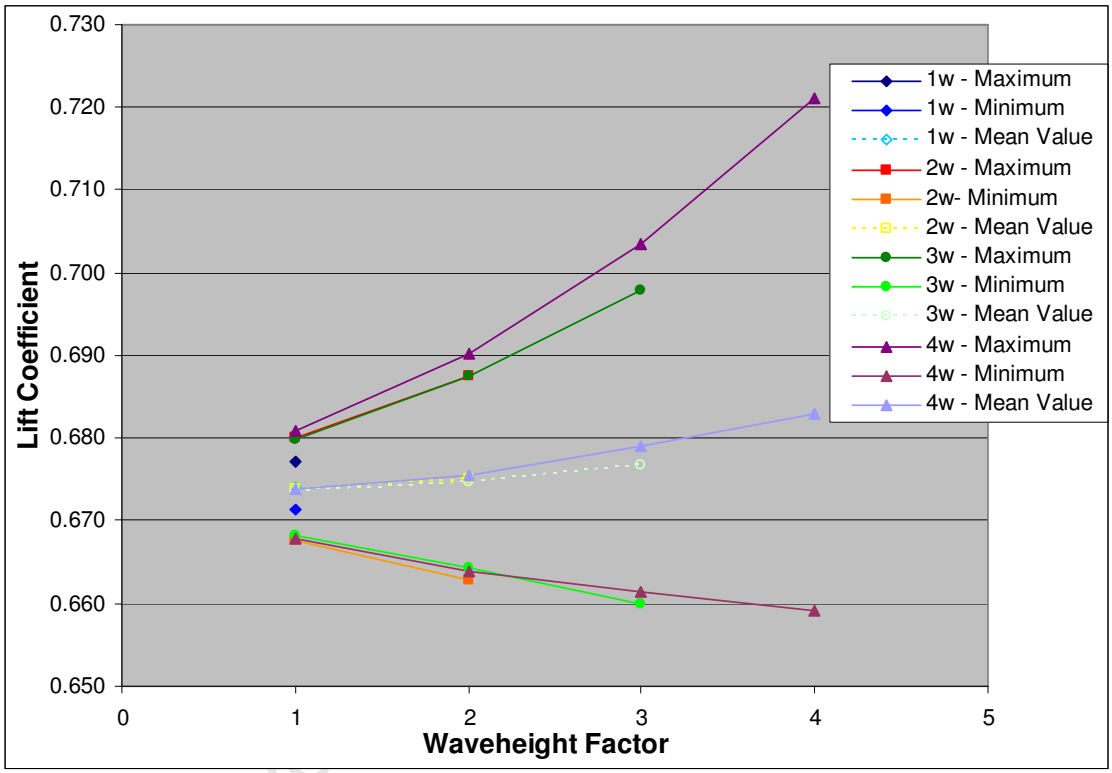


Figure 54: $C_L$ vs. wave height for α = 7° (lines of constant wavelength)

An interesting observation can be made when comparing the coefficient behaviours of the different wavelengths. For the longer wavelengths, the troughs of the coefficient oscillations tend to be much flatter than the crests (see Figure 55). Moreover, the slope of $C_L$ curve drops off quicker than it builds up. This shows that it takes longer for the $C_L$ value to increase than it does to decrease. The wing also spends more time with a lower coefficient than with a high $C_L$ value. However, the peak $C_L$ values are higher than the minimum values, so on average, the $C_L$ value is higher for the wavy ground plane.

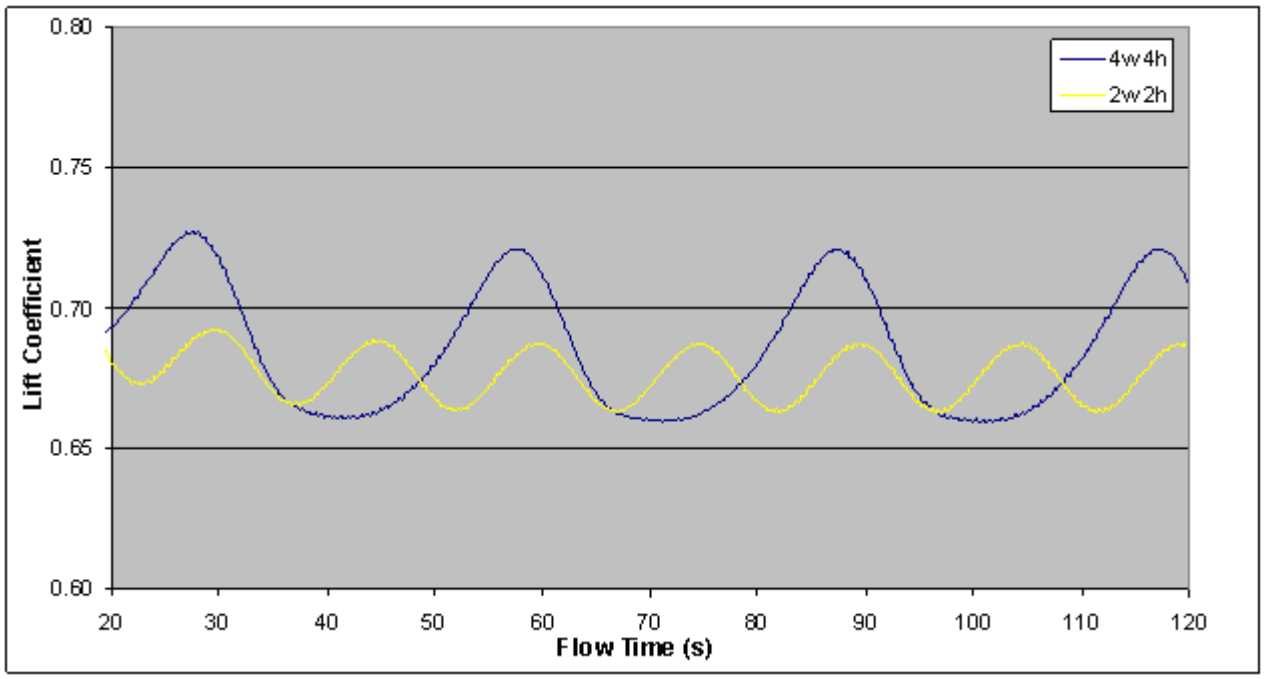


Figure 55: $C_L$ vs. flow time for different wavelengths ($\alpha = 7°$)

## 7.2 DRAG COEFFICIENT

As for the flat ground plane, the $C_D$ results for the wavy ground plane seemed totally erroneous. The $C_D$ values were the same as those obtained for the flat ground plane ($C_D$ = 0.039). There was no apparent trend to the values, but as the magnitude of the values hardly changed from one set to another, no clear trend would be shown. It could be, however, that the drag values do not change significantly for differing wave profiles, but there was no data available to either prove or disprove this comment. A graph of $C_D$ values for the different wave profiles is shown in Figure 56.

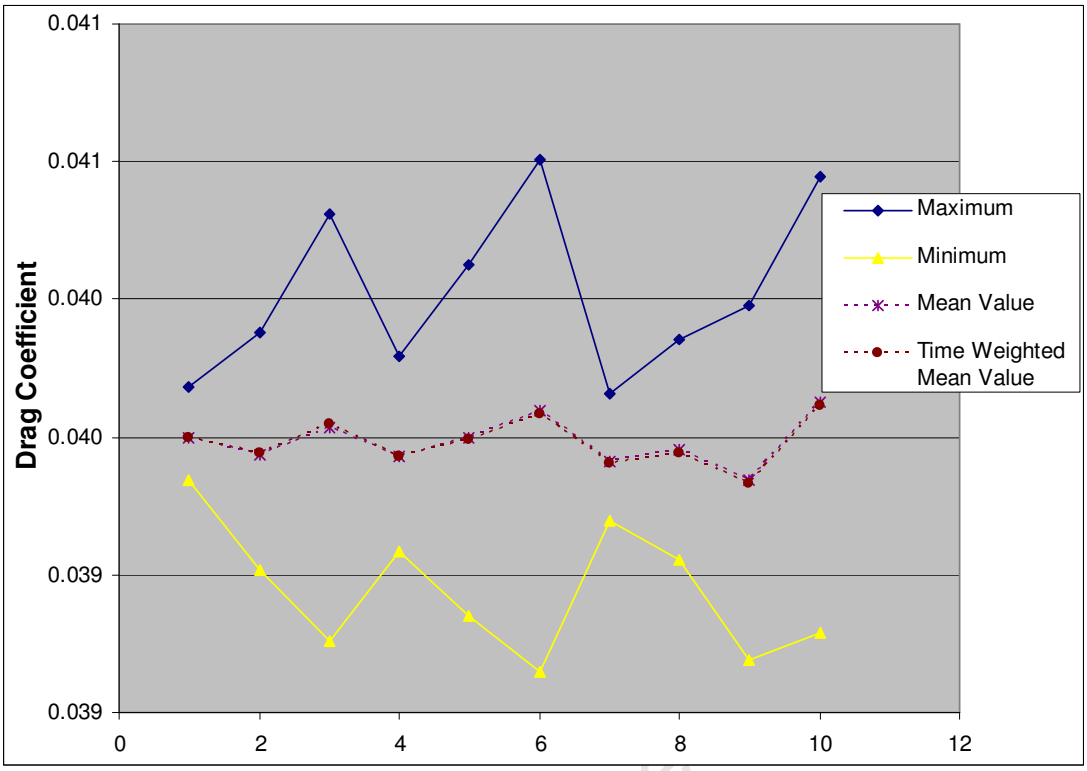


Figure 56: $C_D$ for wing at 7° for each wavelength and wave height combination

## 7.3 PITCHING MOMENT COEFFICIENT

The performance of the moment coefficient is again dominated by the performance of the lift coefficient. This is illustrated in Figure 57 where the $C_{M1/4MAC}$ values are plotted for the wing at 7° angle of attack. In general, the $C_M$ values are shown to increase in magnitude for an increasing wave height. An increase in the wavelength (for the same wave height) also increases the pitching moment. As the wing encounters the peaks in the ground plane, the $C_M$ becomes more negative, increasing the nose down pitching moment of the wing. Alternatively, as the wing flies over the troughs, the $C_M$ becomes less negative. When these oscillations are averaged out (mean value curve in Figure 57), they show that an increase in wave size slightly increases the nose down pitching moment of the wing. Most of the $C_{M1/4MAC}$ values calculated for a wavy ground plane at $\alpha$ = 7° are greater in magnitude (more negative) than for the flat ground plane value ($C_{M1/4MAC}$ = -0.053).

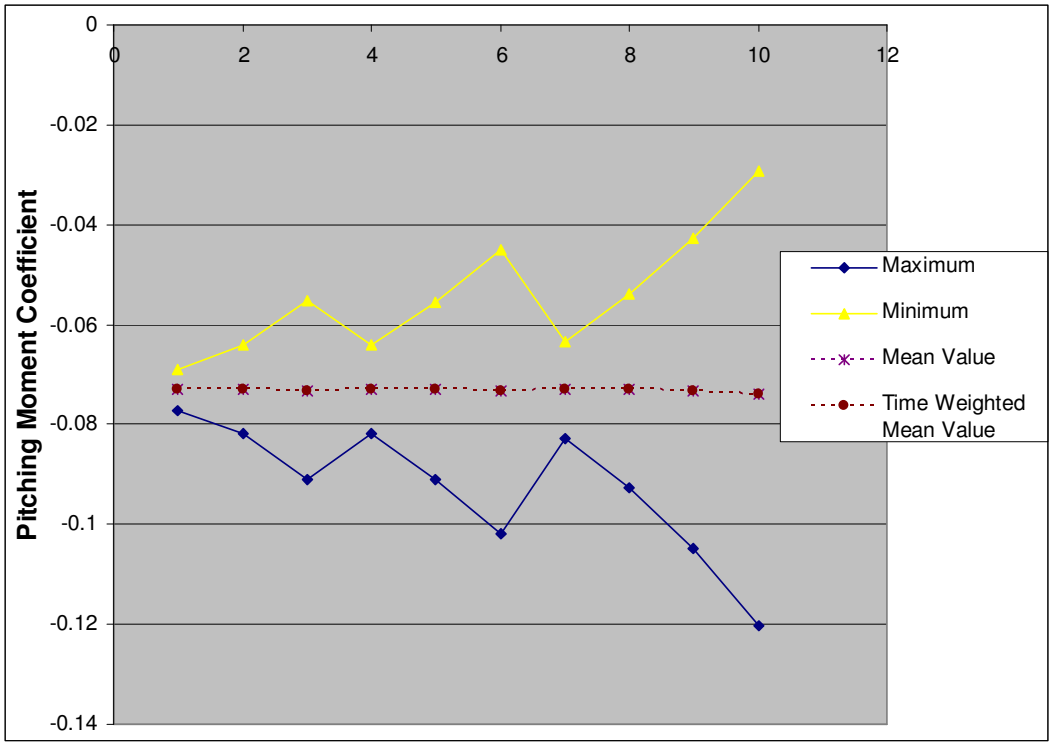


Figure 57: $C_{M1/4MAC}$ for wing at 7° for each wavelength and wave height combination

## 7.4 PHASE ANGLE

The variation in the phase angle was also investigated. Due to the unreliability of the drag values, only the phase angle of the $C_L$ was considered. It should be noted that the phase angle variation was different for both the $C_D$ and $C_M$ when compared to the lift phase angles. Figure 58 shows the variation in the $C_L$ phase angle (in radians) plotted against the wavelength ($L_W$). The phase angles for both the minimum and maximum $C_L$ values ($\alpha$ = 7°) have been plotted, but it is clear that they are nearly identical. For the two longer wavelengths, the phase angles are negative, which indicates a leading phase. This means that the peak $C_L$ values occur before the peak of the ground plane wave. The phase angle then switches to positive, or a lagging phase angle for a $L_W$ = 2. At a $L_W$ = 1 the phase returns to a leading phase. Similar trends and similar phase angles are found for the wing at 11°.

When plotted against wave height, the phase angle for each wavelength does not change significantly when the wave height is changed. Therefore the phase angle is independent of wave height, and is only affected by the wavelength.

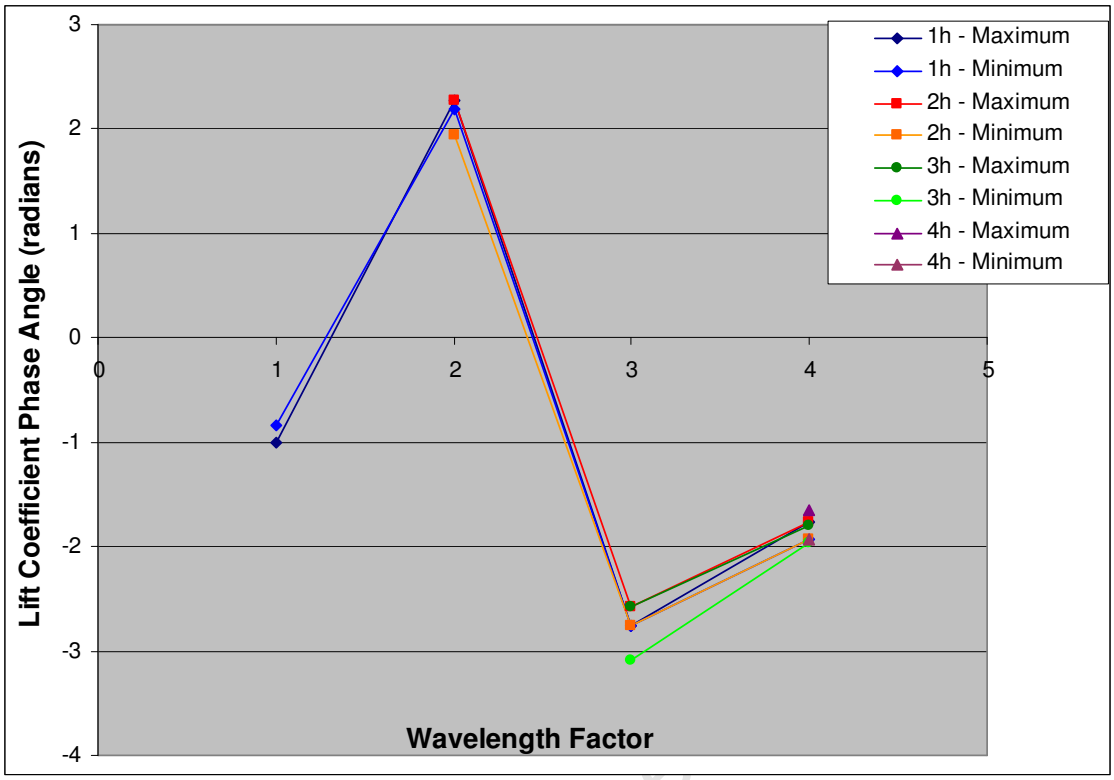


Figure 58: $C_L$ phase angle vs. relative wavelength ($\alpha = 7°$) (lines of constant wave height)

It should be noted that these phase angles are rather large when considered against the position of the physical wave under the wing. In some cases, the peak $C_L$ value is already decreasing while the wave is just beginning to increase in size. However, there is no data with which to compare these results, therefore these trends may actually be correct.

## 7.5 NON-DIMENSIONAL NUMBER PLOTS AGAINST STROUHAL NUMBER

Rozhdestvensky [14] developed a mathematical theory to describe the behaviour of wings in extreme ground effect (EGE). Seeing as there was no experimental data to compare the wavy ground plane model to, it was decided to investigate whether there were any correlations between the CFD model and the data presented by Rozhdestvensky. However, Rozhdestvensky did not specify the exact test conditions to which his data applied. If important variables in his tests were different to the CFD conditions (e.g. the relative ground clearance), then his data would not be applicable to the CFD data.

### 7.5.1 Lift Coefficient vs. Strouhal Number

When the $C_L$ values are plotted against Strouhal Number, the trends are similar to that of $C_L$ versus wavelength. The $C_L$ values decrease for increasing Strouhal Number (decreasing wavelength). The $C_L$ values also decrease for decreasing wave heights.

In order to compare the CFD values to that of Rozhdestvensky, a graph of $F/F_0$ was generated. This graph, given in Figure 59, is comparable to Figure 17 which shows Rozhdestvensky's results. The $F/F_0$ ratio is related to the ratio of the oscillating component of the $C_L$ to the $C_L$ for the flat ground plane by the wave amplitude and the relative ground clearance. Here the values show similar trends to the plain $C_L$ values versus Strouhal Number, but do not entirely match the trends proposed by Rozhdestvensky. The value at Strouhal Numbers 2.09 and 3.14 are almost twice as high as expected. These values should be lower than that for Strouhal Number of 6.28, but instead are much higher. Therefore these values do not correlate well with the Rozhdestvensky's theory.

Furthermore, the CFD results indicate that $C_L$ decreases towards the value for the flat ground plane as the wavelength is reduced. Conversely, Rozhdestvensky's theory suggests that the $C_L$ values should only tend towards the flat ground plane values for wave of infinite length (Strouhal Number of zero).

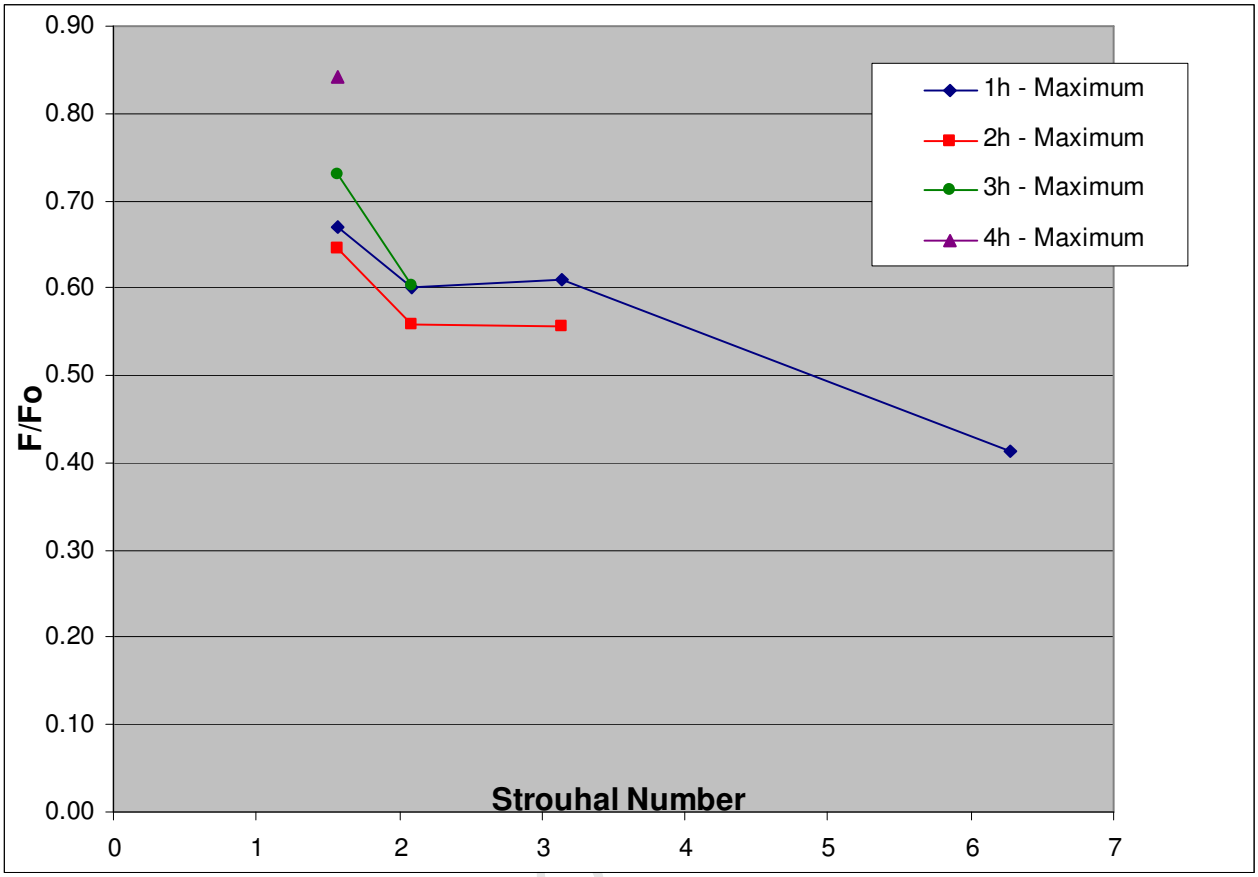


Figure 59: $F/F_0$ ratio vs. Strouhal Number ($\alpha = 7°$)

### 7.5.2 Phase Angle vs. Strouhal Number

Figure 60 shows the variation in the $C_L$ phase angle (in radians) plotted against the Strouhal Number. The phase angles for both the minimum and maximum $C_L$ values ($\alpha = 7°$) have been plotted, but it is clear that they are very much identical. For the two lower Strouhal Numbers, the phase angle is negative, which indicates a leading phase. This means that the peak $C_L$ values occur before the peak of the ground plane wave. The phase angle then switches to positive, or a lagging phase angle for a Strouhal Number of 3.14 ($L_W = 2$). At a Strouhal Number of 6.28 ($L_W = 1$), the phase returns to a leading phase.

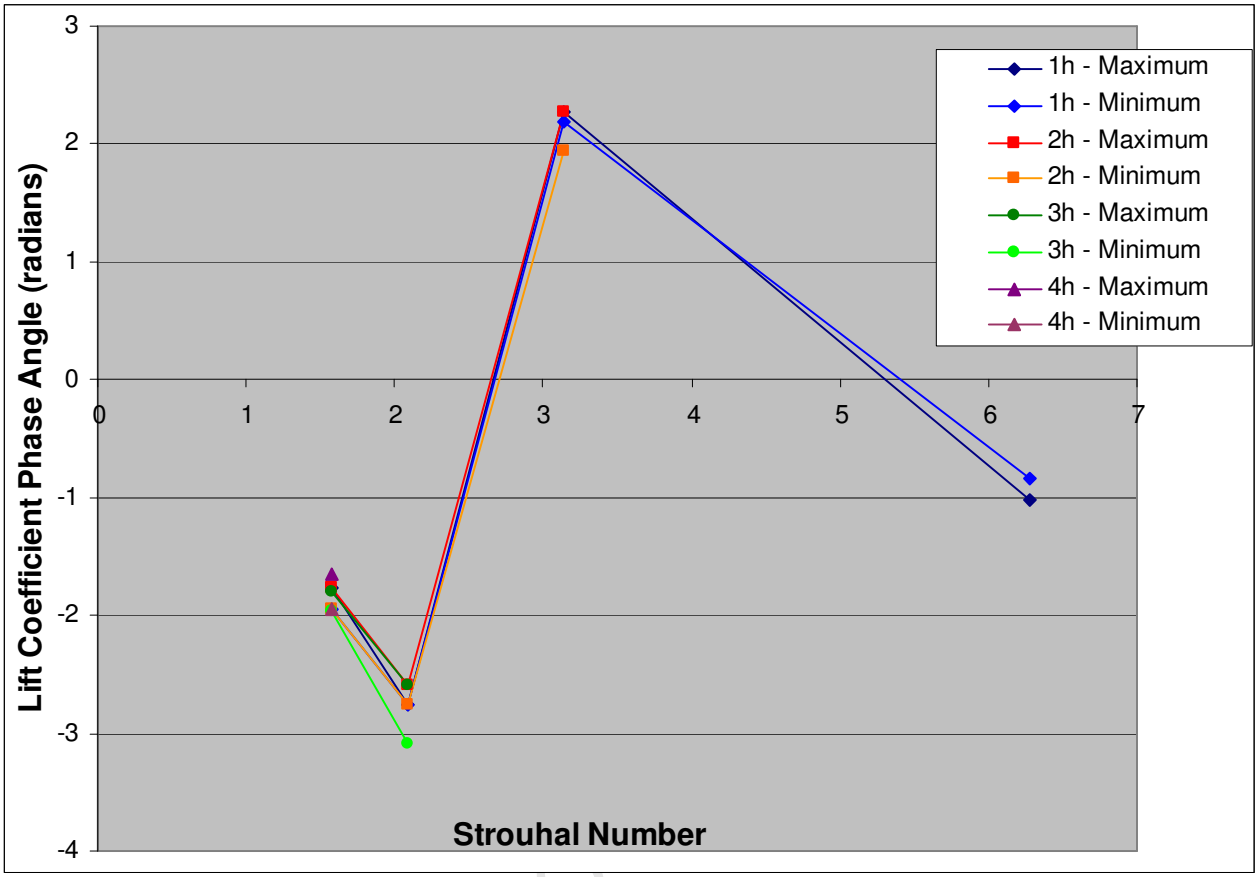


Figure 60: $C_L$ phase angle vs. relative wavelength ($\alpha = 7°$) (lines of constant wave height)

When compared to the theory presented by Rozhdestvensky (Figure 18), these results are very different. In fact, Rozhdestvensky calculated that the two lower Strouhal Numbers (1.57 and 2.09) should have a lagging phase angle, and that the phase angle should be leading at a Strouhal Number of 3.14. Therefore the values are completely reversed. In addition, the magnitudes of the values seem to be about 5 to 10 times too large.

## 7.6 OBSERVATIONS FROM CFD POST-PROCESSING

Once again, the post-processing features of Fluent® have been used to study the flow patterns around the wing in the presence of the wavy ground.

### 7.6.1 Increased Static Pressure on Lower Surface of Wing

The pressure on the underside of the wing is important, particularly as the wing approaches the ground. However the effective ground clearance keeps changing, so the

change in the pressure build up is now analysed. This is illustrated in Figure 61 where the pressure distribution on the symmetry plane is shown for the wing at three different positions in time. The figure shows the wing is at 7°, for a wavelength of 4*c* and a wave height of 4*h*. The scale that was used for the flat ground plane pressure plots has been used here again.

The changing gap between the wing and waves tends to influence the extent of the pressure region under the wing, which ultimately changes the lift characteristics of the wing. The top of Figure 61 shows the wing flying over a wave trough. As the wave crest disappears below the wing, the cushion of air under the wing dissipates into the open air of the trough and results in a reduction of the lift force. The approaching wave face then compresses the air between the wing and wave, creating the rise in the lift values (bottom left). While the crest of the wave passes under the wing, the wing experiences a cushion of high pressure air, resulting in the peak lift values (bottom right).

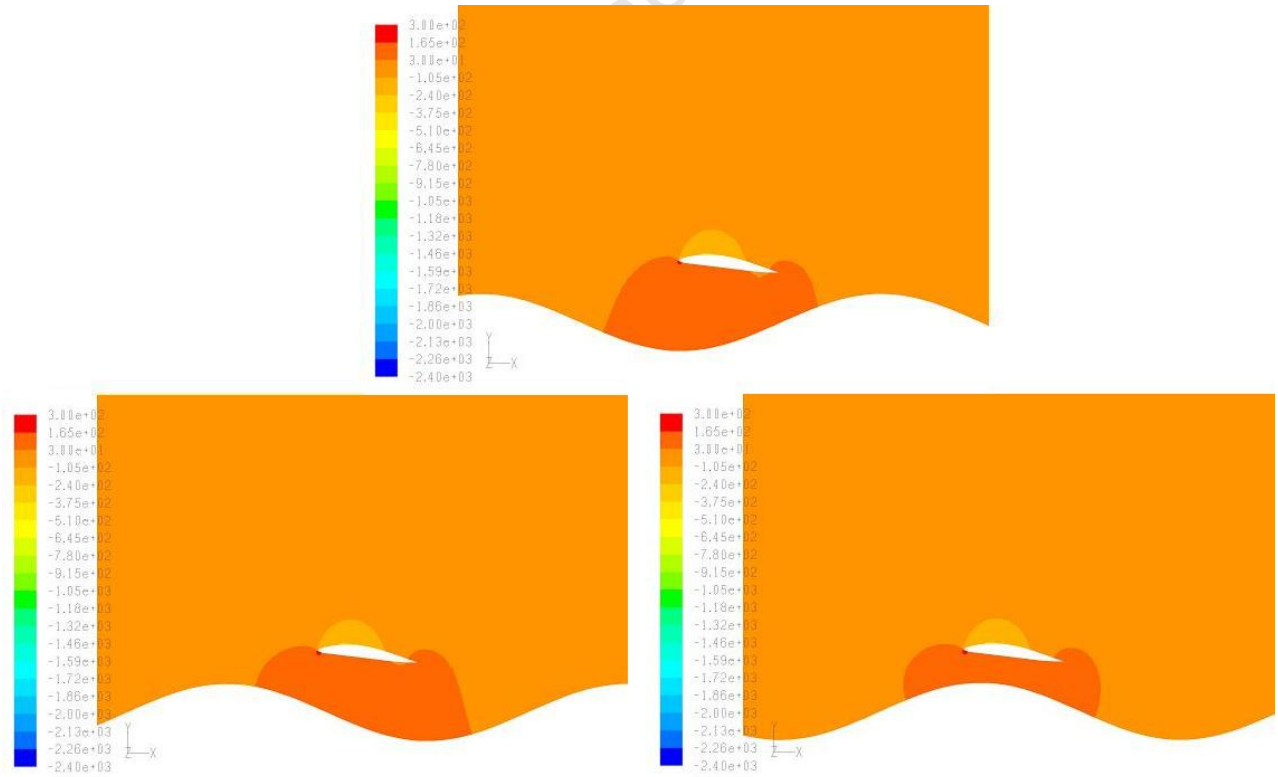

Figure 61: Pressure plots of underside of wing at 7° for a wavelength of 4*c* and a wave height of 4*h*

For the lower wave heights, the variations in pressure with the movement of the waves are less noticeable, at least visually. There is also little difference between wavelength changes for the lower wave heights. Therefore these pressure plots have not been shown.

### 7.6.2 Vortex Development over the Waves

Pathlines are again used to investigate the behaviour of the wingtip vortices. Figure 62 shows the pathlines for the wing flying over a wavy ground plane of wavelength 4$c$ and a wave height of 4$h$. The pathlines for the wavy ground plane show similar trends to those of the flat ground plane. The vortex leaves the wingtip and travels almost directly downstream of the wing, with little spanwise movement. At an $h_0$ of 0.50, only a little spanwise motion would be expected as the wing is still relatively far from the ground. However, due to the waves reducing the clearance between the wing and ground, the vortices would be pushed outwards slightly more than for the flat ground plane with the same $h_0$.

The pathlines did not show any significant movement or changes in the vortex size or shape caused by the oscillation of the clearance between the wing and the ground plane. This was mostly due to the air travelling at the same forward velocity as the waves, which meant that the air would not have seen the waves as obstructions in its path as it was moving with the waves. The pathlines in the figure are not as concentrated as before, as if the uneven surface of the waves has prevented some of flow from neatly merging with the vortex. Instead, most of the flow from under the wing follows the wave troughs and flows away from the wing, before rejoining the flow further downstream.

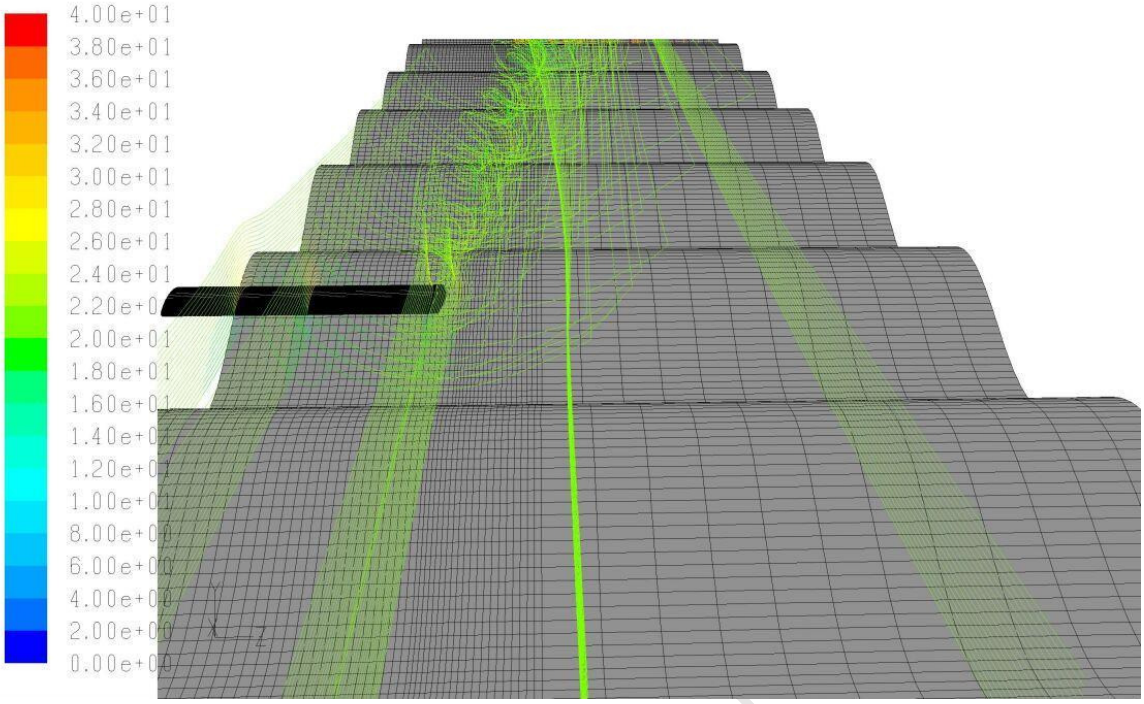


Figure 62: Flow pathlines over a wavy ground plane ($\alpha = 7°$)

# 8. CONCLUSIONS

After analysing the results of the simulations and comparing them to experimental results, conclusions can be drawn about the validity of the results, and even the reliability of the simulations done with waves in the ground plane.

## 8.1 REASONABLE PERFORMANCE OF THE FLAT GROUND PLANE MODEL

The CFD model did not perform well at low angles of attack. The large discrepancies in these values were due to the inability of the CFD software to correctly resolve the viscous forces acting on the wing. It is an inherent weakness of CFD codes in that they cannot always correctly determine the subtleties of the viscous nature of fluids. At low angles of attack, airfoils are particularly dependant on viscous force for lift because there is not yet enough wing area exposed to the flow to produce lift through having a higher pressure pushing up on the lower surface of the wing. At high angles of attack, it was evident that Fluent® could detect the general form of the wing and so could easily calculate this contribution from the pressure force. This is probably what led Fluent® to overestimate the lift produced by the wing at the higher angles of attack. At lower ground clearances, the effect of the increased pressure underneath the wing exacerbated the overestimation of lift.



Despite these discrepancies, it seemed that for the majority of geometries that were tested, Fluent® performed well, obtaining $C_L$ values that were within 10% of experimental values in some cases. The $C_D$ and $C_M$ values were less accurate however. Based on these results, this combination of mesh and flow model performed well for the purposes of this study. The SA turbulence model provided good results for the aerofoil in the presence of the ground plane, without being as computationally expensive as the two-equation models considered for this study. Therefore the model used in this study can provide a good qualitative assessment of wing operating in ground effect, though there is room for improvement.

## 8.2 SUCCESSFUL MODELLING OF WAVES WITH SLIDING MESH MODEL

In general, the coefficient values for the wavy ground plane performed equally well as for the flat ground plane. In other words, the $C_L$ values performed as expected, and their behaviour was realistic. Yet again, the $C_D$ values were not very accurate, matching the values for the flat ground plane. Correspondingly, the behaviour of $C_M$ values was again dominated by the greater magnitude of the $C_L$ values.

The results for the wavy ground plane at a relative ground clearance of 0.50, do not match the theory developed by Rozhdestvensky (Section 2.6). In his book, Rozhdestvensky did not indicate at which $h_0$ the wings were operating at. As his work was largely on wings in extreme ground effect (EGE), it was most likely that the graphs generated by Rozhdestvensky (Figures 17 and 18) were generated for EGE ($h_0 < 0.1c$). Consequently, the data presented in these graphs would not be applicable to an $h_0$ of 0.50 as the ground effect dynamics would be very different. Therefore the lack of agreement between the two sets of data is not considered to be relevant and as such does not reflect poorly on this CFD model.

The large phase angles produced by some of the wavelengths did not seem very realistic, with the $C_L$ values often decreasing while the wave was still growing in size. However, until there is some relevant experimental data to compare this model to, the performance of the phase angle cannot be confirmed. Any changes in the CFD model did not bring about any changes in the phase angles produced. Therefore the model was at least reliable in that it produced repeatable results.

Therefore it can be concluded that the use of a sliding mesh to model waves in the ground plane was successful. Once the poor performance of $C_D$ values can be corrected, this model should prove to be a simple and efficient method for modelling WIG airfoils in close proximity to moving waves.

## 8.3 TURBULENT VISCOSITY PROBLEMS AND MESH QUALITY

While problems with turbulent viscosity values did not affect the final values that were obtained in this report, they did present problems within the development of the model. Moreover, the fact that this problem did occur, indicated that the mesh may not have been particularly well constructed for this problem. Poor mesh quality was the primary cause of high turbulent viscosity ratios [21]. So, while this mesh used in this study did perform well and was of good quality, it could be improved upon, particularly in the region around the wing.

The simplest solution would be to increase the number of cells around the wingtip, but also along the upper surface of the wing. Another solution would be to develop a structured mesh around the wing that would be suitable for all angles of attack and ground clearances.

## 8.4 PERFORMANCE OF THE WING IN THE PRESENCE OF WAVES

For the particular relative ground clearance tested in this study ($h_0$ = 0.50), it would seem that the wing performed very well. In all wavelength and wave height variations, the peak $C_L$ values were higher than for the flat ground plane, if only by a few percent. In fact the value increased considerably more for the higher wave heights. However, to ensure proper performance of a WIG craft, the limiting case of the minimum lift coefficient must be taken into account. The minimum $C_L$ values were generally lower than the flat ground plane values. An important result is that the average $C_L$ values of the wavy ground plane model were generally higher than for the flat ground plane model, though not by much.

Following from the performance of the $C_L$, the $C_{M1/4MAC}$ grew in magnitude as the wavelength and wave heights increased. As a result the wing would experience an increased nose down pitching moment as the wave increased in height and wavelength.

# 9. RECOMMENDATIONS

Following from the findings of the report, some recommendations are made.

## 9.1 RESOLVE POOR $C_D$ PERFORMANCE

The cause of the poor $C_D$ values should be investigated. If it is possible to achieve better drag values by manipulating different aspects of the flow settings (e.g. turbulence model), then these steps should be implemented. Once the poor performance of the $C_D$ can be corrected, then this model should not need any extra work to make it reliable.

## 9.2 INVESTIGATE THE PERFORMANCE OF A FINER MESH

Placing more cells over the surface of the wing would result in a more accurate solution. The limited cell refinement tests carried out in this study did not result in better force and moment coefficient values. However, a radical increase in the amount of cells may produce better results. Therefore if the hardware resources allow, a mesh of 3 million cells or more should be tested.

## 9.3 INVESTIGATE WING PERFORMANCE AT SMALLER $h_0$ WITH A WAVY GROUND PLANE

The values determined for the wavy model at $h_0$ 0.50 show that while the wing was affected by the waves, the effects were not very large due to the wing being far out of ground effect. Also the benefits of travelling closer to the ground plane would mean that WIG craft are likely to travel a lot closer to the ground plane. Therefore ground clearances smaller than 0.50 should be tested.

# 10. REFERENCES


1. Rozhdestvensky, K.V., "Wing-in-Ground Effect Vehicles", Progress in Aerospace Sciences, 42, 2006, pp. 211-283.

2. Aerospaceweb.org, "Ground Effect and WIG Vehicles", Article by Scott, J., 2003.
   Site: http://www.aerospaceweb.org/question/aerodynamics/q0130.shtml
   Site last visited: 27 January 2009.

3. van Opstal, E., The WIG Page, "Commercial Viability of WIG Boats", 2008.
   Site: http://www.se-technology.com/wig/index.php
   Site last visited: 27 January 2009.

4. Rhodes, S.C., "An Experimental Study of the Aerodynamic Characteristics of a Wing in Close proximity to a Moving Ground Plane", MSc Thesis, University of Cape Town, Cape Town, 2006.

5. Moore, N., Wilson, P.A., Peters, A.J., "An Investigation into Wing in Ground Effect Airfoil Geometry", School of Engineering Sciences, University of Southampton, United Kingdom.

6. Barlow, J.B., Rae, W.H., and Pope, A., "Low-Speed Wind Tunnel Testing" 3rd ed., John Wiley & Sons, New York, 1999.

7. Douglas, J.F., Gasiorek, J.M., and Swaffield, J.A., "Fluid Mechanics" 4th ed., Pearson Education Ltd., England, 2001.

8. Clancy, L.J., "Aerodynamics", Pitman Publishing Limited, London, 1975.

9. Houghton, E.L., Carpenter, P.W., "Aerodynamics for Engineering Students", 4th Ed., Edward Arnold, London, 1993.

10. Halloran, M., O'Meara, S., "Wing in Ground Effect Craft Review", Aeronautical and Maritime Research Laboratory, Melbourne, 1999.

11. Kinsman, B., "Wind Waves – their generation and propagation on the ocean surface", Prentice-Hall Inc., New Jersey, 1965.

12. Office of Naval Research - Science and Technology Focus Site, "Ocean in Motion: Waves – Characteristics".
Site: http://www.onr.navy.mil/Focus/ocean/motion/waves1.htm
Site last visited: 31 January 2009.

13. Philips, O.M., "The Dynamics of the Upper Ocean", Cambridge University Press, London, 1966.

14. Rozhdestvensky, K.V., "Aerodynamics of a Lifting System in Extreme Ground Effect", Springer, Germany, 2000.

15. Versteeg, H.K., Malalasekera, W., "An Introduction to Computational Fluid Mechanics", Pearson Education Limited, England, 1995.

16. User Documentation, Gambit® version 2.4.

17. Vu, P., "CFD study of Wingtip Vortices for Inverted Airfoils in Ground Effect", MSc Thesis, School of Engineering, Cranfield University, England, 2006.

18. Shin, M.-S., Yang, C.-J., Yang, S.I., Wang, G.-Q., "Numerical Simulation of Viscous Flow Around a Three-Dimensional Wing in Ground Effect with Endplates", School of Naval Architecture and Ocean Engineering, Shanghai Jiao Tong University, China.

19. Gasparovic, P., "CFD Simulation of Dynamic Lift on Airfoil", 2007.
Available at: buteo.szm.sk/published/gasparovic_2007_mosatt_en.pdf

20. Moon, Y.J., Oh, H.-J., Seo, J.-H., "Aerodynamic Investigation of Three-Dimensional Wings in Ground Effect for aero-Levitation Electric Vehicle", Aerospace Science and Technology 9, 2005, pp. 485-494.

21. User Documentation, Fluent® version 6.3.

22. Wilcox, D.C., "Turbulence Modeling for CFD", 2nd ed., DCW Industries, La Canada, California, 1994.

23. Menter, F.R., "Two-Equation Eddy-Viscosity Turbulence Models for Engineering Applications", AIAA Journal 32, 1994, pp 1598-1605.

# APPENDIX A: RESULTS FOR FLAT GROUND PLANE

List of Figures A-ii
List of Tables A-ii

A.1. Tables of Fluent® Results A-1
A.2. Tables of Experimental Results A-2
A.3. Comparison of Results A-3

# LIST OF FIGURES

Figure A.1: $C_L$ vs. $\alpha$ for experimental and Fluent® models A-3
Figure A.2: $C_L$ vs. $h_0$ for experimental and Fluent® models A-3
Figure A.3: $C_D$ vs. $\alpha$ for experimental and Fluent® models A-4
Figure A.4: $C_D$ vs. $h_0$ for experimental and Fluent® models A-4
Figure A.5: $C_{M1/4MAC}$ vs. $\alpha$ for experimental and Fluent® models A-5
Figure A.6: $C_{M1/4MAC}$ vs. $h_0$ for experimental and Fluent® models A-5
Figure A.7: $C_L$ vs. $C_D$ (grouped according to $h_0$) A-6
Figure A.8: $C_L$ vs. $C_{M1/4MAC}$ (grouped according to $h_0$) A-6
Figure A.9: $L/D$ vs. $C_L$ (grouped according to $h_0$) A-7
Figure A.10: $L/D$ vs. $h_0$ (grouped according to $\alpha$) A-7

# LIST OF TABLES

**CFD Results**

Table A.1: Lift coefficients of Fluent® simulations A-1
Table A.2: Drag coefficients of Fluent® simulations A-1
Table A.3: Original moment coefficients of Fluent® simulations * A-1
Table A.4: Corrected moment coefficients of Fluent® simulations ** A-1

**Experimental Values**

Table A.5: Experimental lift coefficients A-2
Table A.6: Experimental drag coefficients A-2
Table A.7: Experimental moment coefficients ($C_{M1/4MAC}$) A-2

# A.1 TABLES OF FLUENT® RESULTS

Table A.1: Lift coefficients of Fluent® simulations

| $h_0$ (h/c) | Angle of Attack (°) | | | | | | |
|---|---|---|---|---|---|---|---|
| | **1** | **3** | **5** | **7** | **9** | **11** | **13** |
| **0.06** | 0.214 | 0.567 | 0.794 | 0.958 | 1.075 | 1.113 | 1.120 |
| **0.12** | 0.262 | 0.502 | 0.698 | 0.857 | 0.990 | 1.095 | 1.110 |
| **0.50** | 0.253 | 0.395 | 0.536 | 0.671 | 0.801 | 0.930 | 1.035 |
| **1.30** | 0.233 | 0.357 | 0.483 | 0.674 | 0.736 | 0.861 | 0.979 |

Table A.2: Drag coefficients of Fluent® simulations

| $h_0$ (h/c) | Angle of Attack (°) | | | | | | |
|---|---|---|---|---|---|---|---|
| | **1** | **3** | **5** | **7** | **9** | **11** | **13** |
| **0.06** | 0.008 | 0.013 | 0.023 | 0.035 | 0.049 | 0.084 | 0.166 |
| **0.12** | 0.008 | 0.015 | 0.024 | 0.037 | 0.051 | 0.067 | 0.117 |
| **0.50** | 0.016 | 0.017 | 0.034 | 0.039 | 0.053 | 0.073 | 0.093 |
| **1.30** | 0.011 | 0.018 | 0.028 | 0.039 | 0.058 | 0.077 | 0.099 |

Table A.3: Original moment coefficients of Fluent® simulations *

| $h_0$ (h/c) | Angle of Attack (°) | | | | | | |
|---|---|---|---|---|---|---|---|
| | **1** | **3** | **5** | **7** | **9** | **11** | **13** |
| **0.06** | -0.111 | -0.262 | -0.356 | -0.425 | -0.477 | -0.52 | -0.528 |
| **0.12** | -0.110 | -0.223 | -0.312 | -0.385 | -0.446 | -0.496 | -0.504 |
| **0.50** | -0.099 | -0.172 | -0.243 | -0.313 | -0.382 | -0.447 | -0.507 |
| **1.30** | -0.094 | -0.163 | -0.234 | -0.309 | -0.385 | -0.462 | -0.539 |

Table A.4: Corrected moment coefficients of Fluent® simulations **

| $h_0$ (h/c) | Angle of Attack (°) | | | | | | |
|---|---|---|---|---|---|---|---|
| | **1** | **3** | **5** | **7** | **9** | **11** | **13** |
| **0.06** | 0.0054 | -0.0330 | -0.0621 | -0.0809 | -0.0895 | -0.0565 | -0.0644 |
| **0.12** | -0.0325 | -0.0439 | -0.0580 | -0.0683 | -0.0765 | -0.0798 | -0.0890 |
| **0.50** | -0.0494 | -0.0470 | -0.0552 | -0.0531 | -0.0531 | -0.0570 | -0.0581 |
| **1.30** | -0.0482 | -0.0470 | -0.0481 | -0.0925 | -0.0499 | -0.0520 | -0.0522 |

* Moment values taken about trailing edge of wing

** Moment values corrected to be relative to the ¼ MAC

# A.2 TABLES OF EXPERIMENTAL RESULTS

Table A.5: Experimental lift coefficients

| $h_0$ ($h/c$) | Angle of Attack (°) | | | | | | |
|---|---|---|---|---|---|---|---|
| | **1** | **3** | **5** | **7** | **9** | **11** | **13** |
| **0.06** | 0.344 | 0.617 | 0.742 | 0.829 | 0.913 | 0.977 | 1.036 |
| **0.12** | 0.348 | 0.530 | 0.675 | 0.771 | 0.860 | 0.929 | 0.983 |
| **0.50** | 0.372 | 0.528 | 0.641 | 0.732 | 0.834 | 0.913 | 0.954 |
| **1.30** | 0.287 | 0.454 | 0.570 | 0.664 | 0.761 | 0.850 | 0.925 |

Table A.6: Experimental drag coefficients

| $h_0$ ($h/c$) | Angle of Attack (°) | | | | | | |
|---|---|---|---|---|---|---|---|
| | **1** | **3** | **5** | **7** | **9** | **11** | **13** |
| **0.06** | 0.043 | 0.048 | 0.057 | 0.070 | 0.083 | 0.097 | 0.124 |
| **0.12** | 0.045 | 0.050 | 0.059 | 0.074 | 0.084 | 0.103 | 0.125 |
| **0.50** | 0.046 | 0.061 | 0.074 | 0.084 | 0.096 | 0.112 | 0.135 |
| **1.30** | 0.033 | 0.050 | 0.066 | 0.077 | 0.093 | 0.112 | 0.131 |

Table A.7: Experimental moment coefficients ($C_{M1/4MAC}$)

| $h_0$ ($h/c$) | Angle of Attack (°) | | | | | | |
|---|---|---|---|---|---|---|---|
| | **1** | **3** | **5** | **7** | **9** | **11** | **13** |
| **0.06** | -0.027 | -0.051 | -0.058 | -0.053 | -0.052 | -0.053 | -0.059 |
| **0.12** | -0.050 | -0.054 | -0.056 | -0.052 | -0.048 | -0.045 | -0.045 |
| **0.50** | -0.080 | -0.083 | -0.078 | -0.071 | -0.062 | -0.056 | -0.044 |
| **1.30** | -0.072 | -0.083 | -0.080 | -0.073 | -0.064 | -0.058 | -0.050 |

# A.3 COMPARISON OF RESULTS

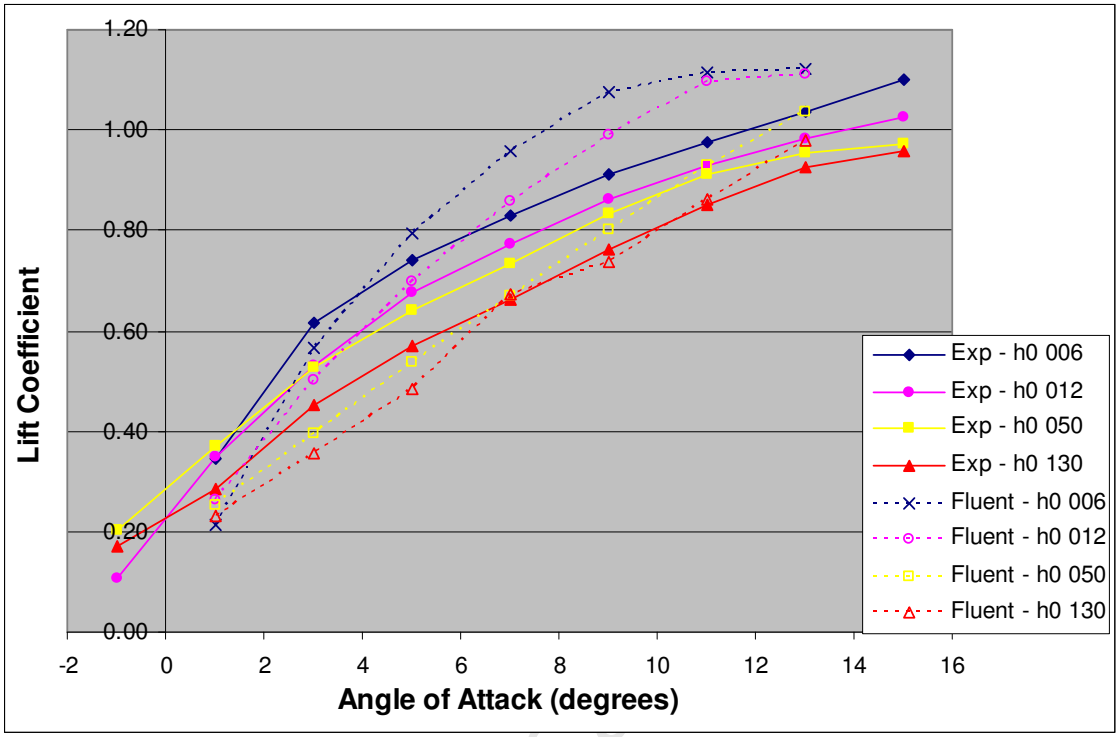


Figure A.1: $C_L$ vs. $\alpha$ for experimental and Fluent® models

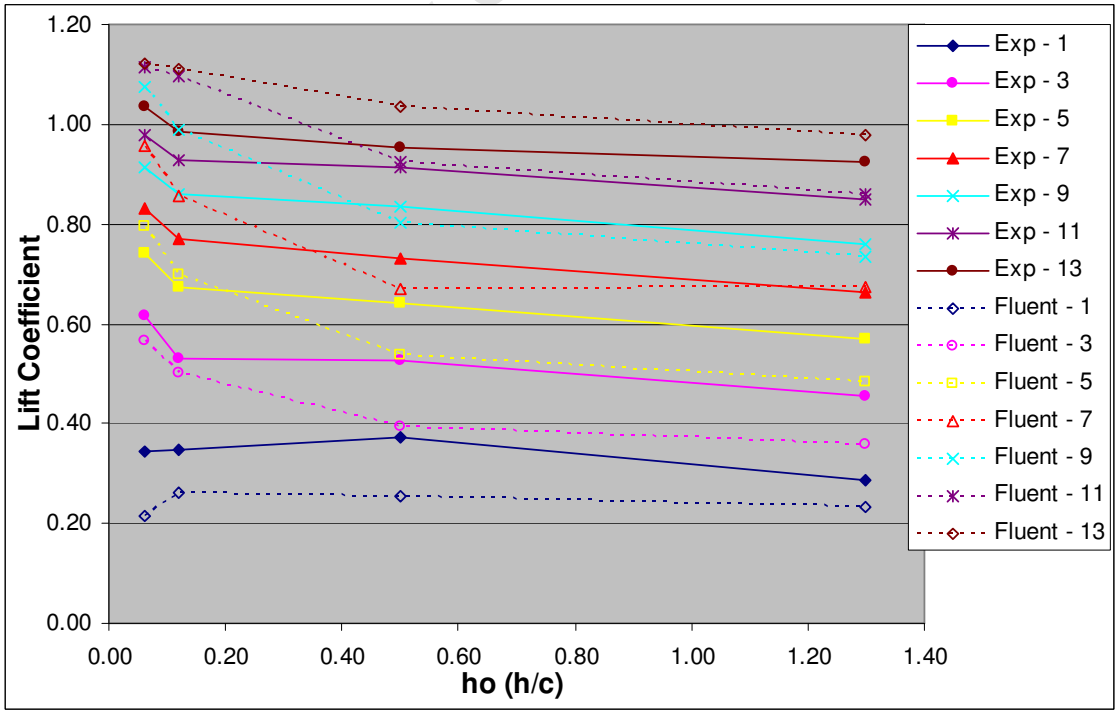


Figure A.2: $C_L$ vs. $h_0$ for experimental and Fluent® models

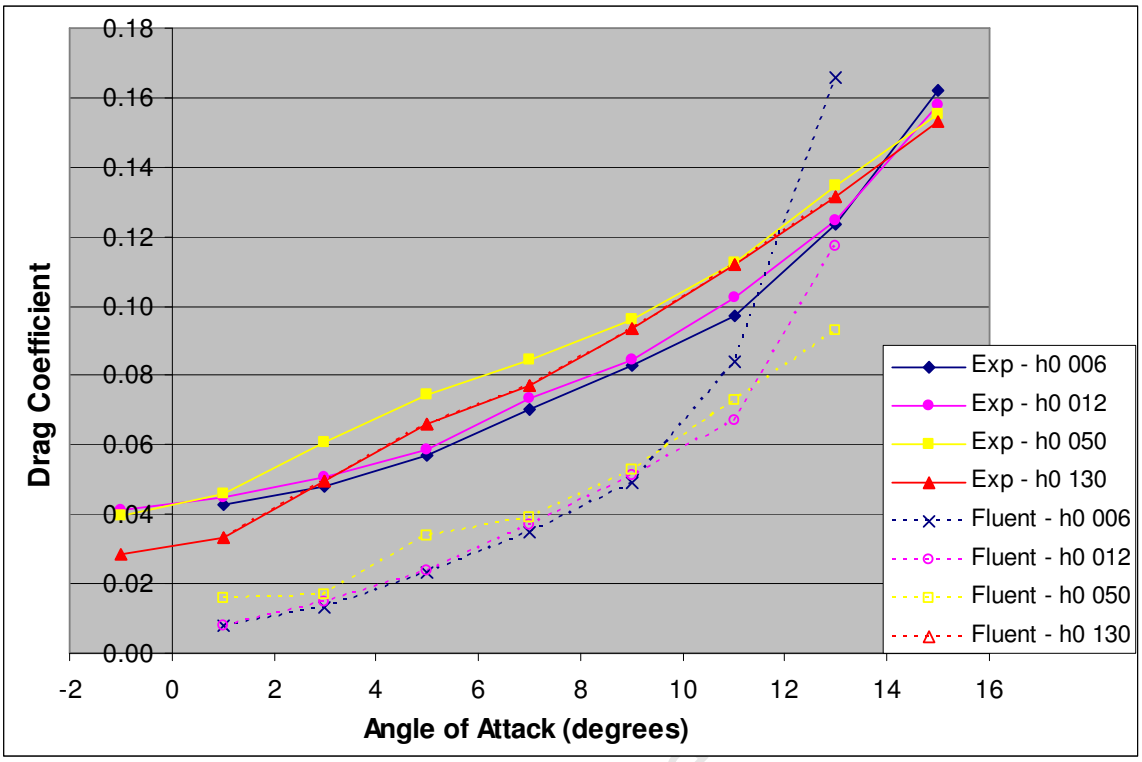


Figure A.3: $C_D$ vs. $\alpha$ for experimental and Fluent® models

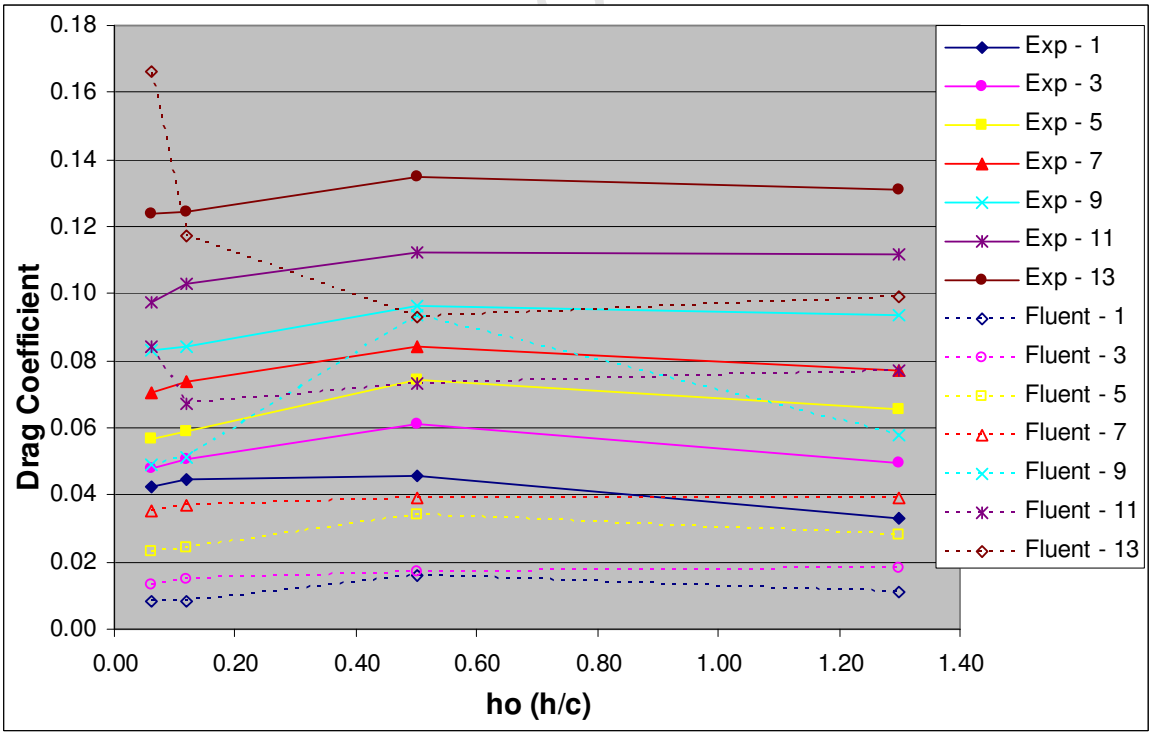


Figure A.4: $C_D$ vs. $h_0$ for experimental and Fluent® models

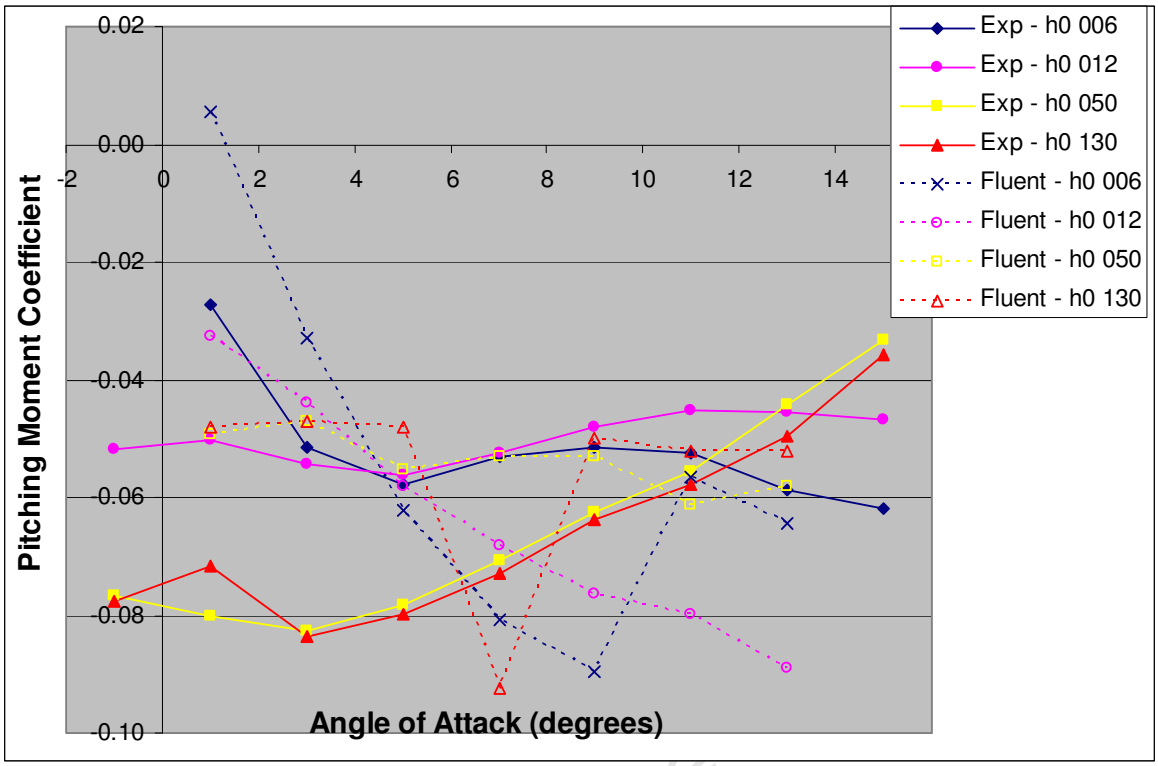


Figure A.5: $C_{M1/4MAC}$ vs. $\alpha$ for experimental and Fluent® models

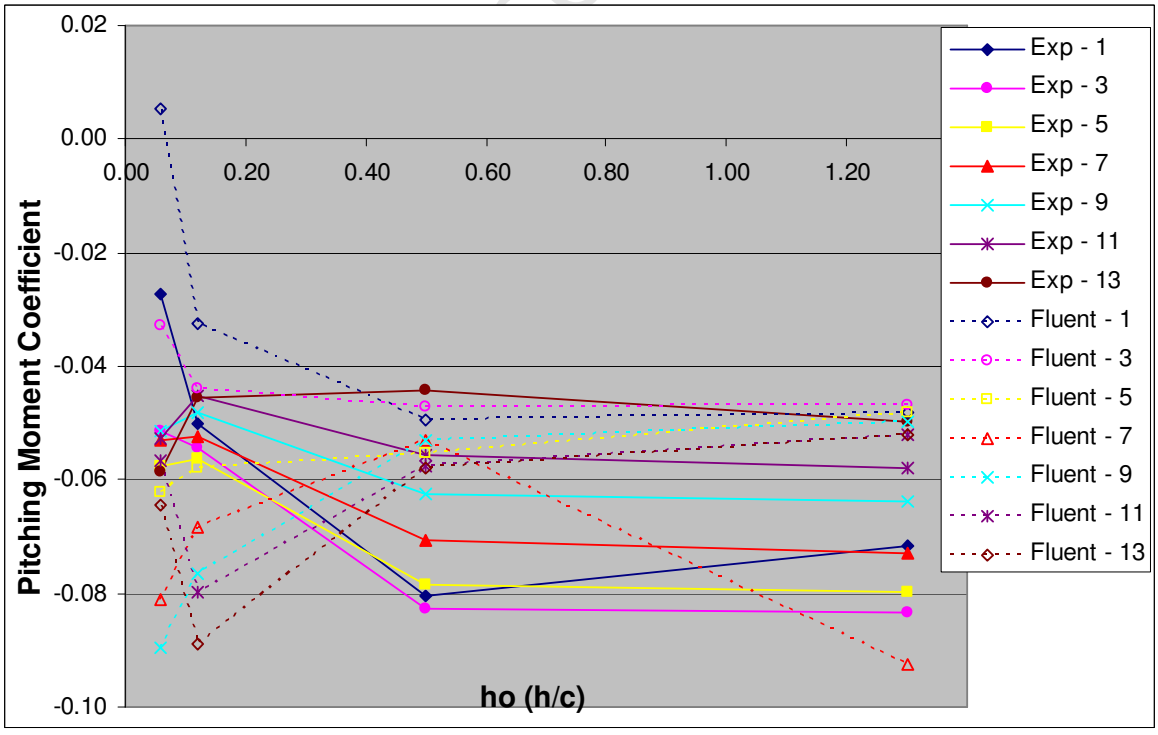


Figure A.6: $C_{M1/4MAC}$ vs. $h_0$ for experimental and Fluent® models

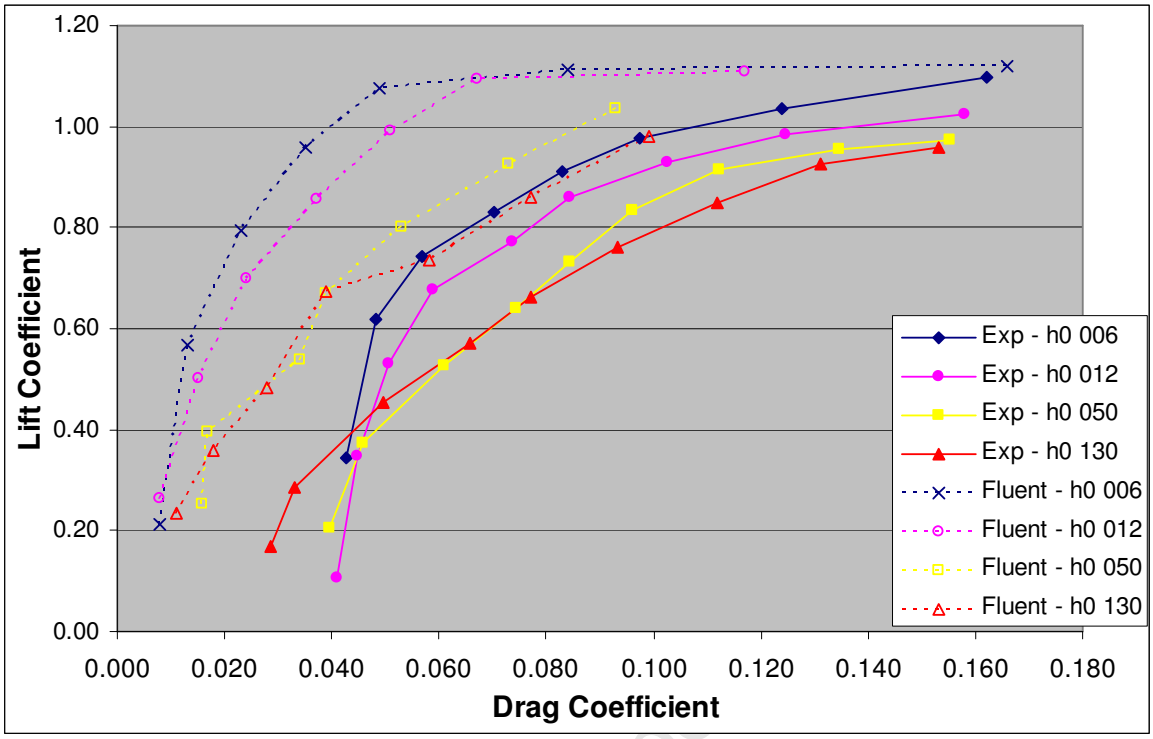


Figure A.7: $C_L$ vs. $C_D$ (grouped according to $h_0$)

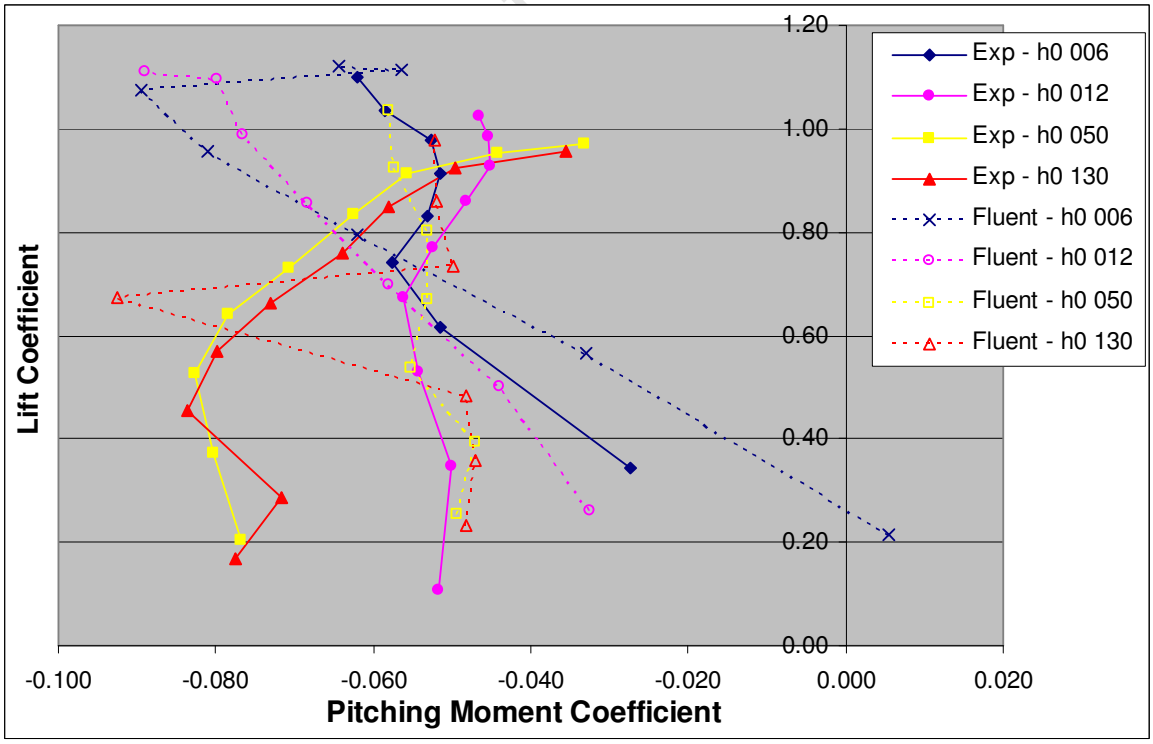


Figure A.8: $C_L$ vs. $C_{M1/4MAC}$ (grouped according to $h_0$)

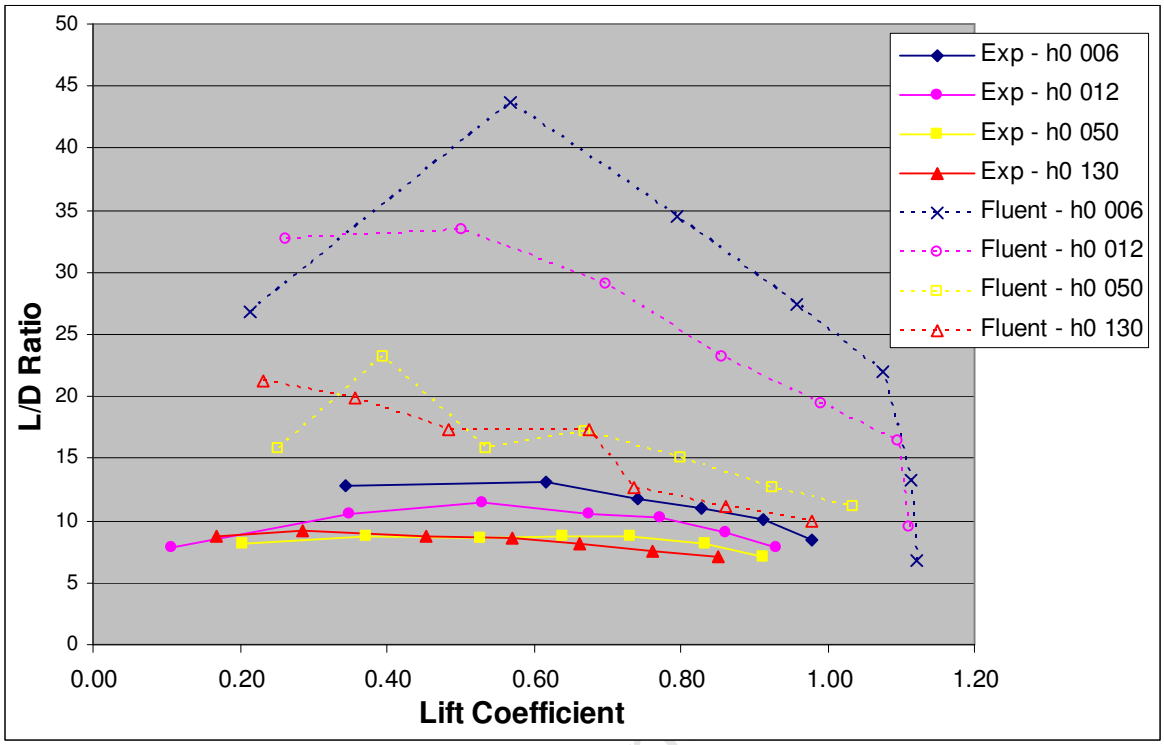


Figure A.9: *L/D* vs. $C_L$ (grouped according to $h_0$)

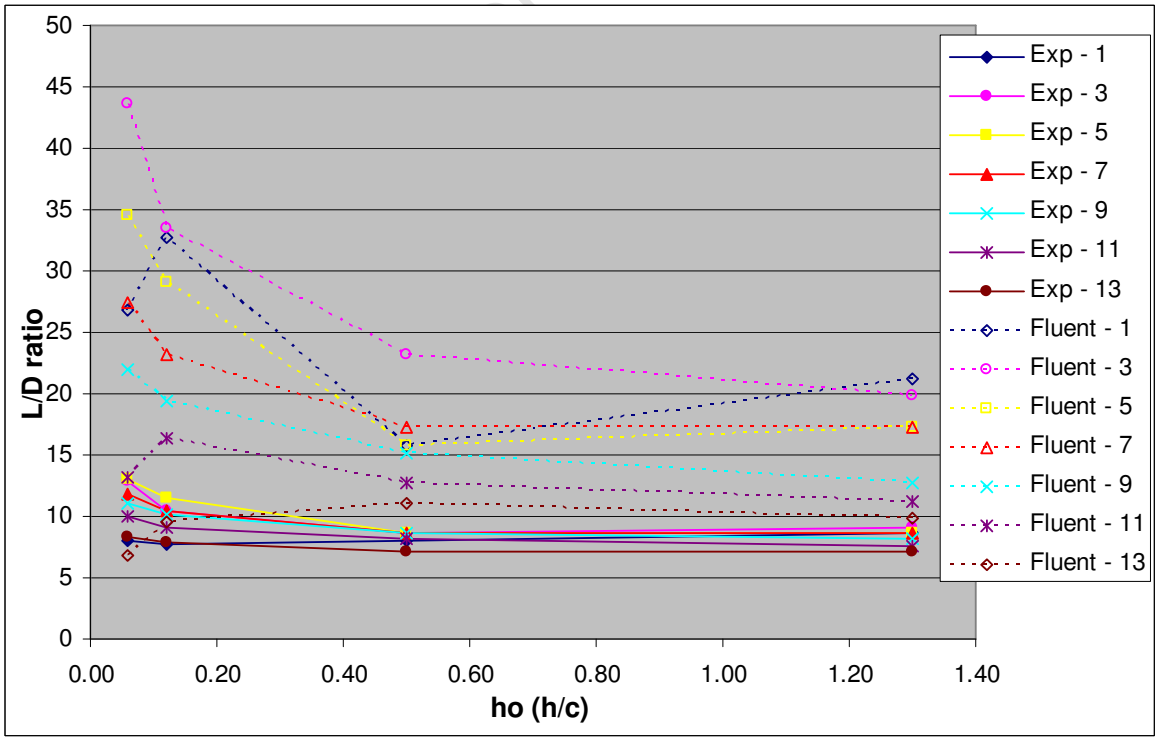


Figure A.10: *L/D* vs. $h_0$ (grouped according to $\alpha$)

# APPENDIX B: RESULTS FOR WAVY GROUND PLANE

List of Figures B-i
List of Tables B-ii

B.1. Tables of Results - 7° B-1
B.2. Tables of Results - 11° B-2
B.3. Strouhal Number B-3
B.4. Graphs of Results - 7° B-3
B.5. Graphs of Results - 11° B-3



## LIST OF FIGURES

**α = 7°**

Figure B.1: $C_L$ for $\alpha = 7°$ B-3
Figure B.2: $C_L$ vs. wavelength for $\alpha = 7°$ (lines of constant wave height) B-4
Figure B.3: $C_L$ vs. wave height for $\alpha = 7°$ (lines of constant wavelength) B-4
Figure B.4: $C_L$ phase angle vs. wavelength (lines of constant wave height) B-5
Figure B.5: $C_L$ phase angle vs. wave height (lines of constant wavelength) B-5
Figure B.6: $C_L$ vs. Strouhal Number for $\alpha = 7°$ (lines of constant wavelength) B-6
Figure B.7: $C_L$ phase angle vs. Strouhal Number ($\alpha = 7°$) (lines of constant wave height) B-6
Figure B.8: $C_D$ for $\alpha = 7°$ B-7
Figure B.9: $C_D$ vs. wavelength for $\alpha = 7°$ (lines of constant wave height) B-7
Figure B.10: $C_D$ vs. wave height for $\alpha = 7°$ (lines of constant wavelength) B-8
Figure B.11: $C_{M1/4MAC}$ for $\alpha = 7°$ B-8

Figure B.12: $C_{M1/4MAC}$ vs. wavelength for $\alpha$ = 7° (lines of constant wave height) B-9
Figure B.13: $C_{M1/4MAC}$ vs. wave height for $\alpha$ = 7° (lines of constant wavelength) B-9

**α = 11°**

Figure B.14: $C_L$ for $\alpha$ = 11° B-10
Figure B.15: $C_L$ vs. wavelength for $\alpha$ = 11° (lines of constant wave height) B-10
Figure B.16: $C_L$ vs. wave height for $\alpha$ = 11° (lines of constant wavelength) B-11
Figure B.17: $C_L$ vs. Strouhal Number for $\alpha$ = 11° (lines of constant wavelength) B-11
Figure B.18: $C_L$ phase angle vs Strouhal Number for 11° (lines of constant wave height) B-12
Figure B.19: $C_D$ for $\alpha$ = 11° B-12
Figure B.20: $C_D$ vs. wavelength for $\alpha$ = 11° (lines of constant wave height) B-13
Figure B.21: $C_D$ vs. wave height for $\alpha$ = 11° (lines of constant wavelength) B-13
Figure B.22: $C_{M1/4MAC}$ for $\alpha$ = 11° B-14
Figure B.23: $C_{M1/4MAC}$ vs. wavelength for $\alpha$ = 11° (lines of constant wave height) B-14
Figure B.24: $C_{M1/4MAC}$ vs. wave height for $\alpha$ = 11° (lines of constant wavelength) B-15

## LIST OF TABLES

**α = 7°**

Table B.1: Lift coefficient for $\alpha$ of 7° B-1
Table B.2: Drag coefficient for $\alpha$ of 7° B-1
Table B.3: Moment coefficient for $\alpha$ of 7° B-1
Table B.4: $C_{M1/4MAC}$ for $\alpha$ of 7° B-1

**α = 11°**

Table B.5: Lift coefficient for $\alpha$ of 11° B-2
Table B.6: Drag coefficient for $\alpha$ of 11° B-2
Table B.7: Moment coefficient for $\alpha$ of 11° B-2
Table B.8: $C_{M1/4MAC}$ for $\alpha$ of 11° B-2

Table B.9: Strouhal Number B-3

# B.1 TABLES OF RESULTS - 7°

Table B.1: Lift coefficient for $\alpha$ of 7°

| | 1wave 1h | 2wave 1h | 2wave 2h | 3wave 1h | 3wave 2h | 3wave 3h | 4wave 1h | 4wave 2h | 4wave 3h | 4wave 4h |
|---|---|---|---|---|---|---|---|---|---|---|
| **Maximum** | 0.677 | 0.680 | 0.687 | 0.680 | 0.688 | 0.698 | 0.681 | 0.690 | 0.704 | 0.721 |
| **$\varphi$ (rad)** | -1.011 | 2.276 | 2.276 | -2.753 | -2.585 | -2.585 | -1.770 | -1.770 | -1.791 | -1.644 |
| **Minimum** | 0.671 | 0.668 | 0.663 | 0.668 | 0.664 | 0.660 | 0.668 | 0.664 | 0.661 | 0.659 |
| **$\varphi$ (rad)** | -0.843 | 2.191 | 1.939 | -2.753 | -2.753 | -3.091 | -1.939 | -1.939 | -1.960 | -1.939 |
| **Mean $C_L$** | 0.674 | 0.674 | 0.675 | 0.674 | 0.675 | 0.677 | 0.674 | 0.676 | 0.679 | 0.683 |
| **Mean (time weighted)** | 0.674 | 0.674 | 0.675 | 0.674 | 0.675 | 0.677 | 0.674 | 0.676 | 0.680 | 0.684 |

Table B.2: Drag coefficient for $\alpha$ of 7°

| | 1wave 1h | 2wave 1h | 2wave 2h | 3wave 1h | 3wave 2h | 3wave 3h | 4wave 1h | 4wave 2h | 4wave 3h | 4wave 4h |
|---|---|---|---|---|---|---|---|---|---|---|
| **Maximum** | 0.040 | 0.040 | 0.040 | 0.040 | 0.040 | 0.041 | 0.040 | 0.040 | 0.040 | 0.040 |
| **$\varphi$ (rad)** | -3.034 | 0.000 | 0.253 | 0.506 | 0.674 | 0.843 | 0.885 | 0.885 | 1.117 | 1.011 |
| **Minimum** | 0.039 | 0.039 | 0.039 | 0.039 | 0.039 | 0.039 | 0.039 | 0.039 | 0.039 | 0.039 |
| **$\varphi$ (rad)** | -3.372 | -0.084 | -0.084 | 0.337 | 0.337 | 0.337 | 0.506 | 0.464 | 0.358 | 0.337 |
| **Mean $C_D$** | 0.039 | 0.039 | 0.040 | 0.039 | 0.039 | 0.040 | 0.039 | 0.039 | 0.039 | 0.040 |
| **Mean (time weighted)** | 0.039 | 0.039 | 0.040 | 0.039 | 0.039 | 0.040 | 0.039 | 0.039 | 0.039 | 0.040 |

Table B.3: Moment coefficient for $\alpha$ of 7°

| | 1wave 1h | 2wave 1h | 2wave 2h | 3wave 1h | 3wave 2h | 3wave 3h | 4wave 1h | 4wave 2h | 4wave 3h | 4wave 4h |
|---|---|---|---|---|---|---|---|---|---|---|
| **Maximum** | -0.300 | -0.299 | -0.296 | -0.299 | -0.296 | -0.294 | -0.298 | -0.296 | -0.295 | -0.294 |
| **φ (rad)** | 1.854 | -0.927 | -0.927 | 0.056 | 0.056 | 0.056 | 1.180 | 1.054 | 0.969 | 0.927 |
| **Minimum** | -0.303 | -0.304 | -0.307 | -0.304 | -0.308 | -0.313 | -0.305 | -0.309 | -0.315 | -0.323 |
| **φ (rad)** | 2.023 | -0.927 | -0.927 | 0.393 | 0.562 | 0.562 | 1.306 | 1.306 | 1.285 | 1.433 |
| **Mean $C_M$** | -0.301 | -0.301 | -0.302 | -0.301 | -0.302 | -0.302 | -0.301 | -0.302 | -0.304 | -0.305 |
| **Mean (time weighted)** | -0.301 | -0.301 | -0.302 | -0.301 | -0.302 | -0.303 | -0.301 | -0.302 | -0.304 | -0.306 |

Table B.4: $C_{M1/4MAC}$ for $\alpha$ of 7°

| | 1wave 1h | 2wave 1h | 2wave 2h | 3wave 1h | 3wave 2h | 3wave 3h | 4wave 1h | 4wave 2h | 4wave 3h | 4wave 4h |
|---|---|---|---|---|---|---|---|---|---|---|
| **Maximum** | -0.077 | -0.082 | -0.091 | -0.082 | -0.091 | -0.102 | -0.083 | -0.093 | -0.105 | -0.120 |
| **Minimum** | -0.069 | -0.064 | -0.055 | -0.064 | -0.056 | -0.045 | -0.063 | -0.054 | -0.043 | -0.029 |
| **Mean $C_L$** | -0.073 | -0.073 | -0.073 | -0.073 | -0.073 | -0.073 | -0.073 | -0.073 | -0.073 | -0.074 |

# B.2 TABLES OF RESULTS - 11°

Table B.5: Lift coefficient for $\alpha$ of 11°

| | 1wave 1h | 2wave 1h | 2wave 2h | 3wave 1h | 3wave 2h | 3wave 3h | 4wave 1h | 4wave 2h | 4wave 3h | 4wave 4h |
|---|---|---|---|---|---|---|---|---|---|---|
| **Maximum** | 0.677 | 0.680 | 0.687 | 0.680 | 0.688 | 0.698 | 0.681 | 0.690 | 0.704 | 0.721 |
| **$\varphi$ (rad)** | -0.844 | 2.279 | 2.195 | -2.758 | -2.645 | -2.589 | -1.857 | -1.942 | -1.773 | -1.731 |
| **Minimum** | 0.671 | 0.668 | 0.663 | 0.668 | 0.664 | 0.660 | 0.668 | 0.664 | 0.661 | 0.659 |
| **$\varphi$ (rad)** | -0.507 | 1.942 | 1.942 | -2.927 | -2.927 | -2.927 | -2.068 | -2.026 | -2.195 | -2.279 |
| **Mean $C_L$** | 0.674 | 0.674 | 0.675 | 0.674 | 0.675 | 0.677 | 0.674 | 0.676 | 0.679 | 0.683 |
| **Mean (time weighted)** | 0.674 | 0.674 | 0.675 | 0.674 | 0.675 | 0.677 | 0.674 | 0.676 | 0.680 | 0.684 |

Table B.6: Drag coefficient for $\alpha$ of 11°

| | 1wave 1h | 2wave 1h | 2wave 2h | 3wave 1h | 3wave 2h | 3wave 3h | 4wave 1h | 4wave 2h | 4wave 3h | 4wave 4h |
|---|---|---|---|---|---|---|---|---|---|---|
| **Maximum** | 0.040 | 0.040 | 0.040 | 0.040 | 0.040 | 0.041 | 0.040 | 0.040 | 0.040 | 0.040 |
| **$\varphi$ (rad)** | 1.520 | 0.760 | 0.844 | 0.675 | 0.844 | 0.901 | 0.760 | 0.844 | 0.844 | 0.844 |
| **Minimum** | 0.039 | 0.039 | 0.039 | 0.039 | 0.039 | 0.039 | 0.039 | 0.039 | 0.039 | 0.039 |
| **$\varphi$ (rad)** | 1.013 | 0.507 | 0.422 | 0.450 | 0.281 | 0.281 | 0.422 | 0.338 | 0.338 | 0.211 |
| **Mean $C_D$** | 0.039 | 0.039 | 0.040 | 0.039 | 0.039 | 0.040 | 0.039 | 0.039 | 0.039 | 0.040 |
| **Mean (time weighted)** | 0.039 | 0.039 | 0.040 | 0.039 | 0.039 | 0.040 | 0.039 | 0.039 | 0.039 | 0.040 |

Table B.7: Moment coefficient for $\alpha$ of 11°

| | 1wave 1h | 2wave 1h | 2wave 2h | 3wave 1h | 3wave 2h | 3wave 3h | 4wave 1h | 4wave 2h | 4wave 3h | 4wave 4h |
|---|---|---|---|---|---|---|---|---|---|---|
| **Maximum** | -0.300 | -0.299 | -0.296 | -0.299 | -0.296 | -0.294 | -0.298 | -0.296 | -0.295 | -0.294 |
| **$\varphi$ (rad)** | 2.026 | -1.182 | -1.182 | 0.056 | 0.056 | 0.056 | 0.295 | 1.013 | 0.802 | 0.675 |
| **Minimum** | -0.303 | -0.304 | -0.307 | -0.304 | -0.308 | -0.313 | -0.305 | -0.309 | -0.315 | -0.323 |
| **$\varphi$ (rad)** | 2.195 | -0.894 | -1.013 | 0.225 | 0.338 | 0.338 | 1.140 | 1.182 | 1.309 | 1.309 |
| **Mean $C_M$** | -0.301 | -0.301 | -0.302 | -0.301 | -0.302 | -0.302 | -0.301 | -0.302 | -0.304 | -0.305 |
| **Mean (time weighted)** | -0.301 | -0.301 | -0.302 | -0.301 | -0.302 | -0.303 | -0.301 | -0.302 | -0.304 | -0.306 |

Table B.8: $C_{M1/4MAC}$ for $\alpha$ of 11°

| | 1wave 1h | 2wave 1h | 2wave 2h | 3wave 1h | 3wave 2h | 3wave 3h | 4wave 1h | 4wave 2h | 4wave 3h | 4wave 4h |
|---|---|---|---|---|---|---|---|---|---|---|
| **Maximum** | -0.097 | -0.101 | -0.115 | -0.102 | -0.114 | -0.125 | -0.099 | -0.103 | -0.130 | -0.148 |
| **Minimum** | -0.087 | -0.084 | -0.071 | -0.082 | -0.071 | -0.065 | -0.084 | -0.081 | -0.058 | -0.043 |
| **Mean $C_M$** | -0.092 | -0.092 | -0.093 | -0.092 | -0.093 | -0.095 | -0.089 | -0.092 | -0.093 | -0.094 |

# B.3 STROUHAL NUMBER

The Strouhal number, as defined by Rozhdestvensky [14], is essentially the wavenumber that has been non-dimensionalised by multiplying it by the chord of the wing. The Strouhal numbers that were used during this study are given in Table B.7.

Table B.9: Strouhal Number

| $L_W$ | 1 | 2 | 3 | 4 |
|---|---|---|---|---|
| **Strouhal Number** | 6.283 | 3.142 | 3.142 | 2.094 |

# B.4 GRAPHS OF RESULTS - 7°

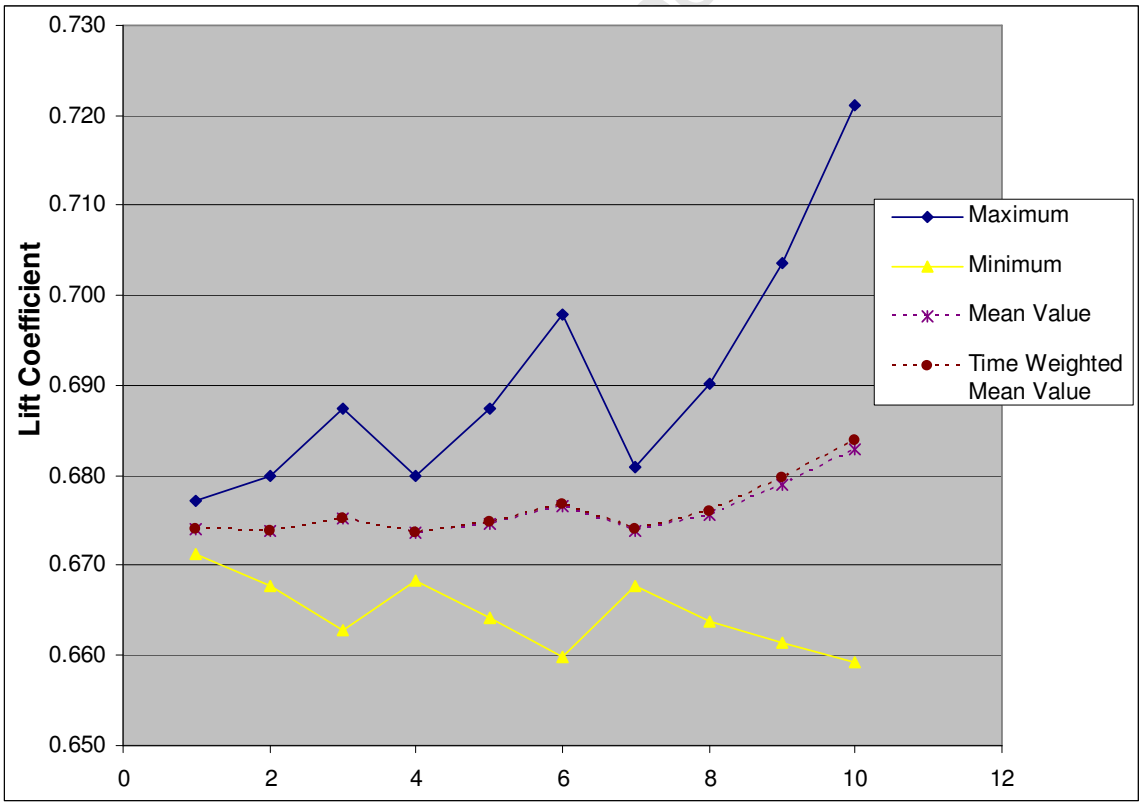


Figure B.1: $C_L$ for $\alpha = 7°$

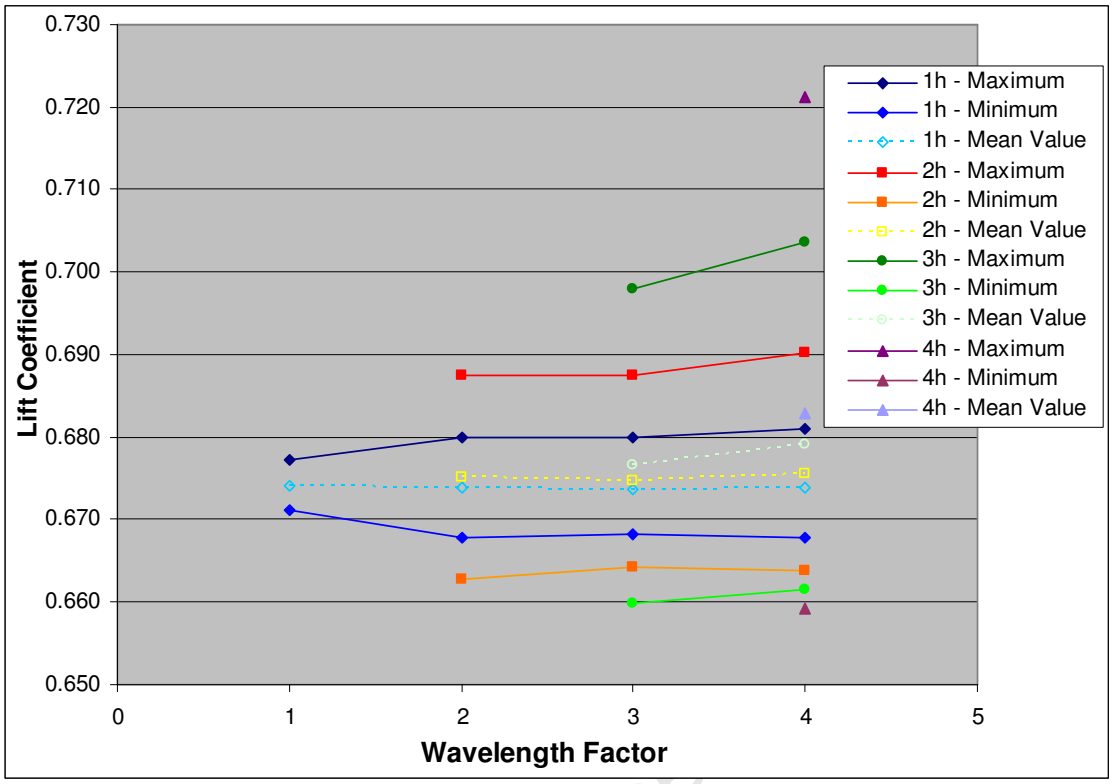


Figure B.2: $C_L$ vs. wavelength for $\alpha = 7°$ (lines of constant wave height)

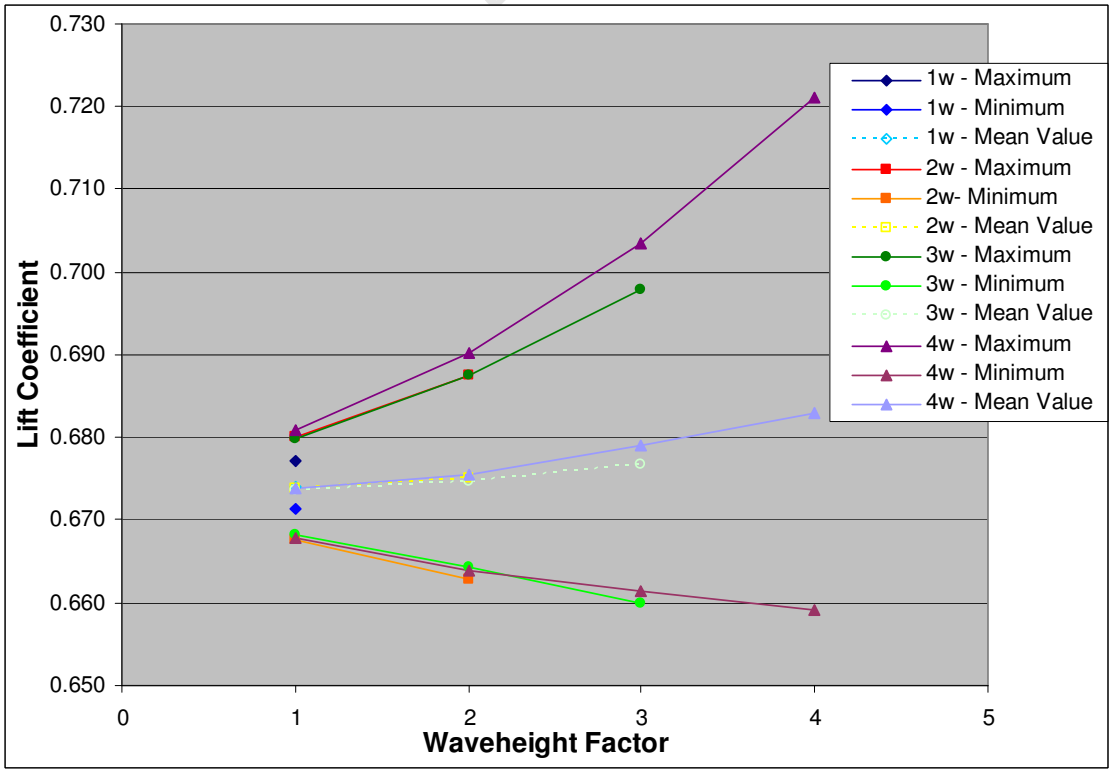


Figure B.3: $C_L$ vs. wave height for $\alpha = 7°$ (lines of constant wavelength)

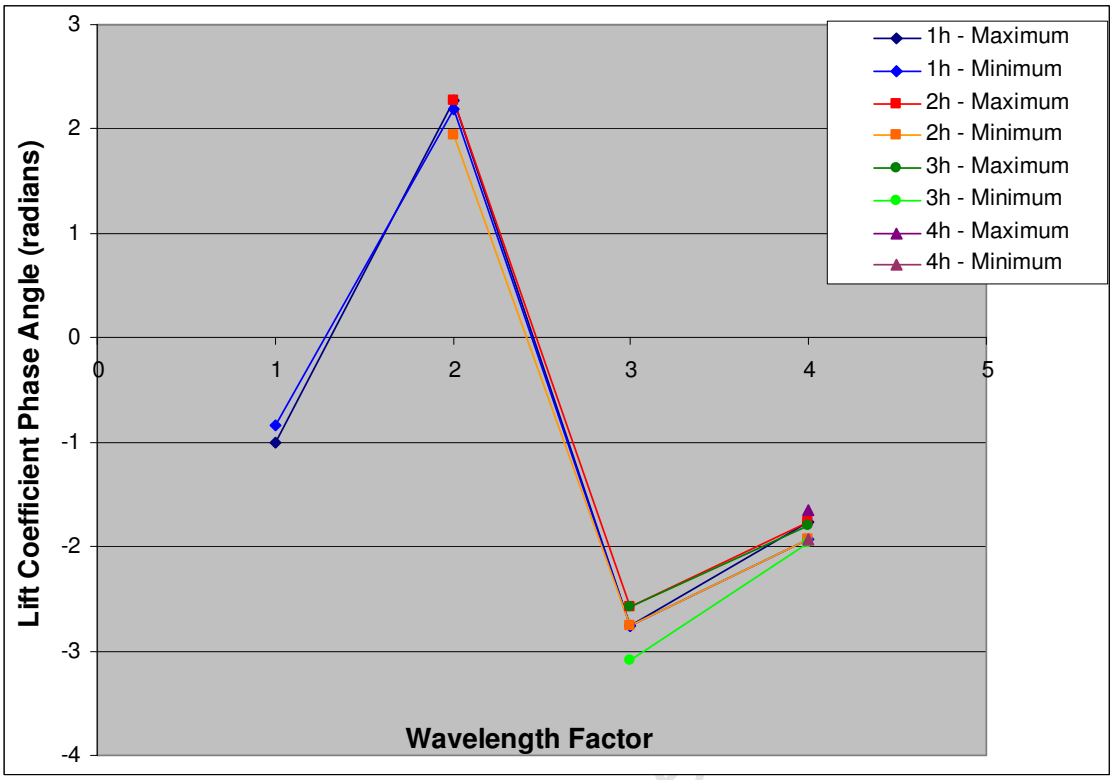


Figure B.4: $C_L$ phase angle vs. wavelength (lines of constant wave height)

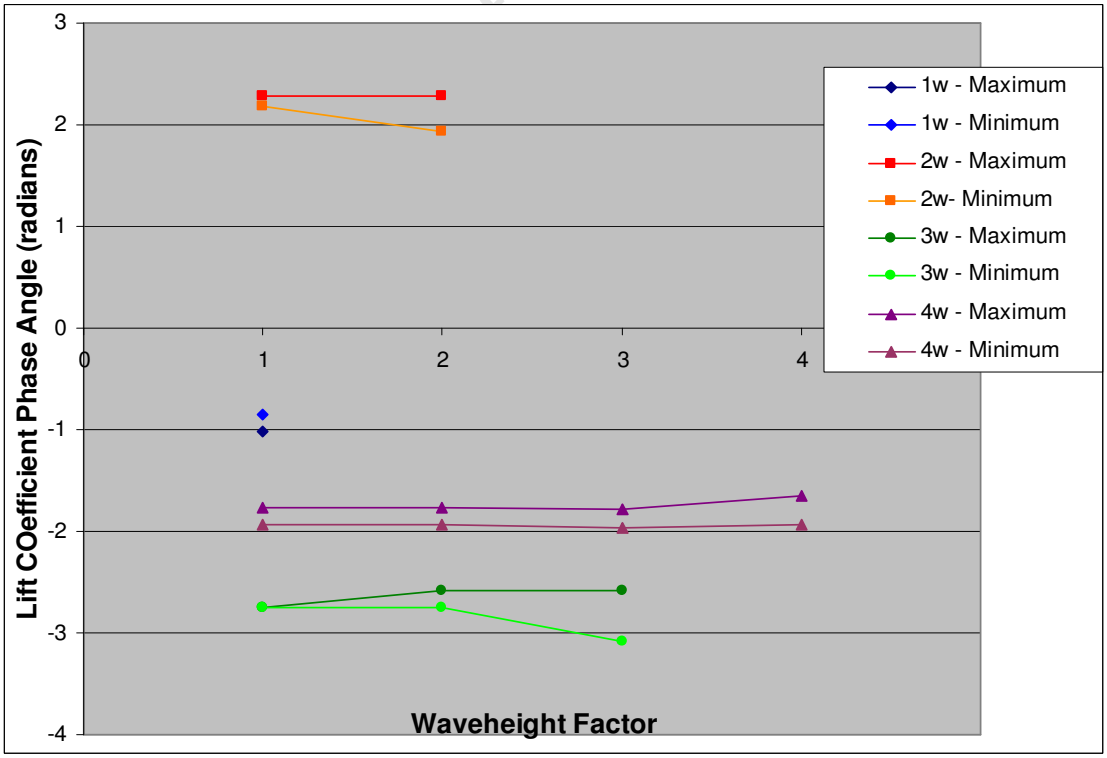


Figure B.5: $C_L$ phase angle vs. wave height (lines of constant wavelength)

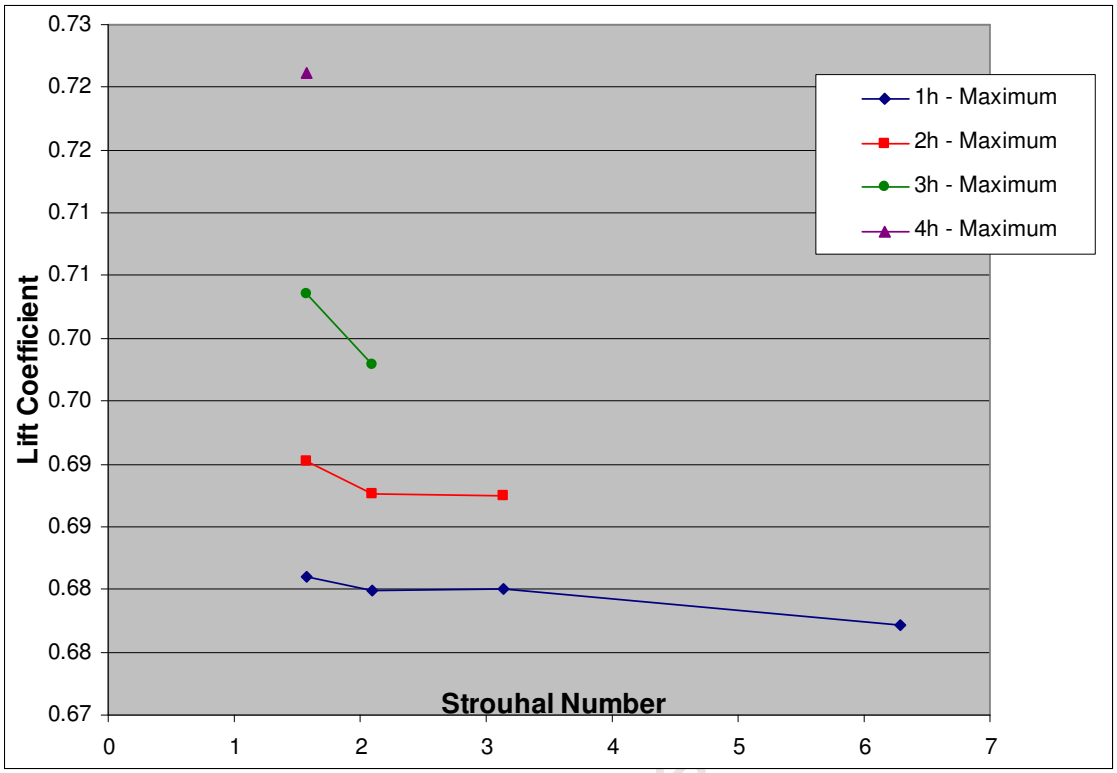


Figure B.6: $C_L$ vs. Strouhal Number for $\alpha = 7°$ (lines of constant wavelength)

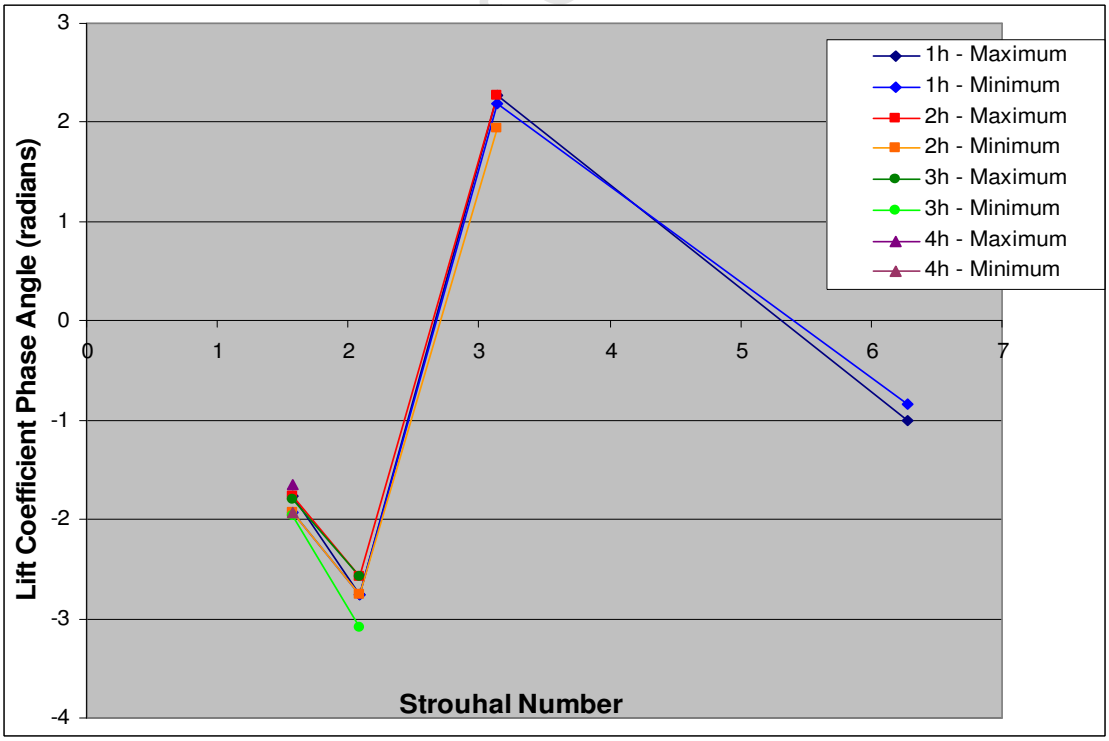


Figure B.7: $C_L$ phase angle vs. Strouhal Number ($\alpha = 7°$) (lines of constant wave height)

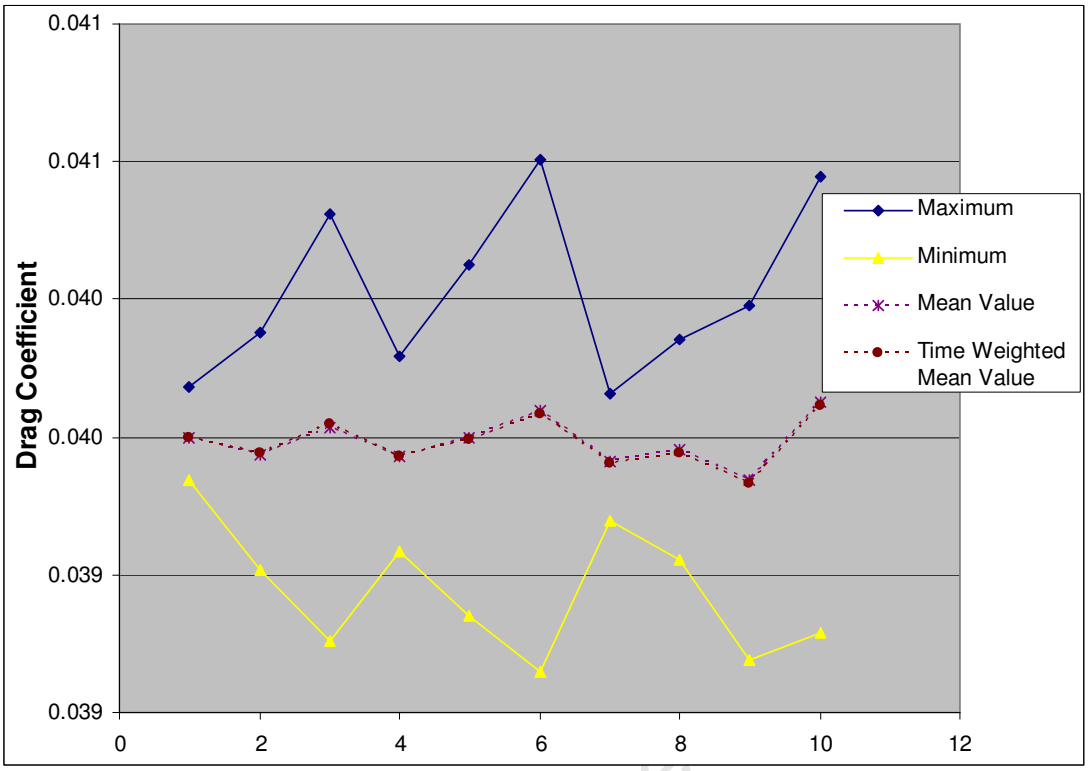


Figure B.8: $C_D$ for $\alpha = 7°$

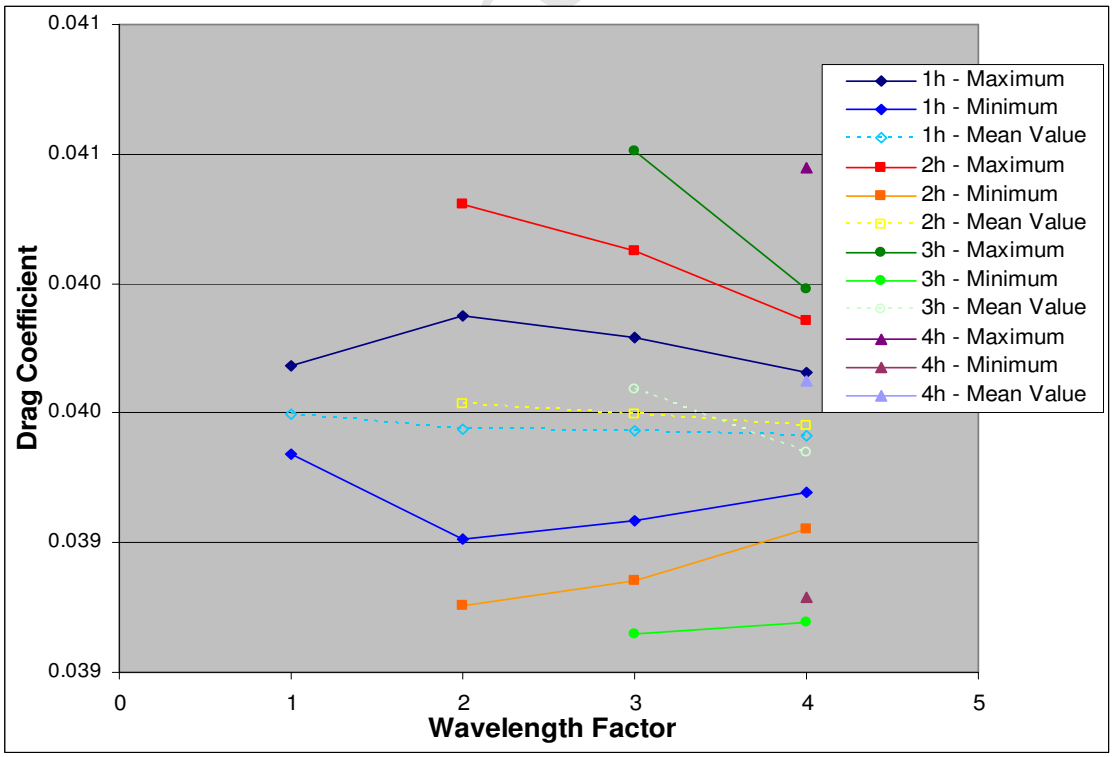


Figure B.9: $C_D$ vs. wavelength for $\alpha = 7°$ (lines of constant wave height)

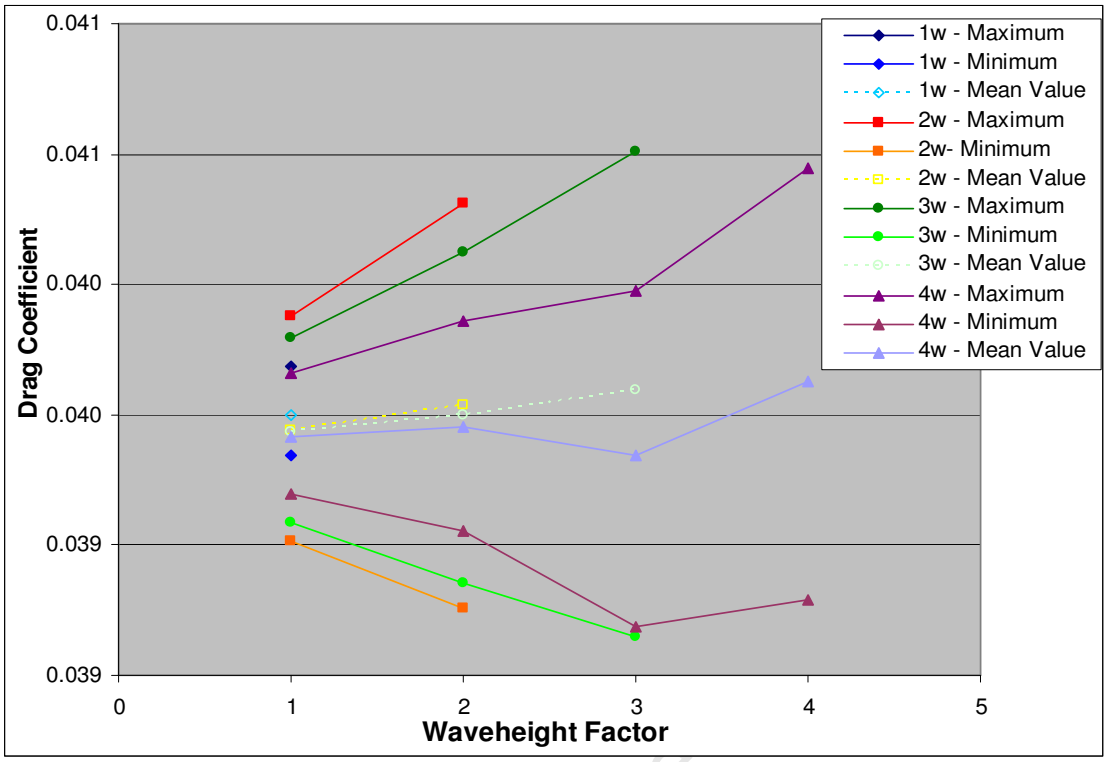


Figure B.10: $C_D$ vs. wave height for $\alpha = 7°$ (lines of constant wavelength)

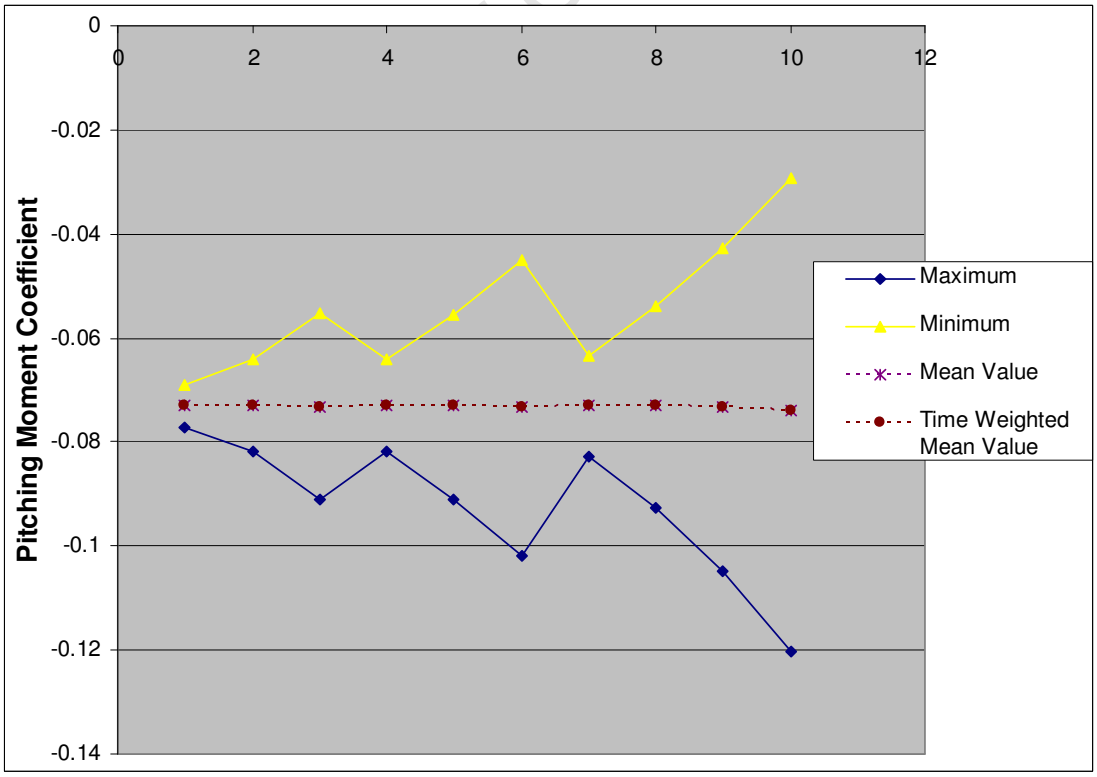


Figure B.11: $C_{M1/4MAC}$ for $\alpha = 7°$

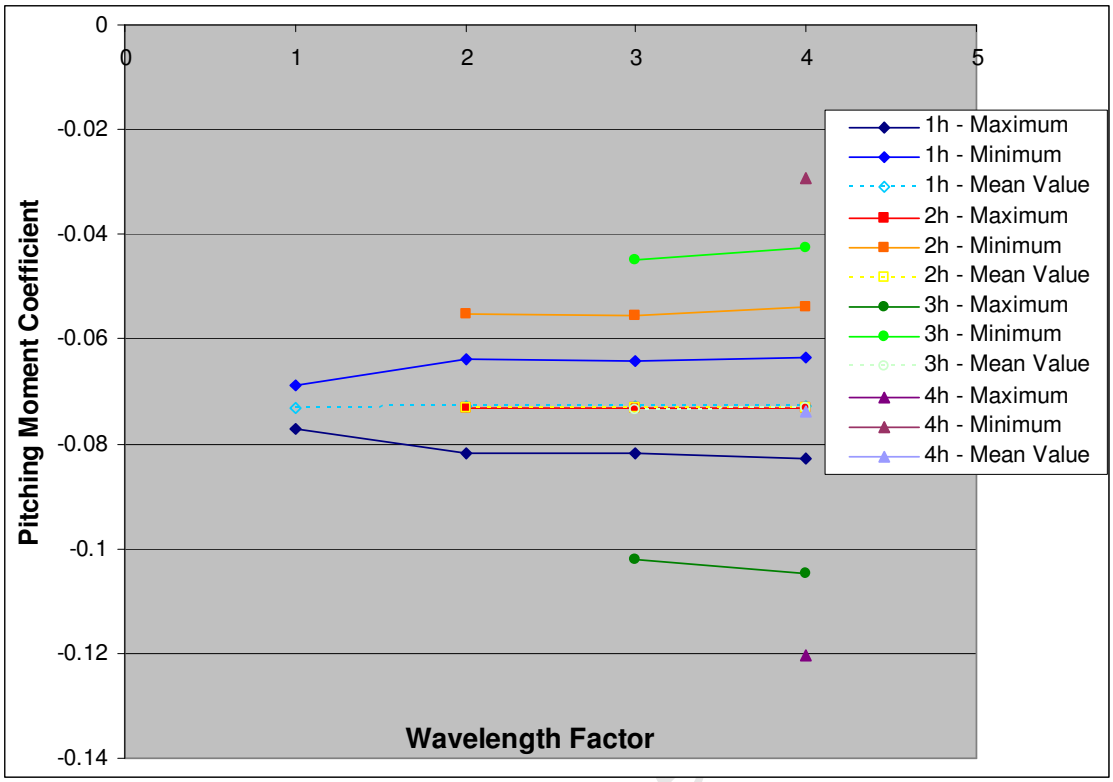


Figure B.12: $C_{M1/4MAC}$ vs. wavelength for $\alpha = 7°$ (lines of constant wave height)

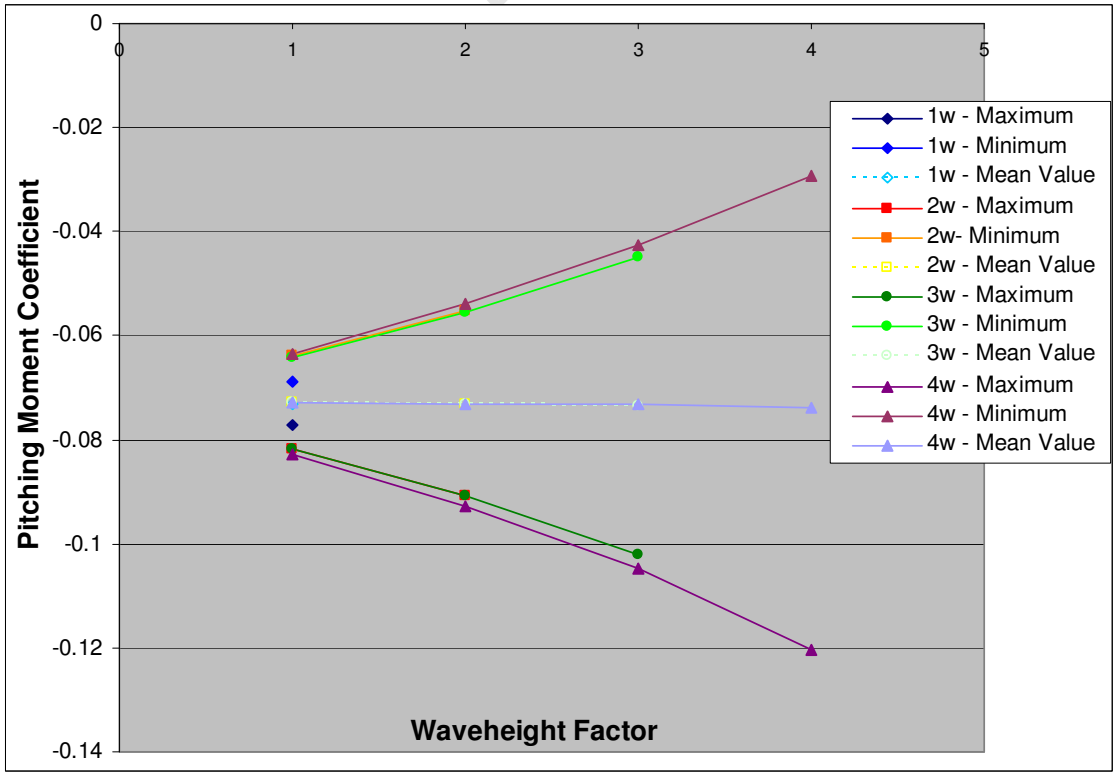


Figure B.13: $C_{M1/4MAC}$ vs. wave height for $\alpha = 7°$ (lines of constant wavelength)

# B.5 GRAPHS OF RESULTS - 11°

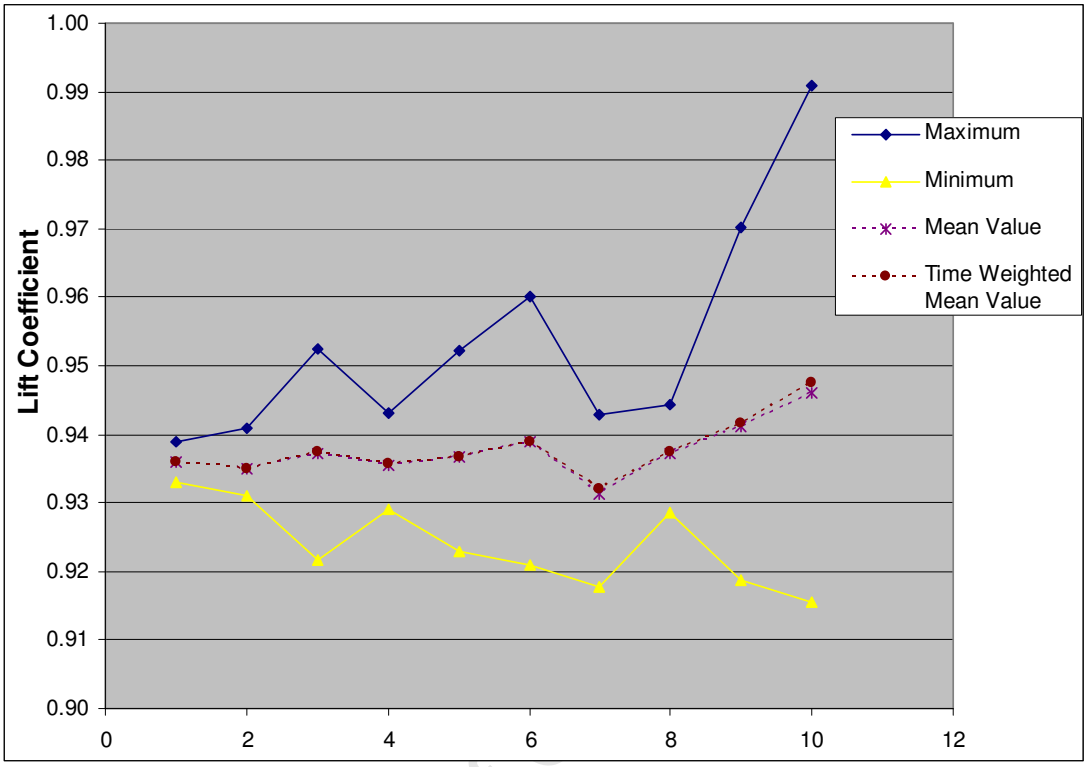


Figure B.14: $C_L$ for $\alpha = 11°$

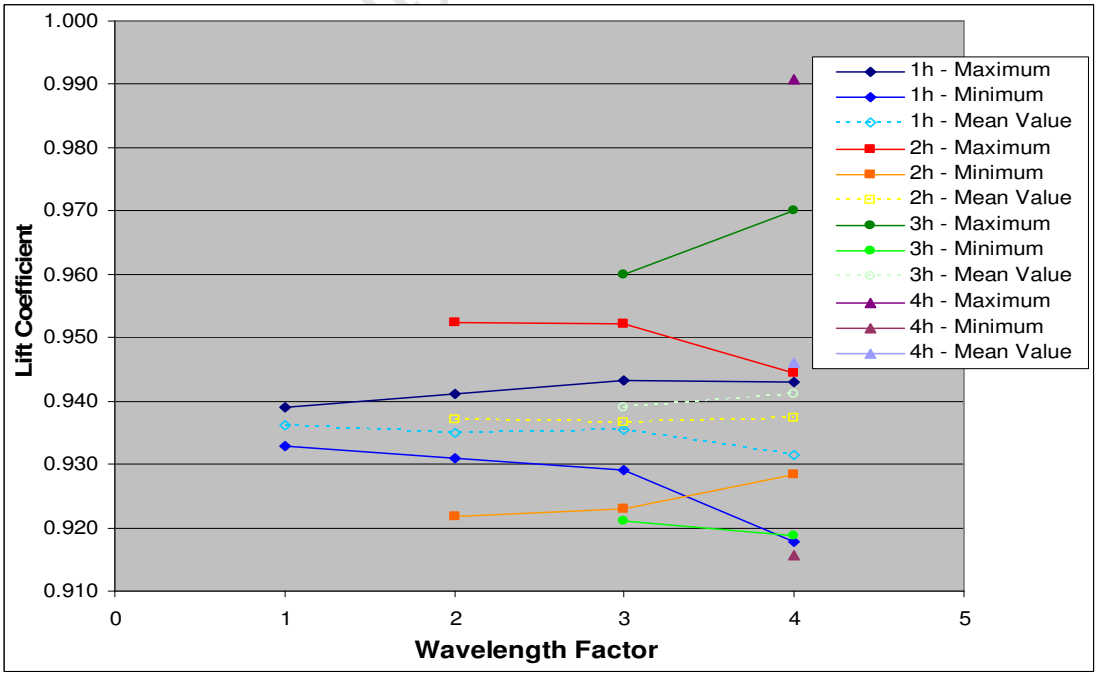


Figure B.15: $C_L$ vs. wavelength for $\alpha = 11°$ (lines of constant wave height)

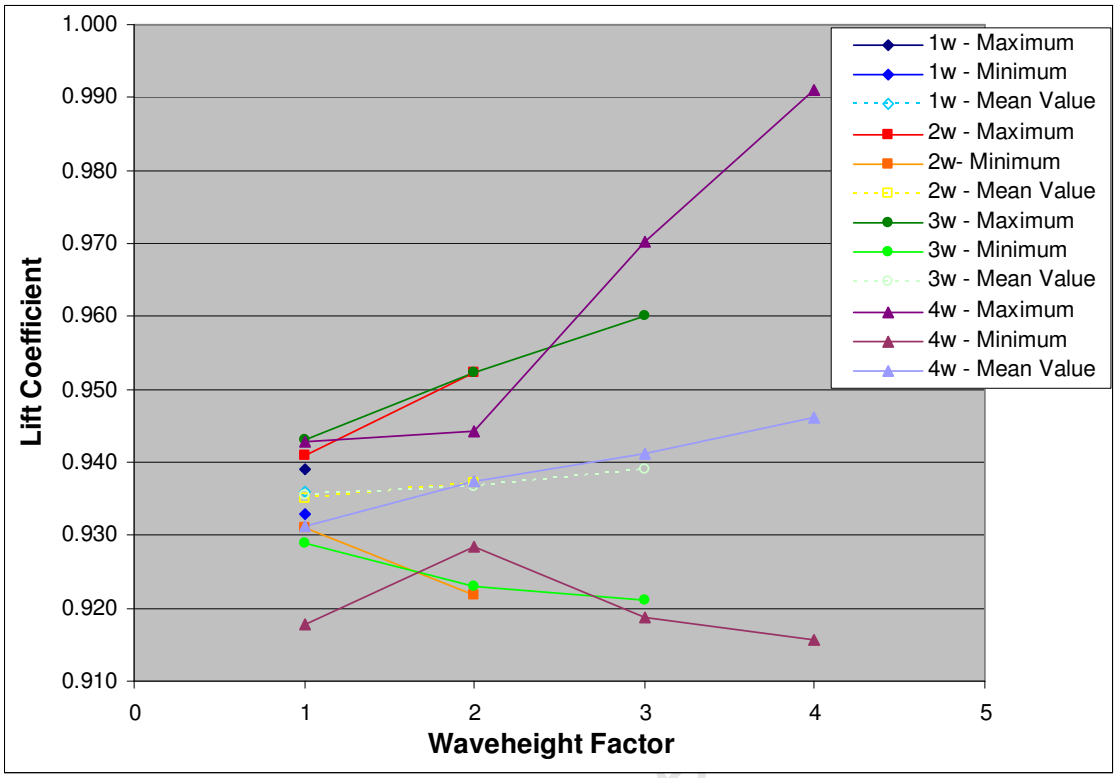


Figure B.16: $C_L$ vs. wave height for $\alpha = 11°$ (lines of constant wavelength)

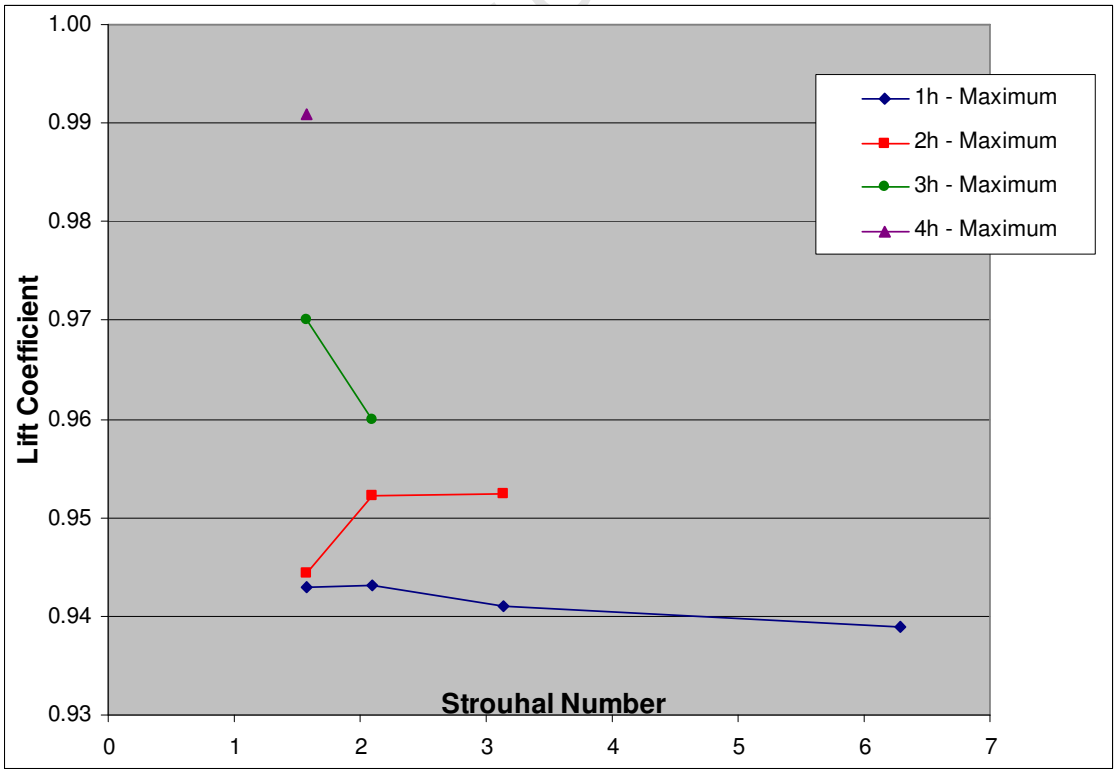


Figure B.17: $C_L$ vs. Strouhal Number for $\alpha = 11°$ (lines of constant wavelength)

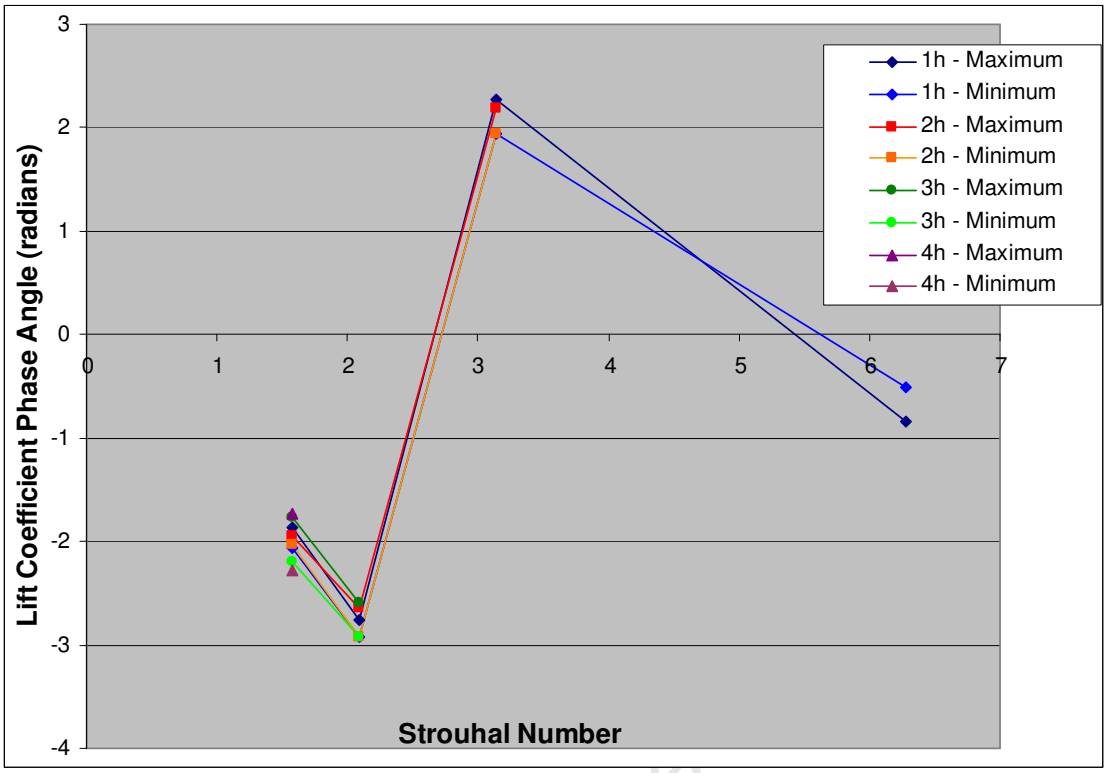


Figure B.18: $C_L$ phase angle vs Strouhal Number for 11° (lines of constant wave height)

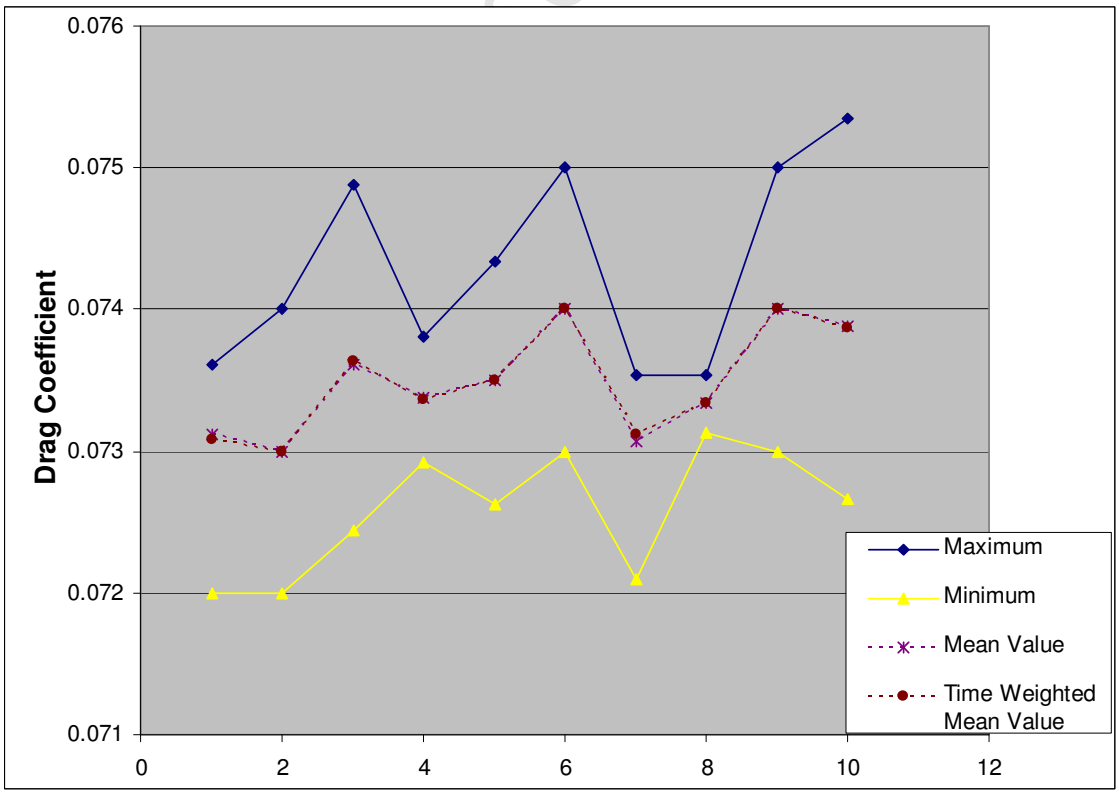


Figure B.19: $C_D$ for $\alpha = 11°$

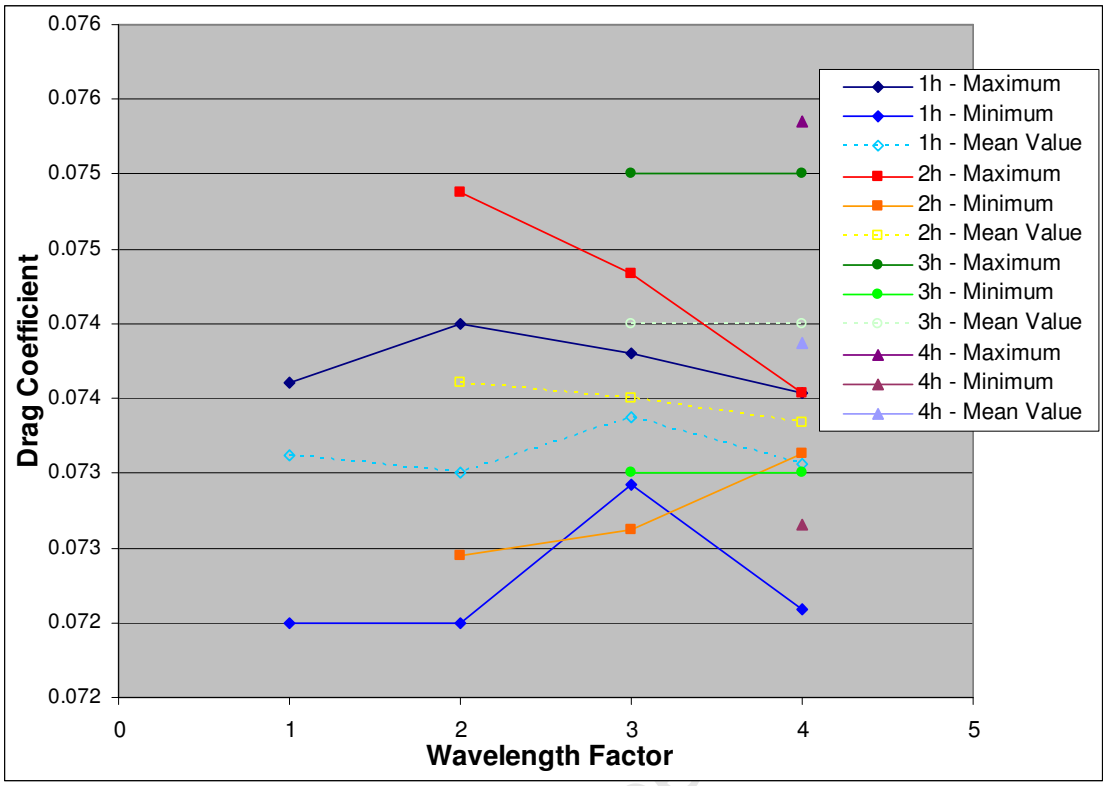


Figure B.20: $C_D$ vs. wavelength for $\alpha = 11°$ (lines of constant wave height)

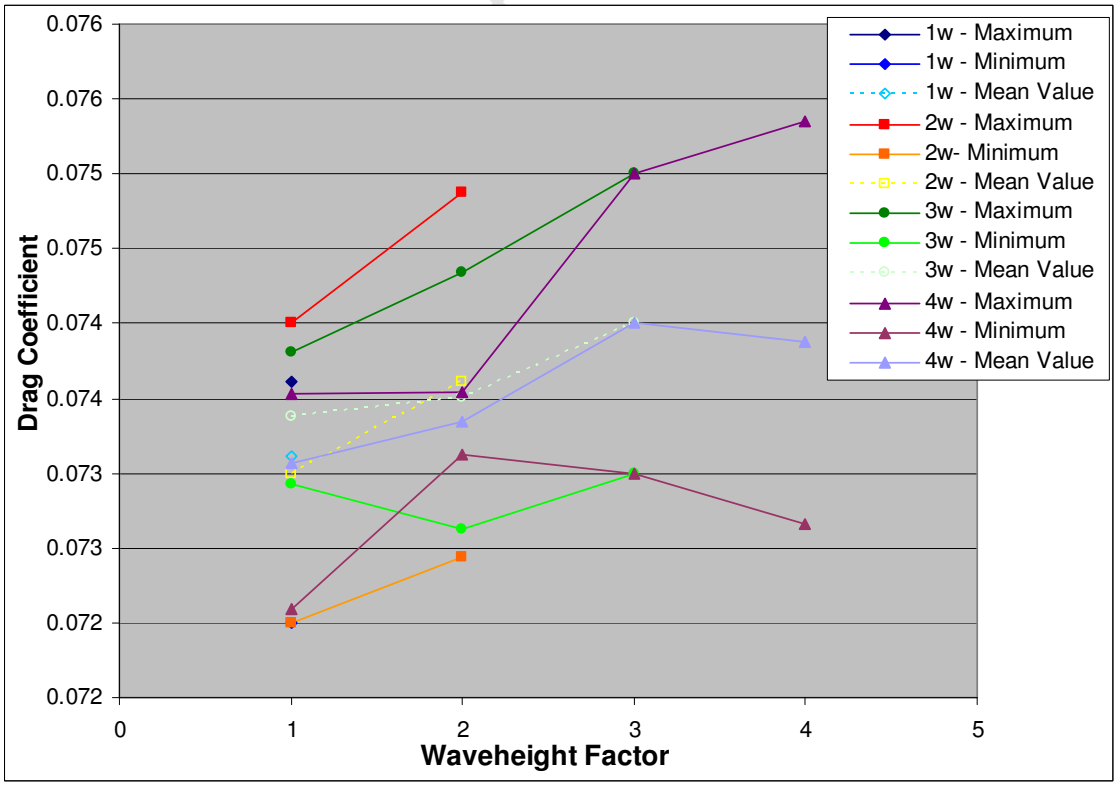


Figure B.21: $C_D$ vs. wave height for $\alpha = 11°$ (lines of constant wavelength)

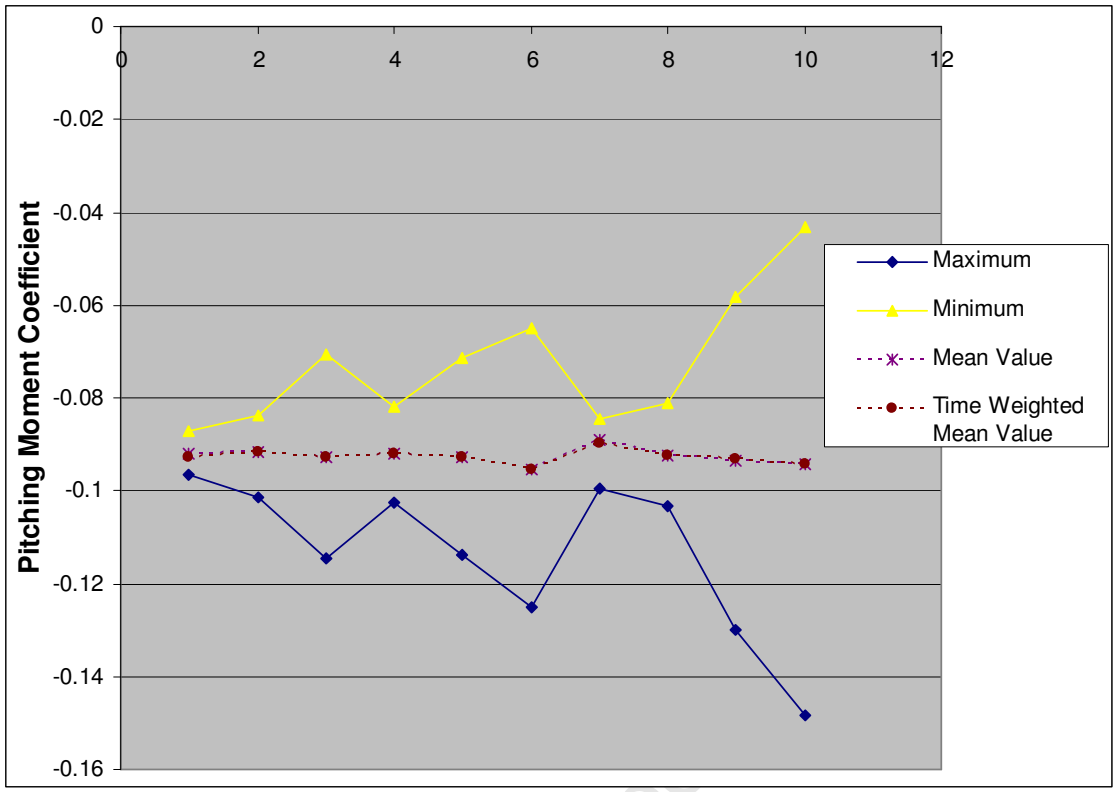


Figure B.22: $C_{M1/4MAC}$ for $\alpha = 11°$

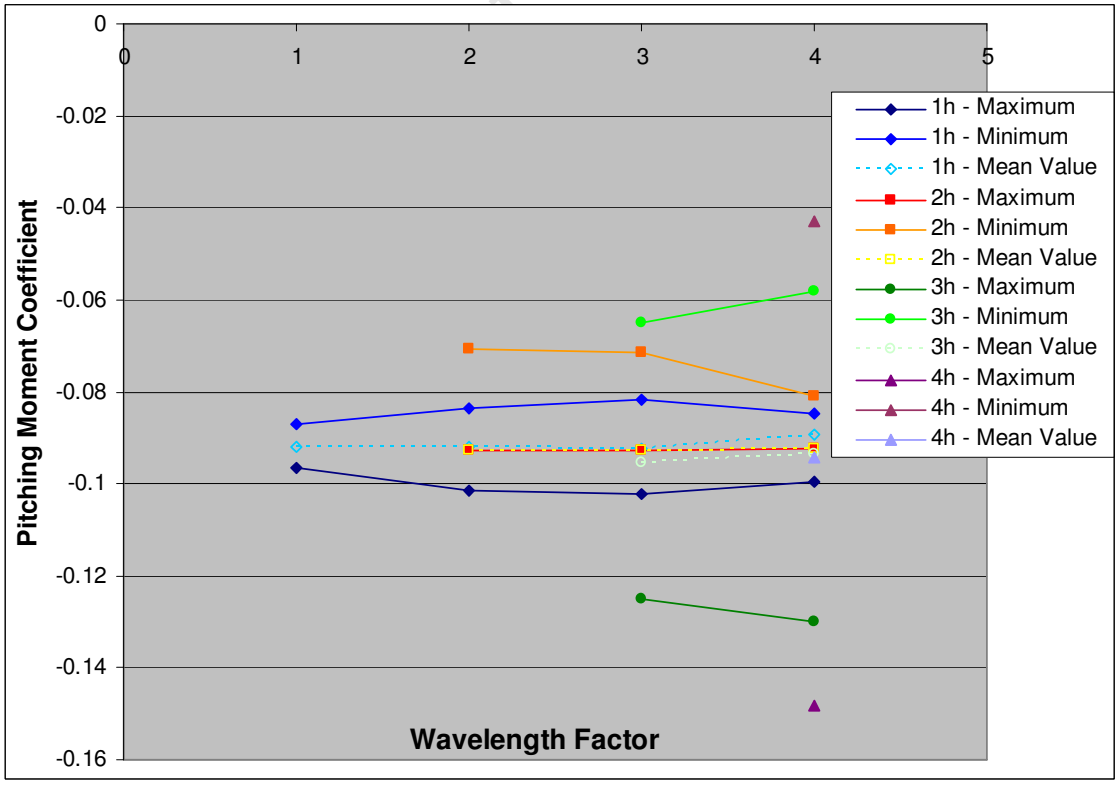


Figure B.23: $C_{M1/4MAC}$ vs. wavelength for $\alpha = 11°$ (lines of constant wave height)

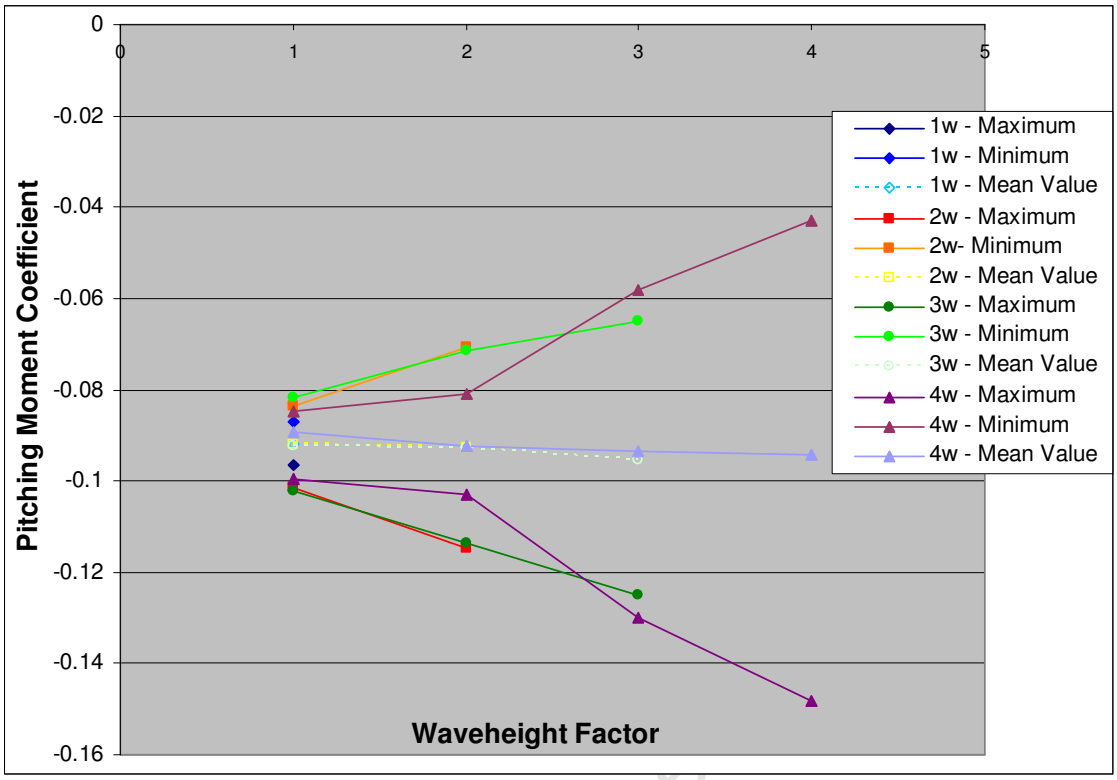


Figure B.24: $C_{M1/4MAC}$ vs. wave height for $\alpha = 11°$ (lines of constant wavelength)

# APPENDIX C: SUMMARY OF MESH SETTINGS

List of Figures C-ii
List of Tables C-ii

C.1. Mesh around the Aerofoil C-1
C.1.1 Cells on Upper Surface of Aerofoil C-1
C.1.2 Aerofoil Boundary Layer C-3
C.1.3 Cell Distribution along Span of Wing C-4
C.1.4 Mesh around the Wingtip C-5
C.2. Flat Ground Plane Model C-6
C.2.1 Computational Domain Shape C-6
C.2.2 Use of an Unstructured Mesh C-6
C.2.3 Spanwise Distribution of Cells C-7
C.2.4 Model for $h_0$ 0.06 and 0.12 C-8
C.2.4.1 Ground Boundary Layer C-8
C.2.4.2 Structured Mesh along Domain Border C-10
C.2.5 Model for $h_0$ 0.50 C-11
C.2.6 Model for $h_0$ 1.30 C-12
C.2.7 Mesh Quality C-13
C.2.7.1 Cell Skewness – EquiAngle Skew C-14
C.2.7.2 Cell Aspect Ratio C-15
C.2.8 Total Number of Cells C-15
C.3. Wavy Ground Plane Model C-16
C.3.1 $h_0$ 0.06 Domain without Boundary Layer C-17
C.3.2 Sliding Region Mesh C-17
C.3.2.1 Streamwise and Vertical Distribution of Cells C-17
C.3.2.2 Spanwise Distribution C-19
C.3.3 Mesh Quality of the Sliding Region C-20
C.3.3.1 Cell Skewness – EquiAngle Skew C-20
C.3.3.2 Cell Aspect Ratio C-21
C.3.4 Total Number of Cells C-21

# LIST OF FIGURES

Figure C.1: Cell distribution around the wing C-2
Figure C.2: Boundary layer specification in Gambit® C-3
Figure C.3: Side view of resultant boundary layer C-4
Figure C.4: Spanwise cell distribution along the wing C-4
Figure C.5: Different spanwise mesh distributions for $h_0$ = 0.06 ($\alpha$ = 7°) C-8
Figure C.6: Different spanwise mesh distributions for $h_0$ = 0.50 ($\alpha$ = 7°) C-8
Figure C.7: Ground boundary layer specifications C-9
Figure C.8: Visualisation of the ground boundary layer C-9
Figure C.9: Cell distribution in vertical and spanwise directions for $h_0$ 0.06 and 0.12 C-10
Figure C.10: Cell distribution along streamwise direction for $h_0$ 0.06 and 0.12 C-10
Figure C.11: Cell distribution along vertical and spanwise directions for $h_0$ 0.50 C-11
Figure C.12: Cell distribution along streamwise direction for $h_0$ 0.50 C-11
Figure C.13: Close up side view of mesh around wing at $h_0$ 0.50 C-12
Figure C.14: Cell distribution along vertical and spanwise directions for $h_0$ 1.30 C-12
Figure C.15: Cell distribution along streamwise direction for $h_0$ 1.30 C-13
Figure C.16: Close up side view of mesh around wing at $h_0$ 1.30 C-13
Figure C.17: Original mesh domain with new sliding mesh region below C-16
Figure C.18: Side view of new mesh without the fine ground boundary layer C-17
Figure C.19: $C_L$ comparison between different sliding region mesh densities C-18
Figure C.20: Side view of sliding region mesh C-18
Figure C.21: Spanwise cell distribution for the sliding region C-19

# LIST OF TABLES

Table C.1: Summary of wing upper surface grid dependency test C-2
Table C.2: Comparison of different spanwise mesh distributions C-7
Table C.3: EquiAngle skewness comparison for flat ground plane mesh C-14
Table C.4: Average total number of cells for the flat ground plane model C-15
Table C.5: Comparison of new spanwise mesh with old mesh C-20
Table C.6: EquiAngle skewness comparison between wavy ground plane meshes C-21

# C.1 MESH AROUND THE AEROFOIL

This section outlines how the mesh distribution for the aerofoil was determined.

## C.1.1 CELLS ON UPPER SURFACE OF AEROFOIL

The number of cells along the streamwise length of the wing was also important. The behaviour of the flow over the wing can determine a wing's lift, drag, and pitching moment. A fine cell distribution would be better suited to accurately determine the flow features and correctly resolve the forces on the wing. This will obviously increase the computational expense of the model. Therefore the model needed to be tested with different cell distributions to determine how sensitive the force and moment values were to the number of cells around the wing.

The upper surfaces of airfoils usually encounter the more complex flow effects than the lower surfaces, as the flow tries to flow around the leading edge of the aerofoil. Moreover, considering that the DHMTU wing used for this study was essentially flat along its entire lower surface, there would not be any complex flow along this surface. Therefore a more coarse mesh could be used here on the lower surface, while the mesh on the upper surface had to be investigated

Four different configurations were created to test the difference made by the number of cells in the mesh and how they were distributed along the wing's upper surface. The four configurations were tested at an $\alpha$ of 1°, 7°, 13° and at two different $h_0$ positions (0.06 an 0.50). The results of the investigation are summarised in Table C.1. The two different sets of data for the 150 cells model show the difference made by re-distributing the cells along the upper surface. The 1.035 ratio, compared to the 1.01 ratio, indicates that more cells are positioned near the leading edge of the wing. As a result of more cells at the leading edge, the denser cell spacing means smaller cells.

While the results for the different meshes are all very similar, they do indicate an important point. The number of cells in the mesh does not affect the values as much as the distribution of the cells. In other words, the more cells that are distributed near the leading edge, the better the flow is resolved. This assumes however, that the wing is not near the stall angle. When the flow starts separating near the trailing edge at higher angles of attack, more cells would be needed near the trailing edge as well.

Table C.1: Summary of wing upper surface grid dependency test

| $\alpha$ (°) | $h_0$ ($h/c$) | 90 cells (1.02) | | 150 cells (1.01) | | 150 cells (1.035) | | 220 cells (1.02) | |
|---|---|---|---|---|---|---|---|---|---|
| | | $C_D$ | $C_L$ | $C_D$ | $C_L$ | $C_D$ | $C_L$ | $C_D$ | $C_L$ |
| 1 | 0.06 | 0.0075 | 0.221 | 0.0074 | 0.0214 | 0.0073 | 0.220 | 0.0073 | 0.211 |
| 7 | 0.06 | 0.0344 | 0.965 | 0.0343 | 0.961 | 0.0338 | 0.971 | 0.0338 | 0.965 |
| 13 | 0.06 | 0.1655 | 1.161 | | | 0.1368 | 1.259 | 0.1868 | 0.959 |
| 7 | 0.50 | 0.0399 | 0.676 | 0.0395 | 0.673 | 0.0390 | 0.673 | 0.0390 | 0.670 |
| 13 | 0.50 | 0.0936 | 1.047 | 0.0929 | 1.039 | 0.0931 | 1.057 | 0.0904 | 1.025 |

From the results, the 150 cell mesh with the leading edge ratio of 1.035 was chosen. This gave the model better accuracy than the 90 cell model, without the excessive number of cells of the 220 cell model. The ratio of 1.035 would distribute more cells around the leading edge of the wing, which would more accurately predict the flow behaviour here. The final wing mesh distribution is given in Figure C.1.

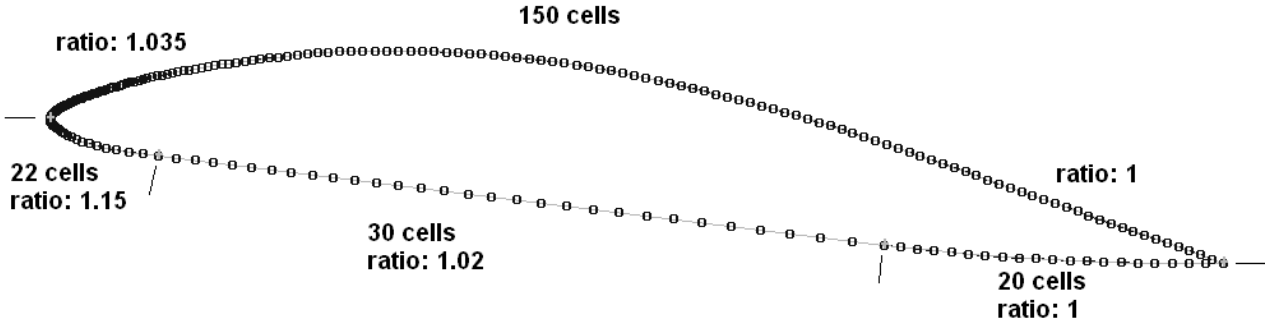


Figure C.1: Cell distribution around the wing

## C.1.2 AEROFOIL BOUNDARY LAYER

This section outlines the specification of the boundary layer using Gambit's® boundary layer tool. The values used to specify the boundary layer are shown in Figure C.2. The Spalart-Allmaras turbulence model was chosen for this study. Therefore the *y*+ values in the first cell adjacent to the wall had to be maintained to within 1 and 5. To meet this requirement, it was found that the first cell height had to be 0.2mm. This resulted in a *y*+ value of 1 to 4 being maintained around the wing. The cell height growth factor was limited to 1.26. A larger value would distort the mesh. The final thickness of the boundary layer is 5.01mm. Figure C.3 shows a side view of the resultant boundary layer.

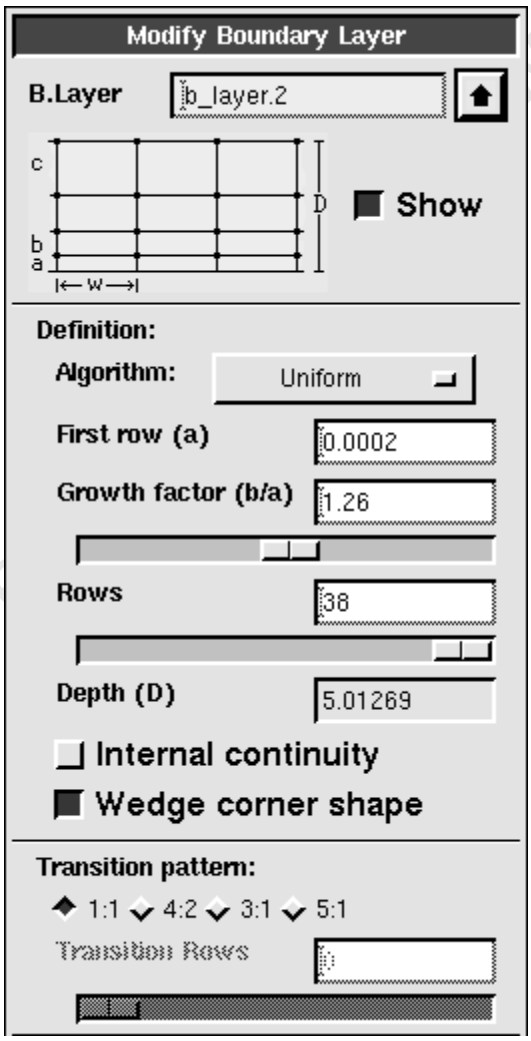


Figure C.2: Boundary layer specification in Gambit®

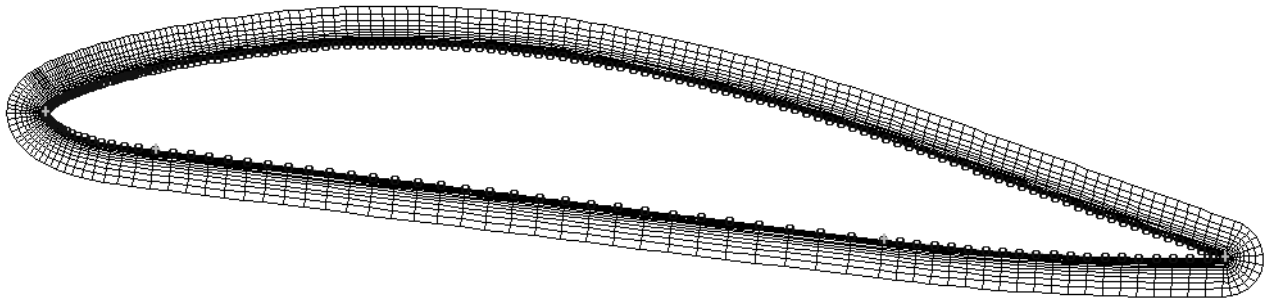

Figure C.3: Side view of resultant boundary layer

The *y*+ values at the wingtip also had to be considered as the wingtip face was also modelled as a solid boundary, or wall. Therefore the first cell height at the wingtip was also selected to be 0.2mm. As a result, the *y*+ values at the wingtip were maintained at about 4. The treatment of the wall is discussed more in Section C.1.4.

## C.1.3 CELL DISTRIBUTION ALONG SPAN OF WING

The cell distribution along the wingspan was not as vital to the accuracy of the results. This was because the flow variation in the spanwise direction of the wing was not as intense, or complex, as the streamwise flow variations. The cell distribution around the wingtip region however did need to be considered. Here the mesh had to be refined enough to capture the wingtip vortices as the started to form. Therefore the position of the cells on the wing was biased so that more cells would be position near the wingtip.

A total of 34 cells along the wing were chosen as it gave good results without creating an excessive number of cells in the domain. The distribution is shown in Figure C.4.

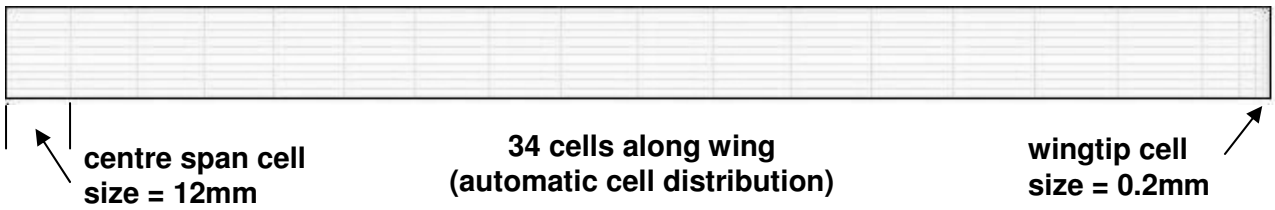


Figure C.4: Spanwise cell distribution along the wing

### C.1.4 MESH AROUND THE WINGTIP

The irregular shape of the wingtip made it difficult to mesh with a regular structure mesh. Therefore and unstructured mesh was used. Gambit's® "pave" style of meshing was used to mesh the face of the wingtip.

The spanwise distribution of cells from the wingtip towards the free stream flow was also considered. The wingtip face was part of the wing, and so was also modelled as a solid boundary. Therefore the *y*+ values had to be considered here as well. For that reason the first cell height was also chosen as 0.2mm. The rate at which the cell size grew outwards from the wingtip was a result of the different meshes used (see Section C.2.4).

# C.2 FLAT GROUND PLANE MODEL

This section describes the mesh used for the flat ground plane models. Three different styles of meshes were used for the four different ground clearances. For the $h_0$ values of 0.06 and 0.12, the mesh models used the same basic mesh. The differences between the meshed are discussed below.

## C.2.1 COMPUTATIONAL DOMAIN SHAPE

In order to have a mesh that was as structured as possible, it was decided to create a hexagonal (3D rectangle) shaped domain. This allowed the block shaped hexagonal elements to fit into the domain exactly without any distortions. This had the added bonus that the majority of the cells would be neatly aligned with the flow, which would reduce the error generated by numerical diffusion [21]. The resulting domain would then also have a flat surface in the correct position for the flat ground plane that would need to be modelled.

## C.2.2 USE OF AN UNSTRUCTURED MESH

In all meshes it would be preferable to use a fully structured mesh. However, when meshing the curved sides of an aerofoil, it becomes more difficult to match the regular cells on the boundary with cells at different orientations along the wing's surface. It becomes particularly difficult at higher angles of attack. Moreover, due to the presence of the flat ground plane, the traditional structured aerofoil meshes were not suitable for use in this application. Therefore a compromise needed to be obtained.

It was decided that the mesh of primary importance, was that around the wing's surface. Therefore the boundary layer tool in Gambit® was used to mesh the region around the upper and lower surface of the wing. This created a layer of cells that wrapped around the contour of the aerofoil (shown in Figure C.3).

To blend the mesh around the wing with the structured, orthogonal mesh of the rest of the domain it was decided to use a region of unstructured mesh. Gambit's® "pave" mesh scheme was used to create this unstructured region.

Unstructured regions are not ideal, especially around regions of importance, as they can lead to numerical diffusion in the solution [21]. However, since there would be a structured boundary layer around the wing, this unstructured region would be far enough away from the really important flow. An additional benefit of this unstructured region was that it allowed the fine mesh around the wing to be coarsened in order to match the coarser mesh of the rest of the domain.

## C.2.3 SPANWISE DISTRIBUTION OF CELLS

To determine the sensitivity of the force and moment coefficients to the distribution of cells along the wing and around the wingtip, a comparison of different mesh densities was performed. The results for the wing at 7° angle of attack at $h_0$ = 0.06 and 0.50 are given in Table C.2. The mesh distributions for $h_0$ = 0.06 (A to D) are illustrated in Figure C.5 and the distributions for $h_0$ = 0.50 (E to H) are shown in Figure C.6. Increasing the number of cells on the wing, at least to 40 cells, does not make a significant difference to the results. Furthermore, increasing the number of cells does not make much difference either. Therefore it can be concluded that the results are independent of the spanwise mesh densities that were tested. Therefore the meshes of B and F were chosen as they would be less computationally expensive than the other meshes.



Table C.2: Comparison of different spanwise mesh distributions

| $h_0$ | A | | B | | C | | D | |
|---|---|---|---|---|---|---|---|---|
| | $C_D$ | $C_L$ | $C_D$ | $C_L$ | $C_D$ | $C_L$ | $C_D$ | $C_L$ |
| **0.06** | 0.0339 | 0.971 | 0.0342 | 0.969 | 0.0342 | 0.970 | 0.0335 | 0.965 |
| | **E** | | **F** | | **G** | | **H** | |
| **0.50** | 0.0389 | 0.672 | 0.03865 | 0.669 | 0.0387 | 0.669 | 0.0388 | 0.669 |

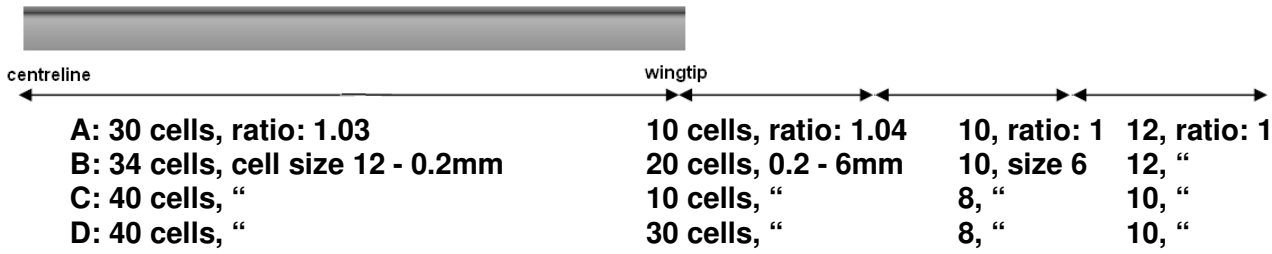


Figure C.5: Different spanwise mesh distributions for $h_0 = 0.06$ ($\alpha = 7°$)

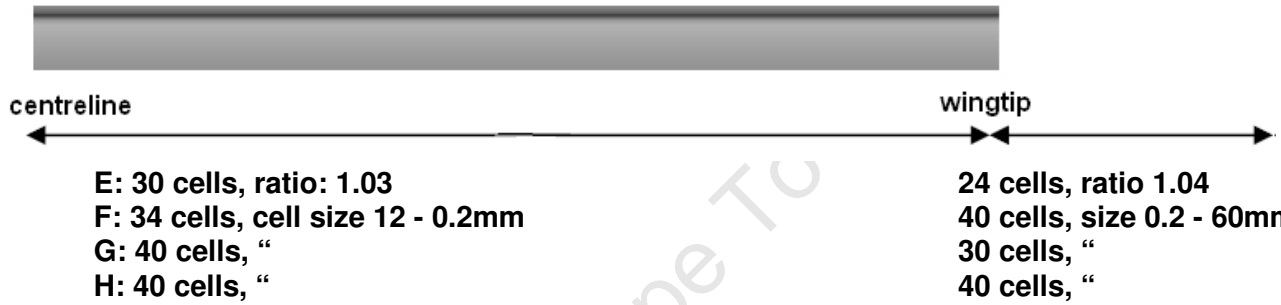


Figure C.6: Different spanwise mesh distributions for $h_0 = 0.50$ ($\alpha = 7°$)

## C.2.4 MODEL FOR $h_0$ 0.06 AND 0.12

For the $h_0$ values of 0.06 and 0.12, the meshes were very similar. The only differences were the ground clearance of the wing and the resulting unstructured mesh region surrounding the wing.

### C.2.4.1 Ground Boundary Layer

For these two ground clearances, the presence of the ground and its boundary layer were of importance. Therefore a fine layer of cells was positioned on the ground covering the area under, and surrounding, the wing. The specifications used for this boundary layer is shown in Figure C.7. Figure C.8 illustrates the ground boundary layer in relation to the wing's boundary layer and the unstructured mesh around the wing. The small cells of the boundary layer are force to grow in size toward the upstream and downstream boundaries. This was done to ensure smooth transition from the small cell under the wing, to the larger cells at the boundaries.

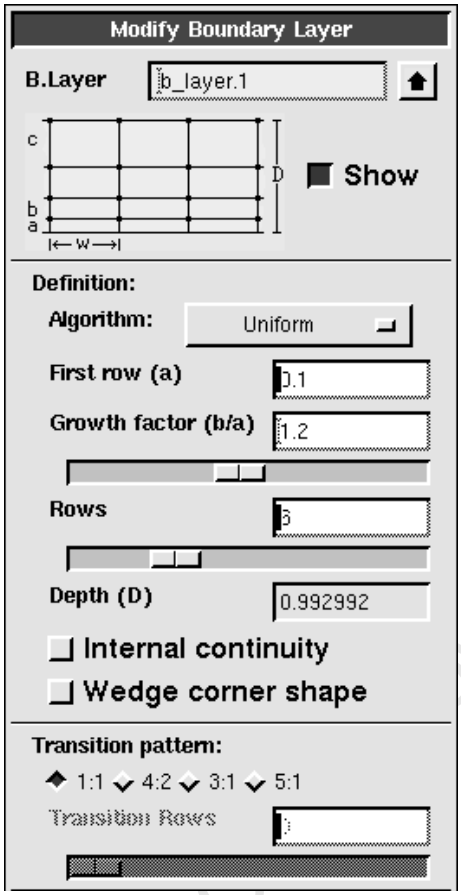


Figure C.7: Ground boundary layer specifications

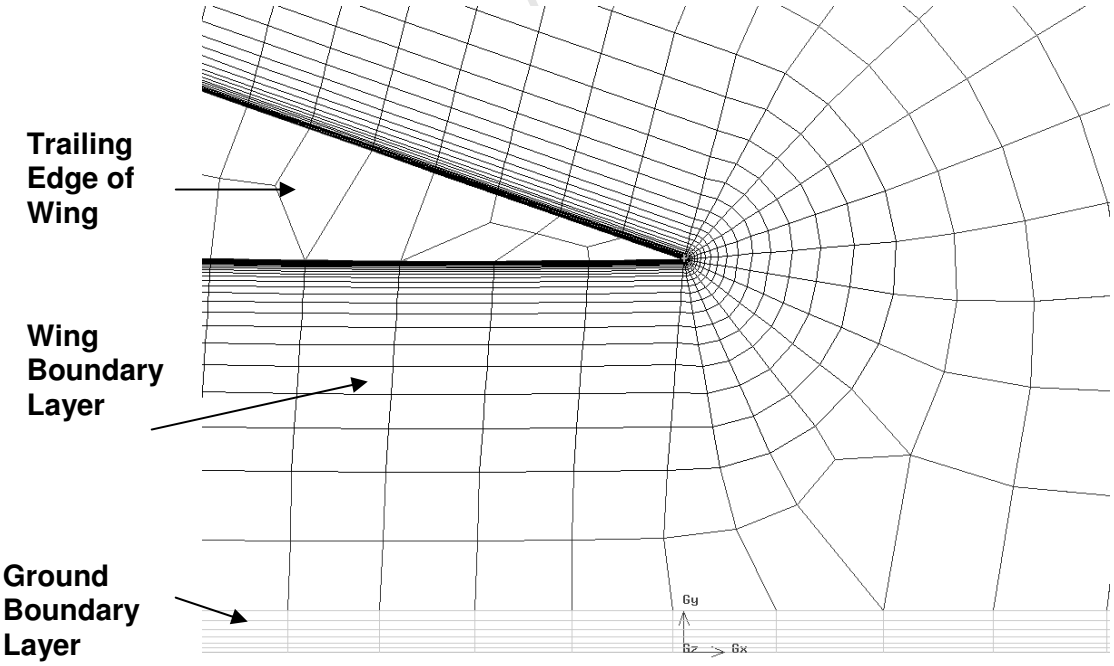


Figure C.8: Visualisation of the ground boundary layer

### C.2.4.2 Structured Mesh along Domain Border

The cell distribution of the structured region for the $h_0$ = 0.06 and 0.12 model is described in the two figures below.

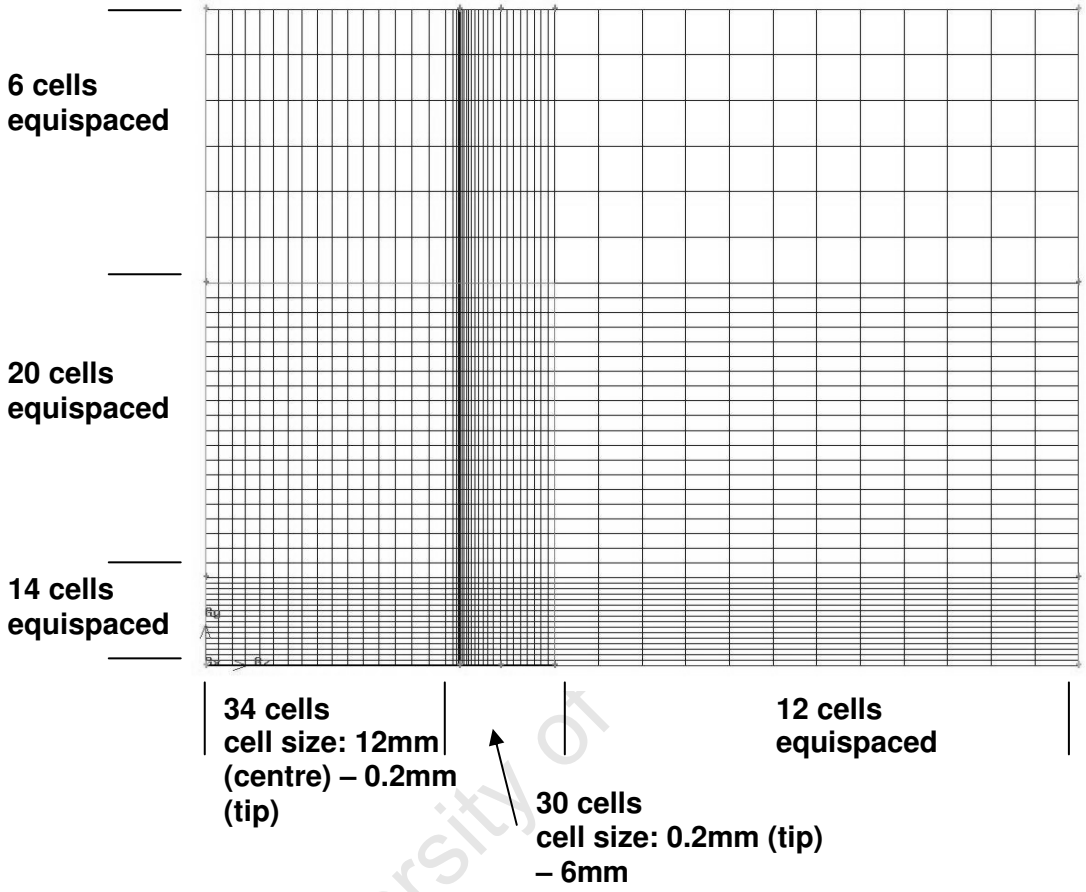


Figure C.9: Cell distribution in vertical and spanwise directions for $h_0$ 0.06 and 0.12

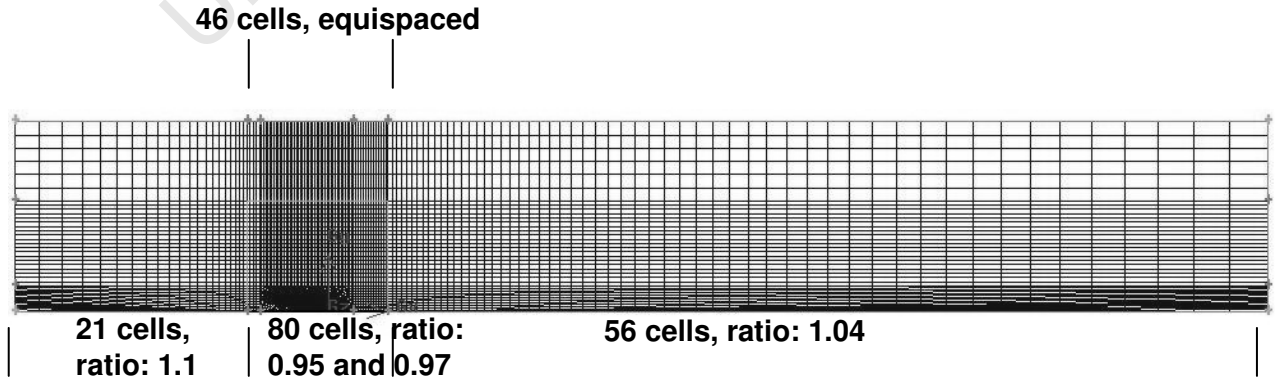


Figure C.10: Cell distribution along streamwise direction for $h_0$ 0.06 and 0.12

## C.2.5 MODEL FOR $h_0$ 0.50

The mesh distribution for the $h_0$ = 0.50 model was similar to the model for the 0.06 and 0.12 ground clearances. The main differences being the lack of a boundary layer mesh on the ground boundary and the distribution of cells under the wing. The cell distribution of the structured region for the $h_0$ = 0.50 model is described in Figure C.11 and Figure C.12. Figure C.13 gives a closer view of the mesh around the wing.

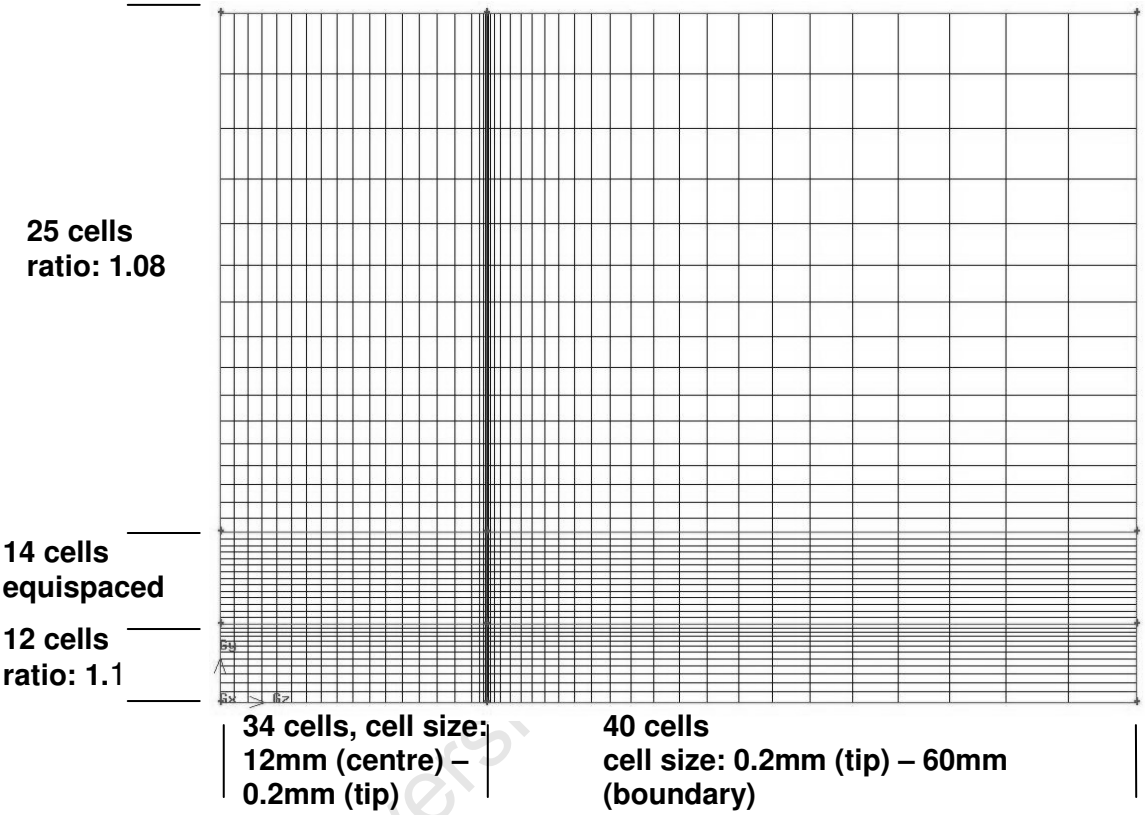


Figure C.11: Cell distribution along vertical and spanwise directions for $h_0$ 0.50

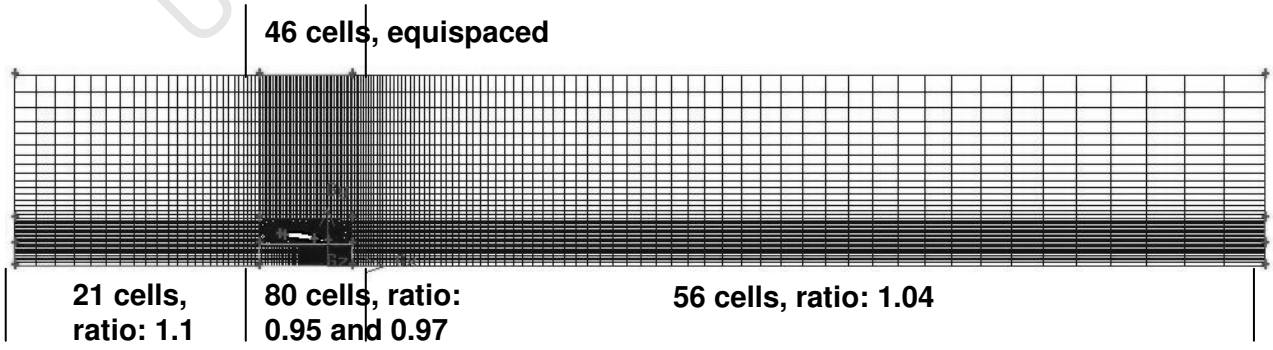


Figure C.12: Cell distribution along streamwise direction for $h_0$ 0.50

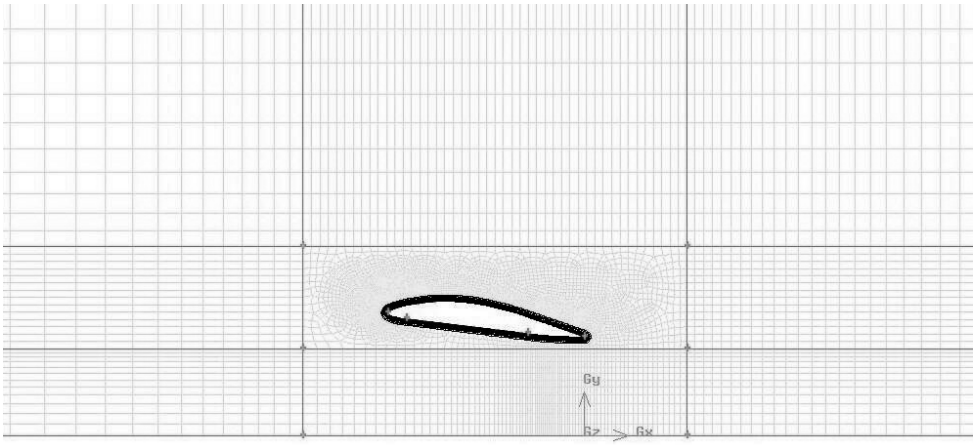

Figure C.13: Close up side view of mesh around wing at $h_0$ 0.50

## C.2.6 MODEL FOR $h_0$ 0.130

The mesh for the $h_0$ = 1.30 model was similar to the $h_0$ = 0.50 model, except that the different ground clearance required a different mesh between the wing and the ground plane. The cell distribution of the structured region for the $h_0$ = 1.30 model is described in the two figures below.

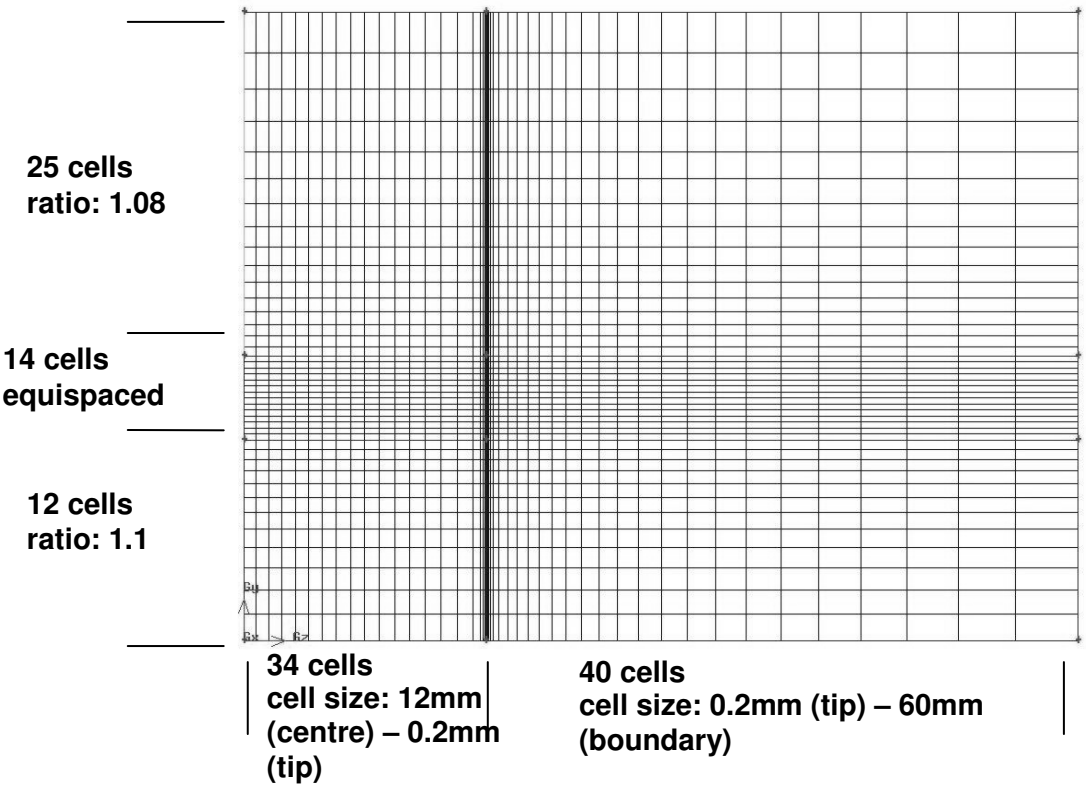


Figure C.14: Cell distribution along vertical and spanwise directions for $h_0$ 1.30

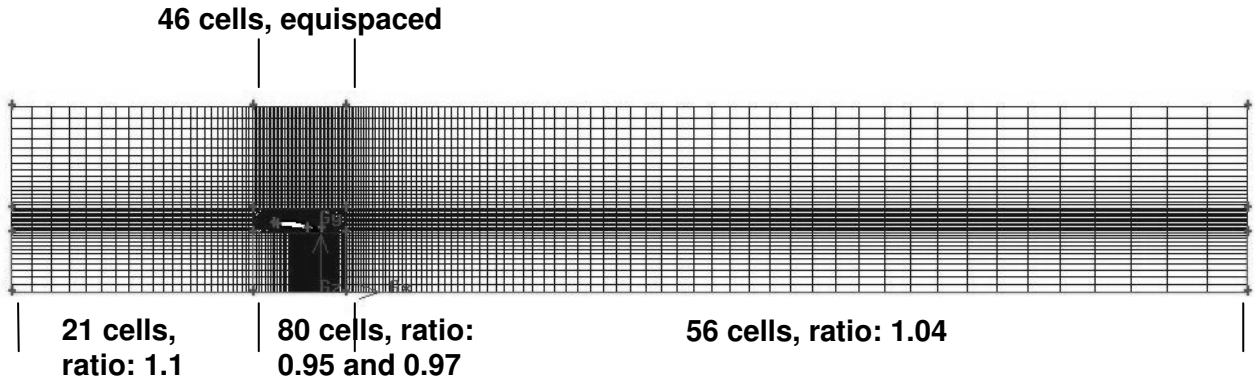


Figure C.15: Cell distribution along streamwise direction for $h_0$ 1.30

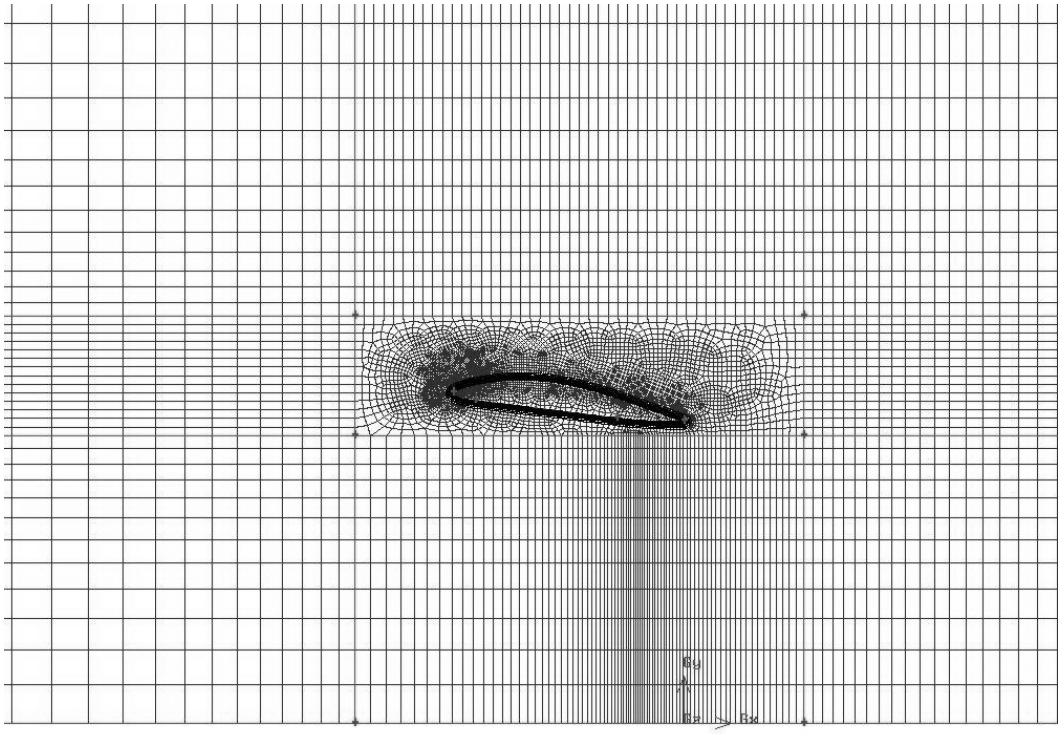

Figure C.16: Close up side view of mesh around wing at $h_0$ 1.30

## C.2.7 MESH QUALITY

It is important to monitor the quality of the cells in the mesh. A highly skewed or misshapen cell could decrease accuracy and destabilise the solution [21]. If too many cells in a domain or area are skewed, then the inaccuracies could affect the validity of the entire solution.

Rapid changes in cell volume between adjacent cells translate into larger truncation errors. A truncation error is the difference between the partial derivatives in the governing equations and their discrete approximations. Therefore smooth transitions between cell sizes should be an important consideration when generating a mesh.

### C.2.7.1 Cell Skewness – EquiAngle Skew

Skewness is defined as the difference between the shape of the cell and the shape of an equilateral cell of equivalent volume [21]. Ideal quadrilateral (hexahedral) meshes will have vertex angles close to 90 degrees. The "EquiAngle Skew" feature of Gambit® allows the user to determine the skewness of the cells in the mesh. The higher the skewness factor, the more skew the cell is. Cells with a skewness factor of 1are characterised by nodes that are nearly coplanar [21]. Table C.3 shows the resultant EquiAngle skewness rating of the different flat ground plane models.

Table C.3: EquiAngle skewness comparison for flat ground plane mesh

| **Skewness Factor** | | **% of Total No. of Cells** | | | |
|---|---|---|---|---|---|
| **From** | **To** | **0.06** | **0.12** | **0.50** | **1.30** |
| 0 | 0.1 | 86.82 | 86.73 | 86.53 | 87.02 |
| 0.1 | 0.2 | 7.86 | 8.14 | 8.54 | 8.04 |
| 0.2 | 0.3 | 2.33 | 2.13 | 2.10 | 2.15 |
| 0.3 | 0.4 | 0.40 | 2.48 | 2.24 | 2.25 |
| 0.4 | 0.5 | 0.15 | 0.33 | 0.27 | 0.36 |
| 0.5 | 0.6 | 0.03 | 0.15 | 0.19 | 0.14 |
| 0.6 | 0.7 | 0.03 | 0.02 | 0.08 | 0.02 |
| 0.7 | 0.8 | 0.00 | 0.03 | 0.03 | 0.03 |
| .08 | 0.9 | 0.00 | 0.00 | 0.02 | 0.00 |



This shows that the vast majority of cells were not very skewed at all. Furthermore, the maximum value for most of the models was about 0.77, with very few cells exceeding this value.

### C.2.7.2 Cell Aspect Ratio

Aspect ratio is a measure of the stretching of the cell. High aspect ratio cells can cause large increase in cell size, which can lead to large truncation errors in the solution. However, if the flow is mostly aligned with the cells, then high aspect ratio cells may yield an accurate result, while reducing the number of cells in the mesh due to the larger cell size. However, a general rule of thumb is to avoid aspect ratios in excess of 5:1 [21].

In these meshes, the cells with the largest aspect ratio are at the extremities of the domain, and so are far away from the wing. Therefore they should not cause any inaccuracies to the flow around the wing.

## C.2.8 TOTAL NUMBER OF CELLS

The total number of cells for the different meshes is given in Table C.4. These are averaged values because slight differences are caused by the varying number of cells in the unstructured mesh region around the airfoil.

Table C.4: Average total number of cells for the flat ground plane model

| $h_0$ | **0.06** | **0.12** | **0.50** | **1.30** |
|---|---|---|---|---|
| **No. of cells** | 1.30 million | 1.30 million | 1.32 million | 1.32 million |

# C.3 WAVY GROUND PLANE MODEL

In order to simulate waves in the ground plane, a sliding mesh model was used. The waves were modelled as a solid wall boundary and then made to translate past the wing. After the results for the flat ground plane model were analysed, it was found that the mesh used for the flat ground plane model was acceptable. Therefore it was decided that the old model would be used, with a new region added on below that would form the sliding region. The mesh for the $h_0$ = 0.06 ground clearance (without the ground boundary layer) would be used for the stationary region as this allowed the entire waveform of the highest waves to fit into the new sliding region, while maintaining the correct clearances.

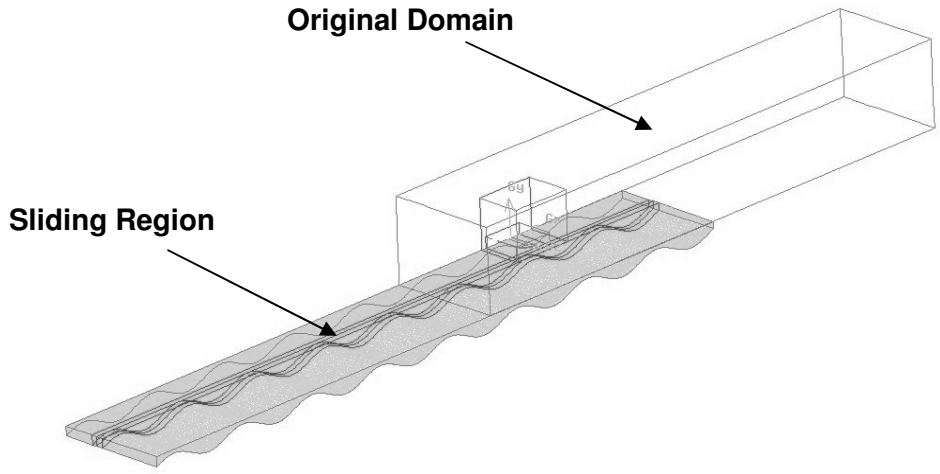


Figure C.17: Original mesh domain with new sliding mesh region below

The sliding mesh region will translate along the bottom surface of the stationary domain. As the waves had to move at the same velocity as the air, the whole domain was made to translate at 20.827 m/s. The upper surface of the sliding domain and the lower surface of the stationary domain had to intersect in order to allow proper mating between the two regions. By setting the correct boundary conditions, Fluent® would detect where the two domains would or wouldn't overlap.

## C.3.1 $h_0$ 0.06 DOMAIN WITHOUT GROUND BOUNDARY LAYER

As there was no longer a flat ground plane in close proximity to the wing, it was decided to coarsen the ground boundary layer mesh. This would reduce the number of cells in the mesh, but more importantly would even out the cell size and so prevent any large changes in cell size in that area. Figure C.18 shows the resulting mesh. The new mesh distribution is labelled in Figure C.18. The resulting domain had a total of 1.05 million cells.

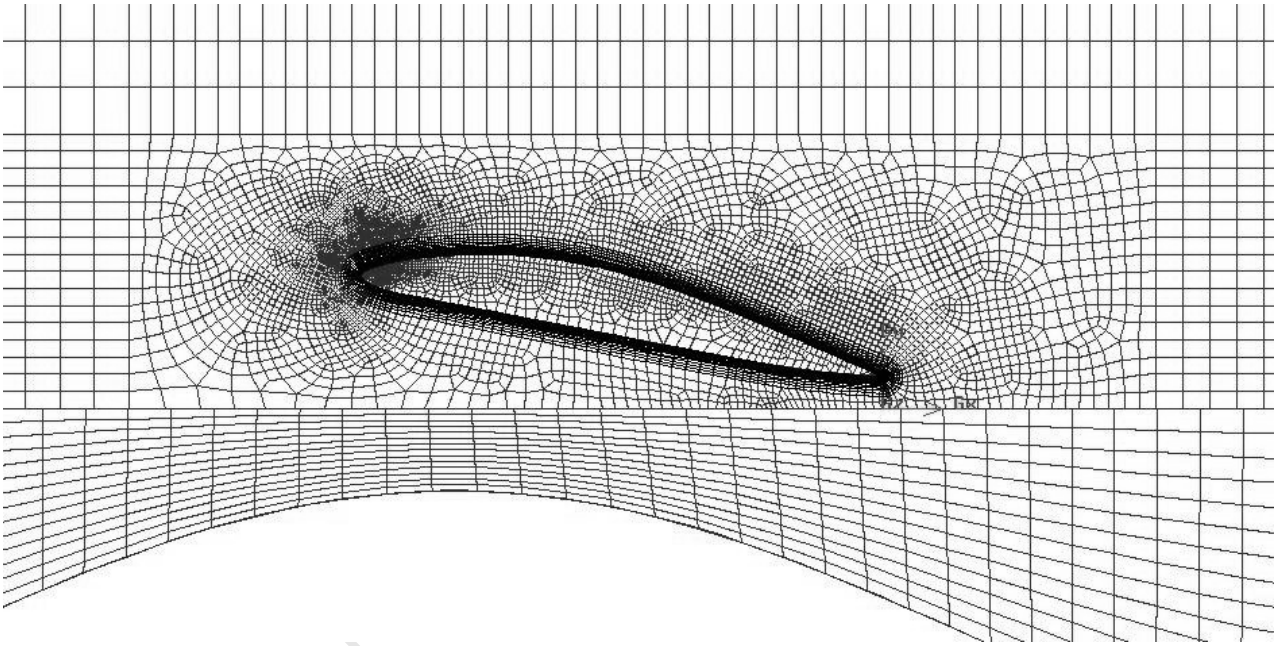

Figure C.18: Side view of new mesh without the fine ground boundary layer

## C.3.2 SLIDING REGION MESH

This section outlines how the mesh distribution for the sliding region was determined.

### C.3.2.1 Streamwise and Vertical Cell Distribution

In order to determine the best cell distribution in the region, the 2D model was again used for quick comparisons between different mesh densities. Initially, an arbitrary mesh distribution of 500 cells in the streamwise direction and 16 cells vertically was chosen. It was thought that cells 10 units long would be sufficient to model the flow in the sliding region. A denser mesh could have been used as only the region below the wing was of

real importance, but as a large portion of the sliding region would move under the wing, it would have resulted in a very large cell count.

Finally it was decided that a cell distribution of 400 (streamwise) by 14 (vertical) cells would be adequate, as it produced similar results to the 500 x 16 mesh. The graph in Figure C.19 illustrates the $C_L$ values for three different meshes that were compared against each other. A higher mesh density was not tested as the cell count would have been too high for the RAM specification of the computer. Figure C.20 illustrates the mesh distribution that was used.

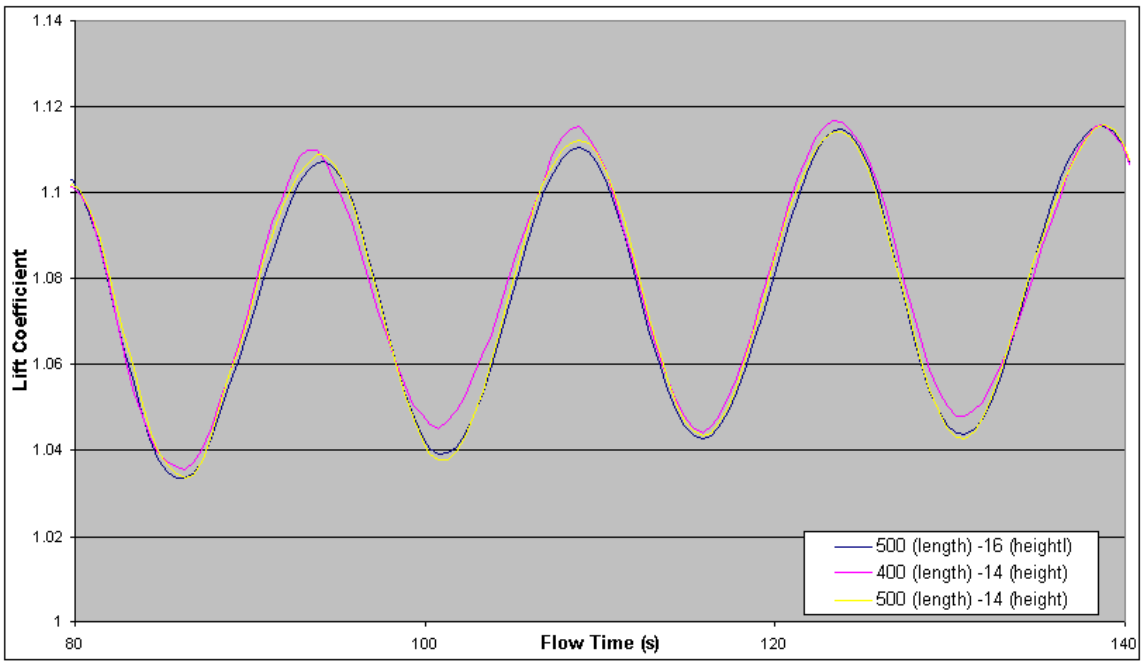


Figure C.19: $C_L$ comparison between different sliding region mesh densities

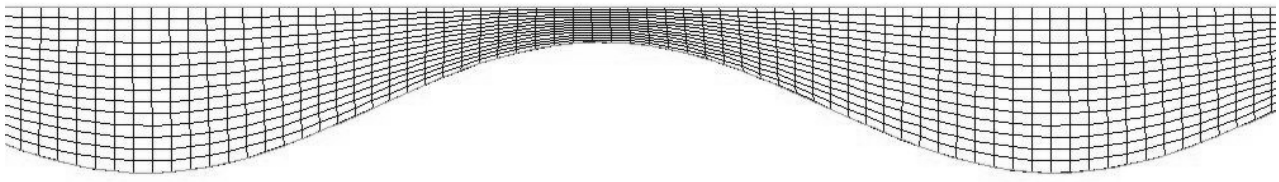

Figure C.20: Side view of sliding region mesh

### C.3.2.2 Spanwise Distribution

The spanwise distribution of cells was chosen to be identical to that of the stationary domain. This was done in order to minimise the error introduced by interpolating values between the stationary and moving nodes. This meant that the values would only have to be interpolated in the streamwise direction.

After subsequent testing however, it was found that the spanwise distribution of cells was causing turbulent viscosity ratio problems. This was probably due to the large changes in cell size from cell to cell. This meant that the grid could not properly resolve any extreme flow effects and so would generate high viscosity in the turbulent region which is not realistic. So, with the added affect of the waves, this mesh would not work as well as for the flat ground plane model.

For that reason it was decided to use a much coarser cell distribution in order to alleviate this problem.. The resultant spanwise cell distribution is shown in Figure C.21.



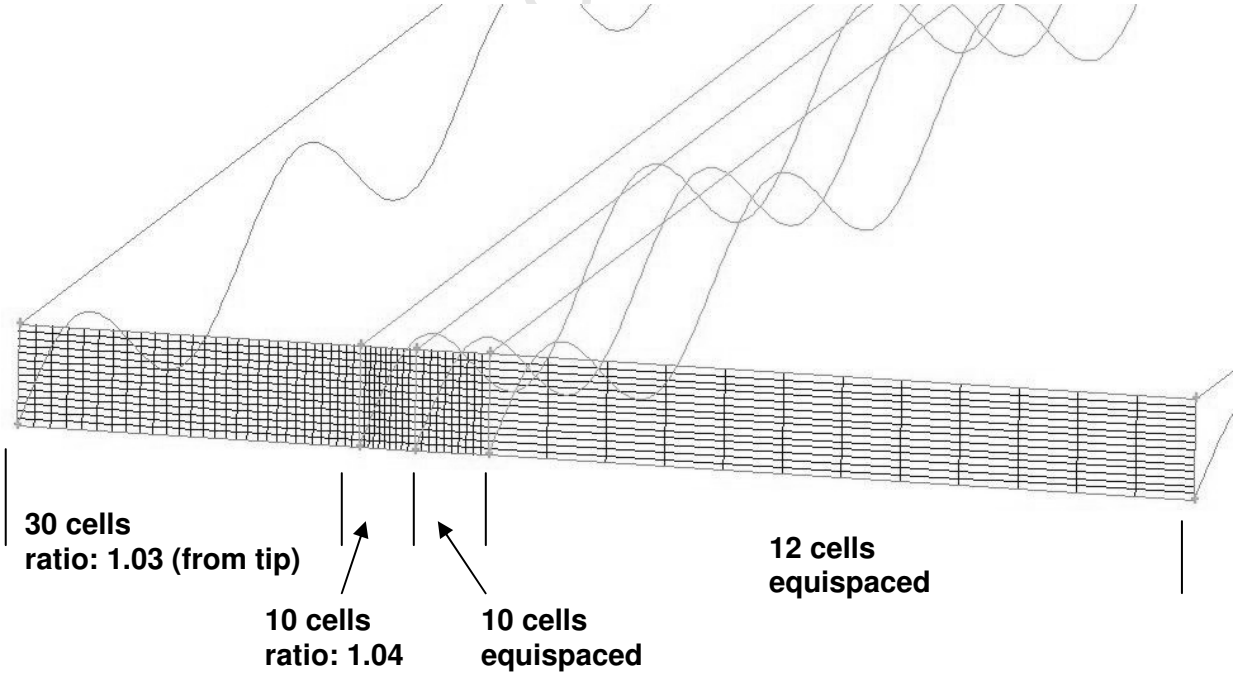


Figure C.21: Spanwise cell distribution for the sliding region

To ensure that the results would not be compromised by the new mesh, it was compared against the original mesh for the simple flat ground plane. The mesh was tested at different $h_0$ values and at two different angles of attack. The results of the comparison are shown in Table C.5. The new mesh was found to produce similar results to the original model. Therefore it was decided that this new cell distribution was acceptable, since the resultant force coefficients did not change significantly with the new cell distribution.

Table C.5: Comparison of new spanwise mesh with old mesh

| $h_0$ | $\alpha$ (°) | Original Mesh | | New Mesh | |
|---|---|---|---|---|---|
| | | $C_D$ | $C_L$ | $C_D$ | $C_L$ |
| 0.06 | 1 | 0.008 | 0.214 | 0.007 | 0.219 |
| 0.06 | 7 | 0.035 | 0.958 | 0.033 | 0.961 |
| 0.50 | 1 | 0.016 | 0.253 | 0.011 | 0.253 |
| 0.50 | 7 | 0.039 | 0.671 | 0.039 | 0.670 |

## C.3.3 MESH QUALITY OF THE SLIDING REGION

The mesh created for the sliding region was fairly regular and very structured. Therefore the resulting mesh would not have been very badly distorted, and would therefore have been of high quality.

### C.3.3.1 Cell Skewness - EquiAngle Skew

The mesh for the sliding region was a regular, structured grid. This meant that the cells would not have been skewed in this region. Therefore the skewness values for the entire mesh were looked at. As the 1$c$ wavelength and the 4$c$ wavelength represented the extremes of the wavy ground plane meshes, these values have been supplied in Table C.6 for analysis. These values show that the vast majority of cells were not very skewed at all. The maximum value for most of the models was about 0.77.

Table C.6: EquiAngle skewness comparison between wavy ground plane meshes

| Skewness Factor | | % of Total No. of Cells | |
|---|---|---|---|
| **From** | **To** | **1wave_1h** | **4wave_4h** |
| 0 | 0.1 | 79.36 | 77.65 |
| 0.1 | 0.2 | 13.71 | 14.96 |
| 0.2 | 0.3 | 4.74 | 5.27 |
| 0.3 | 0.4 | 1.93 | 1.88 |
| 0.4 | 0.5 | 0.2 | 0.20 |
| 0.5 | 0.6 | 0.05 | 0.03 |
| 0.6 | 0.7 | 0.01 | 0.01 |
| 0.7 | 0.8 | 0.00 | 0.00 |

### C.3.3.2 Aspect Ratio

In general the aspect ratios for the cells in the sliding region were low. It was only for the case of the highest wave height that the cells became squashed. But the aspect ratio was still acceptable for this mesh.

## C.3.4 Total Number of cells

The number of cells in the sliding region was kept constant at 347 200 cells. The same stationary region was also used each time, which had almost 1.05 million cells. Therefore the total number of cells in the wavy ground plane model was approximately 1.65 million cells.

# APPENDIX D: WAVE PROFILE DATA

List of Tables D-i

D.1. Introduction D-1
D.2. Wavelength Calculation D-1
D.3. Wave Height Calculation D-1
D.4. Setting the Ground Clearance D-2
D.5. Sinusoidal Wave Shape D-2
D.6. Vertical (Y) Co-ordinates D-3
D.7. Streamwise (X) Co-ordinates D-3
D.8. Spanwise (Z) Co-ordinates D-3



## LIST OF TABLES

Table D.1: Length of waves D-1
Table D.2: Suitable wave heights to wavelength ratios D-2
Table D.3: Relative wave amplitude values D-2

# D.1 INTRODUCTION

To generate the waves for the 3D model, first a 2D profile was created. This 2D profile was then extruded outwards from the symmetry plane to form a 3D shape. This section describes the procedure used to generate the 2D profiles. The actual data points used to generate the 2D profile have not been provided here for the reader as there are far too many of them. Following the procedure below would generate the same points for the 2D profiles used in this study.

# D.2 WAVELENGTH CALCULATION

Four different wavelengths were selected for this study. The wavelengths were chosen relative to the wing chord length, in other words they would be multiples of the chord. Therefore four $L_W$ values were selected to represent the four different wavelengths. To calculate the physical length of the wave, the chord was multiplied by the $L_W$. The resultant wavelengths are given in Table D.1.

Table D.1: Length of waves

| $L_W$ | 1 | 2 | 3 | 4 |
|---|---|---|---|---|
| **Wavelength (mm)** | 155 | 310 | 465 | 620 |

# D.3 WAVE HEIGHT CALCULATION

The maximum wave height for each wavelength was set at 1/7 of the wavelength. Furthermore, other wave heights were also selected for the different wavelengths in order to test the effect of changing wavelengths. The longer wavelengths could assume the same heights as the smaller waves, since these height would be smaller than 1/7 of the wavelength. Therefore these same heights would be used for the wavelengths as long as they were below 1/7 of the wavelength. The wave amplitudes ($a_w$) were taken as half of the total wave height. Table D.2 shows the wave height to wavelength ratios that were used during this study. Table D.3 gives the relative wave amplitude values ($a_w/h$).

Table D.2: Suitable wave heights to wavelength ratios

| Wave Height (mm) | Total Wave Height relative to Wavelength | | | |
|---|---|---|---|---|
| | **1** | **2** | **3** | **4** |
| **22.143** | 1/7 | 1/14 | 1/21 | 1/28 |
| **44.286** | | 1/7 | 2/21 | 1/14 |
| **66.429** | | | 1/7 | 3/28 |
| **88.572** | | | | 1/7 |

Table D.3: Relative wave amplitude values

| Wave Height (mm) | Relative Wave Height ($a_w/h$) |
|---|---|
| **22.143** | 0.143 |
| **44.286** | 0.286 |
| **66.429** | 0.429 |
| **88.572** | 0.571 |

# D.4 SETTING THE GROUND CLEARANCE

Due to the oscillating nature of the wave profile, the centre line of the mean wave height was used as the reference line to determine the clearance between the wing and the "ground plane". Since the performance of the wing was known at the four ground clearances used for the flat ground plane, it was decided to use one of these ground clearances for the wavy ground plane model. Out of the ground clearances tested for the flat ground plane, the smallest ground clearance that would be high enough to accommodate all of the wave heights was the $h_0$ of 0.50. This resulted in a height of 77.5mm between the trailing edge of the wing and the wave centre line.

# D.5 SINUSOIDAL WAVE SHAPE

For simplicity, a sine wave was chosen for the wave profile. It would only model an "ideal" wave profile though, because in reality most waves are not true sine waves. A single wave in the ground plane would be modelled as a single sine wave, and would be copied to create the other waves in the ground plane. To create the wave shape, the sine wave was plotted for a unit wavelength. The wavelength was then broken up into $20L_W$ intervals of equal size. In other words, for a $L_W$ of 4, the sine wave was divided into 80 intervals, while for a $L_W$ of 2, only 40 intervals were used. This meant that the distances between each point on the wave would be the same for each wavelength. The height of

the sine wave was calculated at each interval. To obtain the final wave shape, the wavelength and height of the sine wave was scaled up according to the wavelength ($\lambda$) and wave amplitude ($a_w$) respectively.

# D.6 VERTICAL (Y) CO-ORDINATES

To simplify the mesh generation process, the mesh of the flat ground plane ($h_0$ = 0.06) was used. This meant that the trailing edge of the wing was 9.3mm above the bottom of the mesh. The bottom of the mesh was equivalent to an absolute value of zero in the vertical, or y direction. In order to obtain an $h_0$ of 0.50 between the wing and the wave centre line, the wave centre line would have to be 68.2mm below the original mesh, or -68.2mm absolute. The y co-ordinates of the wave shape were calculated by adding the height of the scaled up sine wave to the absolute height of the wave centre line. This resulted in the absolute vertical co-ordinates for the wave profile.

# D.7 STREAMWISE (X) CO-ORDINATES

The length of the sliding region of the mesh was chosen to be 5m. The start position of this region was chosen to be 4m ahead of the trailing edge of the wing. The trailing edge of the wing was equivalent to an absolute value of zero in the streamwise, or x direction. Therefore the wavelength intervals of the scaled sine wave were added to the absolute value of -4m to obtain the x co-ordinates of the wave profile. Consequently, the first wave was plotted from -4m (absolute) until -4m+$\lambda$ (absolute). The following waves were all plotted directly after one another so that they created a seamless sine wave pattern. It follows from this that the number of waves in the domain would be equal to 5m divided by the $\lambda$ of that wave.

# D.8 SPANWISE (Z) CO-ORDINATES

As the profile was created in 2D, all the z values were chosen as zero, so that the wave profile would lie on the symmetry plane of the model. The 2D wave shape was then extruded to generate the 3D wave profile.